

University of Strathclyde,  
Department of Naval Architecture, Ocean and Marine Engineering

# **Structural Health Monitoring of Offshore Wind Turbines Using iFEM and Peridynamics**

By  
Mingyang Li

A thesis submitted in fulfilment of the requirements for the Degree of  
Philosophy

Glasgow, U.K.

July, 2022

## **AUTHOR STATEMENT**

This thesis is the result of the author's original research. It has been composed by the author and has not been previously submitted for the examination which has led to the award of a degree.

The copyright of this thesis belongs to the author under the terms of the United Kingdom Copyright Acts as qualified by University of Strathclyde Regulation 3.50. Due acknowledgement must always be made of the use of any material contained in, or derived from, this thesis.

Signed: 李铭扬

Date: 05/07/2022

# ACKNOWLEDGEMENT

First of all, I would like to express my greatest and most sincere gratitude to my supervisors- Prof. Erkan Oterkus and Dr. Selda Oterkus, who showed me the meaning of being a real researcher, guided me to carry out academic research and lead me in the way to the success. I am very grateful for their kindest, humblest, and most passive support during my entire PhD period not only for my research but also for my personal life. My deepest appreciation would be given to them for creating the free research environment and building the PMMA research family for us who do not have the chance to live with our family members. I would also thank the opportunities provided by them to meet and communicate with various researchers, universities, and industries. It would be the luckiest thing to have them as my supervisors during this critical stage of my life.

I would like to show my special thanks to my third supervisor and my friend- Dr. Adnan Kefal, who hosted me for three months as a visiting researcher at the Istanbul Technical University, Turkey. I am particularly grateful for his kindness to share his iFEM knowledge with me and for his technical support for my iFEM research. With his help, I can have a better understanding and comprehensive knowledge of the iFEM methodology. I will never forget the moments when we are together, drink tea, and discuss both the iFEM theory and academic life.

I would like to thank Prof. Peilin Zhou for introducing me to University of Strathclyde. Besides, I am also pretty grateful to Prof. Chengi Kuo and Dr. Julia Race for their suggestions and feedback throughout my student and research period.

The financial support from ORE Catapult, Carbon Trust, and University of Strathclyde is greatly acknowledged.

Dr. Xu Ji, Dr. Hanlin Wang, Mr. Yildirim Dirik, and all the other friends and colleagues in the Department of Naval Architecture, Ocean and Marine Engineering are appreciated for their collaborative help and discussion of my research. Thank would also be given to Susan Pawson and all the other staff in the department for their friendly and pleasant help.

Finally, I am very grateful to my family for their endless love. Their strong support and beliefs give me the courage to overcome the difficulties and challenges during my PhD.

*“I love three things in the world  
Sun, Moon, and You  
Sun for morning, Moon for night  
and You forever”*

*To my wife, Liwen Yan,  
for your unconditional wait and love*

# ABSTRACT

The Offshore wind turbine (OWT) is one of the most important installations to harvest the wind source. However, the service environment of the OWT is very severe. Aiming to ensure the safety of the OWT and reduce unnecessary maintenance costs, the structural health monitoring (SHM) system can fulfil the requirements. Inverse Finite Element Method (iFEM) which is a state-of-the-art methodology can overtake the diagnosis task. In this thesis, iFEM is adopted for the tower and composite blade of the OWT under close-to-reality loading conditions. The results give an illustration that iQS4 elements can be utilized successfully for the health monitoring of the OWT even with the practical number of sensors. The provided number of sensors and their locations can also be applied to any scaled tower and blade of the OWT. Then a novel dent damage identification parameter is introduced, which allows the iFEM with the ability to identify the location and shape of the structural defects. Four cases with different damage locations and varying damage sizes are presented to verify the feasibility and accuracy of this new judgment criterion. Attention is also given to the creation of the general inverse plane elements and the major inverse plane crack tip (iPCT) element. The accuracy of this type of element is tested with various numerical examples by estimating the SIF values. With the help of this iPCT element, the limitation of iFEM when dealing with cracked structures can be eliminated and the SIF around the crack tip can also be estimated. Although iFEM can be utilized during the diagnosis process, it would be much better to have another tool for the following prognosis process to establish a comprehensive SHM system for the OWT. Peridynamics (PD) which is very suitable for fracture analysis is chosen. The fatigue and fracture analysis of the triplate on the mooring lines of the OWT is performed. The damage initiation matches well with the expected analytical results and the complete process of the fatigue damage evolution can be captured. Afterward, the PD interaction force equation is updated with the thermal expansion coefficient. Combining with PD cubic polycrystalline model, the porosity effects on brittle fracture and thermally-induced fracture on the microscale are explored. With the increase in the number of grains and pores, the crack especially the newly generated crack will become more serious. But the distribution of the grains and pores will not strongly influence the fracture behaviors. The stronger the grain boundary, the fracture pattern will be willing to convert from intergranular to transgranular. In conclusion, the current study is the first time to apply iFEM and PD to the OWT components, it would be a critical step for the complete SHM system of the OWT, and it can also provide guidance for the real application of iFEM and PD.

# TABLE OF CONTENTS

<b>AUTHOR STATEMENT</b> .....	<b>i</b>
<b>ACKNOWLEDGEMENT</b> .....	<b>ii</b>
<b>ABSTRACT</b> .....	<b>iv</b>
<b>TABLE OF CONTENTS</b> .....	<b>v</b>
<b>LIST OF FIGURES</b> .....	<b>vii</b>
<b>LIST OF TABLES</b> .....	<b>xii</b>
<b>ABBREVIATIONS</b> .....	<b>xiii</b>
<b>1 Introduction</b> .....	<b>1</b>
<b>1.1 Background and motivation</b> .....	<b>1</b>
<b>1.2 Objectives of the research</b> .....	<b>7</b>
<b>1.3 Structure of the thesis</b> .....	<b>7</b>
<b>1.4 Summary</b> .....	<b>8</b>
<b>2 Literature review</b> .....	<b>9</b>
<b>2.1 Introduction</b> .....	<b>9</b>
<b>2.2 Literature review of the iFEM Methodology</b> .....	<b>9</b>
<b>2.3 Literature review of the iPCT element</b> .....	<b>13</b>
<b>2.5 Literature review of the PD theory</b> .....	<b>16</b>
<b>2.6 Literature review of fracture analysis of polycrystalline materials by using PD</b> .....	<b>19</b>
<b>2.7 Summary</b> .....	<b>22</b>
<b>3 Methodology</b> .....	<b>24</b>
<b>3.1 Introduction</b> .....	<b>24</b>
<b>3.2 Approaches against the objectives</b> .....	<b>24</b>
<b>3.3 Summary</b> .....	<b>26</b>
<b>4 Structural health monitoring of the offshore wind turbine using iFEM methodology</b> <b>27</b>	
<b>4.1 Introduction</b> .....	<b>27</b>
<b>4.2 Formulation of the iQS4 element</b> .....	<b>28</b>
<b>4.3 Numerical analysis of the tower</b> .....	<b>35</b>
<b>4.4 Numerical analysis of the NREL 5 MW offshore wind turbine blade</b> .....	<b>52</b>
<b>4.5 Numerical results of the damage identification</b> .....	<b>62</b>
<b>4.6 Summary</b> .....	<b>71</b>
<b>5 Inverse plane crack tip elements</b> .....	<b>74</b>
<b>5.1 Introduction</b> .....	<b>74</b>
<b>5.2 Inverse 4-node and 8-node quadrilateral element</b> .....	<b>74</b>

5.3 The 8-node inverse crack tip element.....	98
5.4 Summary.....	120
<b>6 Fatigue analysis of the triplate of the offshore wind turbine mooring line using Peridynamics .....</b>	<b>122</b>
6.1 Introduction.....	122
6.2 Fundamental Peridynamics theory .....	122
6.3 Peridynamic fatigue model.....	125
6.4 Numerical procedure of the fatigue analysis .....	131
6.5 Numerical results for the fatigue analysis of the triplate .....	131
6.6 Summary.....	151
<b>7 Peridynamic model for cubic polycrystal material.....</b>	<b>153</b>
7.1 Introduction.....	153
7.2 Updated Peridynamic formulations with the thermal expansion coefficient .....	153
7.3 Peridynamic equations for single cubic crystals .....	153
7.4 Peridynamic model for polycrystalline material.....	155
7.5 Investigation of the effect of porosity on intergranular brittle fracture .....	155
7.6 Thermally-Induced Fracture Analysis of Polycrystalline Materials.....	163
7.7 Summary.....	179
<b>8 Discussions.....</b>	<b>181</b>
8.1 Achievements.....	181
8.2 Novelty and contribution to the field.....	182
8.3 Gaps and recommended future work.....	184
8.4 Research outputs.....	185
<b>9 Conclusions.....</b>	<b>188</b>
9.1 Key findings.....	188
9.2 Final remarks .....	189
<b>Appendix.....</b>	<b>190</b>
<b>References.....</b>	<b>195</b>

# LIST OF FIGURES

<b>Figure 3.1</b> The plain dents on the offshore cylindrical structures.....	25
<b>Figure 4.1</b> Tri-floater offshore wind turbine with stiffened cylinders as main columns (Das et al., 2003) .....	28
<b>Figure 4.2</b> (a) iQS4 element with the local coordinate system (LCS) ( $x,y,z$ ) at the central plane and global coordinate system (GCS) ( $X,Y,Z$ ) of the structure (b) the total 6 DOFs in LCS (Kefal et al., 2016) .....	30
<b>Figure 4.3</b> Strain collection for iQS4 element using FBG sensors .....	31
<b>Figure 4.4</b> (a) Discretisation of the structure with inverse finite elements, (Kefal, 2017) (b) overview of iFEM methodology .....	32
<b>Figure 4.5</b> Mesh size (a) dense FEM mesh (b) coarse iFEM mesh .....	36
<b>Figure 4.6</b> Sensor locations for reduced sensors case (a) 328 elements (b) 176 elements .....	38
<b>Figure 4.7</b> Contour plot of $U_T$ (unit: m) for static condition .....	40
<b>Figure 4.8</b> Contour plot of $\sigma_{vm}$ (unit: Pa) for static condition .....	40
<b>Figure 4.9</b> Variation of wind speed at reference height against time .....	41
<b>Figure 4.10</b> The positions of the six nodes on the horizontal x-y plane .....	45
<b>Figure 4.11</b> Variation of total displacements $U_T$ (m) against time (s) for four nodes located at 10 m, 20 m, 40 m, and 60 m .....	46
<b>Figure 4.12</b> Variation of von Mises stresses $\sigma_{vm}$ (Pa) against time (s) for four nodes located at 10 m, 20 m, 40 m, and 60 m .....	47
<b>Figure 4.13</b> Variation of total displacements $U_T$ (m) against time (s) for six nodes located at 40 m .....	48
<b>Figure 4.14</b> Variation of von Mises stresses $\sigma_{vm}$ (Pa) against time (s) for six nodes located at 40 m .....	49
<b>Figure 4.15</b> Contour plot of total displacements, $U_T$ (unit: m) for the dynamic condition at 5 s .....	51
<b>Figure 4.16</b> Contour plot of von Mises stresses, $\sigma_{vm}$ (unit: Pa) for the dynamic condition at 5 s .....	51
<b>Figure 4.17</b> The geometry of the blade from NuMAD .....	54
<b>Figure 4.18</b> The mesh for FEM (a) and iFEM (b) models .....	55
<b>Figure 4.19</b> The selected sensor locations for iFEM analysis.....	55
<b>Figure 4.20</b> The plots of the total displacements ( $m$ ) .....	61
<b>Figure 4.21</b> The plots of the total rotations ( $rad$ ) .....	61
<b>Figure 4.22</b> Damage locations for (a) Case2, (b) Case3, (c) Case4, and (d) Case5.....	63
<b>Figure 4.23</b> (a) Dense mesh for FEM model and (b) Coarse mesh for iFEM model .....	64
<b>Figure 4.24</b> Sensor locations for the reduced sensor model .....	65
<b>Figure 4.25</b> Contour plot of $U_T$ displacement (unit: m) for Case1 .....	66
<b>Figure 4.26</b> Contour plot of $\varepsilon_{vm}$ strain for FEM of Case1 .....	66
<b>Figure 4.27</b> Damage parameter variation for Case2 .....	67
<b>Figure 4.28</b> Von Mises strain variation for Case2 .....	68
<b>Figure 4.29</b> Damage parameter variation for Case3 .....	68
<b>Figure 4.30</b> Von Mises strain variation for Case3 .....	69
<b>Figure 4.31</b> Damage parameter variation for Case4 .....	70

<b>Figure 4.32</b> Von Mises strain variation for Case4 .....	70
<b>Figure 4.33</b> Damage parameter variation for Case5 .....	71
<b>Figure 4.34</b> Von Mises strain variation for Case5 .....	71
<b>Figure 5.1</b> Random and standard 4-node and 8-node quadrilateral element .....	75
<b>Figure 5.2</b> The loading and boundary condition of Case 1 .....	80
<b>Figure 5.3</b> Three different meshes of Case 1 .....	81
<b>Figure 5.4</b> The sensor locations of Case 1 with 1600 elements .....	83
<b>Figure 5.5</b> The plots of displacements of Case 1 with 16 elements .....	84
<b>Figure 5.6</b> The plots of displacements of Case 1 with 100 elements .....	85
<b>Figure 5.7</b> The plots of displacements of Case 1 with 1600 elements .....	86
<b>Figure 5.8</b> The loading and boundary conditions of Case 2 .....	87
<b>Figure 5.9</b> Two different meshes of Case 2 .....	88
<b>Figure 5.10</b> The plots of displacements of Case 2 with 125 elements .....	89
<b>Figure 5.11</b> The plots of displacements of Case 2 with 2000 elements .....	90
<b>Figure 5.12</b> The sensor locations of Case 2 with 2000 elements .....	91
<b>Figure 5.13</b> The loading and boundary conditions of Case 3 .....	92
<b>Figure 5.14</b> The plots of displacements of Case 3 with 2000 elements .....	93
<b>Figure 5.15</b> The loading and boundary condition of Case 4 .....	94
<b>Figure 5.16</b> The mesh for Case 4 .....	94
<b>Figure 5.17</b> The sensor locations for Case 4 .....	96
<b>Figure 5.18</b> The plots of displacements of Case 4 .....	97
<b>Figure 5.19</b> The plots of von Mises stress of Case 4 .....	98
<b>Figure 5.20</b> Quarter-point crack tip element (a) and quarter-point elements around the crack tip .....	98
<b>Figure 5.21</b> The displacements of the crack tip for the displacement extrapolation method (a) full model, (b) half (symmetrical) model .....	101
<b>Figure 5.22</b> The geometry of the plate with edge crack (a) and the loading and symmetrical boundary conditions of the quarter of the plate (b) for Case 1 .....	103
<b>Figure 5.23</b> The fine mesh for Case 1. (a) FEM, (b) iFEM .....	104
<b>Figure 5.24</b> The plots for Case 1. The displacements in x-direction: (a) FEM, (b) iFEM. The displacements in y-direction: (c) FEM, (d) iFEM .....	105
<b>Figure 5.25</b> The geometry of the plate with central crack (a) and the loadings and symmetrical boundary conditions of the quarter of the plate (b) for Case 2 .....	107
<b>Figure 5.26</b> The plots for Case 2. The displacements in x-direction: (a) FEM, (b) iFEM. The displacements in y-direction: (c) FEM, (d) iFEM .....	109
<b>Figure 5.27</b> The mesh for Case 3 (edge crack) and Case 4 (central crack) .....	110
<b>Figure 5.28</b> The sensor locations for Case 3 (a) and Case 4 (b) .....	111
<b>Figure 5.29</b> The plots for Case 3. The displacements in x-direction: (a) FEM, (b) iFEM, (c) iFEM-r. The displacements in y-direction: (d) FEM, (e) iFEM, (f) iFEM-r .....	112
<b>Figure 5.30</b> The plots for Case 4. The displacements in x-direction: (a) FEM, (b) iFEM, (c) iFEM-r. The displacements in y-direction: (d) FEM, (e) iFEM, (f) iFEM-r .....	114
<b>Figure 5.31</b> (a) The geometry, loadings, and boundary conditions for Case 5. (b) The mesh of both FEM and iFEM analysis for Case 5. (c) The sensor locations for Case 5 .....	115
<b>Figure 5.32</b> The plots for Case 5. The displacements in x-direction: (a) FEM, (b) iFEM, (c) iFEM-r. The displacements in y-direction: (d) FEM, (e) iFEM, (f) iFEM-r .....	117

<b>Figure 5.33</b> (a) The geometry, loadings, and boundary conditions for Case 6. (b) The sensor locations for Case 6.....	118
<b>Figure 5.34</b> The plots for Case 6. The displacements in x-direction: (a) FEM, (b) iFEM, (c) iFEM-r. The displacements in y-direction: (d) FEM, (e) iFEM, (f) iFEM-r .....	120
<b>Figure 6.1</b> PD horizon and interactions between material points .....	125
<b>Figure 6.2</b> Calibration phase(I) parameters $A_1$ and $m_1$ (a) without fatigue limit, (b) with fatigue limit.....	127
<b>Figure 6.3</b> Variation of damage index, $\phi$ , on in plate with a pre-existing crack .....	130
<b>Figure 6.4</b> The geometry of the plate (Sajith et al., 2020) .....	131
<b>Figure 6.5</b> The propagation of the crack at different load cycles .....	133
<b>Figure 6.6</b> The length of the crack tip against load cycles.....	134
<b>Figure 6.7</b> The shape of the triplate (Hendrik Veder Group).....	135
<b>Figure 6.8</b> The S-N curve for chain steel (DNV and Lloyd, 2015) .....	136
<b>Figure 6.9</b> The plot for crack tip length versus the number of load cycles.....	137
<b>Figure 6.10</b> The PD model of the triplate .....	139
<b>Figure 6.11</b> The flow chart of processing the loading data.....	140
<b>Figure 6.12</b> The sinusoidal loadings cycle on the bottom bridle eyes .....	141
<b>Figure 6.13</b> The plots of deformations for PD and FEM results .....	143
<b>Figure 6.14</b> The plots of displacements for the triplate under constant amplitude but variable $\theta$ loading condition .....	145
<b>Figure 6.15</b> The distribution of the stretch value for the constant amplitude but variable $\theta$ loading condition .....	145
<b>Figure 6.16</b> Plots of the damage of different load cycles under constant amplitude loading when $\theta = 30^\circ$ .....	147
<b>Figure 6.17</b> Plots of the damage of different load cycles under constant amplitude loading when $\theta = 45^\circ$ .....	148
<b>Figure 6.18</b> Plots of the damage of different load cycles under constant amplitude loading when $\theta = 60^\circ$ .....	149
<b>Figure 6.19</b> Plots of the damage of different load cycles under constant amplitude loading when $\theta = 90^\circ$ .....	150
<b>Figure 7.1</b> PD model for polycrystalline when the orientation of the crystal is $0^\circ$ (blue lines represent Type-1 bonds and red lines represent Type-2 bonds) .....	154
<b>Figure 7.2</b> Crystals generated by the Voronoi tessellation method .....	155
<b>Figure 7.3</b> The polycrystalline material model subjected to velocity boundary conditions .	156
<b>Figure 7.4</b> Results of crack propagation without porosity at $2 \mu\text{s}$ ; (a) crack distribution with grains, (b) damage.....	157
<b>Figure 7.5</b> The case with 150 grains and 2% porosity; (a) the distribution of pores, (b) crack distribution with 150 grains, (c) damage at $0.5 \mu\text{s}$ , (d) damage at $1 \mu\text{s}$ , (e) damage at $1.5 \mu\text{s}$ , (f) damage at $2 \mu\text{s}$ .....	158
<b>Figure 7.6</b> The case with 150 grains but different 2% porosity distribution; (a) the distribution of pores, (b) crack distribution with 150 grains, (c) damage at $0.5 \mu\text{s}$ , (d) damage at $1 \mu\text{s}$ , (e) damage at $1.5 \mu\text{s}$ , (f) damage at $2 \mu\text{s}$ .....	159
<b>Figure 7.7</b> The case with both different grain distribution and 2% porosity, (a) the distribution of pores, (b) crack distribution with 150 grains, (c) damage at $0.5 \mu\text{s}$ , (d) damage at $1 \mu\text{s}$ , (e) damage at $1.5 \mu\text{s}$ , (f) damage at $2 \mu\text{s}$ .....	160

<b>Figure 7.8</b> Porosity distribution (left), crack distribution with grains (middle) and damage at 2 $\mu$ s (right), (a) 150 grains, (b) 100 grains, (c) 50 grains.....	161
<b>Figure 7.9</b> Porosity distribution (left), crack distribution with grains (middle) and damage at 2 $\mu$ s (right), (a) 3% porosity, (b) 4% porosity, (c) 5% porosity.....	162
<b>Figure 7.10</b> Crack distribution with grains (left) and damage at 2 $\mu$ s (right), (a) GBC = 0.5, (b) GBC = 1.0.....	163
<b>Figure 7.11</b> Two-dimensional plate subjected to thermal loading.....	164
<b>Figure 7.12</b> Displacements of material points along the central lines of an isotropic material.....	165
<b>Figure 7.13</b> Displacements of material points along the central lines of a single cubic crystal.....	165
<b>Figure 7.14</b> Polycrystalline structure subjected to thermal loading.....	166
<b>Figure 7.15</b> Displacements of the material points along the central lines of cubic polycrystals.....	166
<b>Figure 7.16</b> Pre-existing cracks (a) horizontal, (b) vertical.....	167
<b>Figure 7.17</b> Crack propagation for the vertical pre-existing crack case for the different number of grains. From the top to the bottom the number of the grains are: 20, 50, and 100.....	168
<b>Figure 7.18</b> Crack propagation for the vertical pre-existing crack case at 3 $\mu$ s for 20, 50, and 100 grains.....	168
<b>Figure 7.19</b> Crack propagation for the horizontal pre-existing crack case for the different number of grains. From the top to the bottom the number of the grains are: 20, 50, and 100.....	169
<b>Figure 7.20</b> Crack propagation for the horizontal pre-existing crack case at 3 $\mu$ s for 20, 50, and 100 grains.....	169
<b>Figure 7.21</b> Crack propagation for the vertical pre-existing crack for different values of GBC. From the top to the bottom the values of GBC are: 0.5, 1, and 2.....	170
<b>Figure 7.22</b> Crack propagation for the vertical pre-existing crack at 3 $\mu$ s for GBC values of (a) 0.5, (b) 1, and (c) 2.....	170
<b>Figure 7.23</b> Crack propagation for the horizontal pre-existing crack case for different values of GBC. From the top to the bottom the values of GBC are: 0.5, 1, and 2.....	171
<b>Figure 7.24</b> Crack propagation for the horizontal pre-existing crack case at 3 $\mu$ s for GBC values of (a) 0.5, (b) 1, and (c) 2.....	171
<b>Figure 7.25</b> Crack propagation for the vertical pre-existing crack case for the different number of grains with 50% silicon carbide. From the top to the bottom the number of the grains are: 20, 50, and 100.....	172
<b>Figure 7.26</b> Crack propagation for the vertical pre-existing crack case with crystals and material composition at 2 $\mu$ s for 20, 50, and 100 grains with 50% silicon carbide.....	173
<b>Figure 7.27</b> Crack propagation for the vertical pre-existing crack for different percentages of silicon carbide with 100 grains. From the top to the bottom the percentages of the silicon carbide are: 50%, 10%, and 0%.....	174
<b>Figure 7.28</b> Crack propagation for the vertical pre-existing crack case with crystals and material composition at 2 $\mu$ s for 50%, 10%, and 0% silicon carbide with 100 grains.....	174
<b>Figure 7.29</b> Crack propagation for the vertical pre-existing crack case for different values of GBC with 100 grains and 50% silicon carbide. From the top to the bottom the values of GBC are: 0.5, 1, and 2.....	175

<b>Figure 7.30</b> Crack propagation for the vertical pre-existing crack case with crystals and material composition at $2 \mu s$ for 0.5, 1, and 2 GBC with 100 grains.....	176
<b>Figure 7.31</b> Crack propagation for the horizontal pre-existing crack case for the different number of grains with 50% silicon carbide. From the top to the bottom the number of the grains are: 20, 50, and 100.....	177
<b>Figure 7.32</b> Crack propagation for the horizontal pre-existing crack case with crystals and material composition at $2 \mu s$ for 20, 50, and 100 grains with 50% silicon carbide.....	177
<b>Figure 7.33</b> Crack propagation for the horizontal pre-existing crack case for different percentages of silicon carbide with 100 grains. From the top to the bottom the percentages of the silicon carbide are: 50%, 10%, and 0% .....	178
<b>Figure 7.34</b> Crack propagation for the horizontal pre-existing crack case with crystals and material composition at $2 \mu s$ for 50%, 10%, and 0% silicon carbide with 100 grains .....	178
<b>Figure 7.35</b> Crack propagation for the horizontal pre-existing crack case for different values of GBC with 100 grains and 50% silicon carbide. From the top to the bottom the values of GBC are: 0.5, 1, and 2.....	179
<b>Figure 7.36</b> Crack propagation for the horizontal pre-existing crack case with crystals and material composition at $2 \mu s$ for 0.5, 1, and 2 GBC with 100 grains.....	179
<b>Figure A.1</b> Crack propagation for the vertical pre-existing crack case for different numbers of PD points. From the top to the bottom the number of the points is: $100 \times 100$ , $200 \times 200$ , and $400 \times 400$ .....	190
<b>Figure A.2</b> Crack propagation for the vertical pre-existing crack case at $2 \mu s$ for $100 \times 100$ , $200 \times 200$ , and $400 \times 400$ points .....	191
<b>Figure A.3</b> Crack propagation for the horizontal pre-existing crack case for different numbers of PD points. From the top to the bottom the number of the points is: $100 \times 100$ , $200 \times 200$ , and $400 \times 400$ .....	191
<b>Figure A.4</b> Crack propagation for the horizontal pre-existing crack case at $2 \mu s$ for $100 \times 100$ , $200 \times 200$ , and $400 \times 400$ points .....	192
<b>Figure A.5</b> Crack propagation for the vertical pre-existing crack case for different horizon sizes. From the top to the bottom the horizon size is: $2dx$ , $3dx$ , $4dx$ , and $5dx$ .....	193
<b>Figure A.6</b> Crack propagation for the vertical pre-existing crack case at $2 \mu s$ for $2dx$ , $3dx$ , $4dx$ , and $5dx$ horizon sizes .....	193
<b>Figure A.7</b> Crack propagation for the horizontal pre-existing crack case for different horizon sizes. From the top to the bottom the horizon size is: $2dx$ , $3dx$ , $4dx$ , and $5dx$ .....	194
<b>Figure A.8</b> Crack propagation for the horizontal pre-existing crack case at $2 \mu s$ for $2dx$ , $3dx$ , $4dx$ , and $5dx$ horizon sizes .....	194

## LIST OF TABLES

<b>Table 4.1</b> Results for static condition.....	39
<b>Table 4.2</b> Differences between iFEM/iFEM-r and FEM for static condition .....	39
<b>Table 4.3</b> Wave parameters .....	43
<b>Table 4.4</b> Results of the dynamic condition at 5 s .....	50
<b>Table 4.5</b> Differences between iFEM/iFEM-r and FEM for the dynamic condition at 5 s ....	50
<b>Table 4.6</b> The parameters of the blade .....	53
<b>Table 4.7</b> The velocities of wind and rotor .....	56
<b>Table 4.8</b> The results of FEM and iFEM analysis.....	60
<b>Table 4.9</b> Case Studies for iFEM analysis .....	62
<b>Table 5.1</b> Numerical cases for comparison between two inverse plane elements .....	79
<b>Table 5.2</b> The results for Case 1 with 16 elements .....	81
<b>Table 5.3</b> The results for Case 1 with 100 elements .....	81
<b>Table 5.4</b> The results for Case 1 with 1600 elements .....	82
<b>Table 5.5</b> The results for Case 2 with 125 elements .....	88
<b>Table 5.6</b> The results for Case 2 with 2000 elements .....	88
<b>Table 5.7</b> The results of Case 3 .....	92
<b>Table 5.8</b> The results of Case 4 .....	95
<b>Table 5.9</b> Cases for estimating the SIF at the crack tip.....	102
<b>Table 5.10</b> The results of Case 1 .....	104
<b>Table 5.11</b> The results of Case 2 .....	108
<b>Table 5.12</b> The results of Case 3 .....	111
<b>Table 5.13</b> The results of Case 4 .....	113
<b>Table 5.14</b> The results of Case 5 .....	116
<b>Table 5.15</b> The results of Case 6 .....	118
<b>Table 6.1</b> The basic material properties of aluminum 6061-T6 (Nguyen et al., 2021).....	131
<b>Table 6.2</b> The geometrical inputs for the triplate model .....	134
<b>Table 6.3</b> The material properties of R4 steel .....	135
<b>Table 6.4</b> The results of different strengths of rigid zones.....	142
<b>Table 6.5</b> The stretch values and number of loading cycles for four different angles .....	146
<b>Table 7.1</b> Material information for silicon carbide and alumina.....	172

# ABBREVIATIONS

iFEM	Inverse Finite Element Method
PD	Peridynamics
OWT	Offshore wind turbine
LCOE	Level cost of energy
FOWT	Floating offshore wind turbine
O&M	Operations and maintenance
SHM	Structural health monitoring
SIF	Stress intensity factor
iQS4	Inverse 4-node quadrilateral shell
iPCT	Inverse plane crack tip
RNA	Rotor Nacelle Assembly
FBG	Fiber Bragg Grating
FSDT	First-order Shear Deformation Theory
AE	Acoustic emission
ESG	Electrical strain guage
CSD	Chi-Square distribution
FIF	Feature information fusion
RZT	Refined Zigzag Theory
MM	Modal Method
DOF	Degree of freedom
FEM	Finite Element Method
FDA	Fatigue design assessment
CCM	Classical continuum mechanics
FIB-SEM	Focused iron beam-scanning electron microscope
EBSD	Electron Back Scattered Diffraction
DCT	Diffraction contrast tomography
CZM	Cohesive zone model
BEM	Boundary element method
MCZM	Multiscale cohesive zone model
X-FEM	Extended-Finite Element Method
BBPD	Bond-based Peridynamics
SCC	Stress corrosion cracking
SBPD	State-based Peridynamics
LCS	Local coordinate system
GCS	Global coordinate system
iFEM-r	iFEM with reduced sensors
BEMT	Blade element momentum theory
iQP4	Inverse 4-node quadrilateral plane
iQP8	Inverse 8-node quadrilateral plane
EOM	Equation of motion
WLL	Working load limit
GBC	Grain boundary coefficient

# 1 Introduction

This chapter is formed by four sections. The first section (Section 1.1) gives basic information about the requirements for wind energy, the development of offshore wind turbines, the challenges of offshore wind turbines, and the need for structural health monitoring systems for offshore wind turbines. Then the existing SHM systems for the OWTs are reviewed and the weaknesses of these SHM systems draw forth the inverse Finite Element Method (iFEM) and Peridynamics (PD). And iFEM and PD are briefly introduced and the benefits of these two theories are also described. In Section 1.2, the objectives of this thesis are presented. The structure of this thesis is highlighted in the third section (Section 1.3). Finally, a brief summary is given in Section 1.4.

## 1.1 Background and motivation

Nowadays, fossil fuels such as coal, natural gas, and oil still play the dominant role in the energy supply of most countries of the world. According to the data provided by the International Energy Agency, around four in five of the global investment is still given to the conventional non-renewable energy field. (IEA, 2017) However, burning of these non-renewable fuels will contribute to the enormous emission of carbon dioxide which then leads to more serious conditions of global warming and climate change. (Koh and Ng, 2016) Aiming to retard the change of the climate and achieve sustainable development of the world, it is necessary to gradually deplete the utilization of fossil fuels. (Wang et al., 2019)

In recent decades, renewable energy is attracting the attention of the whole energy industry. It can fulfil the surge of the global energy demand and the green gas emission-reducing target at the same time. (Wu et al., 2019) With the support of the worldwide government and the development of technology that reduces the cost of renewable energy, renewable resources will occupy an increasing proportion of the global energy supply. (Sieminski, 2014) Among these various renewable resources, wind power is one of the most promising ones. Compared with the other types of resources, the advantages of wind energy are more obvious in the following aspects: wind energy has the lowest influence on the environment; it is a kind of cost-efficient energy; wind energy is abundant, and it can meet the requirement of sustainability and so forth. (Ren et al., 2021; Wang et al., 2018) More importantly, since the technology of utilizing wind energy is well-established compared to other types of renewable energy sources and the cost

of electricity generated from wind is relatively inexpensive, wind energy is expected to experience fast and tremendous development during the following decades (Tchakoua et al., 2014; Ciang et al., 2008). Over the past twenty years, wind power has already reached 591 GW around the world. (Ohlenforst et al, 2019) Only in 2017, with an additional 52.57 GW capacity making the capacity increase by 10.85% in just a single year. (Lian et al., 2019) With the current tendency of development, it is expected that when it comes to the mid-century, 20% of global electricity will be provided by wind power. (Premalatha et al., 2014)

Depending on the locations, the installations for harvesting the wind energy can be categorized as onshore wind turbines and offshore wind turbines (OWTs). Currently, a large number of wind turbines have been installed and the majority of them are located onshore (Mieloszyk and Ostachowicz, 2017). The onshore wind turbines have already experienced success, and this also guided the development of technology in the wind energy industry. The concept of OWT is proposed in the 1970s. (Castro-Santos and Diaz-Casas, 2016) They are located away from the shore and require a foundation or mooring system to keep the turbine at its location. Although there is a delay in the flourish of the OWTs and the level cost of energy (LCOE) is higher than the onshore turbines, OWTs have huge potential and they receive attraction not only from the offshore industry but also from the academic fields. (Castro-Santos and Diaz-Casas, 2016; Salic et al., 2019) The OWTs are more competitive because, firstly, the negative visual and noise weakness of the onshore turbine is overcome. Then, higher wind speed and steadier wind resources can be obtained in the open sea area. An OWT can reach 4000 hours as the functioning time which is almost twice the onshore installations. (Colmenar-Santos et al., 2016) Besides, large land areas as the locations of the turbines are not required. (Wang et al., 2018; Salic et al., 2019) Even from the commercial perspective, the LCOE of the OWTs is rapidly decreasing. (Bosch et al., 2019)

The first OWT was installed in Sweden in 1990. (Sun et al., 2012) And in the next year, the installation of the first offshore wind farm called Vindely was also finished and the wind farm, located within 3 Km of the coast of Denmark, has a capacity of 450 KW. (Olsen and Dyre, 1993) The initial OWTs are in shallow water with a water depth of less than 50 m. (Cheng et al., 2019) With the demand for larger capacity, the OWTs have experienced a tendency for deeper and deeper water. Floating offshore wind turbines (FOWT) provide a reasonable solution. (Li et al., 2020) The first FOWT is called Hywind Demo with a capacity of 23 MW, and it was installed on the west coast of Norway in the June of 2009. (Skaare et al., 2015) The 6 MW FOWT in the North Sea of Scotland can stand a water depth of 100 m. (Skaare et al.,

2015) For the entire global offshore wind energy industry, the capacity has gradually reached 22 GW by the end of 2019 and among which 9945 KW is offered by the UK leading in Europe. (Sun et al., 2012; Micallef and Rezaeiha, 2021) For the future, the European Union is planning to give 12 billion Euro investments to the offshore wind industry. (European Wind Energy Association, 2009) Apart from Europe, China is planning to increase the offshore wind capacity to 200 GW which will be almost 10 times the onshore wind energy. (Wu et al., 2019) And with the improvement of the technology, the power of the OWT will also become 1.5 to 2 times higher than the onshore wind turbine. (Li et al., 2020)

More capacity and deeper water usually mean the OWTs need to have a larger size with a higher tower and longer blades. However, the OWT is a kind of unmanned and remote-controlled structure, and it is usually surrounded by harsh marine environments. (Yang et al., 2014) It has to stand strong hydrodynamic loads from the current and wave and aerodynamic loads caused by the wind. Apart from common loads, OWTs are also facing some short-term extreme loadings caused by storms, heavy snow, and even earthquakes (Yang et al., 2014). Besides, the fatigue contributed by excessive structural vibration, corrosion, and erosion will also result in the thickness reduction of the OWT. (Wang et al., 2018; Sun et al., 2012; Li et al., 2020; Sun and Jahangiri, 2019) The above severe problems together with deep water depth, complex seabed status, structural defects, material degeneration, and even some operating factors may cause the shut-down or even failure of the OWTs. (Wang et al., 2018; Li et al., 2020) Just in 2014, about 1000 accidents are reported for the OWT. (Seyr and Muskuus, 2016) The recent typical accidents in the offshore turbine have been collected by Lian et al. (Lian et al., 2019) Additionally, controlling the operations and maintenance cost (O&M) would be a practical way to lower the LCOE and increase the competitiveness of offshore wind energy. (Castro-Santos and Diaz-Casas, 2016; Yeter et al., 2020) It is reported that, for an OWT project, O&M cost will take one in five portions of the total LCOE. (Blanco, 2009) There is still a large distance from the value of onshore wind turbines which is only about 5%. (Sun et al., 2012) In addition, the maintenance of the OWT is also two to three times that of onshore installations and maintenance would be more significant than operating in controlling the LCOE. (Blanco, 2009; Chen, 2011)

Since the OWT is always not easy to have accessibility and usually the personnel and vessels which can be in-service are limited, the maintenance of the OWT is relatively challenging. To decrease downtime, reduce energy loss, and maximize profit, structural health monitoring (SHM) would be a useful tool. For the typical SHM process, initially, the sensing systems will

be installed on the structure at proper locations. Then, the sensing systems will collect the required real-time data from the structure and report the data to the SHM systems. Finally, utilizing the collected data, the SHM systems can obtain the global or local state of the monitored structure (Kefal, 2017). According to Gherlone et al. (Gherlone et al., 2012), a good SHM system should easily treat complicated structures and their boundary conditions. Moreover, the loading conditions, material properties, and even some inherent errors (which cannot be avoided during the process of measuring data) should not affect the stability and accuracy of the system. In addition, the SHM system must be fast enough to perform a real-time monitoring process. (Gherlone et al., 2012)

With the help of the SHM system, unusual behaviors, such as unhealthy conditions and structural failure, of the structure can be accurately detected. Furthermore, additional management including inspection, maintenance, and repair of the structure can also be enhanced under the guidance of SHM systems (Lu et al., 2009). The process of maintenance can be scheduled in a more orderly manner, which will reduce unnecessary inspection and repair. For an OWT, SHM systems can contribute to generating stable and reliable electricity by decreasing the time of downtime. Therefore, productivity and financial benefit can be maximized. Even if there are no abnormal deformations or damage occurrence, SHM can also be beneficial to investigate the behavior of the OWTs under complex loadings during daily operation which can improve the design and manufacturing of future OWTs (Adams et al., 2011).

For an OWT, Rotor Nacelle Assembly (RNA), tower and foundation are usually the main sections. Recently, some studies have been carried out to explore the application of SHM systems to these components. Weijtjens et al. (Weijtjens et al., 2016) provide an SHM system based on both linear and non-linear regression models for the monopile foundation of an OWT in-service condition. The data generated by the SHM system is compared against the data collected in reality. The feasibility of this type of SHM system has been verified after the comparison. Mieloszyk and Ostachowicz (Mieloszyk and Ostachowicz, 2017) selected an experimental method to test the practicality of applying the SHM systems to a tripod foundation by using Fiber Bragg Grating (FBG) sensors to collect the required data. Benefiting from their research, the SHM process for the foundations of the OWTs becomes clearer and more practical. For the concrete foundations, Currie et al. (Currie et al., 2013) successfully monitored the displacements of the foundation of an onshore wind turbine by using a network of wireless sensors. Although there are some structural differences between the concrete foundations of

the offshore and onshore turbines, this novel SHM approach can be an indicator for the research about the SHM system for the concrete foundations of the OWTs. Yi et al. (Yi et al., 2013) used strain gauges together with accelerometers and tiltmeters to form a SHM system that can be used for a long period for the jacket foundation. Devriendt et al. (Devriendt et al., 2014) and Rolfes et al. (Rolfes et al., 2007) both focused on health monitoring of the tower of the OWTs. Rolfes et al. explored the use of limited wireless sensors for damage detection. Differently, the dynamic behaviors of the tower were monitored by Devriendt (Devriendt et al., 2014).

With respect to traditional materials that are used for offshore installations such as stainless steel, attention should also be given to the blade, one of the most critical components of RNA, which is generally made of fiber-reinforced composites. Nowadays, the blade is usually over 40 m long and consists of two outer surfaces and shear webs (Kim et al., 2019). And the blade is exposed to strong wind environments. Besides, there are also other additional types of loads such as centrifugal force acting on the blade. Therefore, the blades usually experience large structural deformations, and this can result in fatigue or damage problems. It is reported that the damage on an OWT, usually occurs at the tower, the rotor, and the blade regions (Ciang et al., 2008), and it may be necessary to replace the blades (Swartz et al., 2010). If the blades cannot be kept in service, the OWT will suffer a long period of downtime and then financial losses (Antoniadou et al., 2015). For the blade of OWTs, there are mainly three kinds of SHM methods widely used which are the acoustic emission (AE) method, vibration-based method, and strain-based method. The AE method is based on the theory that during the process of the failure of the materials, there will be energy released, and by collecting the transitory elastic waves, whether there is damage/crack occurrence in the structure can be determined (Schubel et al., 2013). At the early stage of the development of the AE method, Joosse and the co-workers applied the AE method to a small blade during the certification test of the blade (Joosse et al., 2002). Although they can successfully identify the critical zone of the blade, they cannot find out all the cracks. Recently, Tang et al. (Tang et al., 2016) focused on utilizing a four-array of sensors to investigate the feasibility of the AE method to determine the damage caused by fatigue and the locations of the damage can be successfully determined after comparing it with the photographic results. For the vibration-based method, Dervilis et al. (Dervilis et al., 2012) experimentally measured the vibration from a composite plate, which has similar characteristics to the materials used for blades, to detect the low-level damage. Tchewialk and Mølgaard (Tchewialk and Mølgaard, 2017) applied the vibration-based method to blades under experimental and real conditions. The strain-based method is also under extensive use, for

example, Schroeder et al. successfully utilized FBG sensors to achieve a SHM system for the estimation of the loading conditions on the blades of the OWTs, and usually, the applications can be categorized by the utilized sensor technology. (Schroeder et al., 2006) According to Schubel et al. (Schubel et al., 2013), the most promising methods for continuous offshore monitoring would be AE and strain-based methods. However, the AE method is confined to the field of damage detection.

Different strategies and different methods have been investigated for the application of SHM systems to OWTs. Usually, these studies focus on one specific component of the OWTs. For instance, usually, the SHM systems used for the stainless-steel structures cannot be applied to the composite blade. It would be much more beneficial to generate a complete and comprehensive SHM system for most of the critical components of the OWT. Furthermore, because of the complex topology of the OWTs and the complex loads caused by wind and waves, most of the current existing SHM systems do not concentrate on monitoring 3-dimensional full-field displacements and stresses of the OWTs. For the purpose of fulfilling these requests, iFEM, developed by Tessler and Spangler (Tessler and Hughes, 1983; Tessler and Spangler, 2003; Tessler and Spangler, 2004), can be used as the state-of-the-art methodology for the SHM system of the OWTs. In this study, iFEM is utilized to perform health monitoring for the tower and blade of the OWTs. Besides, iFEM is also extended to detect dent damage and estimate the Stress Intensity Factor (SIF) at the crack tip.

Another common weakness of the previously mentioned SHM method is that only the monitoring stage is considered. However, after the occurrence of the structural failure, which is usually fracture, these methods cannot be utilized anymore. A complete SHM system should take not only the diagnosis but also the prognosis process into consideration. Besides, fatigue assessment and related fracture should also be taken into consideration during both diagnosis and prognosis processes. Since iFEM is usually suitable for diagnosis purposes, Peridynamics (PD), which is a recent approach with inherent advantages for fracture analysis, is chosen for the fatigue-diagnosis and fracture-prognosis analysis. The PD fatigue model will be firstly applied to the triplate of the mooring lines since the underwater components of the OWT are always suffering the fatigue problems. Moreover, some fracture analysis related to the cubic polycrystalline material, which is the most common crystal type for the materials used for the OWT like steel, will also be explored.

## **1.2 Objectives of the research**

In this thesis, there are 5 main objectives for the research:

- Establish the fundamental framework of the SHM system for the OWT.
- Enrich the iFEM monitoring with the function of damage detection.
- Overcome the weakness of the current iFEM element when facing cracked structures.
- Provide a feasible tool for the fatigue analysis of the OWT to further complete the monitoring.
- Build the post-prognosis of the monitoring with the fracture analysis to explore the related fracture phenomenon of the OWT material from the microscale perspective.

In conclusion, the goal of the research is to use both the iFEM and PD methods to conduct the diagnosis and prognosis processes and establish a relatively complete SHM system for the OWTs.

## **1.3 Structure of the thesis**

Chapter 1. This chapter gives the basic background of the requirements of wind energy, the development of OWTs, and the challenges and difficulties met by the OWT industry which will show the necessity for research in this field. The existing SHM systems for individual components are also briefly introduced, which leads to the innovation of the research. The objectives of the research and the basic structure of the thesis will also be provided.

Chapter 2. This chapter will be formed by four capital and two auxiliary sections, and the capital sections provide the historical literature review related to the above 5 main objectives, respectively.

Chapter 3. This chapter will be the summative approaches related to the above 5 main objectives, respectively. The reasons for the numerical cases are explained and the connection between each numerical chapter is highlighted.

Chapter 4. This chapter will provide basic formulations for the iQS4 iFEM element and the SHM analysis for the tower and blade of the OWT will be given. For the tower, aerodynamic and hydrodynamic loadings will be considered and for the blade, just the aerodynamic force is considered. The practical number of sensors and their locations are also suggested, and future research directions are also given. At the end of this chapter, it will focus on applying the newly

introduced damage parameter to offshore cylindrical structures. Different damage locations, different damage sizes, and different numbers of damages are taken into consideration. With the help of these parameters, even with limited sensors, dent damage can be detected.

Chapter 5. This chapter first introduces the formulations for the 4-node and 8-node inverse plane elements. Followed by some comparisons between these two elements. Then the formulations of the iPCT element will be presented and several numerical examples are provided to prove the accuracy of these elements.

Chapter 6. This chapter shows the basic PD fatigue model. And then this model is applied to the real given triplate with simplified real loadings and the fatigue analysis and the fracture analysis of this triplate will be given.

Chapter 7. This chapter describes the basic PD cubic polycrystal model and the updated model for the thermal expansion phenomenon. Porosity and fracture phenomena under thermal loadings are considered for several types of polycrystalline materials. The results from the analysis are compared with the reference.

Chapter 8. This chapter reviews the 4 numerical chapters, summarises the outputs of this study, and emphasizes the novelty and contribution of the current research. The gaps and future work are also discussed.

Chapter 9: The key findings will be highlighted in the last conclusion chapter and final remarks will be presented to close the whole thesis.

## **1.4 Summary**

OWTs are becoming more and more important in the global energy production field. However, OWT is surrounded by harsh marine environments. To further increase the competitiveness of the OWTs by reducing the maintenance cost, SHM is necessary for the safety of the OWTs. In this study, iFEM is used for the diagnosis process which can show the health conditions of the OWT. And PD will be used for the prognosis process which contains fatigue and fracture aspects. The ultimate goal is to use both two methods to provide a comprehensive SHM system for the OWTs. This thesis is formed by 9 chapters. The 5 main objectives of this study are: 1. Establish the SHM system for the OWT; 2. Enrich iFEM with damage detection; 3. Overcome the weakness of the current iFEM; 4. Provide a fatigue analysis tool; 5. Build the post-fracture-prognosis for the monitoring.

## **2 Literature review**

### **2.1 Introduction**

This chapter provides a summary of the literature review for each research objective of this work. There are five main research aspects just as described in Chapter 1: 1. Establish the SHM system for the OWT; 2. Enrich iFEM with damage detection; 3. Overcome the weakness of the current iFEM; 4. Provide a fatigue analysis tool; 5. Build the post-fracture-prognosis for the monitoring. Though there are overlaps among the research aspects belonging to the same methodology, the amount is not too much, hence the overviews for these objectives are also preferred to be illustrated separately in 4 sections. Section 2.2 gives a view of the shape-sensing methods and their intercomparisons. The advantages of the iFEM methodology and the development of different types of iFEM elements are also presented. The data collection by sensors of the iFEM analysis is also introduced. Section 2.3 jumps over the iFEM and presents an illustration of the history of the widely used crack tip element together with the importance of SIF. The later process shows the necessity of developing the iPCT element. The PD theory including its merits, development, current application status, and some PD fatigue models is briefly explained in Section 2.4. While Section 2.5 is related to the microscale and the research about the polycrystalline materials and the related fracture phenomenon are mainly emphasized. Finally, the above information will be summarized in Section 2.6.

### **2.2 Literature review of the iFEM Methodology**

Most of the current approaches in SHM cannot be used directly for predicting 3-Dimensional displacement and stress fields because complex boundary conditions and topology of the structures cannot be fully considered. To overcome this problem, real-time shape sensing can play an important role in the development of SHM systems, especially for structures with complex loading conditions. The main benefit of shape sensing is that it allows using the measured strain data to estimate the variation of the displacement field in the structure (Gherlone et al., 2018). These data can then be used to determine strains and stresses for SHM systems. Currently, traditional strain rosettes and embedded fiber-optic sensor networks including FBG sensors are commonly used to collect the required strain data. Although conventional strain rosettes have the benefits of convenience and inexpensive price, FBG technology should be highlighted here because FBG sensors are more suitable for iFEM applications. FBG technology has been developed since the 1990s and it achieves data

acquisition by broadband lights (Ciang et al., 2008). These lights have their own wavelength and their frequency change along with the collected data and by separating the frequency interval, the strain data which contains real-time information on the structure can be obtained (Joosse et al., 2002). With respect to conventional strain gauges, FBG sensors have plenty of advantages. First of all, they have lower weights and smaller sizes. Then, they are suitable for long-distance signal transmission with less loss. Last but not least, they are less affected by harsh environments (Ciang et al., 2008; Joosse et al., 2002; Arsenault et al., 2013). For the sensing of the general components of the OWT, the main feature of the FBG sensor is that one FBG cable can contain multiple sensors and the number of sensors can reach 100. For the blade, there is another feature that should be highlighted. Due to their small size, FBG sensors can be installed inside the composite materials without influencing the properties (Ciang et al., 2008; Joosse et al., 2002; Arsenault et al., 2013). The SHM system of the OWT will benefit from these two characteristics, and they will reduce the required number of sensors and make the whole system more cost-effective. Currently, FBG sensors have already been used to obtain strain data for different components of the OWTs (Schroeder et al., 2006; Bang et al., 2012; Bang et al., 2012; Bang et al., 2012). FBG sensors can also be witnessed for the structural monitoring of blades and the utilizations are not constrained in the field of the OWT. Arsenault et al. (Arsenault et al., 2013) focused on the distribution of the sensors on the blade and they tested their arrangement of sensor placement under various static and dynamic loading conditions. No matter the static case or the dynamic cases, their results matched well with the reference. Kim et al. (Kim et al., 2013) used the FBG sensors to monitor the deflections of the blade. The FBG sensors were embedded in the composite materials located in the zones between the web and the cap. The high accuracy of this type of distribution was verified through experimental procedure after comparisons against the results from electrical strain gauges (ESGs) and theoretical FEM analysis. Damage estimation by FBG sensors was also explored by Tian et al. and they gave their attention to a 13.2 m blade under static loads. By combing the Chi-Square distribution (CSD) theory and the feature information fusion (FIF) theory, the location of the damage can be detected (Tian et al., 2015).

Among various shape-sensing methods, the typical strategies are Ko's Displacement Theory, Modal Method (MM), and iFEM (Gherlone et al., 2018). Ko's Displacement Theory was introduced by Ko et al. (Ko et al., 2007) based on twice integration of measured axial strains from sensors that are located on a different sensing line rather than the traditional axis (Ko et al., 2007). Ko's Displacement theory is based on classical beam equations, and it is very

suitable for beam-type structures. The accuracy of this approach has been proven by FEM comparisons (Ko et al., 2007). Its usage has been extended to wing-boxes and plates using multi-plex sensing lines (Ko et al., 2009; Blandino et al., 2005). On the other hand, depending on the mode shapes of the structure, MM uses the measured strains to calculate the displacements according to the relationships between strains and displacements (Bang et al., 2012). The main advantage of MM is that it can make predictions without knowing its material properties and it can be used widely to analyze beam and plate structures. However, MM is quite sensitive to the frequency and the amount of strain sensors (Kang et al., 2007; Rapp et al., 2009).

As an alternative approach, iFEM is an advanced and powerful concept developed by Tessler and Spangler (Tessler and Hughes, 1983; Tessler and Spangler, 2003). iFEM discretizes the whole structure into suitable inverse finite elements (beam, plate, shell, and solid elements), and the only input data is the strain of each element. iFEM takes into account all strain components including membrane, bending, and transverse shear depending on the element type and structure. It utilizes least-square minimization to minimize differences between measured and numerical strains. This process leads to a system of equations in matrix form. By solving the matrix system, the displacements at each node of iFEM elements can be determined in real-time. After the calculation of the displacements at each node, the strains of the whole structure can be estimated which will then contribute to the evaluation of the stress distribution of the structure. In short, iFEM only uses strain data collected from strain sensors to generate full-field displacements, strains, and then stresses. Gherlone et al. (Gherlone et al., 2018) have recently compared the three main shape-shaping methods using a cantilevered wing-shaped aluminum plate under static conditions. The accuracy of these three methods is investigated by comparing them against experimental results (Gherlone et al., 2018). After comparison, it was concluded that iFEM is more flexible and accurate than the other two techniques (Gherlone et al., 2018). Besides, the additional advantages of iFEM can be summarized as: (1) iFEM analysis can take complex topology and boundary conditions of the structure into consideration, and (2) the loading conditions together with material properties of the structure are not necessary for the determination of the displacement field, (3) iFEM can provide accurate and reliable results for the health condition in real-time regardless of whether the collected strain data has some errors or not and (4) if the locations of the sensors are logically and properly selected, it will not be necessary to install sensors to the entire structure which will drastically

reduce the required number of sensors and make the SHM system more cost-effective (Kefal, 2017; Kefal et al., 2015; Kefal et al., 2016).

There has been steady progress in iFEM studies in the literature. Amongst these, Tessler and Spangler (Tessler and Spangler, 2004) developed a three-node inverse shell element, iMIN3, which has linear in-plane displacements and bending rotations, and quadratic transverse-displacement (deflection) along with in-plane coordinates. To interpolate these displacement fields, Tessler and Spangler (Tessler and Spangler, 2004) utilized the linear area-parametric coordinates of a triangle and its associated anisoparametric shape functions developed based on constant shear-edge constraint conditions (Tessler and Hughes, 1985). Quach et al. (Quach et al., 2005) and Vazquez et al. (Vazquez et al., 2005) proved the reliability and capability of the iMIN3 element by performing an experimental study. Additionally, Tessler et al. (Tessler et al., 2012) improved the iMIN3 element to make it suitable to represent large deformation phenomena occurring in the plate and shell structures. For the beam iFEM element, Cerrachio et al. (Gherlone et al., 2014) and Gherlone et al. (Gherlone et al., 2011; Gherlone et al., 2012; Gherlone et al., 2014) developed an iFEM beam element that can be used to carry out analysis for 1-D beam structures based on the Timoshenko beam formulation. The accuracy of their element has been tested successfully through numerical and experimental studies. For complex materials, Cerracchio et al. (Gherlone et al., 2012; Cerracchio et al., 2015) developed the robust plate element for composite and sandwich structures which then became the foundation for Kefal (Kefal, 2017) to extend it to a new shell element called i3-RZT for composite materials. The functionality and accuracy of the i3-RZT element have been proven by two laminated composite examples (Kefal et al., 2017). Kefal and Yildiz then applied this element to a wing-shaped structure and three loading conditions (bending, torsion, and membrane) were considered. The practical distribution of sensors was explored, and it was concluded that, even with a small number of sparsely distributed FBG sensors, the deformation condition of the wing can be monitored. (Kefal and Yildiz, 2017) Lately, Kefal developed a curved inverse element with 8 nodes (iCS8) by incorporating the First-order Shear Deformation Theory (FSDT) into a shell element (Kefal, 2019). Despite iCS8 having some advantages when dealing with curved structures, the iQS4 element, also developed by Kefal et al. (Kefal et al., 2016), can be easily used for iFEM analysis with high accuracy for shell structures.

iQS4 element is a quadrilateral element and compared to other types of shell elements (including i3-RZT), it is simpler to be used and quadrilateral elements have the advantage of being highly accurate. Besides, the application of the iQS4 element is proficient and well-

established, especially in marine and offshore fields. iQS4 element has been successfully applied by Kefal et al. (Kefal and Oterkus, 2016; Kefal and Oterkus, 2016; Kefal et al., 2018) to perform SHM of a chemical tanker, a Panamax containership, and a bulk carrier, and these vessels are under different hydrodynamic loadings during the analysis. The robustness and accuracy of the iQS4 element have been further demonstrated (Kefal and Oterkus, 2016; Kefal and Oterkus, 2016; Kefal et al., 2018; Li et al., 2019). Although the iFEM has been already widely applied to various types of marine vessels, the application of the iFEM to the OWT has not been done before. As mentioned earlier, it is quite necessary to build a SHM system for OWTs. For this purpose, iFEM provides a feasible and reliable tool. But for an OWT, there are several significant components and there will be specific structural features and loading conditions for each component. The iFEM analysis for these components would be essential. It will not only prove the feasibility of the iQS4 element but also explore the reasonable number of sensors and their locations, which will provide guidance for the real iFEM application. Recently, the iQS4 element has shown its potential to detect damage on the structure during the iFEM process (Kefal and Oterkus, 2017). Colombo et al. (Colombo et al., 2019) continued this research by comparing the strains at single/multiple test locations. A plate with various cracks under a variety of loading conditions has been used to test the feasibility of this approach. By defining the extra judgement criterion, the iQS4 element is promising for crack prediction or structural defect identification. However, structural defects such as dent damage, which is a common problem for offshore cylindrical installations, still has not been detected before by using iFEM. Therefore, it is pressing to make the dent damage predictable by the iFEM during the daily monitoring process. By identifying the damage, action such as repairment can be taken before the failure of the whole structure. And it can also enlarge the application scope of iFEM. Finally, if the above two key issues can be solved, the iQS4 element can contribute to generating a relatively complete and comprehensive SHM system for the entire OWT.

### **2.3 Literature review of the iPCT element**

In the field of linear elastic fracture theory, SIF is one of the most important parameters. (Schijve, 2001) SIF represents the distribution of the stress at the small crack tip region, and it can give an illustration of the strength of the crack tip field when the structure is under certain loadings and deformations. There are three types of SIFs which are Mode-I: Opening, Mode-II: In-plane shear, and Mode-III: Out-of-plane shear, respectively. (Irwin, 1957) And the

determination of the SIF type depends on the applied loadings and the geometry of the structures. By also considering the size of the crack and the material properties, the value of the SIF can be computed. (Albrecht and Yamada, 1977) SIF has the ability to judge the resistance of the structure against the fracture, i.e., SIF can estimate the tendency of the propagation of the fracture. With the help of the SIF, the severity of the crack and the lifetime of the structure can be approached quantitatively. (Hellen and Blackburn, 1975; Rooke et al., 1981) SIF is suitable for practical utilization in the engineering field because of its low costs from both manpower and finance perspectives. (Albrecht and Yamada, 1977) In the offshore field, due to the fact that offshore installations such as the OWTs are usually unavoidable from the fracture phenomenon which may be contributed by fatigue, corrosion, and collision, efforts are also given to the evaluation of the SIF. (Lee, 1999; Ahmadi and Ghaffari, 2015; Bocher et al., 2018; Betgara et al., 2020)

There are many methods introduced to calculate the required SIF like the displacement extrapolation, J-integral, and the stiffness derivative technique. (Banks-Sills and Sherman, 1986) But among these methods, the displacement extrapolation method is still the easiest way with reasonable accuracy for engineering applications. (Banks-Sills and Sherman, 1986) The displacement fields of the structure would be necessary for the use of the extrapolation method. And the most common way to obtain the displacements of the structure is the Finite Element Method (FEM). Therefore, an element that can fulfil the requirement which is stress singularity around the crack tip would be beneficial. (Rybicki and Kanninen, 1977)

Currently, the widely used crack tip element is invented by Barsoum and Henshell & Shaw. (Henshell and Shaw, 1975; Barsoum, 1976; Barsoum, 1977) This type of crack tip element is formed by degenerating the 8-node quadrilateral isoparametric element to a 6-node triangular element. On the one hand, the mid-side nodes which are close to the crack tip will be replaced by the nodes at the quarter length. On the other hand, three nodes on one edge will be transformed to merge with each other but the independence of these three nodes will not be significantly influenced. (Barsoum, 1976) After the transformation, this type of crack tip element can achieve singularity at the crack tip and it will allow the calculation of the SIF of the elastic fracture by the basic parameters of the crack tip and the structure. (Barsoum, 1976; Barsoum, 1977) Apart from this type of element, 2-D quadrilateral crack tip elements and 3-D crack tip elements are also introduced. And the accuracy of these crack tip elements is proved by Barsoum with some examples. (Barsoum, 1976; Barsoum, 1977) The analytical results of these examples match well with the theoretical results. (Barsoum, 1976) The obvious

advantages of the crack tip elements can be summarized as: it can keep the continuity of the displacements; the element can make the model pass the required patch test and so forth (rigid body motion and constant strain modes can converge without other requirements). More importantly, one of the biggest advantages of this crack tip element is its convenience for utilization and it can be widely applied to most engineering structures. (Barsoum, 1976) With the given fracture criterion, the propagation of the crack can be predicted. It should be highlighted that Barsoum also found that the triangular crack tip element is better than the quadrilateral one and the latter is not suggested for practical structures. (Barsoum, 1976; Barsoum, 1977)

For the plane crack tip elements, its theory and application become increasingly further complete by the following work of the researchers. (Freese and Tracey, 1976; Hibbitt, 1977; Yamada et al., 1979) Apart from the plane crack tip elements, Barsoum also introduced a kind of collapsed solid element with 20 nodes for the thick/thin-shell structure. (Barsoum, 1976) Another quarter-point shell crack tip element is also provided by Barsoum et al. and the transverse shear deformations are included in this type of element. (Barsoum et al., 1979)

Lynn and Ingraffea explored the 8-node transition elements which can be used together with the crack tip elements. (Lynn and Ingraffea, 1978) Harrop firstly gave his attention to the size of the crack tip element in the radial direction. (Harrop, 1982) Then Saouma and Schwemmer focused on the mesh around the crack tip in detail and he suggested that in order to keep the engineering accuracy, the length of the singular element over the crack length should be smaller than 0.1 and at least four singular crack tip elements are necessary to be placed at the crack tip. (Saouma and Schwemmer, 1984) Banthia found that not only the element size but also the selection of the Gauss points for collecting the stresses will have an impact on the use of the element. (Banthia, 1985) The element size should be very small (1% of the crack length) to keep the singularity otherwise the stress sampling points should be very close to the crack tip. (Banthia, 1985) Recently, Nikishkov also researched the element size from the SIF perspective by using especially distributed element size in the radial direction, and also increasing the elements in the circumferential direction can improve the accuracy. (Nikishkov, 2013) Manu provided the completed formulations for these crack tip elements. (Manu, 1985) Some other types of crack tip elements like 6-node quarter-point and 8-node collapsed elements were tested by Furguele and Luchi. (Furguele and Luchi, 1989)

With the development of the crack tip element, it starts to be used for linear elastic materials. Banks-Sills and Bortman re-examined the crack tip element and used it for testing the singularity of the crack tip. (Banks-Sills and Bortman, 1984) Martinez and Dominguez used the crack tip element for Mode-I SIF calculation and accurate results can be obtained with coarse mesh. (Martinez and Dominguez, 1984) Murti and Valliappan applied the crack tip element to the transient dynamic analysis and the effect of the element size was also explored. (Murti and Valliappan, 1986) On the basis of this fundamental crack tip element, some improvements have also been promoted. (Gray et al., 2003; Abdelaziz et al., 2010; Abdelaziz, 2013) For example, Gray et al. enhanced the crack tip element, and the SIFs can be calculated with high accuracy under the condition of coarse mesh together with the displacement correlation method. Compared with the general crack tip element, the improved one is better and more useful for simulating the propagation of the crack. (Gray et al., 2003)

The crack tip element can achieve the requirement of singularity at the crack tip and in the field of finite element analysis, it has been widely used to generate the mesh around the crack tip. But according to the critical review of the iFEM methodology, there is no inverse crack tip element available which means that currently iFEM cannot be applied to model the structure with pre-existing crack. The development of the inverse plane crack tip element will fill in the gap and extend the application range of iFEM. Additionally, with the generation of the inverse crack tip element, the SIF at the crack tip can also be monitored which can also be beneficial for structural research in the offshore field.

## **2.5 Literature review of the PD theory**

OWTs are designed with the expectation of a long lifetime in the marine environment. Due to the repetition of the loading caused by wind, waves, current, and other harsh conditions, fatigue damages can occur on the OWTs, which may lead to major accidents. (Price and Figueira, 2017; Ahn and Shin, 2018; Zhang et al., 2021) For the general wind turbine, Liao et al. has shown some typical failure and accidents happen to the blade, gear, and tower. (Liao et al., 2022) Moreover, Li et al. concluded that tower and its transition piece, joints on the foundation, and mooring systems are the most sensitive components to the fatigue problems. (Li et al., 2021) And they also provide a table with the information of the failure mode of the OWT and it can be seen that fatigue is one of the major reasons causing failure. These accidents can result in

very expensive maintenance costs. Therefore, fatigue design assessment (FDA) is one of the design drivers for OWTs.

To date, due to the randomness of the environment, stochastic fatigue analyses are commonly used in the FDA for OWTs. By using the stochastic approach, the total lifetime accumulated fatigue damage (in the long-term fatigue analysis) and the probability of failure (in the reliability fatigue damage analysis) is common outputs. Meanwhile, the details of damage initiation and propagation are still infrequently investigated.

In order to predict fatigue crack growth, the traditional FEM by using the remeshing techniques (Loghin et al., 2012; Branco et al., 2015), or various modified versions of the FEM such as the extended finite element method (Pathak et al., 2013; Bhattacharya et al., 2013), have been used. However, one conceptual problem for classical continuum mechanics (CCM) is that it uses partial differential equations to represent structural behaviors. Therefore, additional criteria are needed to predict crack growth speed and direction or the branching of cracks (Eshelby, 1951; Erdogan and Sih, 1963; Hussain et al., 1974; Maiti and Smith, 1984).

PD is a nonlocal theory reformulating the CCM by using integral-differential equations (Silling, 2000; Silling et al., 2007; Silling and Lehoucq, 2010). In CCM, the state of a point is only influenced by its immediate neighbors. By contrast, the behavior of a material point in PD is governed by its interactions with surrounding material points located within a finite distance  $\delta$ , called the horizon size. Since the integral-differential equations used in PD are valid in both continuous and discontinuous models, PD is very suitable for failure especially progressive damage prediction in materials and structures. (Silling and Askari, 2005; Madenci and Oterkus, 2014) It can be applicable at all scales ranging from macro-scale to micro-scale. There has been rapid progress in Peridynamics, especially in recent years. The application of PD theory is not limited to metals, (Oterkus et al., 2010) but can be used for other materials such as composites (Oterkus et al., 2010; Oterkus and Madenci, 2012; Oterkus and Madenci, 2012), concrete (Oterkus et al., 2012), and graphene (Liu et al., 2018). There are several PD formulations available for simplified structures including the Euler beam (Diyaroglu et al., 2019), Kirchhoff plate (Yang et al., 2020), Timoshenko beam (Diyaroglu et al., 2015), and Mindlin plate (Vazic et al., 2020). It is possible to implement peridynamic beam and plate formulations in commercial finite element packages. (Yang et al., 2019) PD theory was utilized for topology optimization of cracked structures by Kefal et al. (Kefal et al., 2019), Vazic et al., and Basoglu et al. used PD theory to study the effect of microcracks on the propagation of a macrocrack

(Vazic et al., 2017; Basoglu et al., 2019). Imachi et. al. developed a new transition bond approach for failure definition which was applied to dynamic fracture analysis including crack arrest. (Imachi et al., 2019; Imachi et al., 2020) PD theory has been extended to other physical fields including thermal diffusion (Oterkus et al., 2014), moisture diffusion (Diyaroglu et al., 2017; Diyaroglu et al., 2017), and lithiation (Wang et al., 2018). An extensive review of peridynamics has been done by Madenci and Oterkus and Javili et. al. (Madenci and Oterkus, 2014; De Meo et al., 2017) Recently, Madenci et al., based on PD theory, has found an alternative approach to express the PD equations of motion called PD differential operator. (Madenci et al., 2016) And the PD differential operator has been successfully applied to partial differential equations, derivatives of scattered data, and even image recovery. Then the attention was given to the partial differential equations and the numerical solution for no matter linear or non-linear format has been gained. (Madenci et al., 2017) The accuracy and reliability of the PD differential operator was verified by different cases with different boundary conditions. Finally, all the fundamental information and applications of PD differential operator has been summarized by Madenci et al in the published book. (Madenci et al., 2019) Afterwards, Dorduncu and his co-researchers, based on PD differential operator and some other theories like refined zigzag theory, has generated diversified beam and plate formulations, which enriches the application of this operator. (Dorduncu, 2019; Dorduncu, 2020; Dorduncu and Apalak, 2020; Dorduncu, 2021; Dorduncu et al., 2022)

In the field of fatigue analysis, the first PD model is published by Oterkus et al., but this model can only model the fatigue crack growth phase. (Oterkus et al., 2010) Then Silling and Askari developed a bond damage model. By introducing a new variable “remaining life”, the nucleation and growth of the fatigue crack under cyclic loading can be simulated. And this model considered the S-N data and the Paris Law at the same time. An aluminum alloy rod is under torsion loadings to test the helical fatigue and the accuracy of this model was verified. (Silling and Askari, 2014) With the foundation of this model, a series of the following research has been carried out. Bang et al. used this model to predict the fatigue crack growth of 2024-T3 aluminum under various loadings. The results can be obtained with less computational time and the results matched well with the experimental data. (Bang et al., 2021) Hong et al. applied this model to the welded structure. After the verifying process by standard compact tension test, an effort was given to research the growth of the fatigue crack of the fillet welded joint under cyclic loadings. (Hong et al., 2021) The model has also been utilized in the PD polycrystalline model by Ning et al., and a novel method for detecting the crack tip was also proposed. The influence of some variables like the grain boundary strength and the size of the grain on fatigue

propagation was also researched. (Zhu et al., 2021) Karpenko et al. also focused on the microscale application. The effect of the microstructure and porosity on the performance of the fatigue fracture was under exploration. (Karpenko et al., 2022) An ordinary state-based PD model for the prediction of the fatigue crack growth was built based on the model of Silling and Askari by Bang and Ince, and the fatigue rates prediction of two aluminum alloys with four different R-ratios is in good agreement with the experimental results. (Bang and Ince, 2022) Apart from this powerful model, there are also other types of models. For example, the new PD model with a modified wheeler model for the fatigue crack growth rate prediction. (Nguyen et al., 2021) And there is also more research relevant to the fatigue field. (Ma et al., 2020; Liu et al., 2020; Binchao et al., 2021; Wang et al., 2022)

Finally, the energy-based PD model generated by Nguyen et al. should be emphasized. (Nguyen et al., 2021) It overcame the conceptual and mathematical problems of the conventional method. With the newly introduced equations for the initiation and growth phases, the model was suitable for crack predicting crack growth, especially for multiple crack paths. The accuracy of this model was proved by two examples. (single-mode and mixed-mode fatigue growth) This PD model for fatigue cracking presented includes three phases of fatigue failure: crack initiation (phase I), crack growth (phase II), and final failure controlled by quasi-static crack growth (phase III). Each interaction in the PD model has its own remaining life. During the cyclic loading processes, the remaining life is reduced, and the reduction can be updated by using PD fatigue equations based on the cyclic bond strain range. Although the accuracy of this PD fatigue model has been verified by Nguyen et al., this model has never been applied to real structures especially offshore installations. At the same time, fatigue assessment should be one of the most important portions of the monitoring process of the OWT. Performing the fatigue and fracture analysis for a particular component of the OWT is the first time to apply this PD fatigue model to real structures and gain influence for this model. Furthermore, it can also provide a powerful fatigue analysis tool for the SHM system and improve the system with more functions.

## **2.6 Literature review of fracture analysis of polycrystalline materials by using PD**

Most metals, alloys, and ceramics are usually polycrystalline materials. Polycrystalline materials usually consist of numerous crystals at the microscale. Each crystal may have its own

properties such as shape, size, grain orientation, and so forth. These microscale properties can have an impact on the features of materials at the macroscale and finally affect the characteristics of the whole structure. Although research studies concerning polycrystalline materials have been performed for decades, understanding of the fracture phenomenon in these materials, especially at the microscale, is rather limited. This is because not only do the crystals have various characteristics, but also the patterns of the crack can also be diverse (De Meo et al., 2016).

Experiments are powerful tools to carry out research about polycrystalline materials. Traditional experiments, because of lacking advanced photographic and imaging technologies, usually concentrated on one specific aspect of polycrystals (Kuszyk and Bradt, 1973; Case et al., 1980; Adams et al., 1985). Recently, with the development of tomography, even the 3-D microstructures of polycrystalline materials can be clearly observed. By utilizing a dual-beam focused ion beam-scanning electron microscope (FIB-SEM) combined with an Electron Backscattered Diffraction (EBSD) system, Groeber et al. (Groeber et al., 2006) successfully obtained information about grain size and orientations of the nickel-based superalloy in 3-D. By accurately collecting data about grains, the mechanical performance of the material can be estimated and tested. Ludwig et al. (Ludwig et al., 2009) used the x-ray diffraction contrast tomography (DCT) to obtain the shapes and orientations of the grains of a polycrystalline material without considering deformations. Then, by using the same tomography technique together with propagation-based phase-contrast tomography, Herbig et al. (Herbig et al., 2011) investigated the microstructure of the titanium alloy. More importantly, this setup also showed the potential to observe crack propagation. Although experiments can provide important information about the microstructure of polycrystalline materials, experiments about the fracture of polycrystals usually require expensive equipment, and the preparation and analysis process is quite complex and time-consuming (Geraci and Aliabadi, 2017). Computational modeling of polycrystalline materials would be a more practical and economical approach.

The cohesive zone model (CZM) is one of the most popular numerical methods to simulate the fracture of polycrystalline materials. After applying the FEM to CZM, Camacho and Ortiz (Camacho and Ortiz, 1996) simulated the dynamic fracture of brittle materials based on their linear cohesive law. Ortiz and Pandolfi (Ortiz and Pandolfi, 1999) focused on the problem of fracture of metals and the initiation and propagation of the crack were analyzed according to the potential-based law developed by Tvergaard and Hutchinson (Tvergaard and Hutchinson, 1992). CZM combined with FEM was also chosen by Lin et al. (Lin et al., 2017) to study the

role of the properties of the cohesive zone on the transitions of the crack pattern. The boundary element method (BEM) (Sfantos and Aliabadi, 2007) can be a more effective and easier method than CZM and it can overcome some drawbacks of FEM including the complexity of the analysis. BEM has been successfully applied to analyze different types of fractures of polycrystalline materials (Sfantos and Aliabadi, 2007; Benedetti and Aliabadi, 2013). Furthermore, BEM was further extended to model polycrystals to illustrate the crack propagation phenomenon under thermal loading (Geraci and Aliabadi, 2017; Geraci and Aliabadi, 2018; Geraci Aliabadi, 2019). The multiscale cohesive zone model (MCZM) was recently developed from CZM by Zeng and Li (Zeng and Li, 2010) and it is another useful and improved tool for the simulation of fracture of polycrystalline materials. Intergranular/transgranular and brittle/ductile fractures were analyzed using MCZM by Qian and Li (Qian and Li, 2011) and Li et al. (Li et al., 2012), respectively. Galvis and Sollero (Galvis and Sollero, 2016) combined the MCZM with BEM together and the analysis of the intergranular crack propagation in zinc and nickel was performed. Apart from CZM, the Extended Finite Element Method (X-FEM) and Body Force method can also be utilized to simulate the fracture process in polycrystalline materials (Sukumar et al., 2003; Kamaya et al., 2007).

Based on the advantages of PD described in the last section, as an alternative approach, PD can be utilized. In order to apply PD methodology to model polycrystalline materials especially to simulate fracture at the microscale, several research studies have been performed for different types of crystals. First of all, Ghajari et al. (Ghajari et al., 2014) developed a novel model for hexagonal crystals based on Bond-based PD theory (BBPD). This model allows the phenomena of crack nucleation and branching to be automatically simulated during the numerical analysis. The model was verified by comparing PD results against analytical and experimental reference solutions. Then the fracture of the microstructure of alumina was investigated indicating that this PD model can be successfully used to analyze materials with hexagonal crystal structures. Secondly, Askari et al. (Askari et al., 2008) built a PD model for crystals with cubic systems. The effect of the grain boundary on the mechanisms of the fracture was explored for silicon using this model. De Meo et al. (De Meo et al., 2016) introduced another novel model based on BBPD for cubic crystals. The robustness of this model was proven by both static/dynamic analysis of an iron plate without a crack and a steel plate with a pre-existing crack. The influences of the grain size, grain orientation, grain boundary strength, and fracture toughness ( $K_{Ic}$ ) of the materials on the fracture mechanisms of steel were also explored. De Meo et al.

(De Meo et al., 2016) used their model to investigate the stress corrosion cracking (SCC) phenomenon contributed by adsorption-induced decohesion. Their results were quite identical to the reference experimental results. Zhu et al. (Zhu et al., 2016) extended this BBPD model to ordinary state-based PD (SBPD) which eliminates the restriction of the limitations on material constants due to assumptions of BBPD formulation. Similar work can also be found in (De Meo et al., 2017; De Meo and Oterkus, 2017; Lu et al., 2020) and different properties can be specified for both individual grains and grain boundaries.

On the one hand, since the PD theory and its models are practiced to simulate both intergranular and transgranular fracture modes, the fracture behavior of the widely used brittle materials can be significantly influenced by their microstructures and microstructural defects including pores, microcracks, grains, and grain boundaries, can be explored. On the other hand, structures made from metals or ceramics usually suffer from temperature changes. These changes can be due to the heating-up process during the working condition or the cooling-down process during the fabrication procedure. The thermal expansion/shrinkage of the material can result in the initiation and propagation of cracks, especially under the condition that there is a pre-existing crack. The thermal-expansion-induced fracture of polycrystalline materials is mainly caused by: 1) the differences in the thermal expansion coefficients ( $\alpha$ ) among different material compositions, 2) transformations of the crystal systems during the change of the temperature, 3) elastic anisotropy leading to variation of strain distributions (Geraci and Aliabadi, 2017). This phenomenon can also be modeled by updating the PD equation. For the OWT, sometimes the fracture and crack are unavoidable. To fulfil the post-prognosis purpose, the PD cubic polycrystal model, which is suitable for the most commonly used steel, can be fully taken advantage to explore the fracture behaviors from the microscale perspective. By doing so, it can, on the one hand, forecast the propagation of the crack and assess the severity of the fracture. On the other hand, it will provide a better understanding of the fracture phenomenon which can make a contribution to fundamentally avoiding these problems.

## **2.7 Summary**

SHM is necessary for the OWTs. Although there are different types of SHM systems that have been proposed for different components of the OWT, these studies just concentrate on one specific component, and they do not consider the full field deformation monitoring. Relying on its advantages, iFEM can achieve the above purpose. Since iFEM is not limited to any material system, iFEM can also be applied to composite blades. FBG sensor technology is

preferred, and this type of sensor can contribute to the reduction of the required sensors for the iFEM application. iQS4 element is suitable for offshore installations. Besides, damage/crack can be predicted by iFEM with an extra judgment criterion. Therefore, the iFEM-iQS4 element has the potential to generate the entire SHM system for the whole OWTs.

If the structure exists crack, the application and utilization of iFEM would be limited. But with the help of the iPCT element, this problem can be relieved. Furthermore, SIF is very critical for offshore engineering. The crack tip element can fulfil the singularity at the crack tip and the values of the SIFs can be calculated with the help of these elements. The inverse version of this element can offer a tool for SIF estimation.

The non-local theory, PD, is powerful for dealing with fracture problems. It can be applied to no matter macro- or micro- scale. Different PD models have been developed for different tasks. On the macroscale, the PD fatigue model will be applied to real offshore structures for the first time and a useful fatigue analysis tool can be formed based on this model. On the microscale especially for polycrystals, experiments are usually complex and time-consuming. Computational modelling would be a reasonable way and similar to the conventional numerical method like CZM, the PD model would be an alternative approach. Some microscale problems of polycrystalline materials such as thermally-induced fracture and porosity can be explored.

According to the best of the author's knowledge, there are no similar studies available for the research fields shown above.

## **3 Methodology**

### **3.1 Introduction**

In order to achieve the objectives which are introduced in Chapter 1.2, after the critical review, detailed approaches will be presented in this chapter. Before the specific approach for each objective, the reasons for the chosen individual case will be explained. Finally, a brief section will summarize these approaches.

### **3.2 Approaches against the objectives**

- For the first objective, attention is given to the two important components of the OWT which are the tower and blade, respectively. On the one hand, these two structures are standing in harsh marine environments, which causes structural health problems such as failure to occur. On the other hand, the materials for these two components are stainless steel and fiber-reinforced composites, which can represent the majority of the OWT structures. In Chapter 4, the inverse 4-node quadrilateral shell (iQS4) element of the iFEM will be utilized to perform the SHM analysis/shape sensing for the tower and blade of the OWT under the close-to-reality loading conditions. FEM analysis will be performed before the iFEM analysis. On the one hand, it can act as the reference solution for judging the accuracy of the iFEM results. On the other hand, it can provide the “synthetic” experimental strain data for the iFEM methodology. iFEM with full sensors are usually for verification and comparison purposes. The efforts will be given to iFEM with reduced number of sensors (iFEM-r). Because although the price of the sensors is reducing, sensors are still very expensive and one of the most important aspects of the iFEM application would be the minimization of the required sensors. After the analysis, the reasonable number of sensors and their locations will also be explored and suggested. Establishing the SHM system for these two structures can be representative of the whole OWT and the other components can follow the same strategy. More importantly, it also means that iFEM monitoring can be applied to any other scaled OWTs. To the best of the author’s knowledge, in the literature, there is no similar research has been performed in the field of applying the iFEM to the OWTs. The aims are achieved and for the tower monitoring the results have been published

(The first publication of the author), and for the blade analysis, similar work has been submitted as the report for the first academic project.

- Inspired by the former research in the review (Chapter 2), a new numerical parameter that allows the current iFEM monitoring model to detect the size and location of the dent damage is created. The offshore cylindrical structures which are commonly used as the columns and pipelines on offshore installations are selected because usually, they are suffering plain dents caused by collision or corrosion. (Fig. 3.1) Dent damage with different locations and sizes is generated for verifying the feasibility and accuracy of the damage judgment parameter (Chapter 4.5). Both daily health monitoring and damage detection can be performed at the same time. The results of this study have been published as the second paper in the author's research outputs.



**Figure 3.1** The plain dents on the offshore cylindrical structures (Alexander and Brownlee, 2007; Macdonald et al., 2007)

- Since the damage and crack can be detected by iFEM, creation of an inverse plane crack tip (iPCT) element can further enhance the structural monitoring by extending iFEM to the structure with pre-existing crack. By reforming the displacement fields and using the displacement extrapolation method, the SIF at the crack tip can be calculated. And the comparisons of the results of the different types of SIF can finish the task of proving the accuracy of the iPCT element (Chapter 5).
- With the OWT moving to increasingly deep water, station keeping system becomes necessary. However, fatigue problems are always perplexing the OWT, especially the mooring systems, because mooring lines are bearing cyclic tension loadings. (Pham et al., 2019; Barrera et al., 2020; Li and Zhang, 2020; Yang et al., 2020; Gao et al., 2021; Piscopo et al., 2021) And since triplate is one of the most significant components for connection in the mooring system the PD fatigue model will be applied to the triplate

of the mooring lines of the given OWT. By performing the fatigue and fracture analysis for the triplate with varying mooring line angles, the practicability of the current model can be tested. (Chapter 6) And since this model is not constrained to triplate, the monitoring of the OWT can be further consummated. This study has been submitted as one of the major sections of the report for the second academic project.

- For a complete health monitoring process, just diagnosis is not sufficient. If there is fracture occurs, it would be more competitive to have the ability to analyze the propagation of the crack. With the aid of the PD cubic polycrystal model, the fracture on both micro- and macro- scale can be researched numerically. It should be mentioned that the crystal type of steel is cubic, so the current PD model can also be applied straightforwardly. First of all, the PD cubic polycrystal model is improved by considering the thermal expansion coefficient. Then two typical phenomena which are porosity and thermally-induced fracture are explored. (Chapter 7) To the best of the author's knowledge, it is the first time to perform such research and the results have been published as the final two papers.

### **3.3 Summary**

The overall works aiming to achieve the objectives are described in this chapter. In correspondence to the 5 main objectives of this study, the approaches can be concisely summarized as: 1. Apply iFEM to the tower and the blade; 2. Dent damage detection; 3. Generation of the iPCT element; 4. Fatigue analysis of the triplate; 5. PD analysis of the porosity and thermally-induced fracture for the cubic polycrystals. And the detailed numerical procedure of these approaches will be shown in the following several chapters (from Chapter 4 to Chapter 7) correspondingly.

# **4 Structural health monitoring of the offshore wind turbine using iFEM methodology**

## **4.1 Introduction**

This chapter mainly focuses on the application of the iFEM-iQS4 element for the OWT. In Section 4.2, the theory of the iFEM-iQS4 element will be described. Not only the formulations of the iQS4 elements but also the strain data collection and the post-processing steps in the iFEM analysis will also be introduced. Additionally, the newly introduced damage identification parameter will also be highlighted. Then the remaining chapter will be divided into three main sections which are numerical analysis of the tower and blade, and the dent damage detection, respectively.

For the tower application, the model is selected from the reference (Gücüyen, 2017) and the displacements and stresses of the tower under both static and dynamic loading conditions will be monitored. Section 4.3 will demonstrate the numerical procedure including the model generation, sensor selection, and both static and dynamic iFEM analysis. For the blade of the OWT, only the shape-sensing progress which is a critical component of the SHM progress is considered. Apart from the general model generation step, the aerodynamic loading calculation will be emphasized in Section 4.4.2. Besides, gravity and centrifugal force will also be taken into consideration. The practical sensor locations for the blade will be discussed.

Apart from the tower and blade, stiffened thin-walled cylindrical structures are also one of the most common structural components of floating offshore installations (Cerik, 2015; Cerik et al., 2015; Cerracchio et al., 2015; Kefal et al., 2017;). Fig. 4.1 shows a typical application of a floating offshore wind turbine where the columns are orthogonally stiffened cylinders. Considering these structures are commonly subjected to severe environmental conditions, it is necessary to use the SHM system to protect the structure from failure. Therefore, Section 4.5 presents the application of the iFEM approach to identify dent damage in a thin-walled stiffened steel cylindrical structure. This chapter is organized as follows: the properties of the cylindrical structures considered in this study are provided in Section 4.5.1. Moreover, the numerical results for undamaged and damaged cylindrical structure cases are demonstrated. The damage prediction in the stiffened cylindrical structures using the new damage parameter and von Mises strain distributions is also presented.

Finally, a summarized conclusion and some future research aspects will be presented in Section 4.6. To the best of the author's knowledge, it is the first study using the iFEM-iQS4 element for the health monitoring of the tower and composite blade of the OWTs and it is also the first attempt to apply the iQS4 element to the detection of the dent damage.

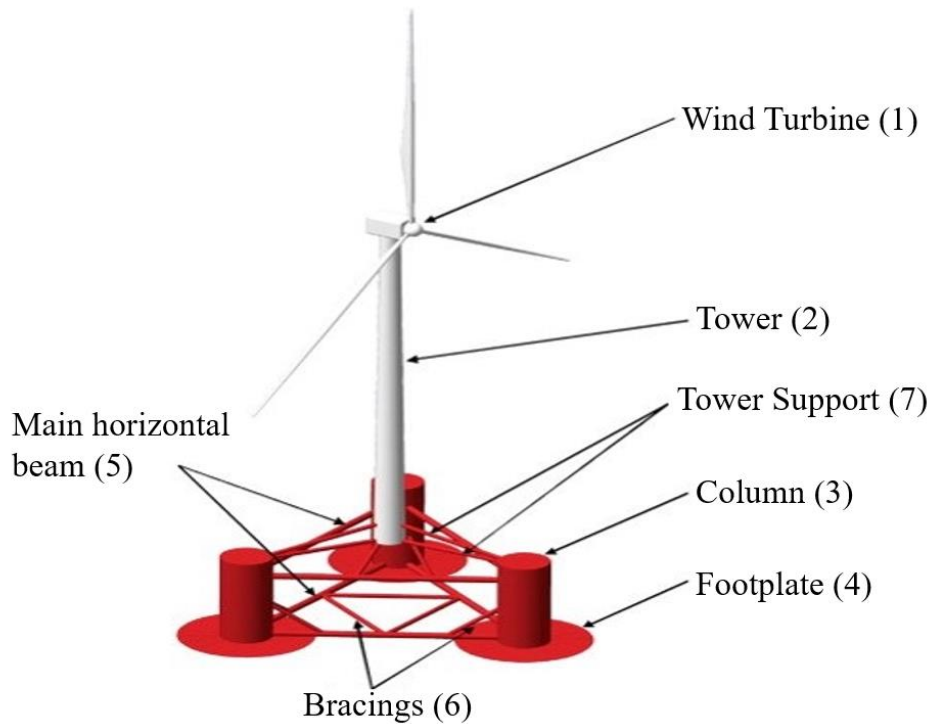


**Figure 4.1** Tri-floater offshore wind turbine with stiffened cylinders as main columns (Das et al., 2003)

## 4.2 Formulation of the iQS4 element

### 4.2.1 iFEM-iQS4 element

The first stage of iFEM analysis is dividing the whole structure into a reasonable number of iQS4 elements. The iQS4 element is defined on the basis of FSDT and has 4 nodes with 6 DOFs per node. Three of them are displacements in the axial directions and the remaining three are nodal rotations. The reason for utilizing this type of element is, first of all, iQS4 elements are thin-shell elements that can represent and be used to model most of the offshore structures. And compared with triangular element, iQS4 elements can provide more accurate results. More importantly, among the DOFs of the iQS4 element, drilling rotation is especially considered. Hence, the singularity problem can be easily solved, and the shear-locking phenomenon can also be minimized which makes the iQS4 element quite suitable for modelling complicated shell structures. The local coordinate system (LCS) of each iQS4 element is located at the

central core of the element (Fig. 4.2). The thickness of the element is evenly separated in the z-direction by the x-y plane of the LCS. The top layer of the element is represented by “ $z = +h$ ” and “ $z = -h$ ” stands for the bottom layer of the element. The shape functions as well as their derivatives, which are widely used in the FEM, can be used to establish the relationship between elemental strains and nodal displacements. According to the linear strain-displacement relationship given in (Kefal et al., 2016), three different matrices that contain the derivatives of shape functions can be constructed for each individual strain measure, namely,  $\mathbf{B}^m$  matrix for the membrane strains,  $\mathbf{B}^b$  matrix for bending curvatures, and  $\mathbf{B}^s$  matrix for transverse shear strains. The explicit form of these matrices is also provided in (Kefal et al., 2016) and not included herein for conciseness. These matrices relate the membrane strains,  $\mathbf{e}$ , bending curvatures,  $\boldsymbol{\kappa}$ , and transverse shear strains,  $\boldsymbol{\gamma}$ , to the nodal displacements and rotations which are given as (Kefal et al., 2016):

$$\mathbf{e} = [e_1 \quad e_2 \quad e_3]^T = \mathbf{B}^m \mathbf{u}_e \quad (4.1a)$$

$$\boldsymbol{\kappa} = [\kappa_1 \quad \kappa_2 \quad \kappa_3]^T = \mathbf{B}^b \mathbf{u}_e \quad (4.1b)$$

$$\boldsymbol{\gamma} = [\gamma_1 \quad \gamma_2]^T = \mathbf{B}^s \mathbf{u}_e \quad (4.1c)$$

where the vector  $\mathbf{u}_e = [\mathbf{u}_1^e \quad \cdots \quad \mathbf{u}_4^e]^T$  represents all nodal DOF of the iQS4 element with  $\mathbf{u}_i^e = [u_i \quad v_i \quad w_i \quad \theta_{xi} \quad \theta_{yi} \quad \theta_{zi}]^T$  ( $i = 1, \dots, 4$ ) denoting the six DOF at each node (Fig. 4.2b). Utilizing the strain measures given in Eq. (4.1), the in-plane and transverse-shear strain components at any point given in the plate geometry can be calculated as:

$$\begin{Bmatrix} \varepsilon_{xx} \\ \varepsilon_{yy} \\ \gamma_{xy} \end{Bmatrix} = \begin{Bmatrix} e_1 \\ e_2 \\ e_3 \end{Bmatrix} + z \begin{Bmatrix} \kappa_1 \\ \kappa_2 \\ \kappa_3 \end{Bmatrix} \quad (4.2a)$$

and

$$\begin{Bmatrix} \gamma_{xz} \\ \gamma_{yz} \end{Bmatrix} = \begin{Bmatrix} \gamma_1 \\ \gamma_2 \end{Bmatrix} \quad (4.2b)$$

where in-plane strains are linearly varying through the thickness of the plate (Eq. (4.2a)), whereas the transverse-shear strains are constant along the thickness coordinate,  $z$ .

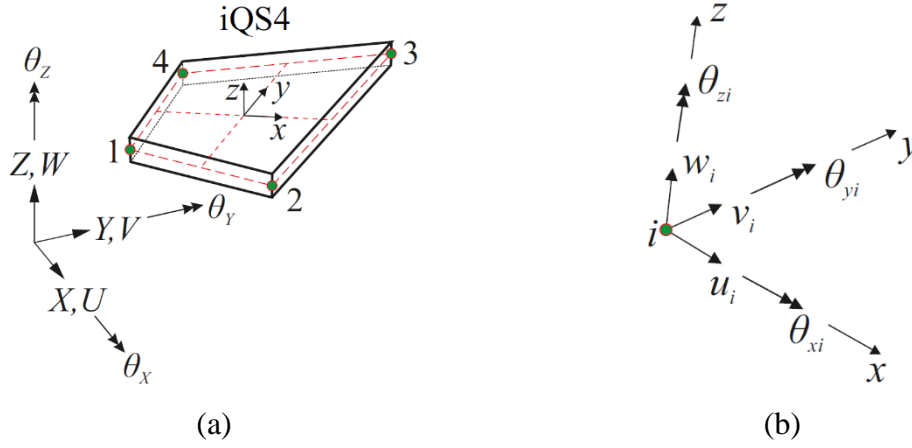


**Figure 4.2** (a) iQS4 element with the local coordinate system (LCS)  $(x,y,z)$  at the central plane and global coordinate system (GCS)  $(X,Y,Z)$  of the structure (b) the total 6 DOFs in LCS (Kefal et al., 2016)

#### 4.2.2 Strain collection by sensors

Strain data collection is one of the most important processes of iFEM analysis. FBG sensors are recommended and preferred for fulfilling this purpose because the required strains can be obtained by just several lines of FBG sensors. After the discretization of the structure, the sensors will be installed on both sides of the iQS4 element (Fig. 4.3). For the current analysis, sensors are placed at the centre of each iQS4 element and there are only two sensors attached at the top and bottom surfaces. The symbol “+” represents the strains obtained from the top surface of the element and “-” represents the strains gathered from the bottom side. The experimental strains of membrane and curvatures can be calculated by the equations shown below:

$$\mathbf{e}^* = \frac{1}{2} \begin{Bmatrix} \varepsilon_{xx}^+ + \varepsilon_{xx}^- \\ \varepsilon_{yy}^+ + \varepsilon_{yy}^- \\ \gamma_{xy}^+ + \gamma_{xy}^- \end{Bmatrix} \quad (4.3a)$$

$$\mathbf{k}^* = \frac{1}{2h} \begin{Bmatrix} \varepsilon_{xx}^+ - \varepsilon_{xx}^- \\ \varepsilon_{yy}^+ - \varepsilon_{yy}^- \\ \gamma_{xy}^+ - \gamma_{xy}^- \end{Bmatrix} \quad (4.3b)$$

In the iFEM methodology, the geometry of the structure to be monitored is discretized by using suitable inverse elements as shown in Fig. 4.4(a). To perform an experimental application of the iFEM methodology for a given structure, triaxial strain measurements should be collected from discrete locations of the top/bottom faces of the structural components. For this purpose, three different conventional strain gauges and/or embedded FBG sensors can be stacked

together to form a strain rosette, which can be mounted on a discrete position to obtain onboard triaxial strain measurements in real-time. Once the data raw data is collected from each strain gauge, it has to be sampled according to the desired frequency interval through an averaging/filtering process. After that, for a particular position, triaxial strain measurements should be transformed to normal strain components and in-plane shear strain of the local iFEM element. This transformation can be readily performed by utilizing direction angles between the local axes of the element and the strain-gauge axis.

It should be mentioned that transverse shear strains cannot be obtained by the sensors. Since the plane stress condition can be utilized as a simplification for most of the offshore structural problems, which means that the shell structure can be regarded as “thin shell”, the transverse shear strains are much smaller than the remaining two. So in such cases, the transverse strains can be ignored without any big impact on the accuracy.

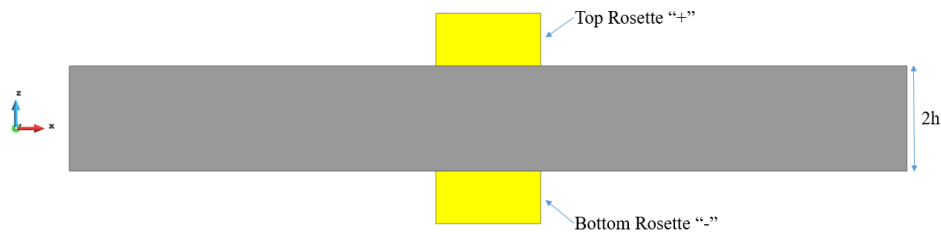
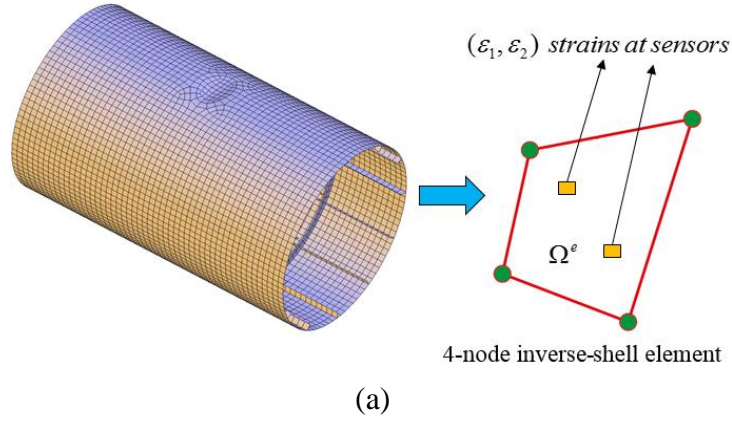
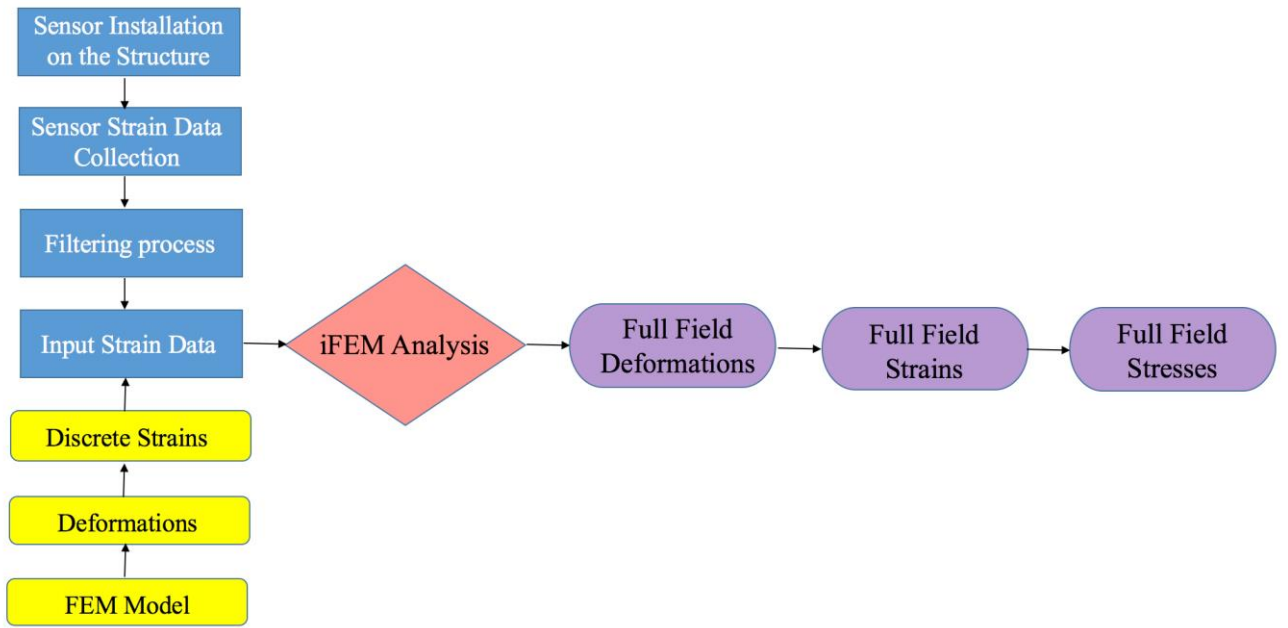


**Figure 4.3** Strain collection for iQS4 element using FBG sensors

In the current study, we generated the discrete (experimental) strain data numerically by performing a high-fidelity finite element analysis on the structures concerned. For this purpose, a relatively dense finite element model is created first. Secondly, the material, loading, and constraint conditions are assigned to the dense FEM model. Third, the nodal displacement and rotation solutions are obtained after the analysis. In the post-processing stage of the FEM analysis, the direct input of iFEM analysis, i.e., discrete normal/shear strain measurements over the local axes of the iQS4 element, are produced by multiplying the displacement and rotation solutions of the high-fidelity FEM model together with the derivatives of the associated FEM element shape functions. As a result, this numerical strain data represents “synthetic” experimental strain readings obtained from surface-patched strain gauges or FBG sensors along the local axes of the iQS4 element. Processing the in-situ strain data collected from discrete locations of the structure, full-field displacements, strains and stresses can be obtained in real-time as depicted in Fig. 4.4(b).



(a)



(b)

**Figure 4.4** (a) Discretisation of the structure with inverse finite elements, (Kefal, 2017)  
 (b) overview of iFEM methodology

### 4.2.3 Basic equations of iQS4 elements

The basic idea of iFEM analysis is to minimize the difference between experimental strains and analytical strains for each iQS4 element. The differences between the numerically calculated  $\mathbf{e}$ ,  $\boldsymbol{\kappa}$ , and  $\boldsymbol{\gamma}$  against the experimental values can be defined by using the functional,  $\boldsymbol{\varphi}_e$ . The expression of  $\boldsymbol{\varphi}_e$  can be written as:

$$\boldsymbol{\varphi}_e = \omega_m \|\mathbf{e} - \mathbf{e}^*\|^2 + \omega_k \|\mathbf{k} - \mathbf{k}^*\|^2 + \omega_s \|\boldsymbol{\gamma} - \boldsymbol{\gamma}^*\|^2 \quad (4.4)$$

where  $\omega_m$ ,  $\omega_k$ , and  $\omega_s$  are the weighting constants. If the experimental strains are available, the weighting constants can be equal to 1. However, if the strain data cannot be measured by the sensors, it is suggested that a small number like  $10^{-4}$  or  $10^{-5}$  can be chosen as the weighting

constants. By doing so, the interpolation connectivity of the iQS4 element can still be guaranteed.

By differentiating  $\boldsymbol{\varphi}_e$  against the unknown displacements, the minimization of the differences between experimental and numerical strains can be achieved. A matrix system (similar to FEM) can be obtained as a consequence of differentiation

$$\frac{\partial \boldsymbol{\varphi}_e}{\partial \mathbf{u}_e} = \mathbf{k}_e \mathbf{u}_e - \mathbf{f}_e = 0 \Rightarrow \mathbf{k}_e \mathbf{u}_e = \mathbf{f}_e \quad (4.5)$$

where  $\mathbf{k}_e$  is a matrix formed by strain-displacement matrices and weighting functions. Once the  $\mathbf{k}_e$  matrix is established, unless the geometry or the boundary condition changes, there is no need to change it during the iFEM analysis and this will contribute to the reduction of the run time which makes iFEM analysis suitable for real-time monitoring. The  $\mathbf{f}_e$  is an array formed by the collected strain data. Finally,  $\mathbf{u}_e$  is the desired nodal displacements. After transforming from LCS to GCS, applying boundary conditions, and assembling the global system of equations, full-field displacements can be reckoned.

#### 4.2.4 Post-processing for iFEM analysis

The health condition of the structure can be assessed with the help of 6 regenerated global displacements and rotations ( $U, V, W, \theta_x, \theta_y, \theta_z$ ). Moreover, by means of additional parameters, such as total displacements, total rotations, and von Mises strain/stress, the health condition can be determined a step further. Total displacements ( $U_T$ ) and von Mises stress ( $\sigma_{vm}$ ) are commonly used. The total displacements can be forthrightly calculated as:

$$U_T = \sqrt{U^2 + V^2 + W^2} \quad (4.6)$$

Three independent displacements can be replaced by  $U_T$  and the extreme values combined with the plots of  $U_T$  can give a comprehensive but brief illustration of the deformation condition of the structure.

The strains of each iQS4 element can also be calculated after obtaining the nodal displacements. Previously introduced  $\mathbf{B}^m$ ,  $\mathbf{B}^k$ , and  $\mathbf{B}^s$  matrices can be used together with predicted  $\mathbf{u}_e$  vectors to establish the individual strain components. Then, the stress distribution of the iQS4 element can be computed utilizing the constitutive relations of the plane-stress condition. Finally, once the normal and shear stress components are obtained, they can be subsequently

used along with the von Mises stress criterion to make a reasonable failure assessment and identification of the structurally unhealthy condition.

#### 4.2.5 Damage identification

After the procedure described in Section 3.2.4, the displacements and rotations corresponding to six DOF of each node can be obtained and this data can be subsequently used to calculate full-field section strain measures as given in Eqs. (4.1) and (4.2). Moreover, the constitutive relationship between stress and strain will yield the full-field stress distribution. In this study, the von Mises strain  $\varepsilon_{vm}$  is considered as an equivalent maximum strain to predict damage. This equivalent strain for isotropic materials can be calculated under the plane-stress condition as:

$$\varepsilon_{vm} = \frac{1}{\sqrt{2}} \sqrt{(\varepsilon_{xx} - \varepsilon_{yy})^2 + (\varepsilon_{xx} - \varepsilon_{zz})^2 + (\varepsilon_{yy} - \varepsilon_{zz})^2 + 6\gamma_{xy}^2} \quad (4.7)$$

with

$$\varepsilon_{zz} = \frac{\nu}{\nu - 1} (\varepsilon_{xx} + \varepsilon_{yy}) \quad (4.8)$$

where  $\nu$  is Poisson's ratio of the material.

In order to clearly show and distinguish the locations of the damage, an additional damage parameter  $D$  is introduced and defined as:

$$D = \left| \frac{\varepsilon_{vm,current} - \varepsilon_{vm,undamaged}}{\varepsilon_{vm,undamaged}} \right| \quad (4.9)$$

where  $\varepsilon_{vm,current}$  represents the current measured von Mises strain value and  $\varepsilon_{vm,undamaged}$  denotes the von Mises strain value measured earlier for an undamaged (intact) structure. Note that although the definition of the damage parameter has a similar form to the anomaly index given by Colombo et al. (Colombo et al., 2019), it has a different meaning. If there is no damage inside the structure, it is expected that the value of the damage parameter  $D$  is zero everywhere inside the structure as long as there is no rapid change in loading acting on the structure. If there is a rapid change in loading acting on the structure, then there is a possibility that the damage parameter  $D$  values can be non-zero. To overcome this problem, once the non-zero damage parameter  $D$  situation occurs, von Mises strain distribution should also be checked

since higher von Mises strain values localize and occur around the damaged areas. Therefore, in this study, both the damage parameter  $D$  and von Mises strain distributions are utilized for dent damage identification in stiffened cylindrical structures.

## 4.3 Numerical analysis of the tower

### 4.3.1 Model generation of the tower

The geometry of the tower is determined based on the studies by Gücüyen (Gücüyen, 2017) and Dagli et al. (Dagli et al., 2018). The tower is divided into 26 sections. Usually, each section should have its own thickness, height, and weight. But for simplification, the thickness of all of the sections is 30 mm and the height of each section is 2.5 m. The total height of the tower is 65 m with 20 m height underwater. The maximum diameter of the tower is 4 m at the bottom and the diameter linearly decreases to 1.5 m at the top of the tower. The material of the tower is entirely considered as steel regardless of the steel grade. The Elastic Modulus is 210 Gpa and the Poisson's ratio is 0.3, respectively. The density of the steel is  $7850 \text{ kg/m}^3$ . However, in reality, there will be paints, cables, and ladders attached to the surface of the tower. Therefore, the weights of these components should also be included. It would be a reasonable way to transform the extra weights being divided by the volume of each section into the density of the shell element. Finally, the density of the structure is decided as  $8500 \text{ kg/m}^3$ . During the analysis, the weights of the structure itself will be applied by defining the gravitational acceleration. Additionally, for static analysis, the weight of the RNA, which is 83000 kg, is acted on the top of the tower. The aerodynamic and hydrodynamic forces are further considered during the dynamic condition. The bottom of the tower will be fixed as the boundary condition for both static and dynamic conditions. The model of the tower is discretized by 8424 elements and 8460 nodes for FEM analysis (shown in Fig. 4.5(a)). The results of FEM analysis are utilized for both reference solutions and to generate "synthetic data" for the iFEM analysis. The mesh of the model in the iFEM process, which only contains 936 elements and 948 nodes (shown in Fig. 4.5(b)), is much coarser than the FEM model. Therefore, for each iFEM element, there will be several FEM elements as the "synthetic" strain data provider.

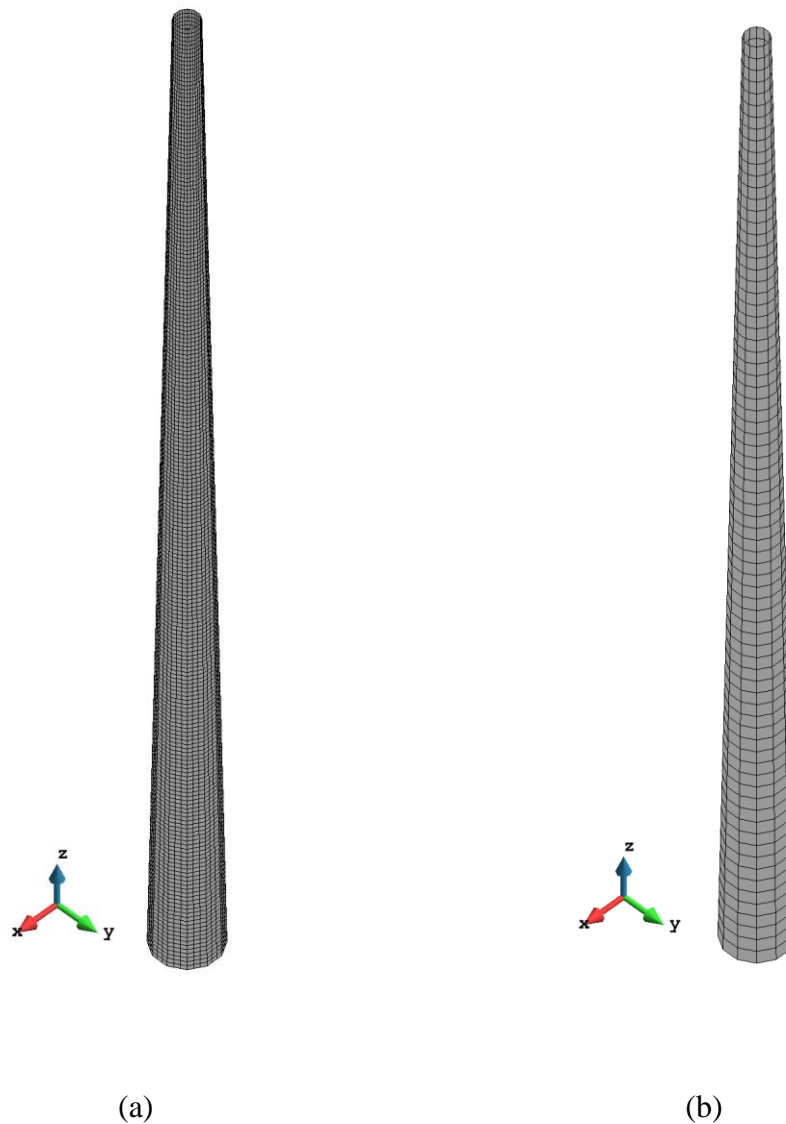


**Figure 4.5** Mesh size (a) dense FEM mesh (b) coarse iFEM mesh

### 4.3.2 Sensor selection and data evaluation

In the first case, it is considered that all iFEM elements are instrumented with strain sensors. Therefore, the number of sensors becomes  $936 \times 2$ . Although a large number of sensors is considered in this case, named as full-sensor condition, it can prove the accuracy and reliability of the iFEM process. Then, the number of elements with sensors is reduced to 328 to make it more practical. As can be seen from Fig. 4.6(a), four longitudinal lines with sensors and two circumferential lines (one at the bottom and another at the top) with sensors are selected. The two ring lines of sensors are aimed to monitor the boundaries of the tower. It can not only reinforce the boundary condition for the analysis but also monitor the extreme deformations

(especially in the z-direction) at the boundary. This distribution of sensors is used for both static and dynamic analysis. Because the directions of the wave and wind are not known in reality, symmetrical boundary conditions cannot be applied. Hence, the purpose of the four vertical lines of sensors is to monitor the health condition of the whole tower for any loading conditions. Besides, during the analysis, it was found that connecting the sensors at different parts of the structure together has the ability to improve the accuracy of the results and these four lines of sensors can strengthen the quality of the deformation estimation. With the help of FBG sensors, since these elements are located continuously, the strain data can be collected by just several lines of FBG sensors. However, with the increase of the sensor locations, although FBG technology can deal with collecting a great deal of data by just a single line, the efficiency of the FBG sensors will be significantly influenced and the process of separating the information into strains will also become complex. In order to relieve this problem, strain data evaluation would be an appropriate method and the missing strains can be estimated by the nearby strains. For the current analysis, after balancing the accurate level of the evaluation and the minimized number of sensors, each vertical line of sensors can be divided into four groups and different strategies can be utilized. Actually, for each section, there are 3 layers of elements in the vertical z-direction. First of all, for the sections around the boundary, all of the three elements are chosen. Secondly, for the sections around the free water surface, all elements will also be selected because the strains around this region, especially in dynamic conditions, usually experience large variations. Then for the remaining underwater sections, the top and bottom elements are preferred to install the sensors. On the contrary, for the sections subjected to the aerodynamic loads, the sensors are only installed at the middle elements. The reason is that the strains of the sections above water are much more stable than the underwater parts. Eventually, the number of elements with sensors is decided as 176 and it only occupies about 2% of the total quantity of the FEM elements. It means that 6x2 lines of FBG sensors are enough to perform the iFEM analysis of the tower. This number can be further reduced, but it can have a negative influence on accuracy.

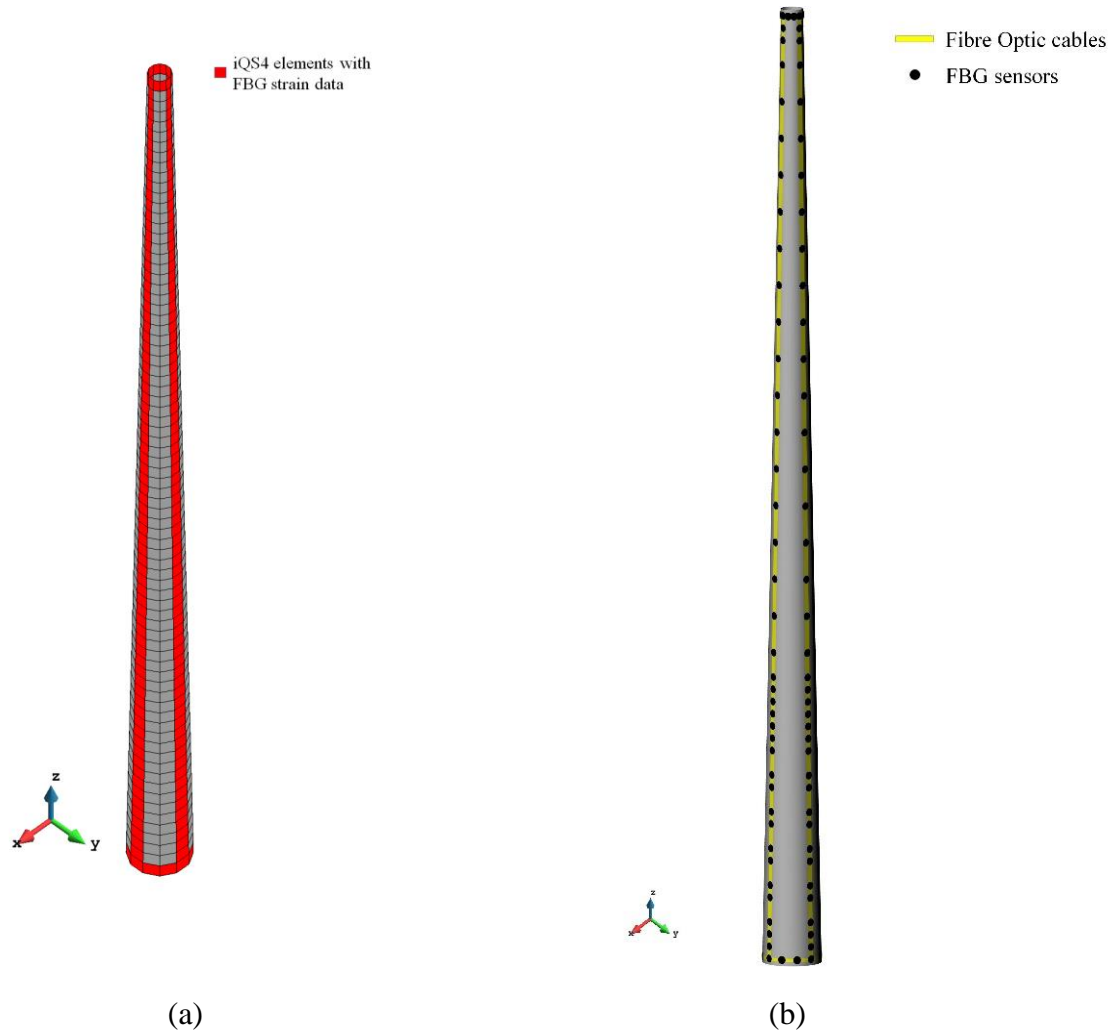


**Figure 4.6** Sensor locations for reduced sensors case (a) 328 elements (b) 176 elements

### 4.3.3 Static analysis of the tower

For the static condition, iFEM analysis with full sensors and reduced sensors is performed. Maximum values of total displacements and von Mises stresses are calculated and listed in Table 4.1 and the differences between iFEM/iFEM-r are also given in Table 4.2. According to the table, it can be seen that iFEM, both with full sensors and with reduced sensors, can predict the maximum value of the total displacements with high accuracy. The differences against the reference value are smaller than 1% for both cases. For the calculation of von Mises stresses, iFEM with full sensors obtains a value of 6.298 Mpa which is 1.368% higher than the reference value. With the reduction of the sensors, the extreme value is further over-estimated as 6.407 Mpa and the difference raises to 3.122%. Even though the difference increases slightly due to the decrease of the number of sensors, the percentage difference is still less than 5%, which means the results of iFEM are very close to the reference FEM results. In addition, plots of the total displacements and von Mises stresses are also provided in Figs. 4.7 and 4.8. Since the

tower only bears the weight of itself and the top structures, it is expected that the displacements in the z-direction will be the dominant one. The extreme value of the total displacements is concentrated at the top of the tower. The displacements have a tendency of increasing from zero to the maximum value along with the height. As Fig. 4.7 shows, the total displacement plots of the full-sensor and reduced-sensor iFEM cases are both indistinguishable from the reference FEM plot showing that the results of iFEM are in good agreement with FEM results. Concerning the von Mises stress, owing to the fact that the thickness of each section is fixed at 30 mm but the diameter of the hull is decreasing from the bottom to the top, the extreme von Mises stress occurs at the bottom boundary of the tower. At the same time, there are also some large stresses shown at the top of the tower. The minimum value of the von Mises stress is located around the middle of the tower. In a summary, the extreme values and plots of iFEM are pretty similar to reference FEM results which shows that in static conditions iFEM, even using a low number of sensors, can provide accurate condition information of the tower.

**Table 4.1** Results for static condition

Static case	$U_T$ (m)	$\sigma_{vm}$ (Pa)
a. FEM	1.700E-03	6.213E+06
b. iFEM	1.701E-03	6.298E+06
c. iFEM-R	1.698E-03	6.407E+06

**Table 4.2** Differences between iFEM/iFEM-r and FEM for static condition

Differences	$U_T$ (m)	$\sigma_{vm}$ (Pa)
FEM & iFEM	0.059%	1.368%
FEM & iFEM-r	0.118%	3.122%

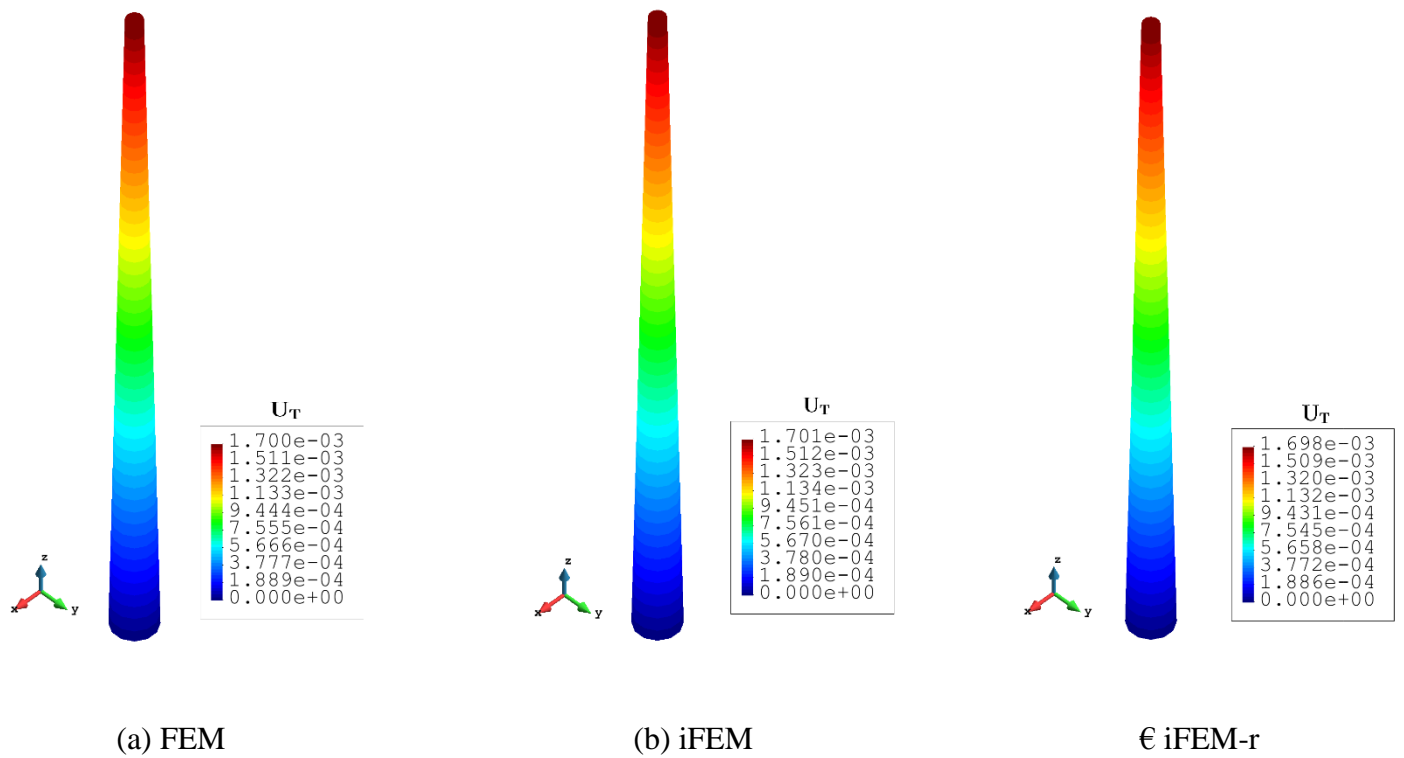


**Figure 4.7** Contour plot of  $U_T$  (unit: m) for static condition

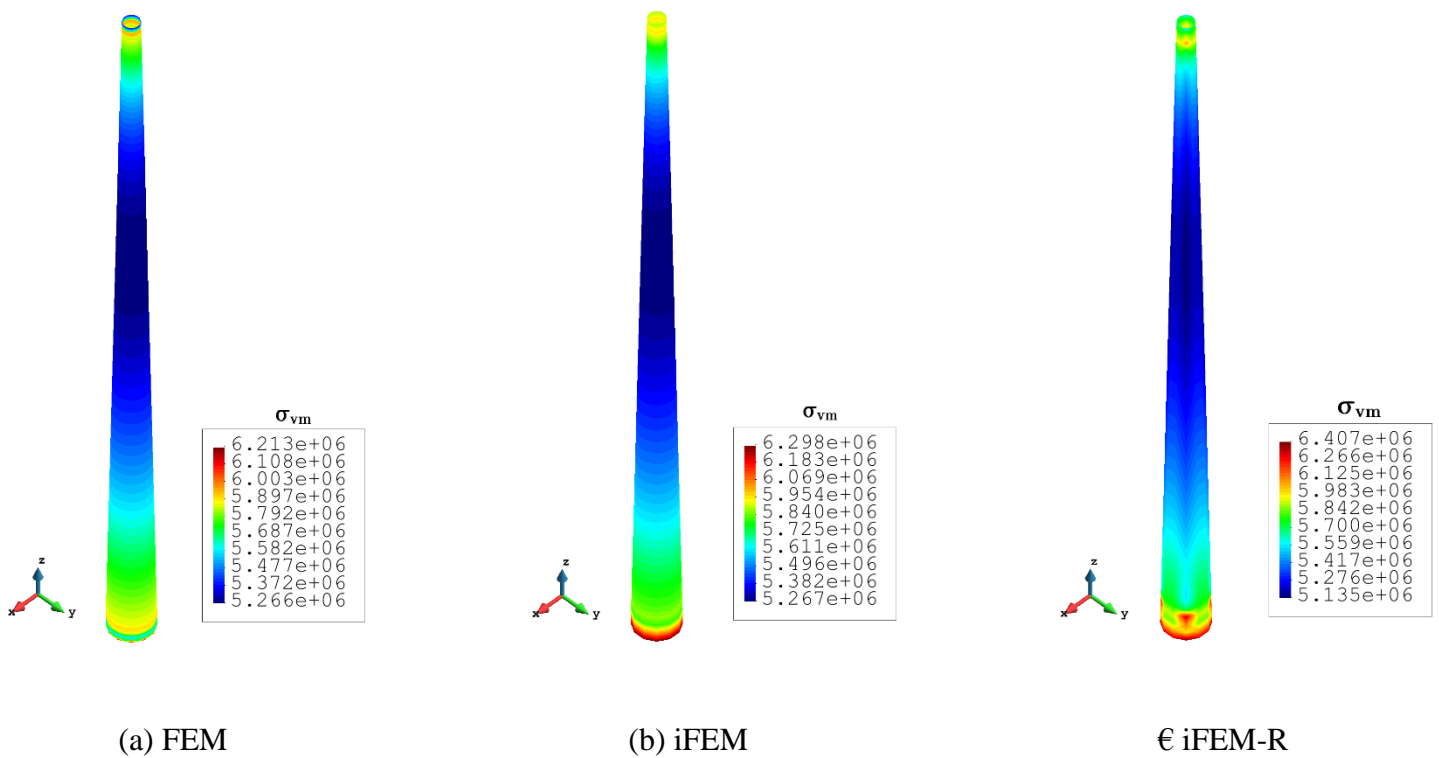


**Figure 4.8** Contour plot of  $\sigma_{vm}$  (unit: Pa) for static condition

#### 4.3.4 Dynamic analysis of the tower

For the health monitoring of the tower under dynamic loadings, aerodynamic and hydrodynamic forces are considered. The time duration of the analysis is 10 s and the total number of time steps is 200 which means that the time scale for each time step is 0.05 s. The average wind speed is assumed to be 18 m/s and the plot of the wind speed varying with time is given in Fig. 4.9.

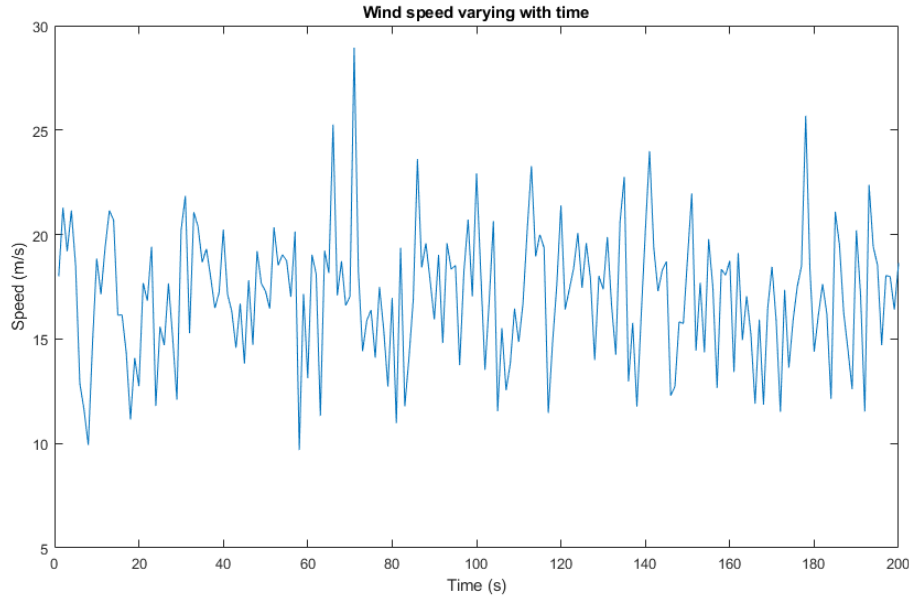


**Figure 4.9** Variation of wind speed at reference height against time

The relationship between the wind velocity and the height is established by the following formula (Van Der Tempel, 2006):

$$V_{air} = V_{ref} \left( \frac{Z}{Z_r} \right)^\alpha \quad (4.10)$$

where  $V_{air}$  is the wind velocity at the corresponding position which has a height of  $Z$ .  $Z_r$  is the reference height, usually 10 m is preferred,  $V_{ref}$  is the wind velocity at the reference height,  $\alpha$  is the Hellman coefficient and 0.12 is suggested for the natural air above the calm sea. (Van Der Tempel, 2006)

After calculating the wind velocity at different elevations, the aerodynamic loads can be obtained by a formula that is identical to the Morrison equation for hydrodynamic force calculation which is given as (Dagli et al., 2018):

$$F_{aero} = \int_0^h \frac{1}{2} C_{aero} \rho_{air} A_{(z)} V_{air(z,t)}^2 dz \quad (4.11)$$

where  $F_{aero}$  is the aerodynamic load at the height of  $Z$ ,  $C_{aero}$  is the aerodynamic coefficient which can be determined by the shape of the structure. For the current analysis, 0.5 is used because of the cylindrical shape.  $\rho_{air}$  is the density of the wind and  $1.25 \text{ kg/m}^3$  is used.  $A_{(z)}$  is the exposed area of the structure at the height of  $Z$ .  $V_{air}$  is the wind velocity calculated by using Eq. (4.10).

The wind forces acting on the tower are calculated section by section and applied as pressure to each section. The aerodynamic load on the blade of the OWT for the working condition can also be estimated by the same equation. The swept area of the blades is  $624 \text{ m}^2$  and this load is treated as a trust force and transformed to the top of the tower (the height of the RNA is selected at 45 m above the water surface for simplification). (Dagli et al., 2018)

Morrison equation is used for the calculation of the hydrodynamic force. According to the Morrison equation, the hydrodynamic forces are formed by Drag force ( $F_D$ ) and Inertia force ( $F_I$ ). The detailed formula for these two forces when acting on the cylindrical structure is given as:

$$F_D = \int_{-d}^0 \frac{1}{2} \rho_{sea} C_d A_{(z)} u_{(z,t)} |u_{(z,t)}| dz \quad (4.12)$$

$$F_I = \int_{-d}^0 \frac{1}{4} \pi \rho_{sea} C_I A_{(z)}^2 u'_{(z,t)} dz \quad (4.13)$$

where  $\rho_{sea}$  is the density of the seawater and  $1025 \text{ kg/m}^3$  is used. The drag coefficient ( $C_d$ ) and inertia coefficient ( $C_I$ ) are 0.7 and 2.0, respectively, just as recommended by ISO 1990-1 (ISO, 2005).  $A_{(z)}$  is the area per unit height.  $u_{(z,t)}$  and  $u'_{(z,t)}$  are the velocities and the accelerations of the water particles, separately. For the current analysis, linear wave theory is used, and the information of the wave is given in Table 4.3:

**Table 4.3** Wave parameters

Items	Values	Units
Wave height ( $W_h$ )	1.8	m
Wave length ( $W_l$ )	40	m
Wave period ( $W_t$ )	5	s
Water depth ( $W_d$ )	20	m

The ratio of water depth to wave height is 0.5, which is properly selected between deep water and middle water conditions. Then the velocity and acceleration of the water particles can be calculated as:

$$u_{(z,t)} = \frac{\pi W_h}{W_t} \frac{\cosh\left(\frac{2\pi Z}{W_l}\right)}{\sinh\left(\frac{2\pi W_d}{W_l}\right)} \cos(\theta) \quad (4.14)$$

$$\dot{u}_{(z,t)} = \frac{2\pi^2 W_h}{W_t^2} \frac{\cosh\left(\frac{2\pi Z}{W_l}\right)}{\sinh\left(\frac{2\pi W_d}{W_l}\right)} \sin(\theta) \quad (4.15)$$

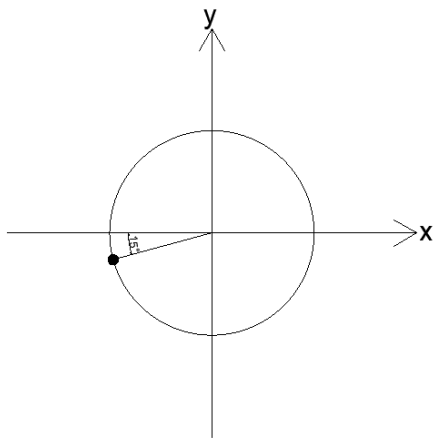
where  $Z$  is the water depth of the reference location.  $\theta$  is the phase angle and it can be calculated based on the position and time as:

$$\theta = \frac{2\pi}{W_l} x - \frac{2\pi}{W_t} t \quad (4.16)$$

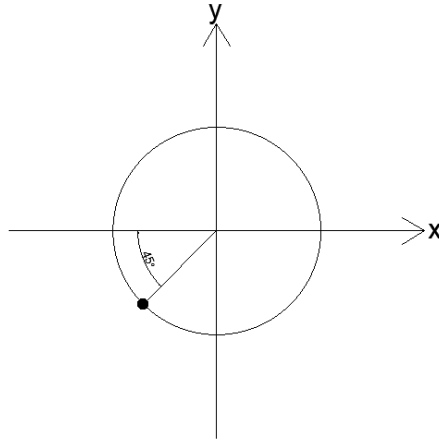
The wave forces are calculated from the bottom of the tower to the free water surface for simplification and they are also applied in the format of pressure to the tower. For the current analysis, the hydrodynamic and aerodynamic forces are in the same direction because it is the most severe loading condition which will lead to the most serious deformations.

Apart from extra loadings, the model is kept the same as the static case, i.e., not only the parameters but also the sensor locations are fixed for both conditions. Every 0.05 s the results of the iFEM analysis are recorded and then the total displacements and von Mises stresses are subsequently calculated for comparison. Six nodes at 40 m height (general height) are selected and the locations of the nodes are varying from the windward direction to the leeward direction (Figure 4.10). Besides, another three nodes, at the same position as node 6 (Figure 3.10(f)) but at different heights, are also chosen. The heights are 10 m (underwater), 20 m (free water surface), and 60 m (near the top boundary).

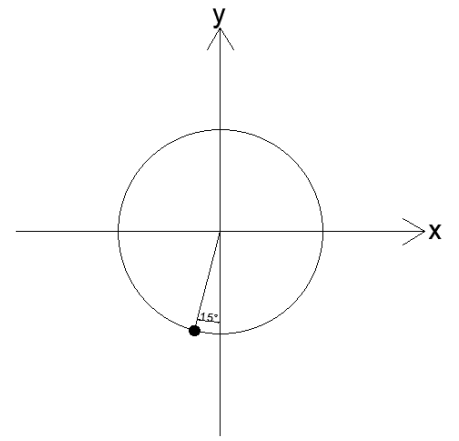
The results of these nodes are collected and shown in Figs. 4.11-4.14. Fig. 4.11 shows the plots of the total displacements for the nodes at different heights. First of all, iFEM with full sensors can obtain accurate results regardless of the heights of the nodes. The reference FEM and iFEM with full sensors results match perfectly with each other for the four diagrams. However, iFEM with reduced sensors (iFEM-r) makes less estimation of the total displacement for all four nodes. However, it can be seen that the differences are becoming smaller with the increase of the height of the nodes. It should also be mentioned that the total displacements at 60 m are much larger than the total displacements at 10 m, i.e., the total displacements will increase with the height of the tower. The large deformations are given more attention because they can obviously show the health condition of the structure. Therefore, the errors in the total displacements at 10 m and 20 m are still reasonable. For the von Mises stress, iFEM can predict the von Mises stress accurately for the nodes at 40 m and 60 m. Even if the values of the von Mises stress are slightly over-valued for some zones by iFEM with reduced sensors, for the majority of parts they are still in good agreement with reference FEM results. For the node at 20 m, the situation is becoming more severe. It is interesting to find that the results of iFEM with reduced sensors are even better than the iFEM with full sensors. The results are not always over-estimated for this node and during the first two seconds, they are slightly less than FEM results. Since this node is at the free water surface and the wave forces and wind forces are both acting on this region, the strains around the free surface will suffer sharp changes resulting in complex variations of results. But the main trend of the iFEM results is still the same as the FEM results. Due to the complexity of loading conditions, the maximum von Mises stress is located at the bottom of the tower in most cases. At 10 m height, the results of both full-sensor and reduced-sensor iFEM are bigger than the reference, but the differences between the full-sensor condition and FEM are smaller than the reduced-sensor condition in general. The results of von Mises stress from iFEM can be very useful for failure judgment.



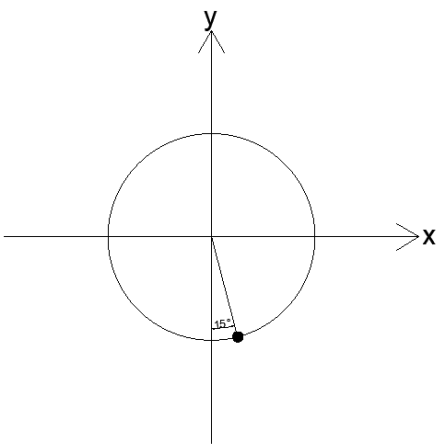
(a) node 1



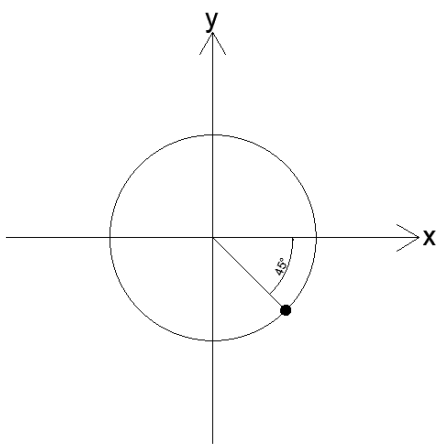
(b) node 2



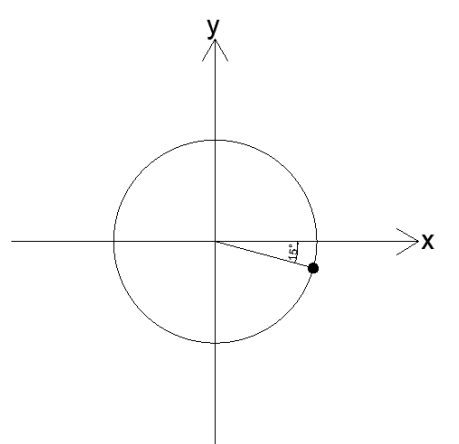
(c) node 3



(d) node 4



(e) node 5



(f) node 6

**Figure 4.10** The positions of the six nodes on the horizontal x-y plane

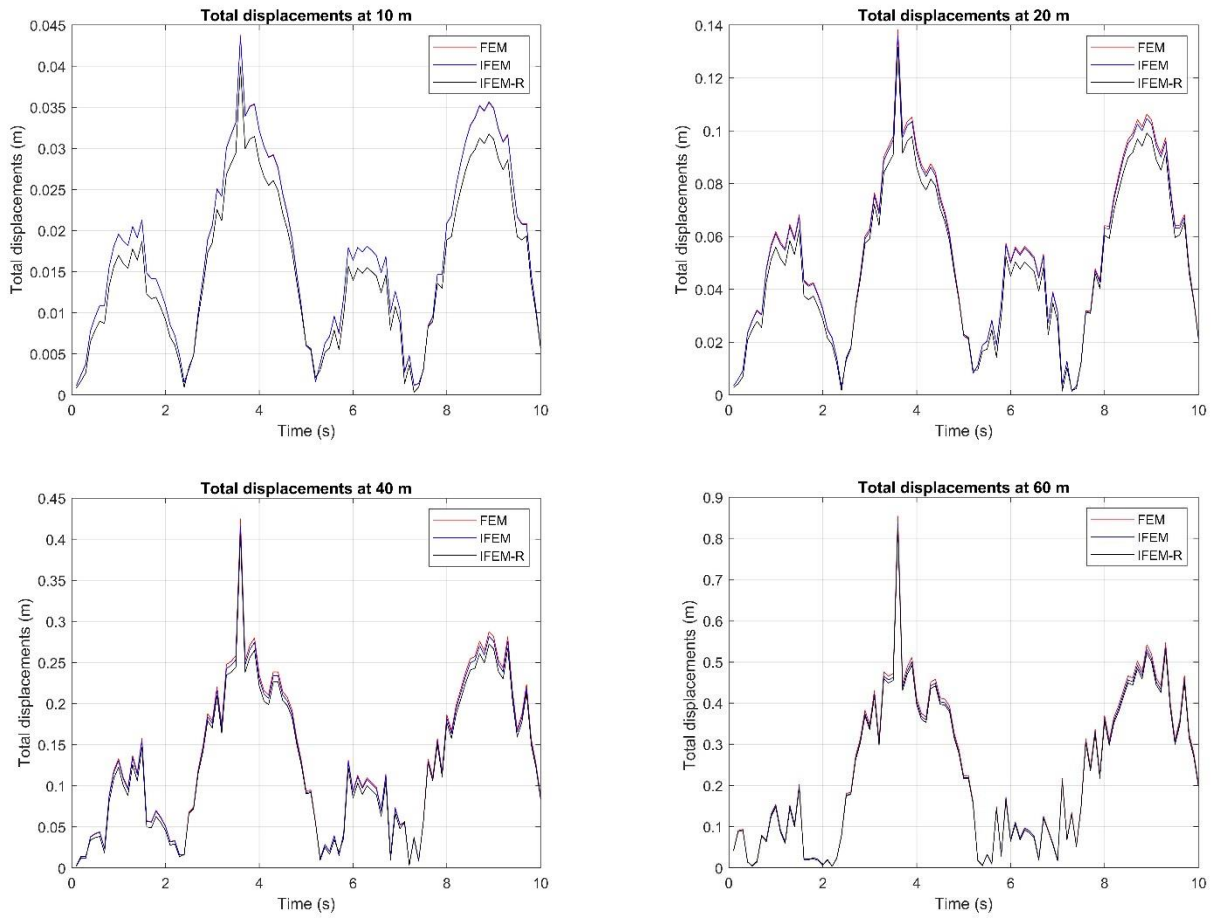


**Figure 4.11** Variation of total displacements  $U_T$  (m) against time (s) for four nodes located at 10 m, 20 m, 40 m, and 60 m

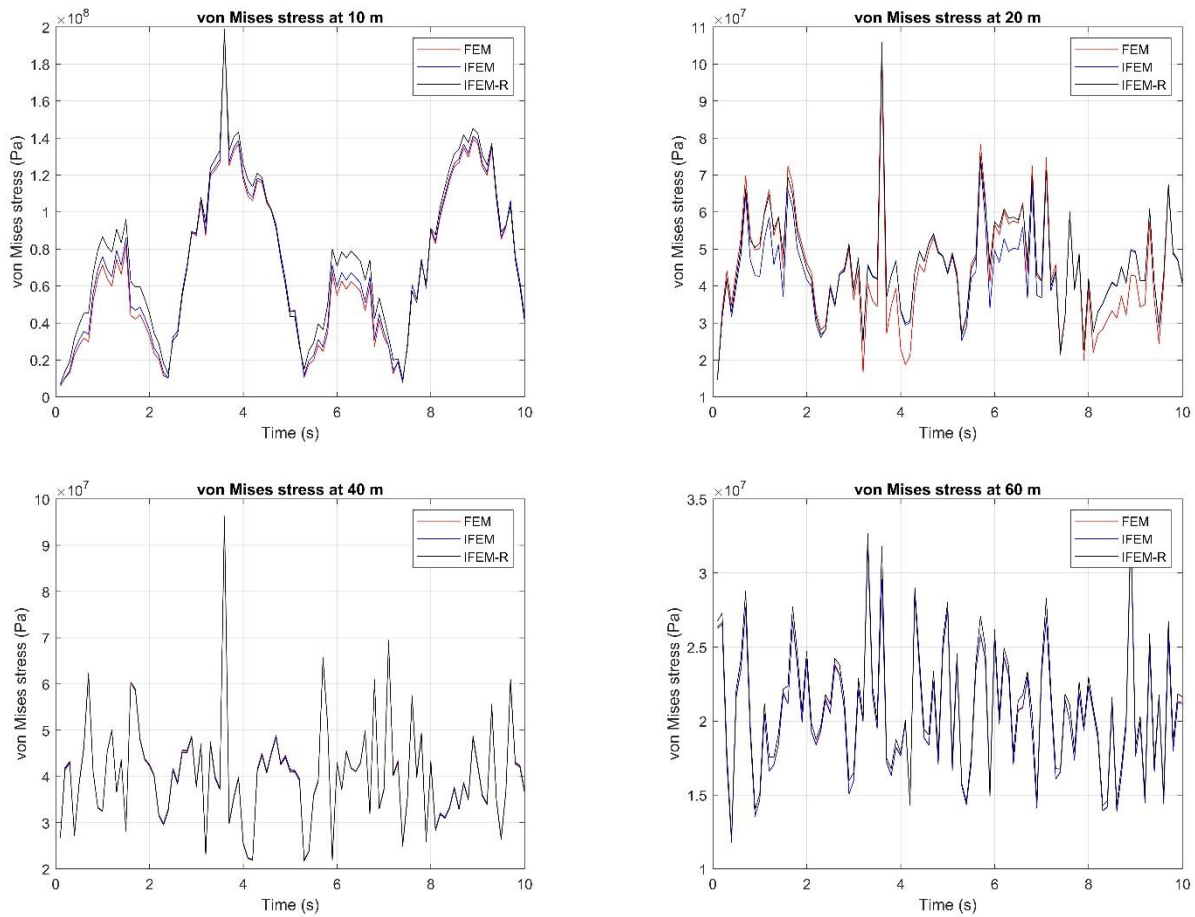


**Figure 4.12** Variation of von Mises stresses  $\sigma_{vm}$  (Pa) against time (s) for four nodes located at 10 m, 20 m, 40 m, and 60 m

Six nodes in half of the ring lines at 40 m height are selected to investigate the effect of the nodal position on the same horizontal plane. For the total displacements, except for the values of the total displacements that are slightly under-estimated, the differences of all six nodes against their FEM results cannot be distinguished. Therefore, the nodal position on the same horizontal plane does not have a big influence on the total displacement monitoring. The von Mises stress of all nodes can also be correctly monitored. However, the differences at node 3 are much bigger than at the remaining nodes. Since this node is at a position where only one side is subjected to wind loads, there are large differences between both sides resulting in these errors. The maximum von Mises stress usually occurs in the x-direction which means that the values at this node are not as important as node 1 and node 6, so the differences are acceptable.

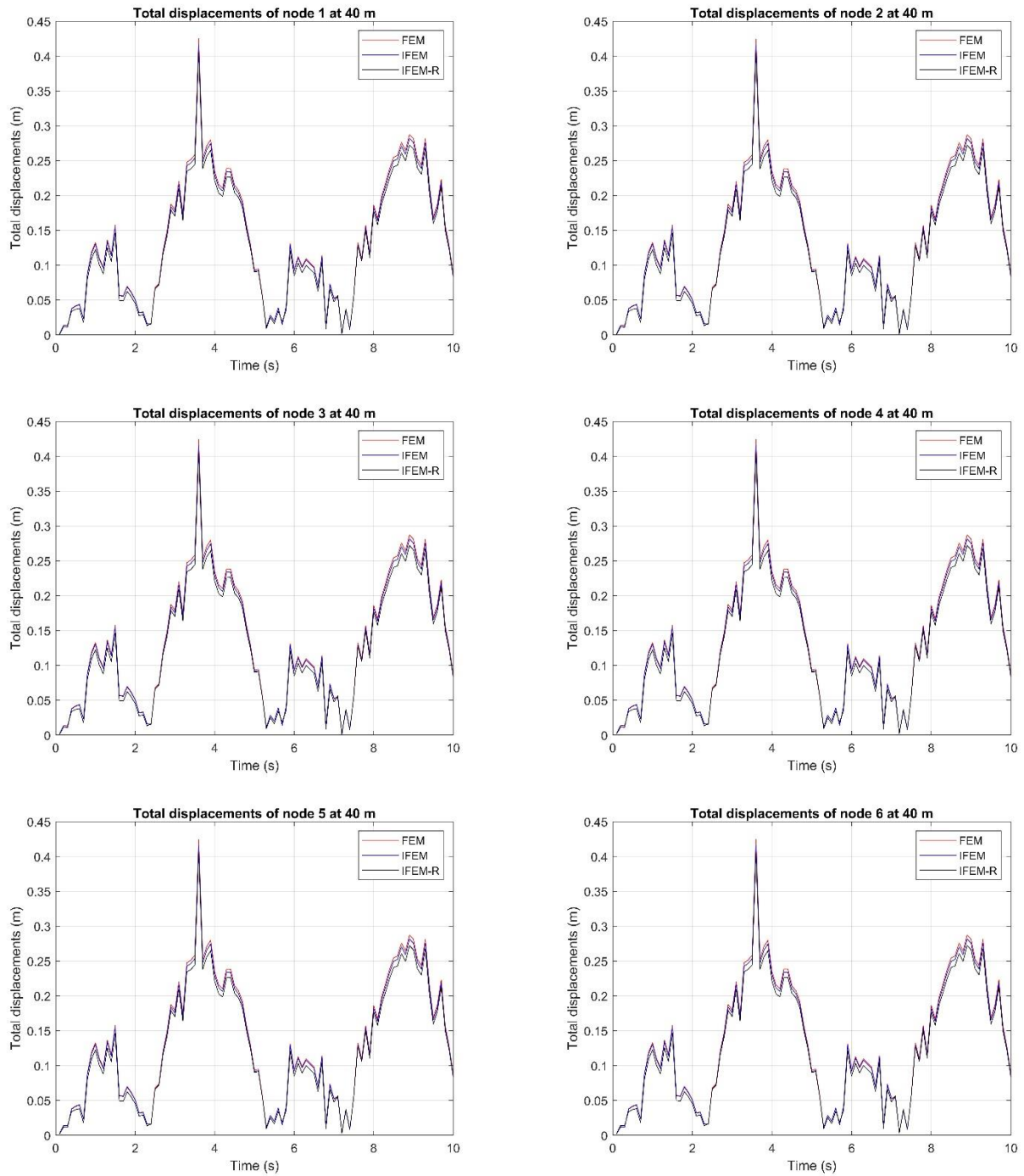


**Figure 4.13** Variation of total displacements  $U_T$  (m) against time (s) for six nodes located at 40 m

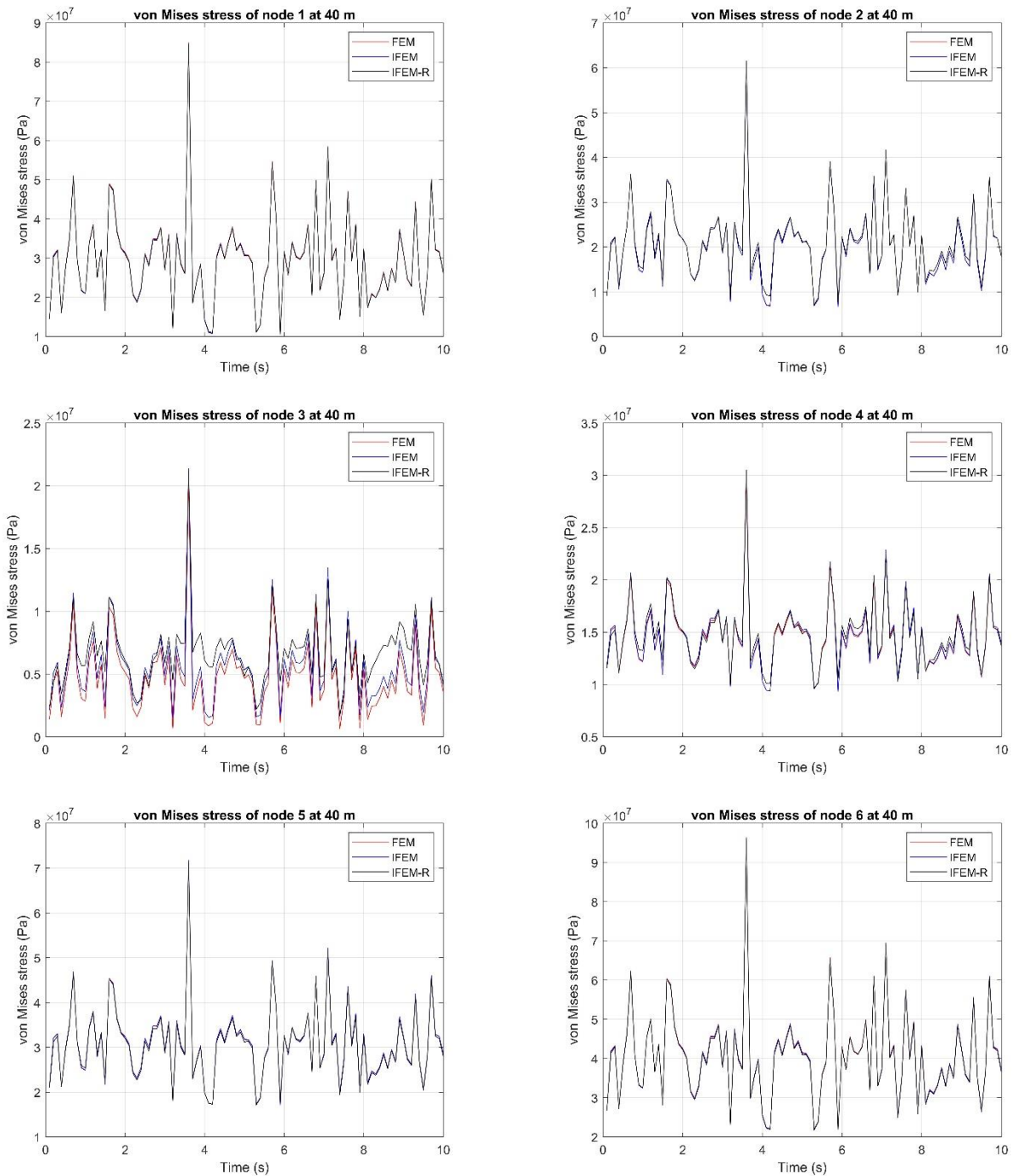


**Figure 4.14** Variation of von Mises stresses  $\sigma_{vm}$  (Pa) against time (s) for six nodes located at 40 m

Finally, the total displacements and von Mises stresses of the whole structure at 5 s are also used to evaluate the iFEM results. The extreme values are listed in Table 4.4 and Table 4.5 and the plots are also given as Figs. 4.15 and 4.16. In light of Table 4.4 and Table 4.5, iFEM whether with full sensors or reduced sensors can predict the correct extreme results with less than 5% difference. The total displacements are also increasing from zero to the maximum value with

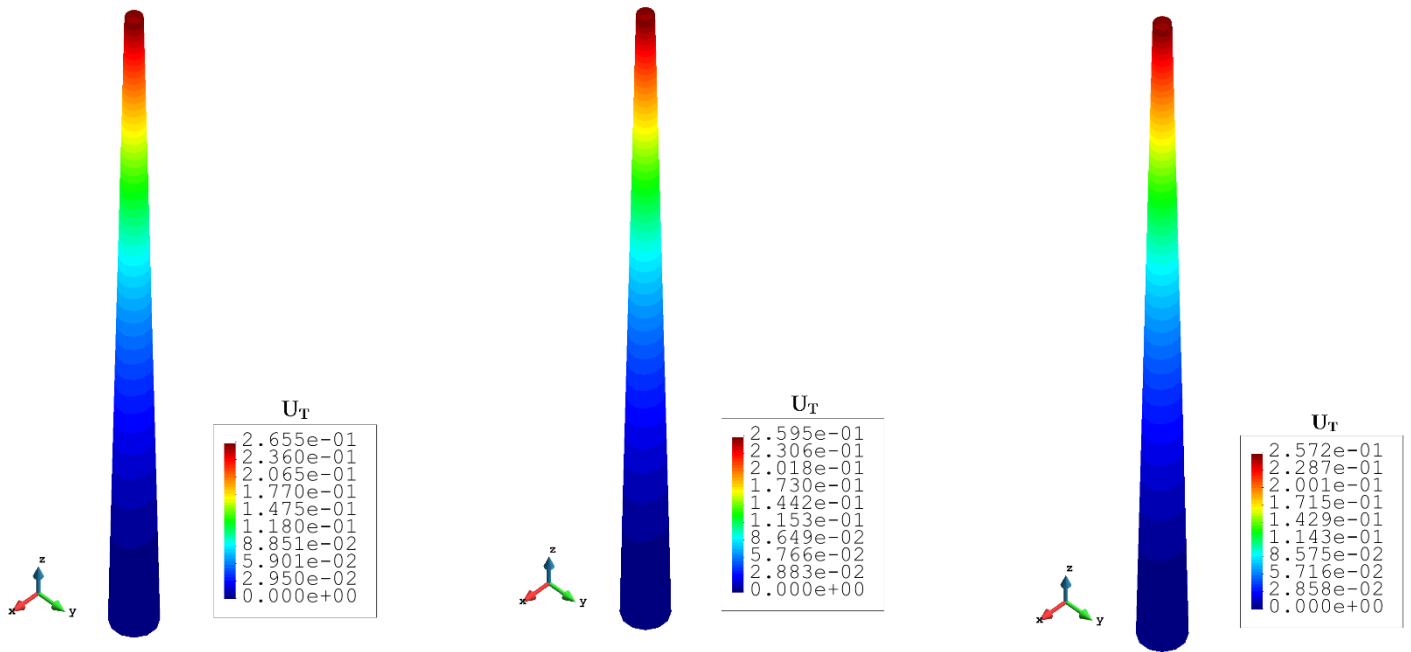
the rise of the height, but the dominated displacements are the deformations in the x-direction. The plots of the total displacements of iFEM are in line with the reference plot. The large stresses are concentrated at the bottom of the tower and the plots of iFEM can show this characteristic clearly. In conclusion, iFEM can perform accurate, reliable, and robust SHM analysis for the tower of the OWT for both static and dynamic loading conditions. Currently used sensors, four longitudinal and two circumferential lines, would be enough for the monitoring process.

**Table 4.4** Results of the dynamic condition at 5 s

Dynamic case (5s)	$U_T$ (m)	$\sigma_{vm}$ (Pa)
a. FEM	2.655E-01	5.072E+07
b. iFEM	2.595E-01	5.155E+07
c. iFEM-R	2.572E-01	5.105E+07

**Table 4.5** Differences between iFEM/iFEM-r and FEM for the dynamic condition at 5 s

Differences	$U_T$ (m)	$\sigma_{vm}$ (Pa)
FEM & iFEM	2.260%	1.636%
FEM & iFEM-r	3.126%	0.651%

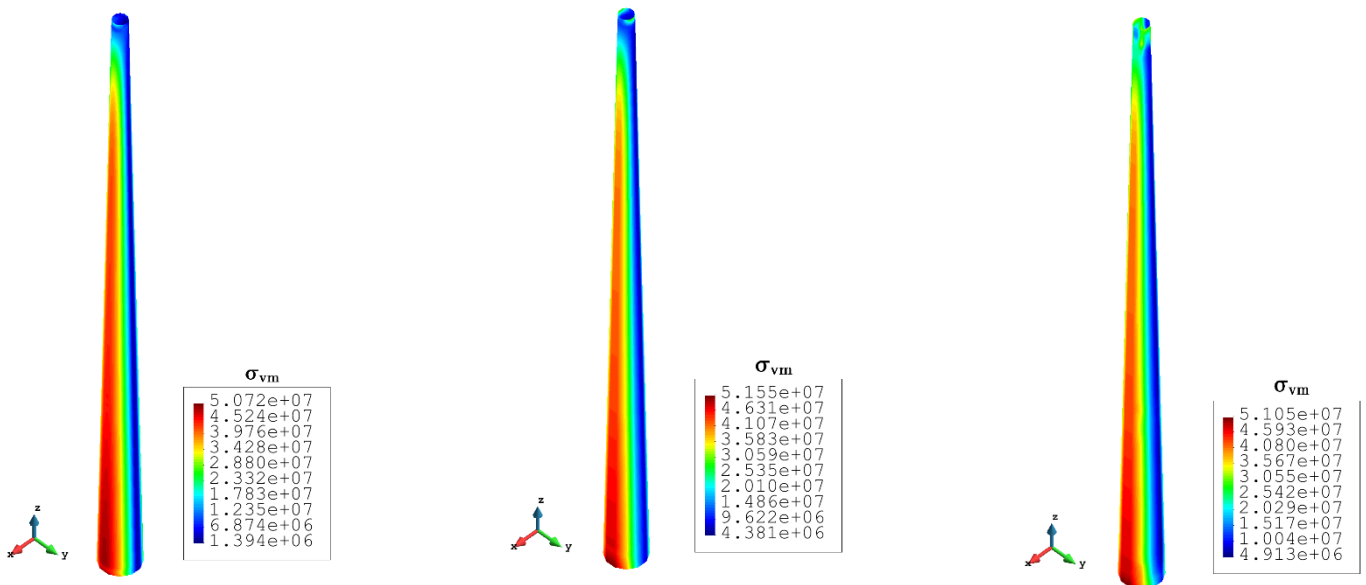


(a) FEM

(b) iFEM

(c) iFEM-r

**Figure 4.15** Contour plot of total displacements,  $U_T$  (unit: m) for the dynamic condition at 5 s



(a) FEM

(b) iFEM

(c) iFEM-r

**Figure 4.16** Contour plot of von Mises stresses,  $\sigma_{vm}$  (unit: Pa) for the dynamic condition at 5 s

## 4.4 Numerical analysis of the NREL 5 MW offshore wind turbine blade

### 4.4.1 Model generation of the blade and sensor selection

In order to generate the model of the blades of offshore wind turbines, the typical and widely used NREL 5MW offshore wind turbine was selected. It has 3 blades with a diameter of 123 m and these blades are installed to a hub, which is located at 90 m above the water surface, and its diameter is 3 m. The pre-cone angle ( $\theta_c$ ) is 2.5 degrees. However, in order to simplify the problem, the tilt angle was ignored. Additional information about this offshore wind turbine can be found in (Jonkman et al., 2009). An open-access software- NuMAD was utilized to create the model of a single blade. NuMAD was developed by Sandia National Laboratories, and it was specifically created to reduce the difficulties of three-dimensional blade model generation (Berg and Resor, 2012). The accuracy of this software has been proved and it has been widely used for FEM analysis of blades (Berg and Resor, 2012; Resor, 2013; Yang and Baeder, 2016; Fernandez et al., 2018; Zhang et al., 2018). For the current analysis, due to the fact that NuMAD can generate some input files which can be used by ANSYS software directly, ANSYS was used for FEM analysis.

First of all, the blade is divided into 18 sections and 19 stations. For each station, there is a chord length ( $c$ ), a twist angle ( $\theta_t$ ), a blade span ( $L_{bs}$ ), and an airfoil table specifically defined. Detailed data can be obtained from (Jonkman et al., 2009; Berg and Resor, 2012). Different from the original reports, several interp-sections were ignored to reduce the complexity of the FEM model. The parameters of each station of the blade are shown in Table 4.6.

**Table 4.6** The parameters of the blade

Section Number	Blade Span (m)	Twist Angle (deg)	Chord Length (m)	Airfoil Table
1	0.00E+00	1.33E+01	3.3860E+00	Cylinder 1
2	1.37E+00	1.33E+01	3.3860E+00	
3	4.10E+00	1.33E+01	3.8540E+00	
4	6.83E+00	1.33E+01	4.1670E+00	Cylinder 2
5	1.03E+01	1.33E+01	4.5570E+00	DU99-W-405
6	1.44E+01	1.15E+01	4.6520E+00	DU99-W-350
7	1.85E+01	1.02E+01	4.4580E+00	
8	2.26E+01	9.01E+00	4.2490E+00	DU97-W-300
9	2.67E+01	7.80E+00	4.0070E+00	DU91-E-250
10	3.08E+01	6.54E+00	3.7480E+00	
11	3.49E+01	5.36E+00	3.5020E+00	DU93-W-210
12	3.90E+01	4.19E+00	3.2560E+00	
13	4.31E+01	3.13E+00	3.0100E+00	NACA-64-618
14	4.72E+01	2.32E+00	2.7640E+00	
15	5.13E+01	1.53E+00	2.5180E+00	
16	5.47E+01	8.63E-01	2.3130E+00	
17	5.74E+01	3.70E-01	2.0860E+00	
18	6.01E+01	1.06E-01	1.4190E+00	
19	6.15E+01	0.00E+00	1.0855E+00	

The information about the airfoil tables is given in (Timmer and Van Roojj, 2003; Schweigler, 2012). The initial pitch angle ( $\theta_p$ ) was defined as 0 degrees and when the wind speed exceeds the rated wind velocity, the pitch angle is applied correspondingly.

After creating the stations, the material properties of each station were specified by defining material division points. The blade consists of six different types of materials, which are Gelcoat, E-LT-5500 (UD), SNL (Triax), Saertex (DB), and Foam and Carbon (UD). Gelcoat and Foam can be treated as isotropic materials and the remaining ones are regarded as orthotropic materials. Material properties, including the composition of these materials in each section, can be obtained from (Griffith, 2013; Griffith, 2013; Resor, 2013). Shear webs are significant and critical components for the blades because they reinforce the strength of the whole blade and make the blade more resistant to bending loadings. For this particular type of blade, the webs are located from 1.3667 m spans to 60.133 m spans, and they are made from a combination of Saertex (DB) and Foam. The geometry of the final model in NuMAD is given in Fig. 4.17.

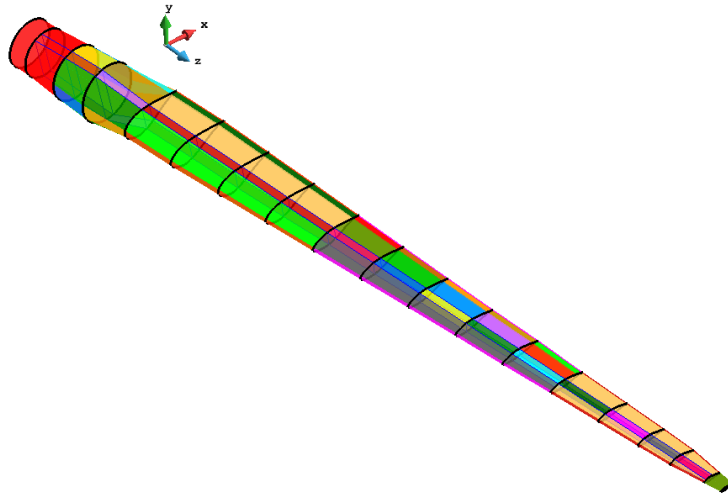


**Figure 4.17** The geometry of the blade from NuMAD

The model generated in NuMAD was exported for ANSYS. To avoid triangular elements, the model was re-meshed again with quadrilateral elements and finally, there are 18630 elements and 18457 nodes. Furthermore, an additional node was defined by using the Mass21 element type at the 61.5 m blade span together and making a rigid region to replace the closed-shell structure at the tip of the blade. The mesh of the FEM model is shown in Fig. 4.18(a). For the iFEM model, the blade was modelled with a much coarser mesh and after balancing the requirements of fulfilling the completeness of the blade and reducing the number of sensors, the number of elements becomes 2070 (see Fig. 4.18(b)). By logical selection of the FEM elements based on their relative positions, each iFEM element has a specific FEM element to offer the strain data for full-sensor conditions. Moreover, attention was also given to the reduction of the required number of sensors. For a blade, the root and tip are usually important regions. Additionally, there are some sharp changes in the zones between different airfoil shapes, especially between the circular station and the DU99-W-405 airfoil station. Therefore, sensors were placed around this region to monitor the blade. Since the length of the blade is much larger than the size of the cross-section, the top and bottom surfaces experience similar deformations, so the majority of the sensors were installed only at the top surface. A line of sensors in the longitudinal span direction was chosen to keep the continuity of the analysis and a shorter line of sensors at the back surface of the blade was preferred. This can help to improve the monitoring of the condition of the leading edge around the tip region. Moreover, this will also strengthen the monitoring of the extreme flap-wise displacements which are usually the most severe deformations suffered by the blades. After testing the accuracy of different

distributions of these sensors, 122 sensor locations were selected, and the locations of these sensors are shown in Fig. 4.19.

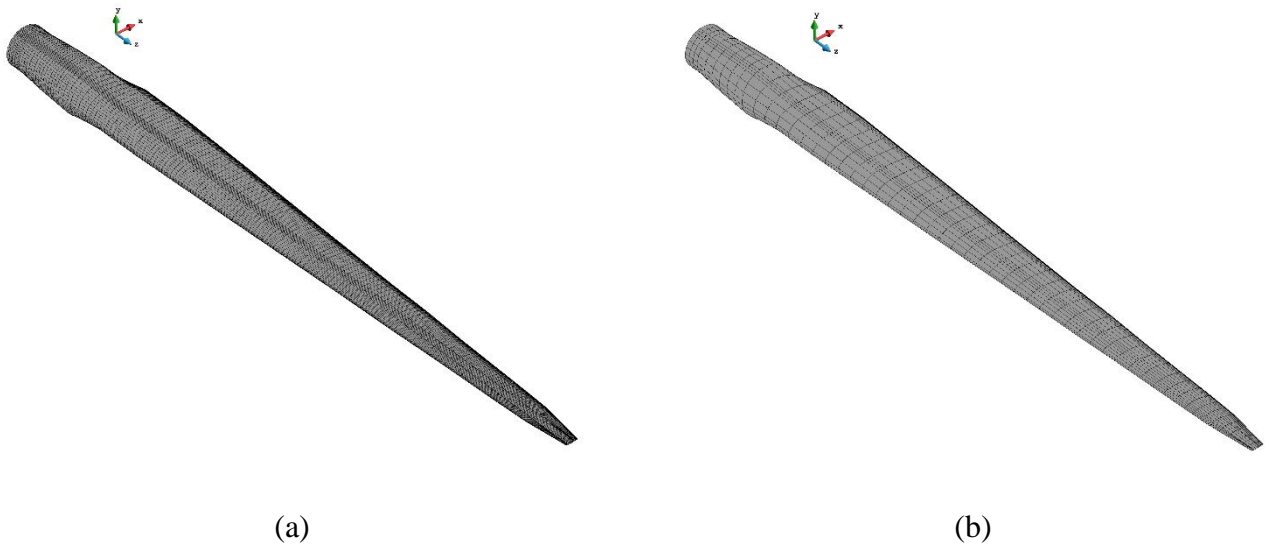


**Figure 4.18** The mesh for FEM (a) and iFEM (b) models

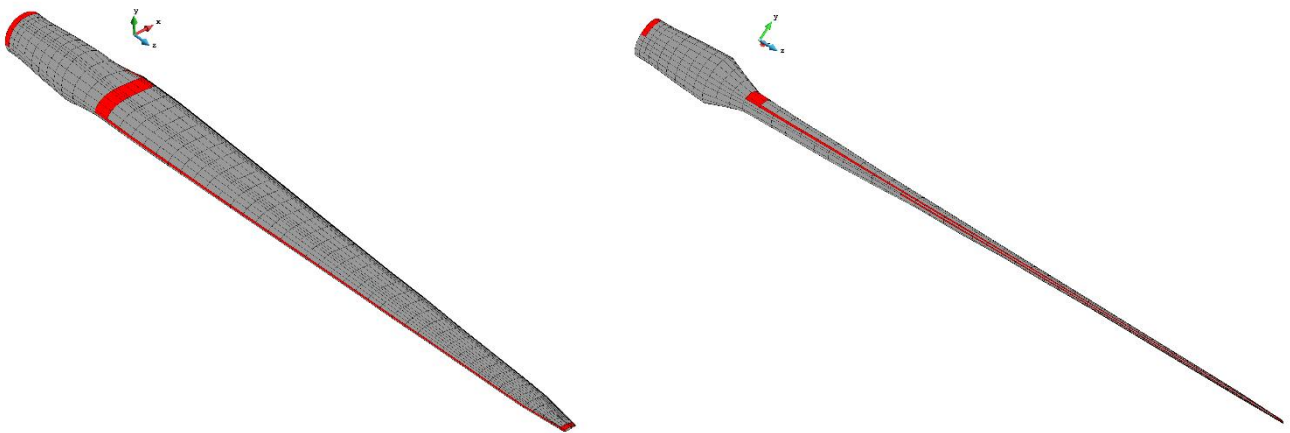


**Figure 4.19** The selected sensor locations for iFEM analysis

Therefore, during the iFEM analysis, only 122 locations were installed with sensors for the reduced-sensor condition, i.e., only 122 iFEM elements can obtain the input strain data. With the help of FBG technology, the sensors can be installed by only  $6 \times 2$  cables. By analyzing the frequency interval, the strain data can be separated into normal and in-plane shear strains, and then they can be inputted into iFEM analysis.

#### 4.4.2 Loading calculation

For the current analysis, three types of loadings were considered including gravity, centrifugal force, and aerodynamic force. For gravity, since the density of the material is defined during the process of model generation, gravity can be applied as acceleration in ANSYS. The basic information about the speeds of the wind and the rotor is given in Table 4.7: (Jonkman et al., 2009)

**Table 4.7** The velocities of wind and rotor

	Wind Speed ( $m/s$ )	Rotor Speed ( $rpm$ )
Cut-In	3	6.9
Rated	11.4	12.1
Cut-Out	25	

The turbine is only in service when the wind velocity is between  $3 m/s$  and  $25 m/s$ . Otherwise, the rotor will be transformed to be parallel to the wind direction by the yaw control system. For the current analysis, the wind velocity is chosen as  $6 m/s$  and according to the diagrams of Jonkman et al. (Jonkman et al., 2009), the blade tip ratio is decided as 8. The expression of the blade tip ratio is given as:

$$r_{bt} = \frac{\omega R \cos(\theta_c)}{V_w} \quad (4.17)$$

where  $V_w$  is the wind velocity,  $\omega$  is the angular velocity of the blade, and  $R$  is the length from the center of the rotor to the tip of the blade.

By using Eq. (3.17), the angular velocity of the blade can be determined as  $7.28 rpm$ . The centrifugal force can also be applied in the format of acceleration:

$$a_c = \omega^2 r \quad (4.18)$$

where  $r$  is the distance from the middle of each section to the center of the rotor.

For the aerodynamic force, the blade element momentum theory (BEMT) was utilized. Although CFD simulation can usually perform more accurate aerodynamic analysis for the blades, CFD is very complex and time-consuming. Moreover, BEMT has been used and is still underutilization for the aerodynamic force calculation of blades (Jureczko et al., 2005; Dai et al., 2011; Bavanish and Thyagarajan, 2013; Wang et al., 2014; Wen et al., 2017; Zhang, 2018). For engineering analysis, BEMT is one of the simplest and most effective ways for wind force calculation. (Zhang, 2018) The process of the BEMT application can be simplified as the following steps: (Zhang, 2018)

1. Set the initial values of the axial and tangential induction factors ( $i_a$  and  $i_t$ ) to 0;
2. The flow angle  $\theta_f$  can be calculated by the following equation:

$$\theta_f = \tan^{-1} \left( \frac{(1-i_a)V_w}{(1+i_t)\omega r} \right) \quad (4.19)$$

3. By subtracting the twist angle ( $\theta_t$ ) and pitch angle ( $\theta_p$ , currently equals 0), the attacking angle ( $\theta_a$ ) can be obtained:

$$\theta_a = \theta_f - \theta_t - \theta_p \quad (4.20)$$

4. With the help of the attacking angle, the coefficients for lift force ( $C_l$ ), drag force ( $C_d$ ), and pitching moment ( $C_m$ ) can be obtained from the available data table. (Zhang, 2018)

5. The method of Shen et al. (Shen et al., 2005) for the tip and hub loss factors calculation is chosen here because they are more reliable after considering the experimental data.

$$g = e^{-0.125(N_b r_{br}^{-2})} + 0.1 \quad (4.21)$$

where  $N_b$  is the number of blades,  $N_b = 3$ .

The tip and hub loss factor can be calculated by the functions given below:

$$f_{tip} = \frac{2}{\pi} \cos^{-1} \left( e^{-g \frac{B(R-r)}{2r \sin(\theta_f)}} \right) \quad (4.22a)$$

$$f_{hub} = \frac{2}{\pi} \cos^{-1} \left( e^{-g \frac{B(r-r_{hub})}{2r_{hub} \sin(\theta_f)}} \right) \quad (4.22b)$$

The final total loss correction factor can be computed by multiplying  $f_{tip}$  with  $f_{hub}$  :

$$f_{lc} = f_{tip} f_{hub} \quad (4.23)$$

6. A pair of new induction factors can be calculated by the following expressions:

$$i'_a = \frac{1}{\frac{4f_{lc} \sin^2(\theta_f)}{r_s \cos^2(\theta_c) (C_l \cos(\theta_f) + C_d \sin(\theta_f))} + 1} \quad (4.24a)$$

$$i'_t = \frac{1}{\frac{4f_{lc} \sin(\theta_f) \cos(\theta_f)}{r_s \cos^2(\theta_c) (C_l \sin(\theta_f) - C_d \cos(\theta_f))} - 1} \quad (4.24b)$$

where  $r_s$  is the solidity ratio and it is defined as  $r_s = \frac{N_b c}{2\pi r \cos(\theta_c)}$ .

7. Comparing the new induction factors against the previous values, if the percentages of the differences are within 1%, the process will be completed. Otherwise, the process will return to the first step and the induction factors will be set as the average values of the newly calculated and previous induction factors. Repeat the whole process until the values are under the tolerance value.

8. Afterward, the relative wind velocity can be computed by the combination of the wind velocity and angular rotation speed as:

$$V_r = \sqrt{(V_w (1 - i_a) \cos(\theta_c))^2 + (\omega r (1 + i_t) \cos(\theta_c))^2} \quad (4.25)$$

9. The lift force ( $F_l$ ), drag force ( $F_d$ ), and pitching moment ( $M_p$ ) for each section can be obtained based on the equations below:

$$F_l = \frac{1}{2} \rho_{air} c V_r^2 C_l d_r \quad (4.26a)$$

$$F_d = \frac{1}{2} \rho_{air} c V_r^2 C_d d_r \quad (4.26b)$$

$$M_p = \frac{1}{2} \rho_{air} c^2 V_r^2 C_m d_r \quad (4.26c)$$

where  $\rho_{air}$  is the density of the air and  $1.225 \text{ kg} / \text{m}^3$  is used and  $d_r$  is the length of each section.

By disassembling and reassembling these forces to the global coordinate system, the forces acting in the tangential and axial directions will be:

$$F_x = -F_l \sin(\theta_f) + F_d \cos(\theta_f) \quad (4.27a)$$

$$F_y = F_l \cos(\theta_f) + F_d \sin(\theta_f) \quad (4.27b)$$

$$M = M_p \quad (4.27c)$$

In order to check the accuracy of the force calculation, the total thrust force and torque are also calculated under the rated wind velocity condition by:

$$T = \sum_{i=1}^n \frac{1}{2} N_b \rho_{air} V_r^2 (C_l \cos(\theta_f) + C_d \sin(\theta_f)) c d_r \cos(\theta_c) \quad (4.28a)$$

$$Q = \sum_{i=1}^n \frac{1}{2} N_b \rho_{air} V_r^2 (C_l \sin(\theta_f) - C_d \cos(\theta_f)) c d_r^2 \cos(\theta_c) \quad (4.28b)$$

where  $n$  is the number of sections. The calculated thrust force and torque are  $734.91 \text{ kN}$  and  $4.33 \text{ MNm}$  which are in the same range as the reference (Zhang, 2018). So, the process of force calculation can be verified.

By utilizing the same approach, the aerodynamic force when the wind velocity is  $6 \text{ m/s}$  can be calculated. For simplification of the FEM analysis, the tangential force is applied at the leading edge of each section. (Yang and Baeder, 2016) However, the axial force and pitching moment were evenly applied to the nodes at the joint of the webs and bottom surface (Yang and Baeder, 2016). For the current analysis, the case that the blade is located horizontally and has a tendency of moving upward was selected. The root boundary of the blade was entirely fixed as the boundary condition. After applying the force to the FEM model, the reference results and strain data can be obtained for the following iFEM analysis.

#### 4.4.3 Results for static condition

For the deformation of a blade, the flap-wise displacements are always more severe than the others. In the current coordinate system, the displacements in the y-direction are the dominant ones and according to the FEM results, they would be around 10 times larger than the  $U$  and  $W$  displacements. In order to clearly and concisely represent the displacement field, total displacements are selected. For the full-sensor condition, the maximum total displacements are estimated as 0.59 m and it is about 4.25% less than the reference result (0.6097 m). But for the reduced sensor condition, the estimation of the extreme total displacements is improved, and it is only about 2.106% over the reference value. On the other hand, as can be seen in Table 4.8, the iFEM with reduced sensors becomes less accurate than the full-sensor iFEM when evaluating the total rotations. iFEM with full sensors can obtain a maximum total rotation of 0.383 *rad* which is just about 2% less than the reference value. Moreover, iFEM with reduced sensors obtain a value of 0.43 *rad* as the extreme total rotations and it is approximately 10% higher than the FEM result.

**Table 4.8** The results of FEM and iFEM analysis

Case 1	UT (m)	T (rad)
FEM (a)	6.197E-01	3.907E-02
iFEM (b)	5.934E-01	3.830E-02
iFEM-122 (c)	6.328E-01	4.300E-02
Differences between a & b	4.251%	1.981%
Differences between a & c	2.106%	10.048%

The variation of the total displacements and total rotations are also given to enhance the explanation of the results of iFEM (Fig. 4.20 and Fig. 4.21). For the total displacements, it can be seen that for all three plots the displacements are smoothly distributed along the span of the

blade. The differences between these three plots are indistinguishable which proves that the iFEM results no matter with full sensors or reduced sensors are in good agreement with the reference FEM results. In terms of total rotations, the maximum value concentrates on the transition region of the blade and this feature can be accurately captured by iFEM with full sensors. However, with the reduction of the sensors, there will not be any sensors placed in the region which contain the information of the maximum total rotations. The value can only be approached by the iFEM elements with sensors, near this region. So it is not surprising that the maximum total rotation occurs in the iFEM elements with sensors, which are located around the transition zone.

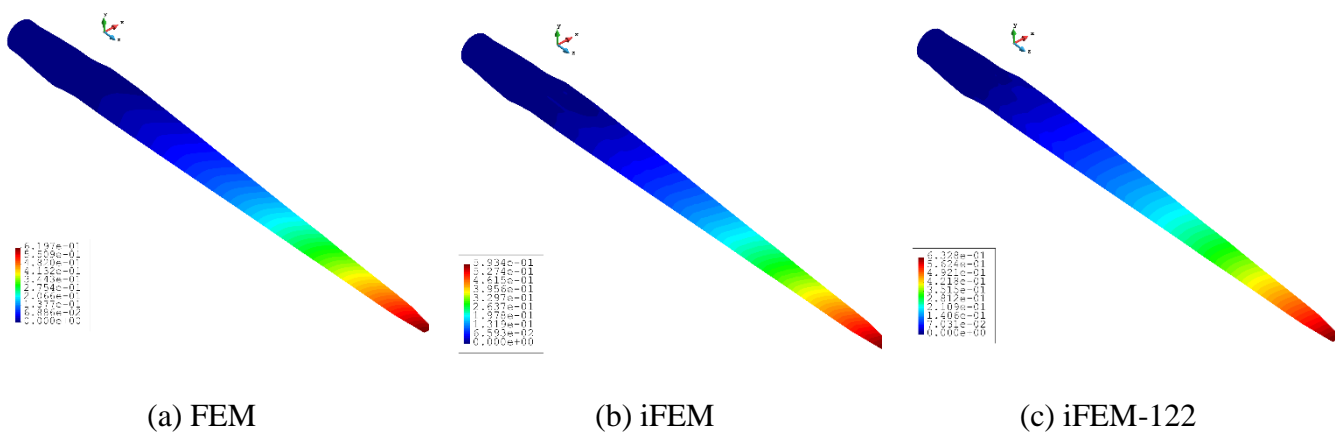


**Figure 4.20** The plots of the total displacements ( $m$ )

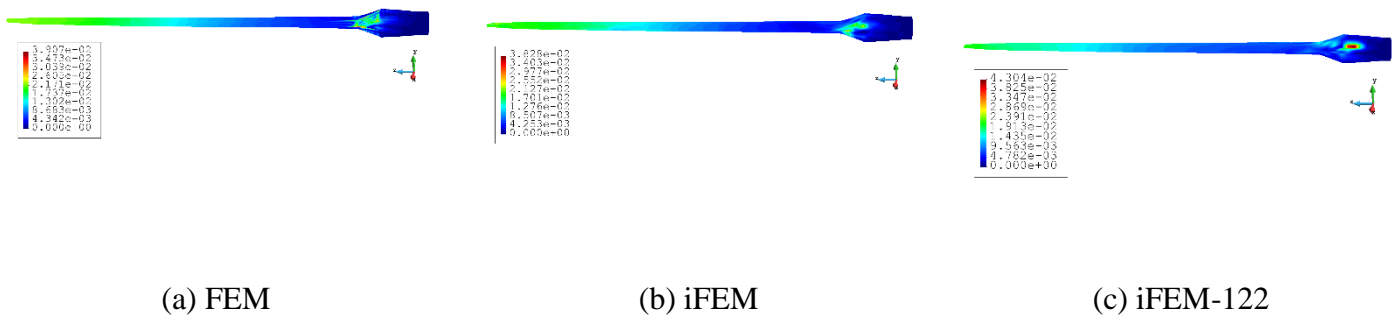


**Figure 4.21** The plots of the total rotations ( $rad$ )

## 4.5 Numerical results of the damage identification

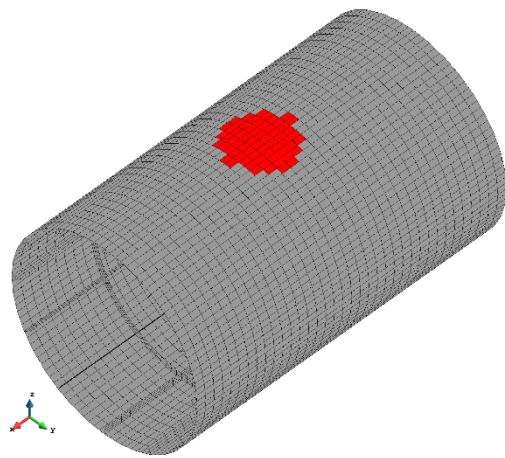
### 4.5.1 Model generation and data evaluation

To demonstrate the capability of iFEM for damage prediction, a longitudinally and transversely stiffened thin-walled cylindrical structure, which was previously considered by Cerik (Cerik, 2015), was analyzed after introducing local dent damage. The length of the cylindrical structure is 10 m and it has a circular cross-section with a radius of 3 m. There are 12 longitudinal stiffeners with a web height of 200 mm at the inner surface. Besides, there are also three ring stiffeners, which have the same web height as the longitudinal stiffeners in the circumferential direction, to provide additional enhancement to the structure. The cylinder and the stiffeners are made from high tensile strength steel with Young's modulus of 210 GPa and Poisson's ratio of 0.3. The structure can be considered as a thin-walled cylinder and the thickness of the cylinder including the stiffeners is 25 mm. There is an initial geometrical defect representing the local dent with a width of 1 m and a depth of 0.1 m (Cerik, 2015). The material degradation approach (Taheri-Behrooz and Bakhshan, 2018) is utilized to represent the pre-existing damage in a rather simple way. Therefore, Young's modulus of the material is assumed to be 210 kPa in the damage zone. The cylinder is fully fixed at the far edge and all DOFs at the front edge are constrained except the displacement along the axial direction,  $x$ . A tensional displacement of 0.005 m is applied in the axial direction to the front edge boundary as the loading condition.

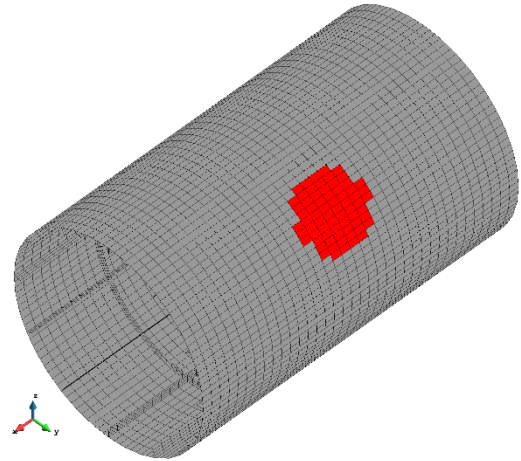
**Table 4.9** Case Studies for iFEM analysis

Cases	Damage Location
Case1	No damage on the cylinder
Case2	Central damage at the joint of the stiffeners
Case3	Central damage crossing two longitudinal stiffeners
Case4	Damage at a quarter length of the cylinder
Case5	Multiple damages at edges and center

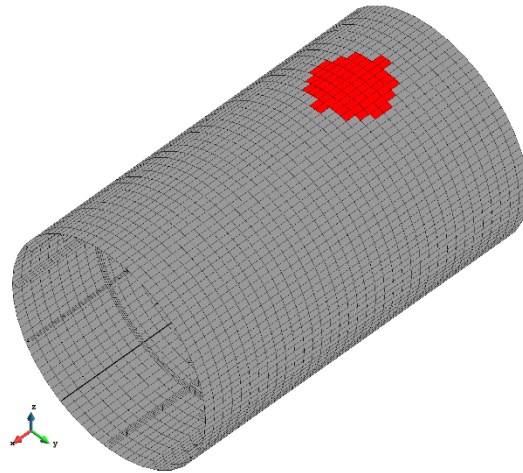
As listed in Table 4.9, five different numerical cases are examined in this section including Case1 representing no damage case whereas Case2 to Case5 representing different damage cases. The damage locations are depicted in Fig. 4.22.



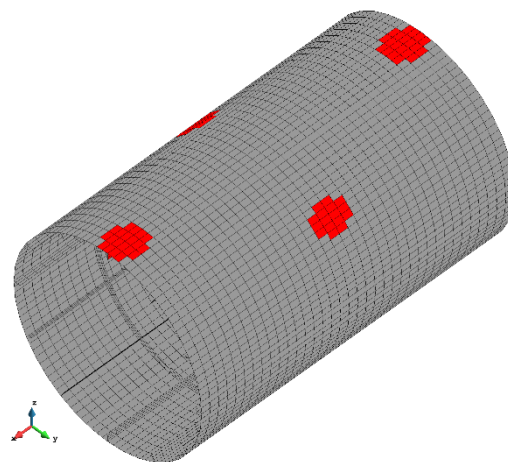
(a)



(b)



(c)



(d)

**Figure 4.22** Damage locations for (a) Case2, (b) Case3, (c) Case4, and (d) Case5

The main aim of Case1 is to validate the iFEM methodology for stiffened cylindrical structures, investigate the possibility of reducing sensors under the premise of obtaining reasonably accurate results and obtain a reference undamaged solution to calculate the damage parameter,  $D$ . For the remaining four cases (Case2-5), the damage prediction study is performed for the cylindrical structure using both full sensors and reduced number of sensors. Through this procedure, we will investigate the practicality of the iFEM methodology for accurate and reliable detection of dent damage locations even with sparse strain data. Note that in this study, the strain data is generated numerically by performing a high-fidelity FEM analysis by using ANSYS, a commercially available finite element software. A very fine mesh of the cylinder model composed of 6156 elements (Fig. 4.23(a)) is utilized in the FEM analysis whereas the iFEM analysis is performed by using an in-house MATLAB code with a relatively coarse mesh having only 684 iQS4 elements (Fig. 4.23(b)).

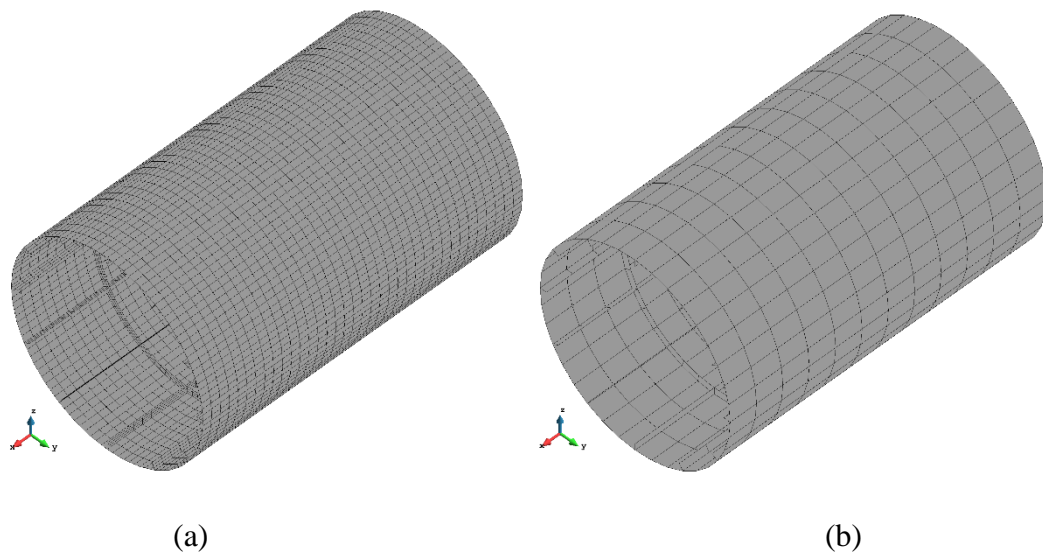


**Figure 4.23** (a) Dense mesh for FEM model and (b) Coarse mesh for iFEM model

#### 4.5.2 Sensor selection and results of the undamaged case

In this section full-sensor placement means that every iQS4 element has corresponding experimental strain measurements which are provided by FEM analysis. If the full-sensor placement is used, the number of strain sensors becomes  $684 \times 2$ . It is beneficial to reduce the number of sensors for practical applications. Therefore, the iFEM model of stiffened cylindrical structures using less number of sensors, a reduced-sensor model, which contains  $192 \times 2$  sensors, is also considered as shown in Fig. 4.24. The selected iQS4 elements are highlighted in blue.

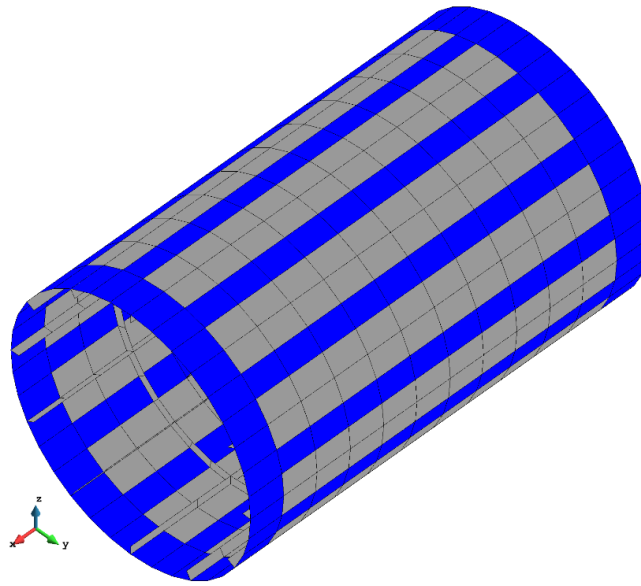


**Figure 4.24** Sensor locations for the reduced sensor model

Twelve longitudinal lines of sensors are used to monitor the whole structure and another two transverse lines of sensors are placed at the boundary of the structure. Note that the number of sensors can be further reduced, but after balancing the requirement of accuracy and the desire to reduce the number of sensors, the current strategy of sensor installations is preferred. More importantly, thanks to the development of FBG sensor technology, the proposed number of strain data can be collected without much difficulty. As shown in Fig. 4.24, the sensor locations of the reduced-sensor model follow continuous paths over the cylindrical surface. Thus, the strain data can be collected from these locations using several fiber optic cables only. For the current structure and analysis, a maximum of 16 FBG sensors can fulfil the requirement of strain data collection.

As mentioned earlier, in this study, strain data for iFEM analysis is provided from a FEM model. Moreover, FEM results are also used to verify the iFEM model for the case without damage. Variations of the total displacements,  $U_T$ , along the stiffened cylindrical structure are obtained both by using the iFEM full sensor and reduced-sensor cases. As shown in Fig. 4.25, both full sensor and reduced sensor cases successfully capture the displacement variation obtained by using FEM. Von Mises strain variation obtained using FEM is also evaluated and presented in Fig. 4.26. These von Mises strain values will be considered as the von Mises strain values for the undamaged case to be used to calculate the damage parameter given in Eq. (4.9).

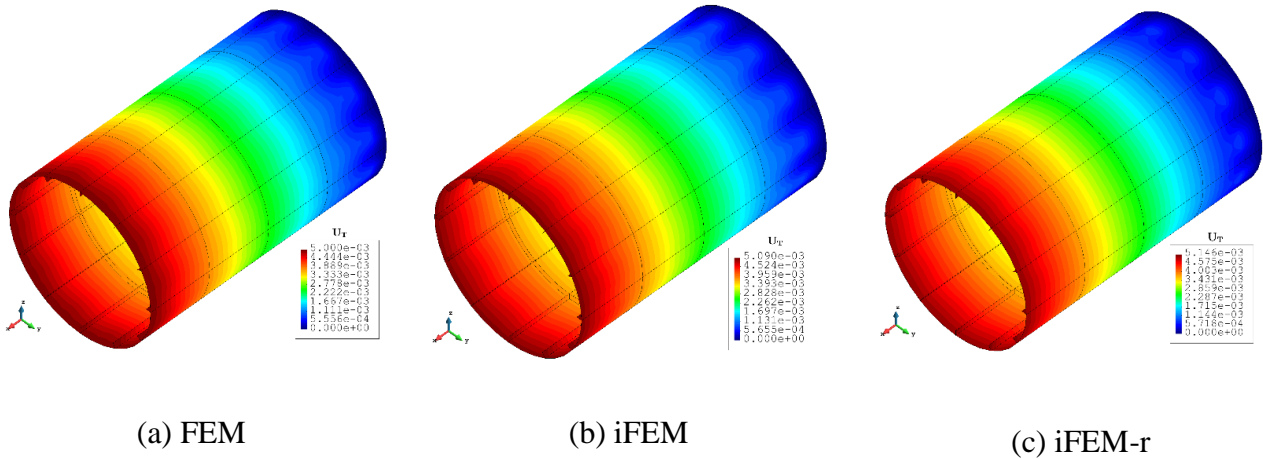


**Figure 4.25** Contour plot of  $U_T$  displacement (unit: m) for Case1

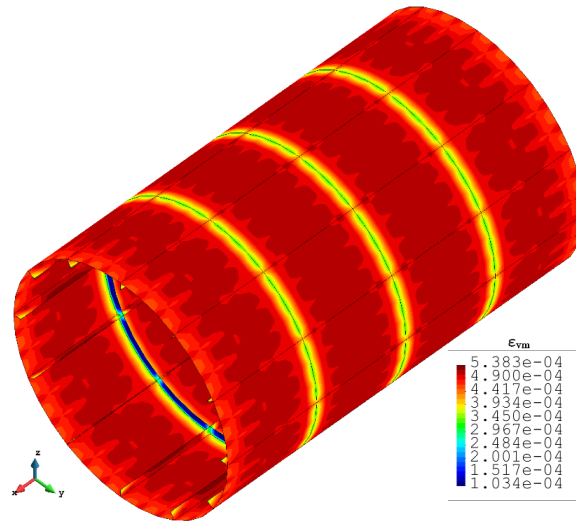


**Figure 4.26** Contour plot of  $\epsilon_{vm}$  strain for FEM of Case1

### 4.5.3 Results for the damage detection

In the first damage case, a central damage located at the joint of the stiffeners is considered as shown in Fig. 4.22(a). The damage parameter variation for full sensor and reduced sensor cases are given in Figure 4.27. As can be seen in this figure, the damage parameter takes very large values at the damage location region. Therefore, it is expected that the damage is likely to exist in this region. This conclusion is also supported by the von Mises strain distributions demonstrated in Fig. 4.28. Although strain localization is less visible for reduced sensor case,

both full sensor and reduced sensor cases identify the same damage location as the damage parameter.

In the second damage case, a central damage crossing two longitudinal stiffeners is considered as depicted in Fig. 4.22(b). The damage parameter values obtained from iFEM analysis for both full sensor and reduced sensor cases are presented in Fig. 4.29. Similar to the previous case, iFEM identified the damage location accurately although the reduced sensor case predicted a slightly larger damage zone. Moreover, von Mises strain distributions are given in Fig. 4.30 obtained from iFEM analysis also clearly demonstrate strain localisations at the damage region.

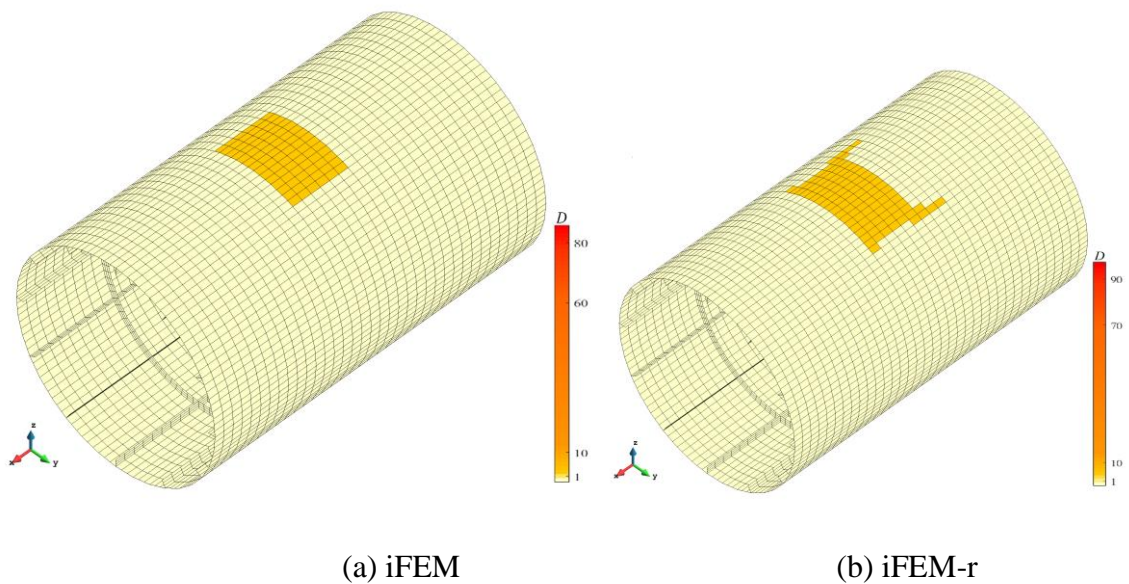
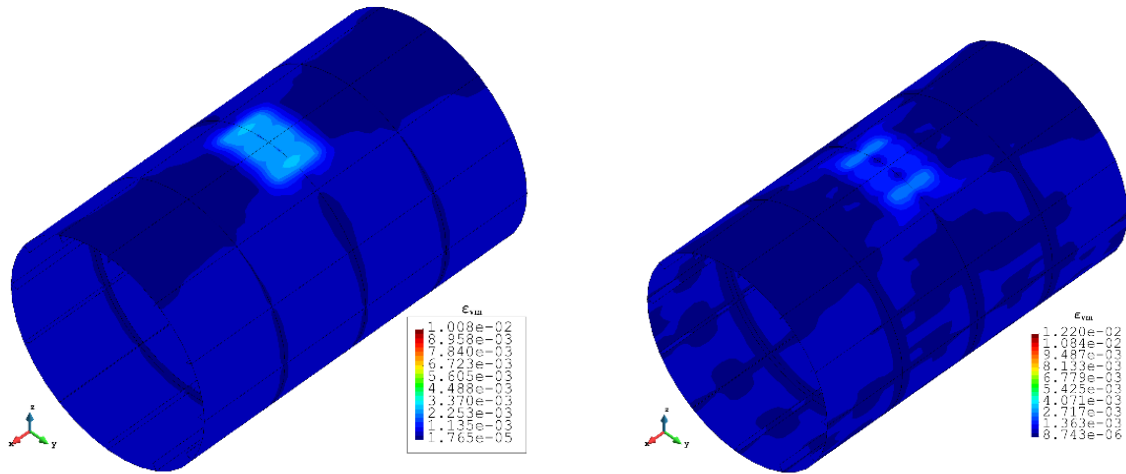


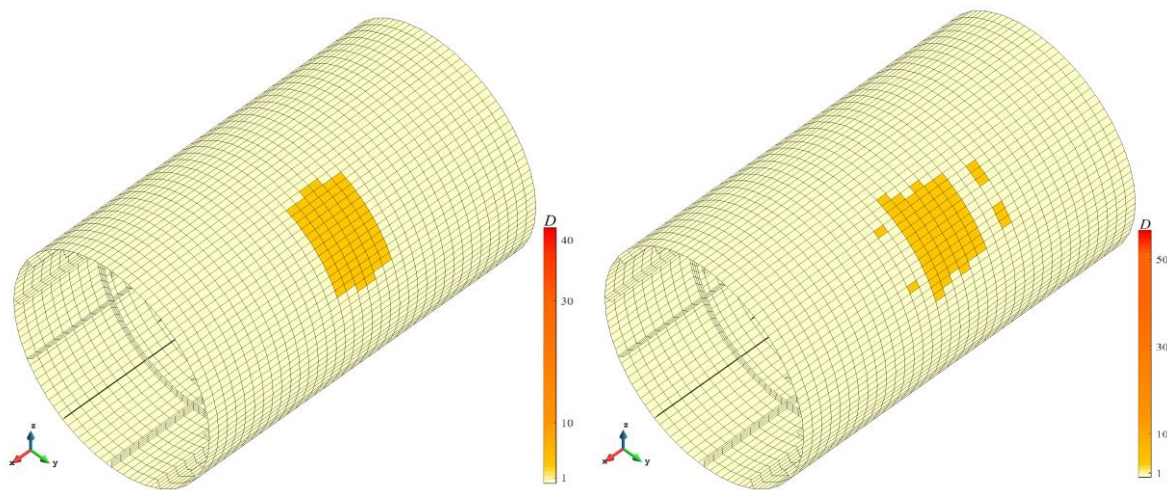
**Figure 4.27** Damage parameter variation for Case2



(a) iFEM

(b) iFEM-r

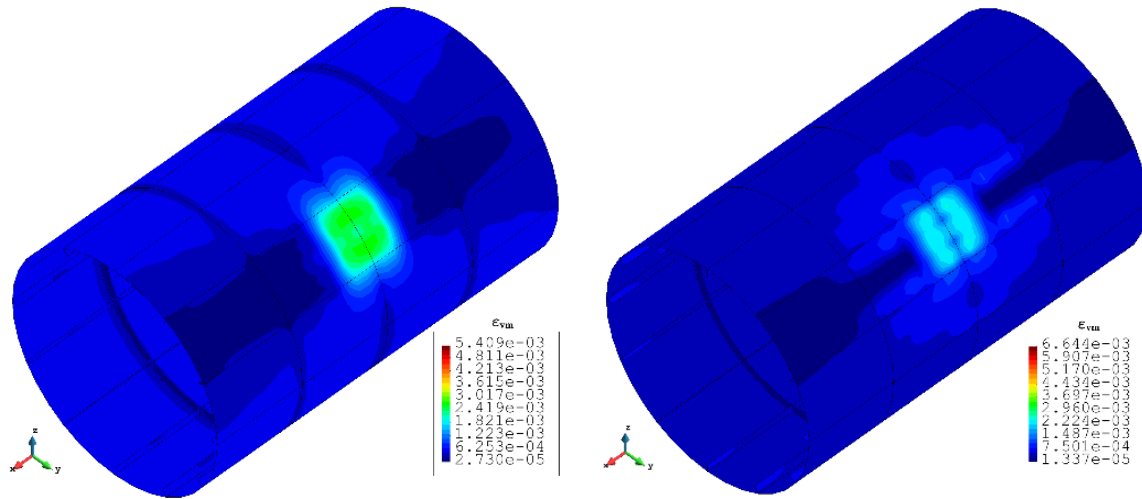
**Figure 4.28** Von Mises strain variation for Case2



(a) iFEM

(b) iFEM-r

**Figure 4.29** Damage parameter variation for Case3



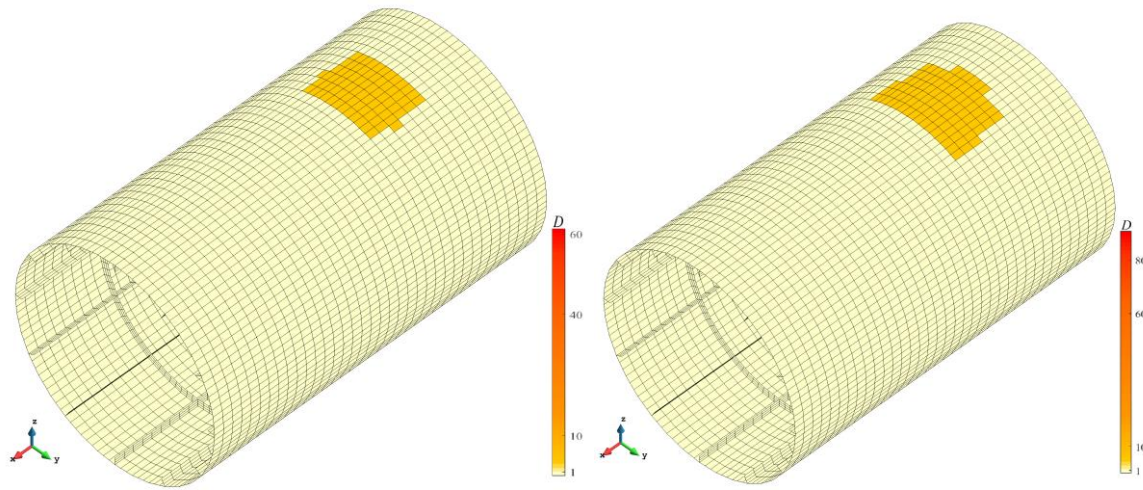
(a) iFEM

(b) iFEM-r

**Figure 4.30** Von Mises strain variation for Case3

As shown in Fig. 4.22(c), the damage is located closer to the fixed boundary for the third damage case. As can be seen in Fig. 4.31, based on the damage parameter variations obtained from iFEM analysis, the correct damage location can be easily identified. The von Mises strain distributions given in Fig. 4.32 also support this conclusion. As the final damage case, multiple and smaller damages located at different parts of the cylindrical structure are considered as depicted in Fig. 4.22(d). Damage parameter variation for both full sensor and reduced sensor cases are given in Fig. 4.33. iFEM performs also very well for this complex scenario. All damage locations are successfully captured. Von Mises strain distributions also highlight the same damage locations clearly as shown in Fig. 4.34.

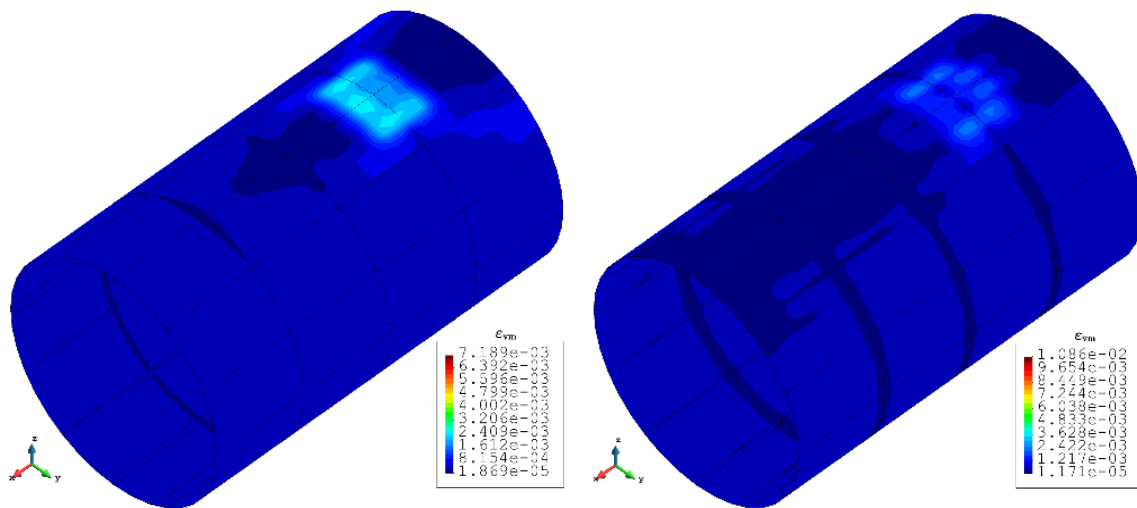
As a summary, for all four different damage cases with different sizes, locations, and the number of damages, iFEM was able to capture the correct damage locations by utilizing the newly introduced damage parameter and von Mises strain distribution.



(a) iFEM

(b) iFEM-r

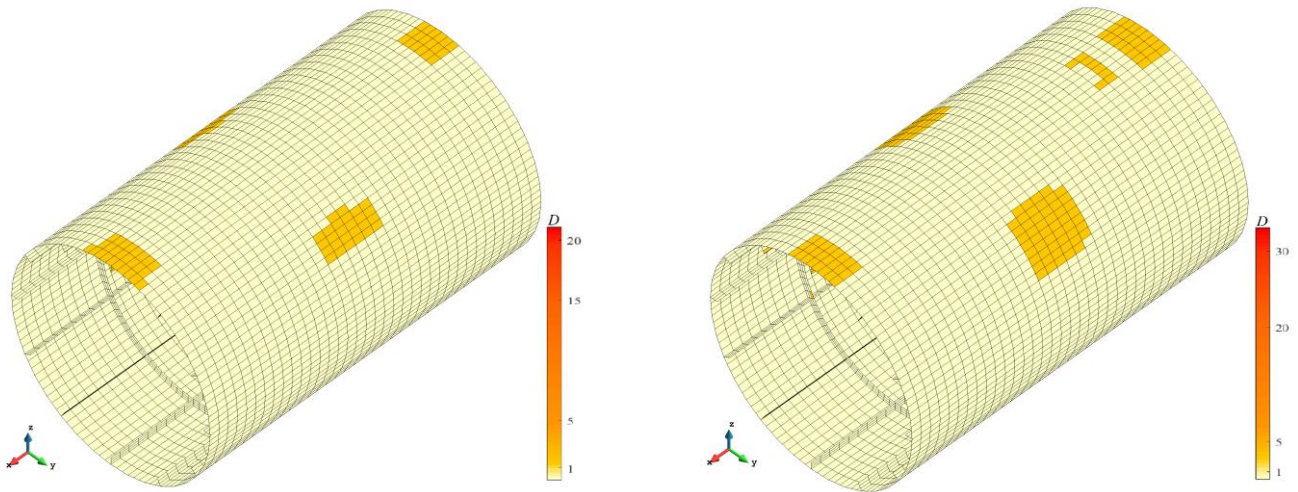
**Figure 4.31** Damage parameter variation for Case4



(a) iFEM

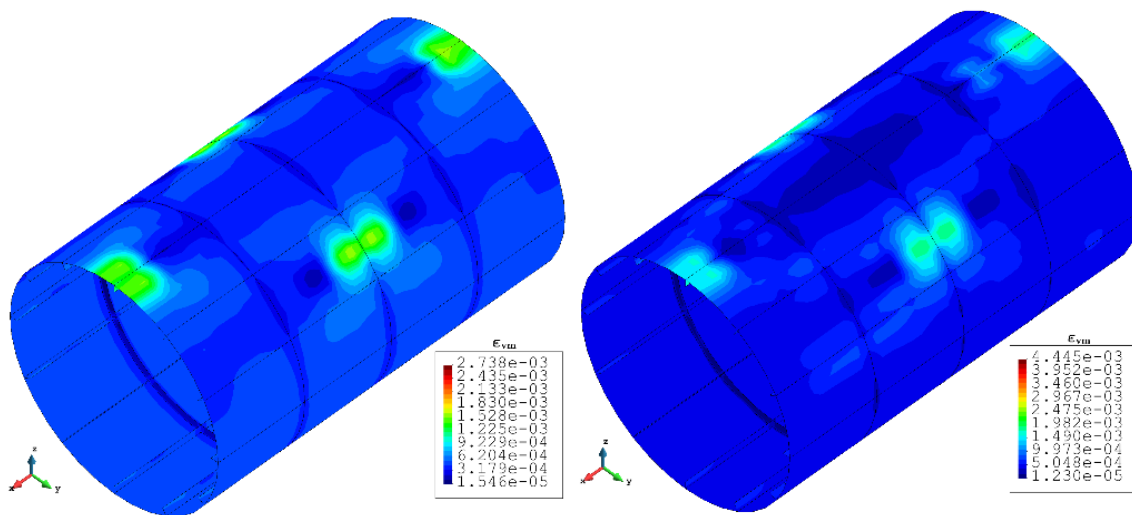
(b) iFEM-r

**Figure 4.32** Von Mises strain variation for Case4



(a) iFEM (b) iFEM-r

**Figure 4.33** Damage parameter variation for Case5



(a) iFEM (b) iFEM-r

**Figure 4.34** Von Mises strain variation for Case5

## 4.6 Summary

In this chapter, the iQS4 element is utilized for the iFEM analysis of the tower and blade of OWTs. For the tower, it is modeled with dense FEM and coarse iFEM meshes. The FEM analysis provides the “synthetic” strain data for the iQS4 element. Both static and dynamic loading conditions are considered. For the static condition, only the gravity of the upper structures and tower itself is taken into account and the aerodynamic and hydrodynamic forces

are applied during the dynamic analysis which makes the analysis more practical. iFEM analysis is performed with both full sensors and reduced sensors. The practical number of sensors and their locations are explored. After balancing the accuracy of the monitoring and the cost-effective purpose, the final sensor locations are decided as four longitudinal and two ring cables, which can guide the real application of iFEM for the tower. In these cables, the current discretized locations of the sensors would be sufficient for monitoring the tower in real loading conditions. It can also be shown that the sections under aerodynamic loadings may need fewer sensors than the underwater sections. Total displacements and von Mises stresses are selected as the judging criteria for the accuracy of the iFEM analysis. For the dynamic analysis, different heights and different locations at the same height are selected for comparison purposes. After comparing the results and plots of the iFEM analysis with the reference FEM analysis, the iFEM-iQS4 element is proven to generate a SHM system with high accuracy for the tower of the OWTs even with reduced sensors during the dynamic condition. Future research can focus on other components of the OWTs to achieve a complete SHM system for the entire OWT based on iFEM. Then for the blade, shape sensing of the blade of the NREL 5MW offshore wind turbine is demonstrated by using the iFEM method. The real loading conditions are considered during the analysis. Similar to the tower analysis, the analysis of FEM is used as a reference solution for the iFEM analysis, and it also provides the strain data for the iQS4 elements. After comparing the results of iFEM with the FEM results, it can be concluded that iFEM can obtain an accurate 3-D displacement field for the blade even with suggested practical numbers of sensors, which is only  $122 \times 2$  sensors and can be replaced by at most  $6 \times 2$  cables of FBG sensors. It can also be concluded that the iQS4 element has the ability to monitor offshore wind turbine blades. For future studies, the analysis can be extended to the dynamic case and the effects of different blade locations and wind velocities can be explored. In addition, the stress monitoring of the composite blade using the iQS4 element can also be one direction.

Finally, in this study, iFEM was utilized to monitor and predict structural damage in terms of geometrical defects in thin-walled stiffened cylindrical structures. The stiffened cylindrical structure is modeled with dense mesh for FEM analysis and coarse mesh for iFEM analysis. A robust iFEM shell element-iQS4 is utilized to generate the model for inverse analysis and at the same time, FEM results are used both to provide strain data for iFEM analysis and for validation purposes. Five different numerical cases were considered. First of all, based on the displacement results obtained from iFEM analysis of an undamaged structure, it was shown

that iFEM can easily and accurately perform SHM process for offshore cylindrical structures. In addition, four different cases with damages were investigated to explore the capability of iFEM for predicting the damage locations and shapes. The four cases include damage at the central and quarter ring lines of the structure, and small and multiple random damages. Regardless of changing the locations of the damages or varying the sizes of the damage, iFEM can obtain accurate results. Besides, the damage locations can be correctly detected using the damage parameter and von Mises strain plots even with the reduced sensor configuration. Finally, it can be concluded that iFEM is suitable for real-time structural health monitoring and damage prediction in offshore cylindrical structures with high accuracy. For the iFEM damage detection research, the current method can be applied to other and larger offshore installations.

## **5 Inverse plane crack tip elements**

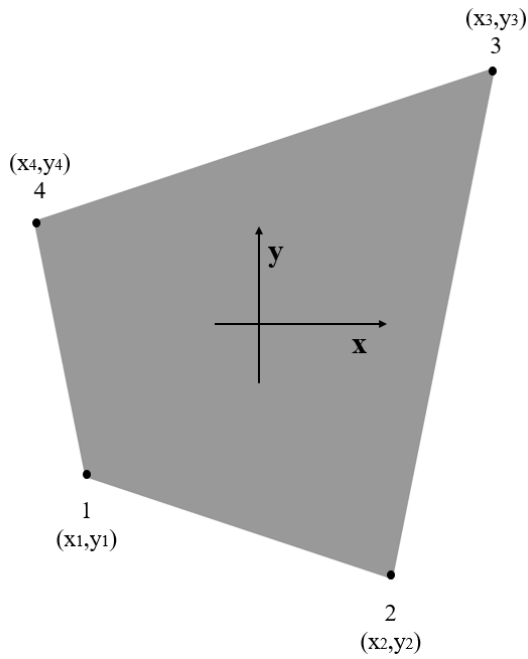
### **5.1 Introduction**

Since the crack tip element can fulfil the requirement of singularity at the crack tip and has been widely used for finite element modeling the crack tip region including commercial software like ANSYS, this work will give attention to introducing an inverse plane crack tip element for the field of iFEM. By placing the iPCT element around the crack tip region and collecting the strain data for these elements, the whole displacement field can be calculated. Combing with the displacement extrapolation method, the SIF can be estimated. (Zhu and Oterkus, 2020) For this chapter, before the iPCT element, inverse 4-node and 8-node quadrilateral plane elements will be defined following the basic rules of the iFEM framework in Section 5.2. And there will be some comparisons between these two elements by some examples. It should be mentioned that the inverse 8-node plane element will usually be employed with the iPCT element to form the whole iFEM model. Then Section 5.3 will move to the iPCT element and after the fundamental formulations, several examples of applications will be given to prove the accuracy of this type of element even in a limited number of sensors condition for Mode-I, Mode-II, and both Mode-I and Mode-II SIT estimations. Finally, the results of the comparison and also the analytical analysis of the iPCT element will be summarized. To the best of the author's knowledge, it is the first time to generate the inverse plane element and inverse crack tip element.

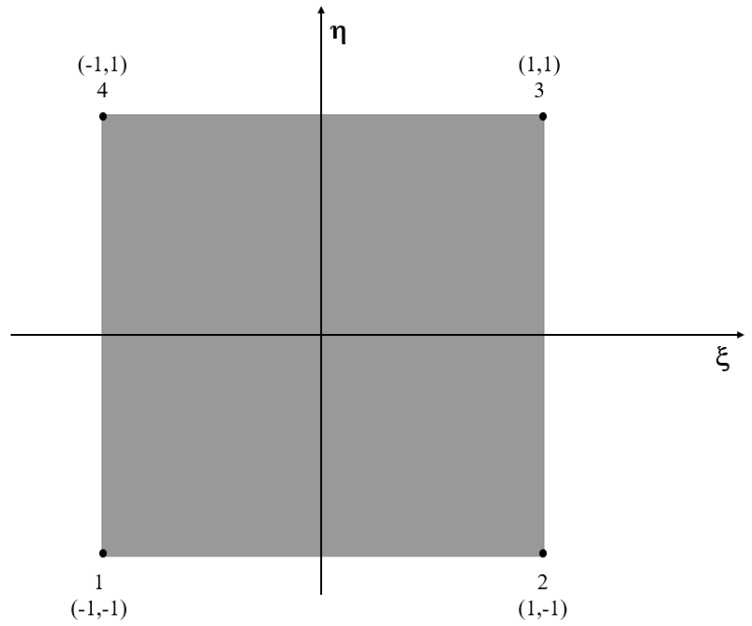
### **5.2 Inverse 4-node and 8-node quadrilateral element**

#### **5.2.1 Formulations for inverse 4-node and 8-node quadrilateral element**

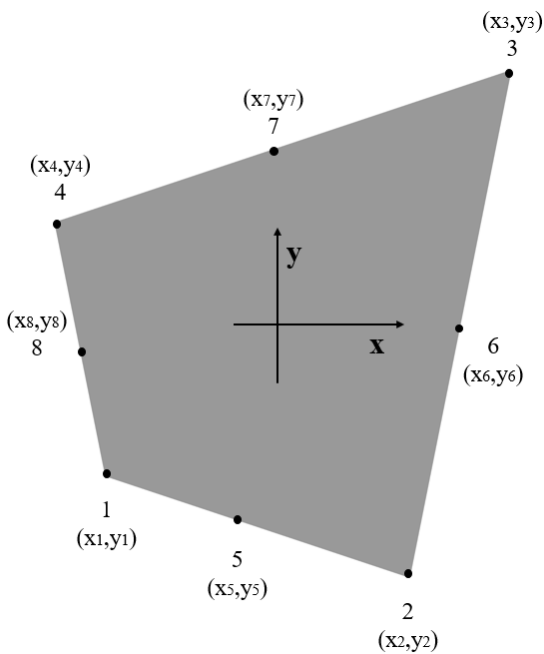
Following the fundamental formulation- weight-least-squares formula of iFEM, the iQP4 (inverse 4-node quadrilateral plane) element, and the iQP8 (inverse 8-node quadrilateral plane) element are developed. Each node of these elements has two degrees of freedom,  $u$  and  $v$ , corresponding to in-plane displacements in  $x$ - and  $y$ -directions, respectively. Since the thickness of the element is not necessary, the strain inputs for the elements can be collected from a single side of the elements which reduces the requirement for the number of sensors.



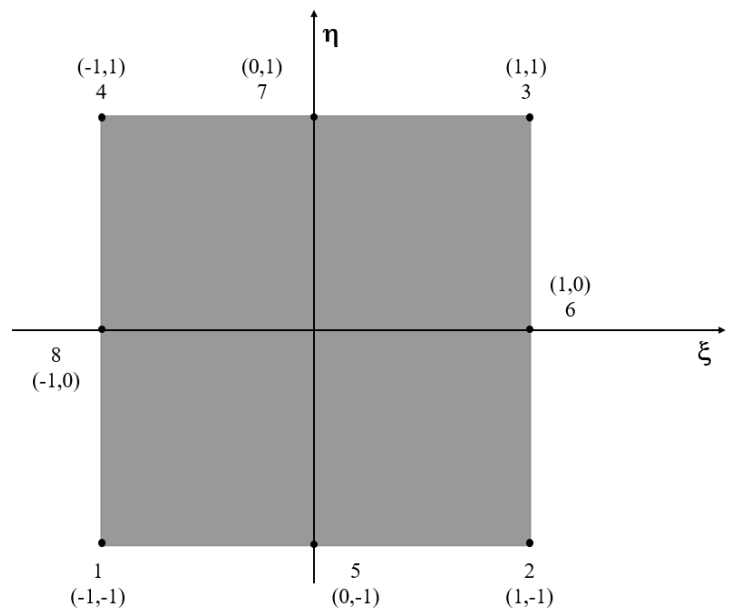
a). Random 4-node quadrilateral element



b). Standard 4-node quadrilateral element



c). Random 8-node quadrilateral element



d). Standard 8-node quadrilateral element

**Figure 5.1** Random and standard 4-node and 8-node quadrilateral element

For both iQP4 and iQP8 elements (see Fig. 5.1), the transformation from the local coordinate system  $(x, y)$  to the natural coordinate system  $(\xi, \eta)$  is required. Moreover, for every single element, the local coordinate system, which is located at the geometric centre of the element, should also be transformed into the global coordinate system  $(X, Y)$  for the global matrix assembly process. The above procedure will be necessary for the matrix assembling process. After transforming to the standard quadrilateral element, the bilinear isoparametric shape

functions will be used to link the local coordinator  $(x, y)$  and the dimensionless isoparametric coordinate  $(\xi, \eta)$ . The equations are given as:

The location of any point on iQP4 and iQP8 elements can be expressed in terms of the location of nodes in the local coordinate system,  $(x_i, y_i)$ , and bilinear isoparametric shape functions,  $N_i(\xi, \eta)$  as:

$$\begin{aligned} x(x, y) &= \sum_{i=1}^4 N_i x_i \\ y(x, y) &= \sum_{i=1}^4 N_i y_i \end{aligned} \quad (5.1a)$$

for the iQP4 element and

$$\begin{aligned} x(x, y) &= \sum_{i=1}^8 N_i x_i \\ y(x, y) &= \sum_{i=1}^8 N_i y_i \end{aligned} \quad (5.1b)$$

for the iQP8 element. The bilinear isoparametric shape functions,  $N_i(\xi, \eta)$ , are defined as:

$$\begin{aligned} N_1 &= \frac{(1-\xi)(1-\eta)}{4} \\ N_2 &= \frac{(1+\xi)(1-\eta)}{4} \\ N_3 &= \frac{(1+\xi)(1+\eta)}{4} \\ N_4 &= \frac{(1-\xi)(1+\eta)}{4} \end{aligned} \quad (5.2a)$$

for the iQP4 element and

$$\begin{aligned} N_1 &= \frac{(1-\xi)(1-\eta)(-1-\xi-\eta)}{4} \\ N_2 &= \frac{(1+\xi)(1-\eta)(-1+\xi-\eta)}{4} \\ N_3 &= \frac{(1+\xi)(1+\eta)(-1+\xi+\eta)}{4} \\ N_4 &= \frac{(1-\xi)(1+\eta)(-1-\xi-\eta)}{4} \end{aligned} \quad (5.2b)$$

$$\begin{aligned} N_5 &= \frac{(1-\xi)(1+\xi)(1-\eta)}{2} \\ N_6 &= \frac{(1+\xi)(1+\eta)(1-\eta)}{2} \\ N_7 &= \frac{(1-\xi)(1+\xi)(1+\eta)}{2} \end{aligned} \quad (5.2c)$$

$$N_8 = \frac{(1-\xi)(1+\eta)(1-\eta)}{2}$$

for the iQP8 element. It should be highlighted that the order of the nodes is not constrained. But the shape functions should be updated correspondingly after changing the order of the nodes. Similarly, by using the shape functions, the local nodal displacements ( $u$  and  $v$ ) at any point  $(x,y)$  can be written in terms of nodal displacements as:

$$\begin{aligned} u(x, y) &= \sum_{i=1}^4 N_i u_i \\ v(x, y) &= \sum_{i=1}^4 N_i v_i \end{aligned} \quad (5.3a)$$

for the iQP4 element and

$$\begin{aligned} u(x, y) &= \sum_{i=1}^8 N_i u_i \\ v(x, y) &= \sum_{i=1}^8 N_i v_i \end{aligned} \quad (5.3b)$$

for the iQP8 element. Strain components can be calculated by using the linear relationships between strain and displacement components. For the plane element, only the membrane deformations will appear. Therefore, only three components of the membrane strains can be obtained as ( $U$  and  $V$  are the global displacements):

$$\begin{aligned} \varepsilon_{xx} &= \frac{\partial U}{\partial x} \\ \varepsilon_{yy} &= \frac{\partial V}{\partial y} \\ \gamma_{xy} &= \frac{\partial U}{\partial y} + \frac{\partial V}{\partial x} \end{aligned} \quad (5.4)$$

By utilising the displacement expressions given in Eqs. (5.3a) and (5.3b) and strain definitions given in Eq. (5.4), the analytical elemental strains can be expressed by the shape functions and nodal displacements as:

$$\mathbf{e}(\mathbf{u}^e) = \begin{Bmatrix} \varepsilon_{xx} \\ \varepsilon_{yy} \\ \gamma_{xy} \end{Bmatrix} = \mathbf{B}^m \mathbf{u}^e \quad (5.5)$$

where  $\mathbf{u}^e$  are the nodal displacements,  $\mathbf{u}^e = [u_1 \ v_1 \ u_2 \ v_2 \ \cdots \ u_i \ v_i]^T$ , for the iQP4 element,  $i = 4$ , for the iQP8 element,  $i = 8$ .  $\mathbf{B}^m$  is the matrix formed by the shape functions of

each node. For each node,  $\mathbf{B}^m$  has a similar expression as:  $\mathbf{B}^m = [\mathbf{B}_1^m \quad \mathbf{B}_2^m \quad \cdots \quad \mathbf{B}_i^m]^T$ . Every single  $\mathbf{B}_i^m$  matrix can be defined as:

$$\mathbf{B}_i^m = \begin{bmatrix} \frac{\partial N_i}{\partial x} & 0 \\ 0 & \frac{\partial N_i}{\partial y} \\ \frac{\partial N_i}{\partial y} & \frac{\partial N_i}{\partial x} \end{bmatrix} \quad (5.6)$$

iFEM solution can be obtained by minimizing a weighted least-squares functional with respect to nodal degrees of freedom for the entire solution domain. For each inverse element, the weighted least-squares functional is slightly different from Eq. (4.4) by just considering the membrane strains and the simplified equation can be written as:

$$\phi^e(\mathbf{u}^e) = w_e \|\mathbf{e}(\mathbf{u}^e) - \mathbf{e}^{inputs}\|^2 \quad (5.7)$$

where  $w_e$  is the weighting coefficient and  $\mathbf{e}^{inputs}$  vector contains the measured strain input data. If the experimental strains for the element are available,  $w_e = 1$ . However, if the data is missing, a small value like  $10^{-3}$  or  $10^{-4}$  would be preferred. By minimizing the differences between the analytical strains and experimental strains for each element, i.e., the derivations of  $\phi^e$  against  $u^e$  are approaching 0, the following equation can be gained:

$$\mathbf{k}^e \mathbf{u}^e - \mathbf{f}^e = 0 \quad (5.8)$$

where  $\mathbf{k}^e$  is a matrix formed by integrating  $w_e (\mathbf{B}^m)^T \mathbf{B}^m$  for the element and  $\mathbf{f}^e$  is a matrix generated by the strain inputs together with  $(\mathbf{B}^m)^T$ . Gauss points (4 or 9) will be utilized for the integration of the elemental components. After assembling these elemental components to the global matrix of the structure and also taking the boundary conditions into account, the global displacements of each node can be calculated.

### 5.2.2 Comparison between two types of inverse plane elements

There are 4 cases, which are listed in Table 5.1, prepared for this section. Different loadings and boundary conditions are considered. Furthermore, different mesh together with reduced sensor conditions for dense mesh is also taken into consideration.

**Table 5.1** Numerical cases for comparison between two inverse plane elements

Case 1	Square plate under tension with different mesh
Case 2	Rectangular plate under tension with different mesh
Case 3	Rectangular plate with nodal force and dense mesh
Case 4	Square plate with a central hole and dense mesh

Case 1 and Case 2, on the one hand, can explore the influence of the mesh size. On the other hand, they can also make contributions to test whether the results will be strongly affected by the element type. Case 3 and Case 4 are introduced for further verifying the accuracy of these two inverse plane elements and making comparisons for accuracy and sensor selection between these two elements.

The results of displacements in two directions are selected as the criteria for comparison. Usually, displacements would be straightforward for judging the health condition of the structure. For complex structure and loading conditions, von Mises stress is also a useful tool especially for judging the yielding and failure of the structure. For the general plane stress condition, the von Mises stress can be calculated by:

$$\sigma_{vm} = \sqrt{\sigma_{xx}^2 - \sigma_{xx}\sigma_{yy} + \sigma_{yy}^2 + 3\sigma_{xy}^2} \quad (5.9)$$

where  $\sigma_{xx}$ ,  $\sigma_{yy}$ , and  $\sigma_{xy}$  are the components of the stress matrix and they can be calculated by the displacements and material properties. von Mises stress (plots and extreme values) will be used for comparison to further test the accuracy of the inverse element in Case 4.

### Case 1

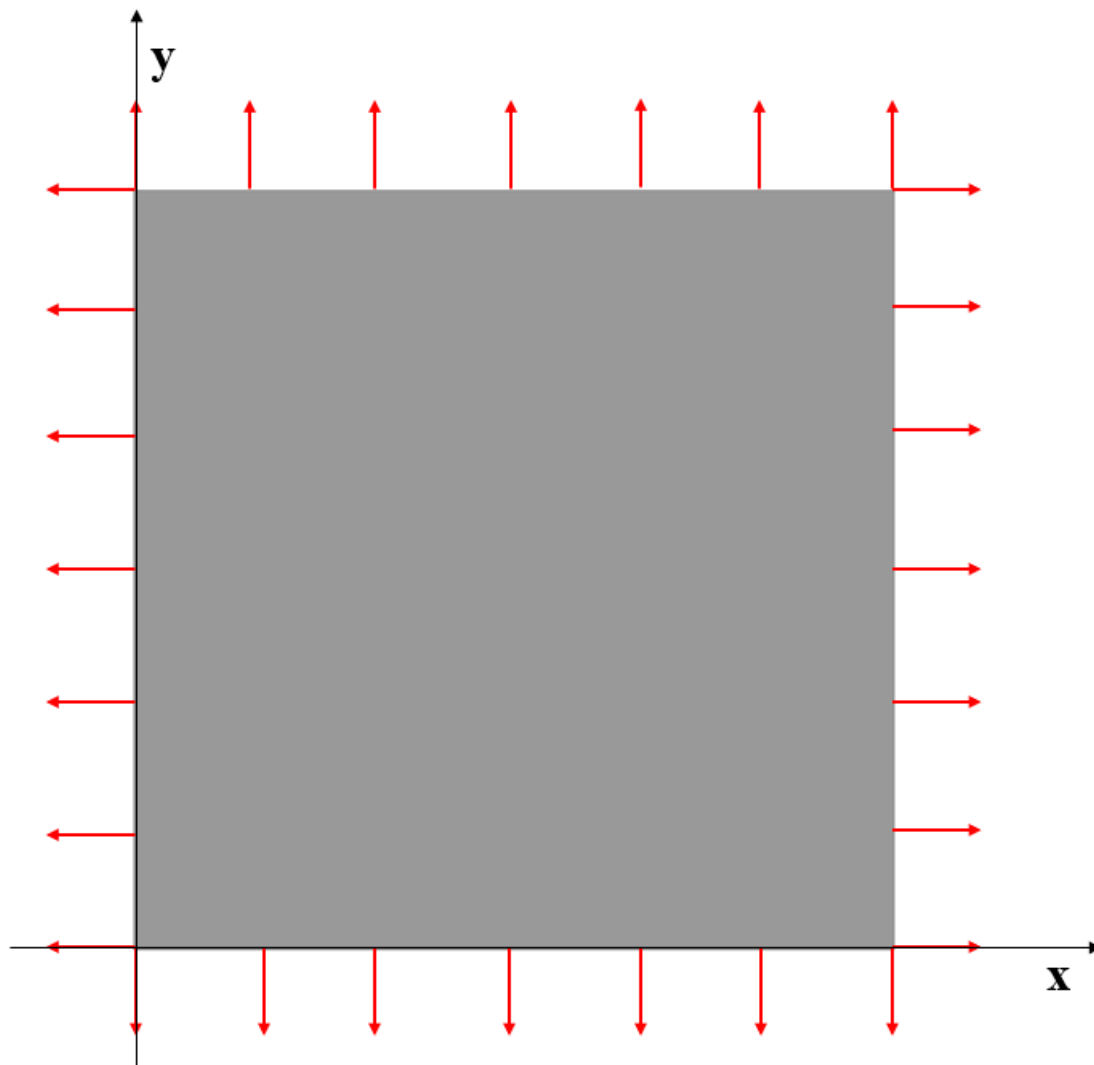


**Figure 5.2** The loading and boundary condition of Case 1

The first case is a square plate ( $2 \times 2$  m) under tension loading, shown in Fig. 5.2. 1000 MN force is evenly distributed to the nodes of each edge of the plate. The plate has meshed with three different numbers of elements which are 16, 100, and 1600, respectively. (Fig. 5.3) The results of the three mesh cases are listed from Table 5.2 to Table 5.4.



**Table 5.4** The results for Case 1 with 1600 elements

Case 1 with 1600 elements		iQP4	iQP8
<i>U</i>	a. FEM	1.847E-03	1.786E-03
	b. iFEM	1.823E-03	1.775E-03
	c. iFEM-r	1.817E-03	1.772E-03
Differences between a and d		1.299%	0.616%
Differences between a and c		1.624%	0.784%
<i>V</i>	d. FEM	1.847E-03	1.786E-03
	e. iFEM	1.823E-03	1.775E-03
	f. iFEM-r	1.817E-03	1.772E-03
Differences between d and e		1.299%	0.616%
Differences between d and f		1.624%	0.784%

For the fine mesh with 16 elements, as can be seen from Table 5.2, no matter for the iQP4 or the iQP8 element, the results are less estimated. But the performance of the iQP8, which just gives a 4.279% error, is slightly better than the iQP4, which leads to a 7.327% error. With the increase of the number of elements, the percentages of the difference of the deformation are reduced dramatically. When the number of elements is 100, iQP4 is just 0.190% overestimating the extreme displacements. Meanwhile, iQP8 provides a percentage of 2.193%. Although the value becomes a little higher than iQP4, it is still much better than the 16-element condition. When the number of elements increases to 1600, both types of elements show matching well results against the FEM reference. More importantly, the reduced sensor condition is applied to the dense mesh case. As Fig. 5.4 shows, only the sensors along the edges of the plate are selected which finally gives the number of sensors as 156. With the strain inputs provided by these 156 sensors, even if the stain data for the remaining elements is missing, iQP4 and iQP8 can still provide accurate results and the percentages of the error are just slightly raised. (From 1.299% to 1.624% for iQP4 and from 0.616% to 0.784% for iQP8)

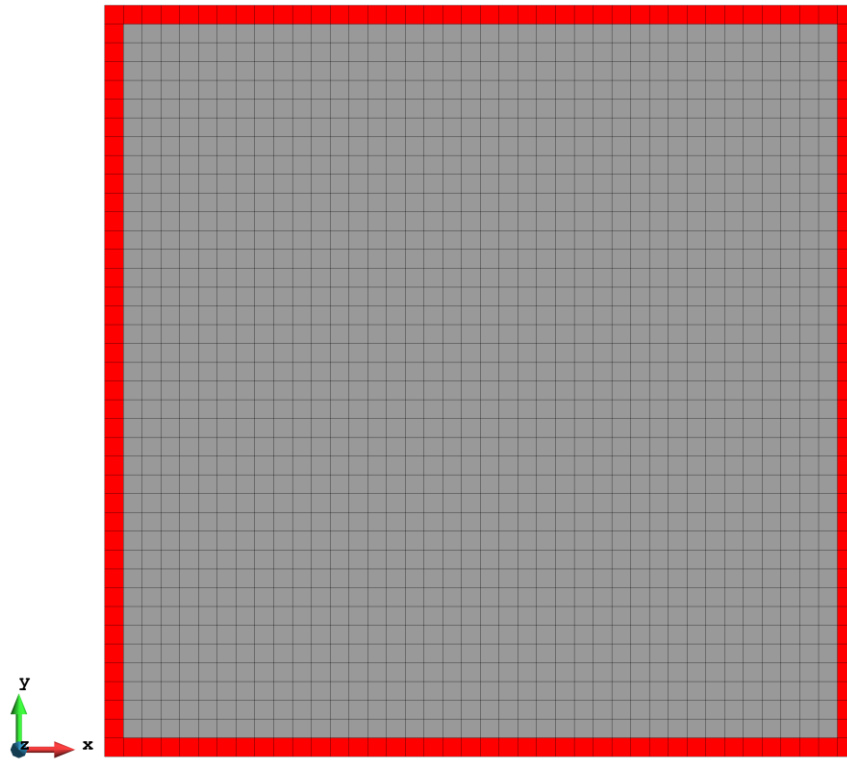
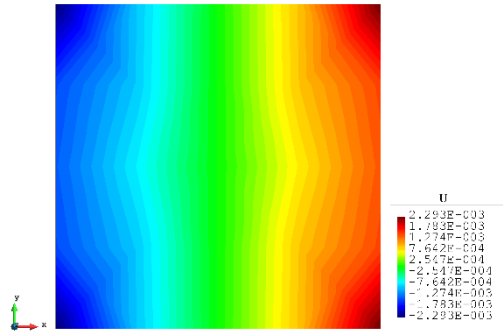
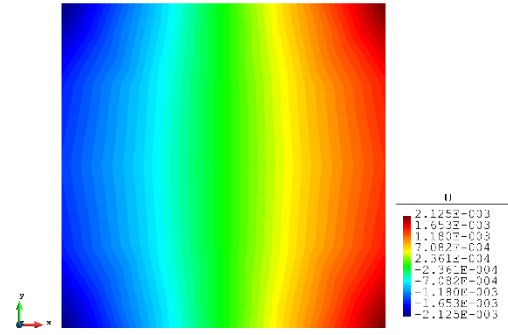


**Figure 5.4** The sensor locations of Case 1 with 1600 elements

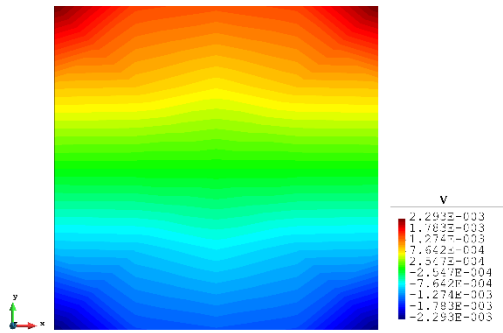
The plots of the deformations are also shown from Fig. 5.5 to Fig. 5.7 to further illustrate the results. It can be witnessed that the displacements are symmetrical along the central axis of the plate and the maximum/minimum values appear on the corners of the plate. These typical features can be captured by the inverse analysis, and they will not be affected by the mesh or the element type, i.e., the plots of the iQP4 and iQP8 elements match well with the FEM plots including the reduced sensor condition.



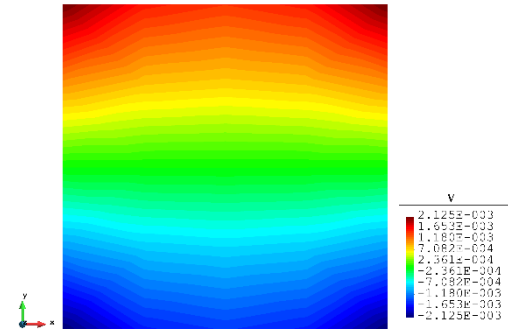
a). x-displacements of FEM QP4



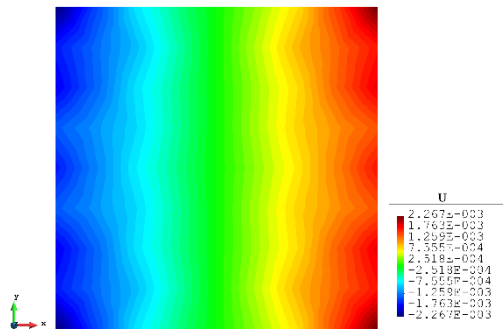
b). x-displacements of iFEM iQP4



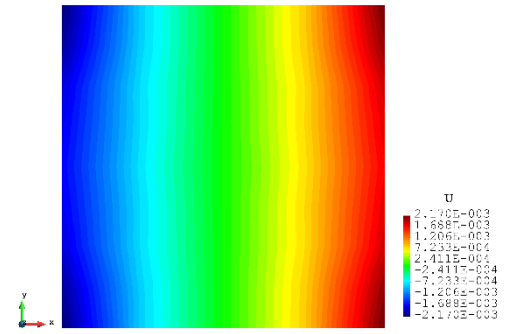
c). y-displacements of FEM QP4



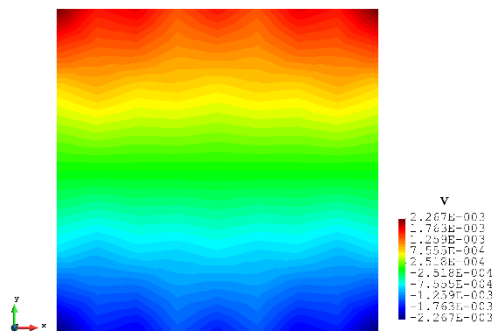
d). y-displacements of iFEM iQP4



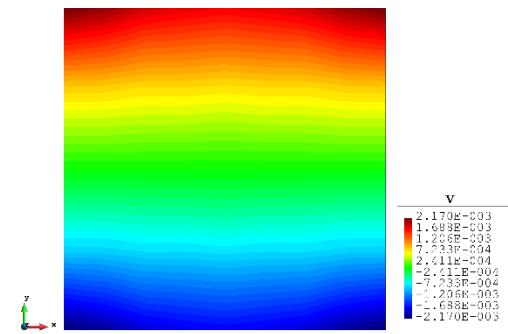
e). x-displacements of FEM QP8



f). x-displacements of iFEM iQP8

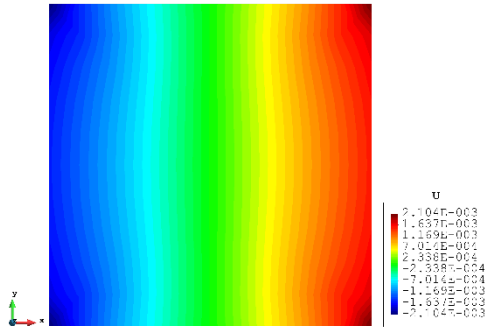


g). y-displacements of FEM QP8

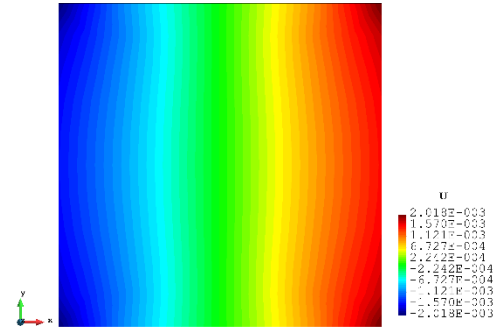


h). y-displacements of iFEM iQP8

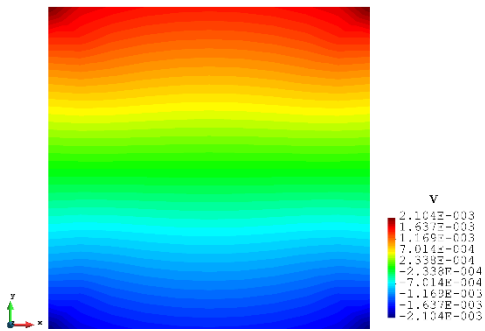
**Figure 5.5** The plots of displacements of Case 1 with 16 elements



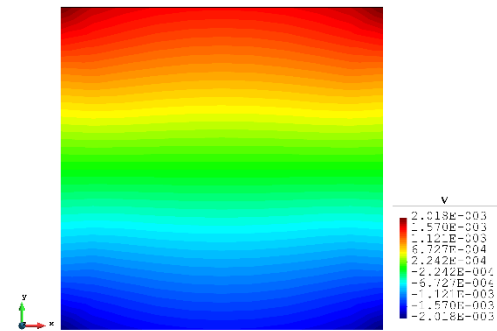
a). x-displacements of FEM QP4



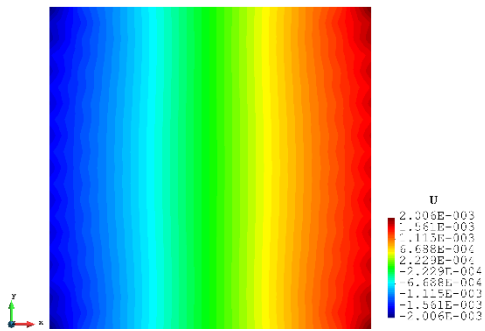
b). x-displacements of iFEM iQP4



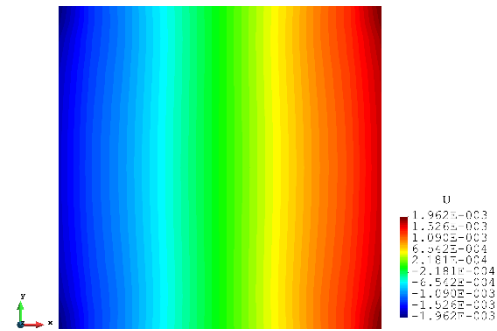
c). y-displacements of FEM QP4



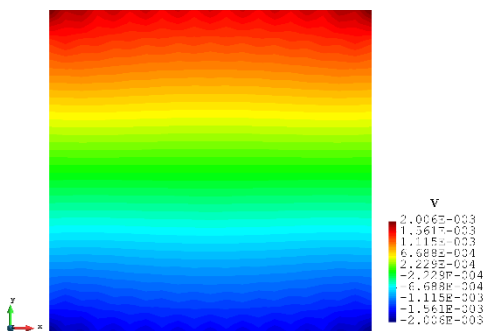
d). y-displacements of iFEM iQP4



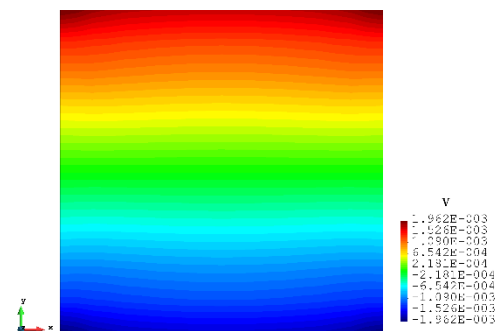
e). x-displacements of FEM QP8



f). x-displacements of iFEM iQP8

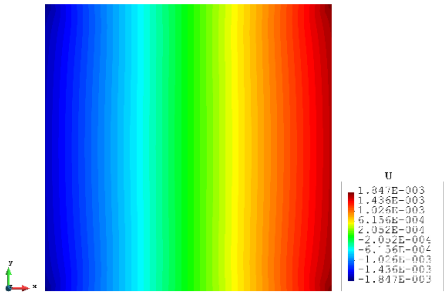


g). y-displacements of FEM QP8

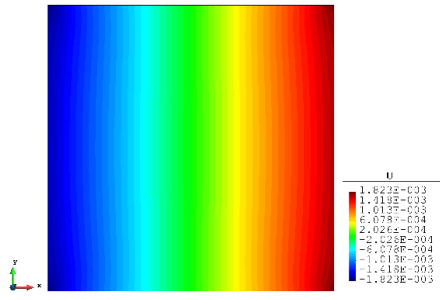


h). y-displacements of iFEM iQP8

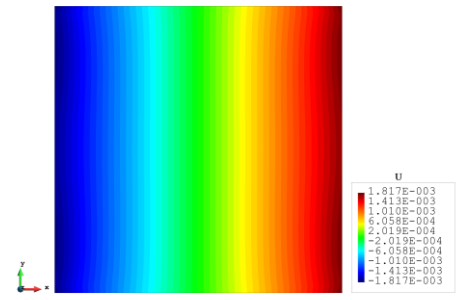
**Figure 5.6** The plots of displacements of Case 1 with 100 elements



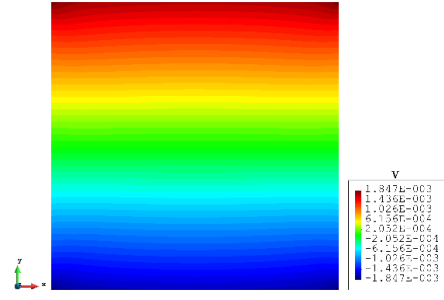
a). x-displacements of FEM QP4



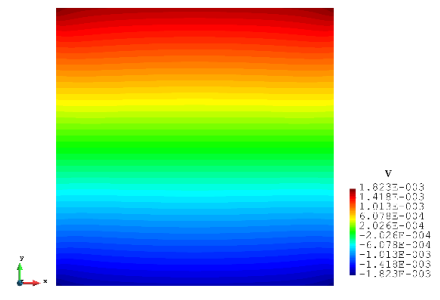
b). x-displacements of iFEM iQP4



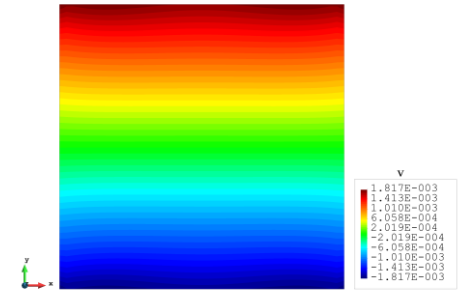
c). x-displacements of iFEM iQP4-r



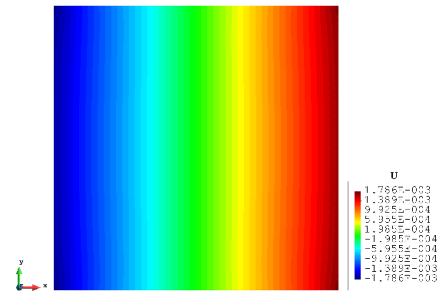
d). y-displacements of FEM QP4



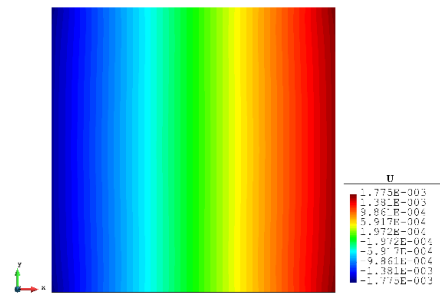
e). y-displacements of iFEM iQP4



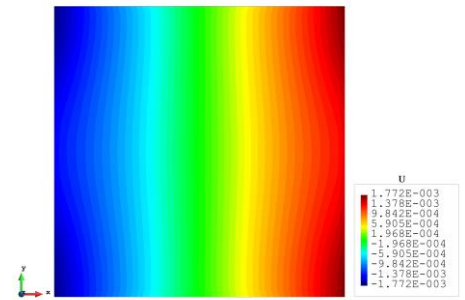
f). x-displacements of iFEM iQP4-r



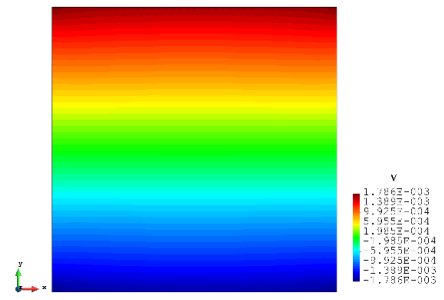
g). x-displacements of FEM QP8



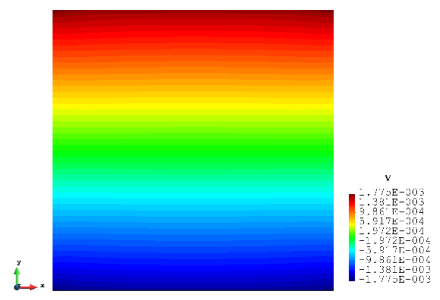
h). x-displacements of iFEM iQP8



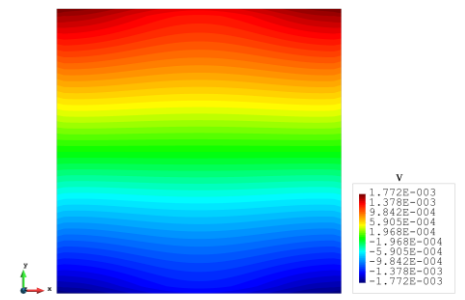
i). x-displacements of iFEM iQP8-r



j). y-displacements of FEM QP8



k). y-displacements of iFEM iQP8



l). x-displacements of iFEM iQP8-r

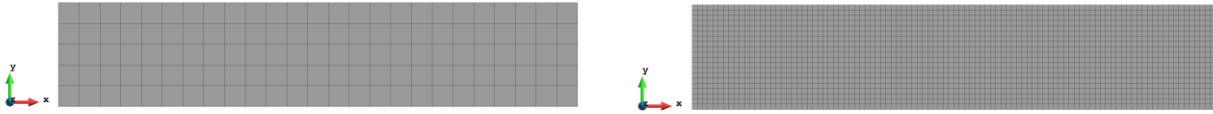
**Figure 5.7** The plots of displacements of Case 1 with 1600 elements

## Case 2



**Figure 5.8** The loading and boundary conditions of Case 2

For Case 2, a rectangular plate, with 5 m length and 1 m height, is fully constrained on the left edge and the same tension loadings as Case 1 is applied to the right edge (Figure 5.8). Similarly, the plate has meshed with both fine mesh (125 elements) and dense mesh (2000 elements). (Figure 9) Table 5.5 and Table 5.6 are the results for Case 2. If the mesh is quite coarse, the estimation of the y-displacements is not as good as the x-direction. The error of the V is about 20% and for iQP8, it is even worse as 26.439%. Since the displacements in the y-direction are much smaller than the displacements in the x-direction (over 15 times). And for the major displacements, both types of elements give reasonable results (1.800% and 2.245%, respectively). It means that the results would be acceptable. If the plate meshes with 2000 elements, the displacements especially in the y-direction are improved. The percentage of the differences is drastically dropped to around or less than 10%, which shows that the inverse results are approaching the FEM reference. But it should be mentioned that the performance of the iQP8 element becomes worse than the iQP4 element, which is the opposite in Case 1.



a). 125 elements

b). 2000 elements

**Figure 5.9** Two different meshes of Case 2

**Table 5.5** The results for Case 2 with 125 elements

Case 2 with 125 elements		iQP4	iQP8
$U$	a. FEM	2.500E-02	2.539E-02
	b. iFEM	2.455E-02	2.482E-02
Differences between a and b		1.800%	2.245%
$V$	c. FEM	1.421E-03	1.842E-03
	d. iFEM	1.121E-03	1.355E-03
Differences between c and d		21.112%	26.439%

**Table 5.6** The results for Case 2 with 2000 elements

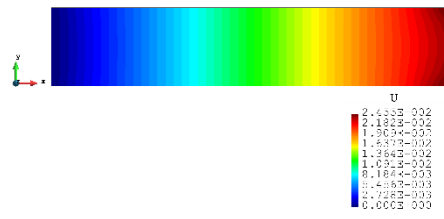
Case2 with 2000 elements		iQP4	iQP8
$U$	a. FEM	2.444E-02	2.437E-02
	b. iFEM	2.431E-02	2.421E-02
	c. iFEM-r	2.411E-02	2.403E-02
Differences between a and d		0.532%	0.657%
Differences between a and c		1.350%	1.395%
$V$	d. FEM	1.127E-03	1.129E-03
	e. iFEM	1.039E-03	9.982E-04
	f. iFEM-r	1.059E-03	1.034E-03
Differences between d and e		7.808%	11.585%
Differences between d and f		6.034%	8.415%

The plots of Case 2 are given in Fig. 5.10 and Fig. 5.11. There is no doubt that, for the full sensor condition, the differences of the plots between the inverse analysis and FEM reference are indistinguishable. For the plots of the reduced sensor condition, the sensors are kept along the edge leading to a total number of 236. (Fig. 5.12) Because of the sensor reduction, some

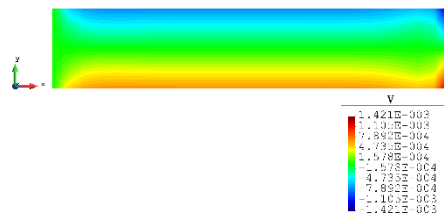
features along the edge are not captured clearly. But the main feature, i.e., the locations of the large deformations, is obviously captured.



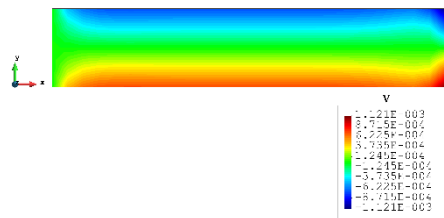
a). x-displacements of FEM QP4



b). x-displacements of iFEM iQP4



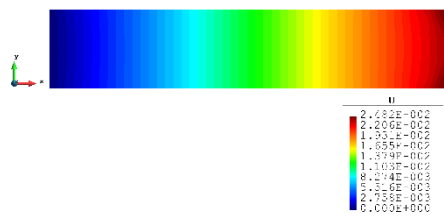
c). y-displacements of FEM QP4



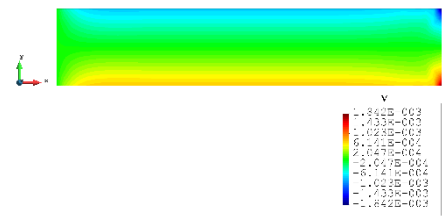
d). y-displacements of iFEM iQP4



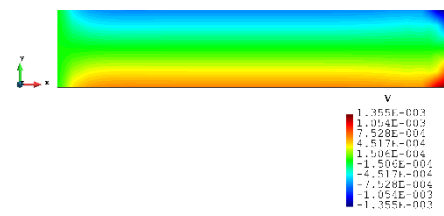
e). x-displacements of FEM QP8



f). x-displacements of iFEM iQP8



g). y-displacements of FEM QP8

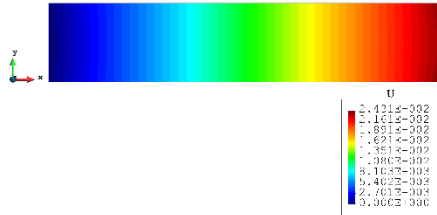


h). y-displacements of iFEM iQP8

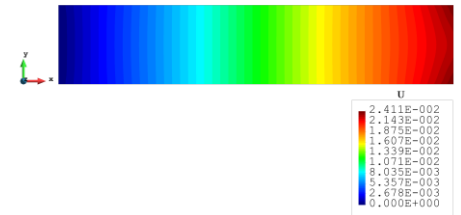
**Figure 5.10** The plots of displacements of Case 2 with 125 elements



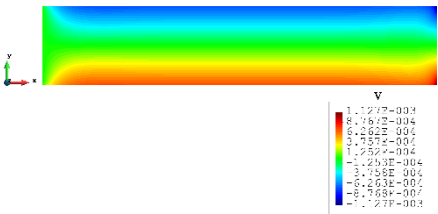
a). x-displacements of FEM QP4



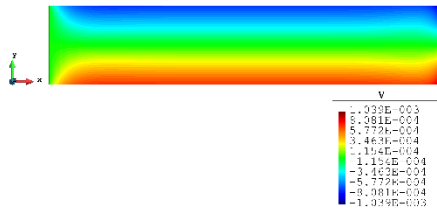
b). x-displacements of iFEM iQP4



c). x-displacements of iFEM iQP4-r



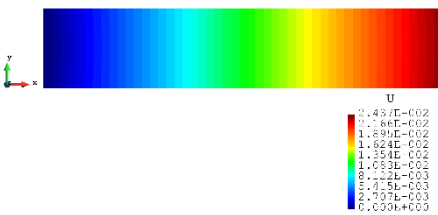
d). y-displacements of FEM QP4



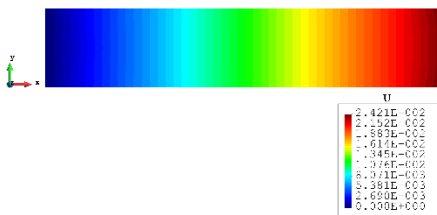
e). y-displacements of iFEM iQP4



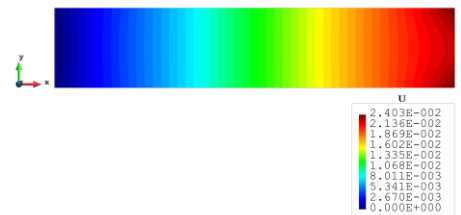
f). y-displacements of iFEM iQP4-r



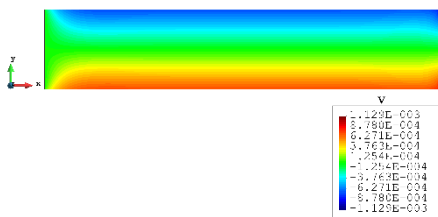
g). x-displacements of FEM QP8



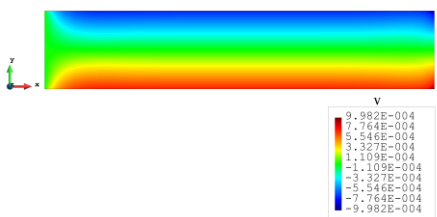
h). x-displacements of iFEM iQP8



i). x-displacements of iFEM iQP8-r



j). y-displacements of FEM QP8



k). y-displacements of iFEM iQP8



l). y-displacements of iFEM iQP8-r

**Figure 5.11** The plots of displacements of Case 2 with 2000 elements

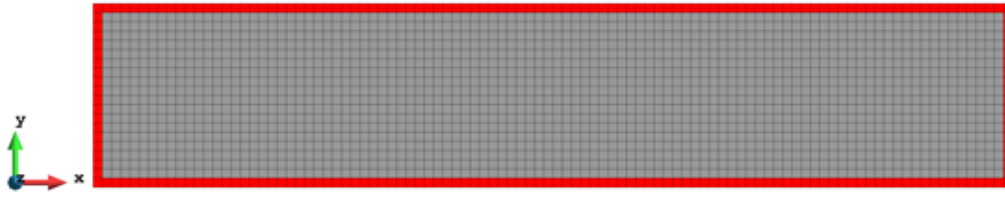


**Figure 5.12** The sensor locations of Case 2 with 2000 elements

### Case 3

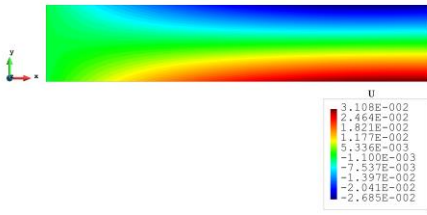


**Figure 5.13** The loading and boundary conditions of Case 3

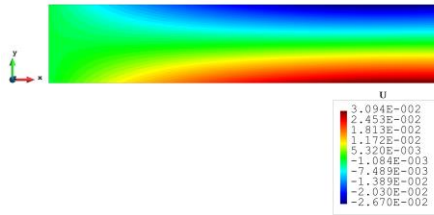
Fig. 5.13 is a simple diagrammatic sketch for Case 3, and it is a further test based on Case 2. The distributed force is replaced by a single nodal force ( $100\sqrt{2}$  MN) at the top corner of the plate. The other parameters and conditions including the sensor locations remain unchanged. The results of the displacements are listed in Table 5.7. For the full sensor condition, all the percentages are smaller than 1%. For the reduced sensor case, the results of x-displacements are still within the 1% range of the FEM results. The y-displacements grow softly to around 4%, which is still accurate. Besides, the plots (Fig. 5.14) of the inverse analysis are identical to the plots of the FEM analysis, which indicates that iQP4 and iQP8 can provide accurate results.

**Table 5.7** The results of Case 3

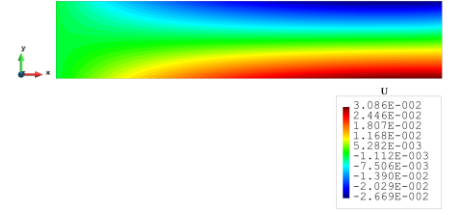
Case3		iQP4	iQP8
$U$	a. FEM	3.108E-02	3.112E-02
	b. iFEM	3.094E-02	3.105E-02
	c. iFEM-r	3.086E-02	3.094E-02
Differences between a and d		0.450%	0.225%
Differences between a and c		0.708%	0.578%
$V$	d. FEM	2.100E-01	2.106E-01
	e. iFEM	2.088E-01	2.098E-01
	f. iFEM-r	2.011E-01	2.026E-01
Differences between d and e		0.571%	0.380%
Differences between d and f		4.238%	3.799%



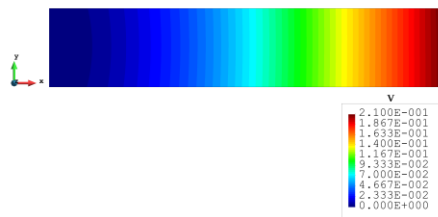
a). x-displacements of FEM QP4



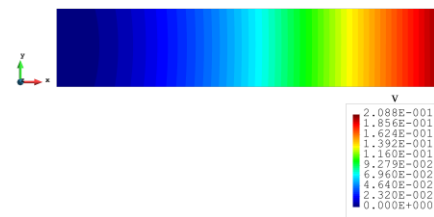
b). x-displacements of iFEM iQP4



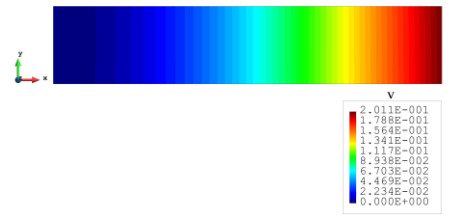
c). x-displacements of iFEM iQP4-r



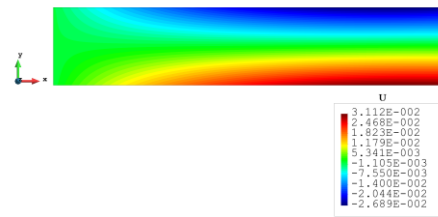
d). y-displacements of FEM QP4



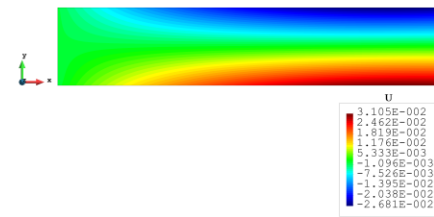
e). y-displacements of iFEM iQP4



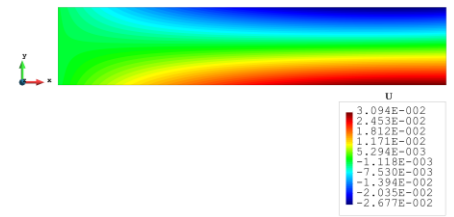
f). y-displacements of iFEM iQP4-r



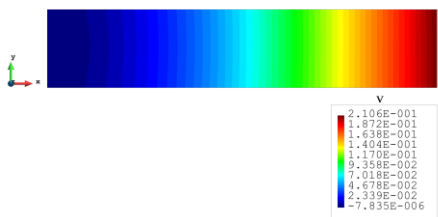
g). x-displacements of FEM QP8



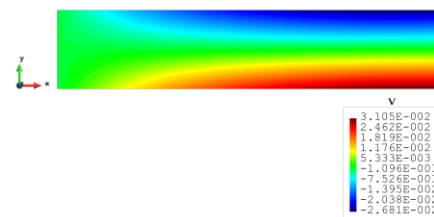
h). x-displacements of iFEM iQP8



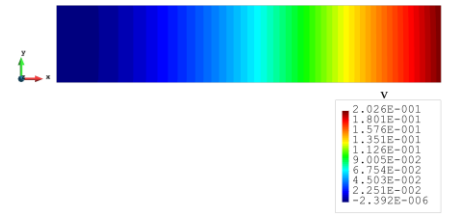
i). x-displacements of iFEM iQP8-r



j). y-displacements of FEM QP8



k). y-displacements of iFEM iQP8



l). y-displacements of iFEM iQP8-r

**Figure 5.14** The plots of displacements of Case 3 with 2000 elements

### Case 4

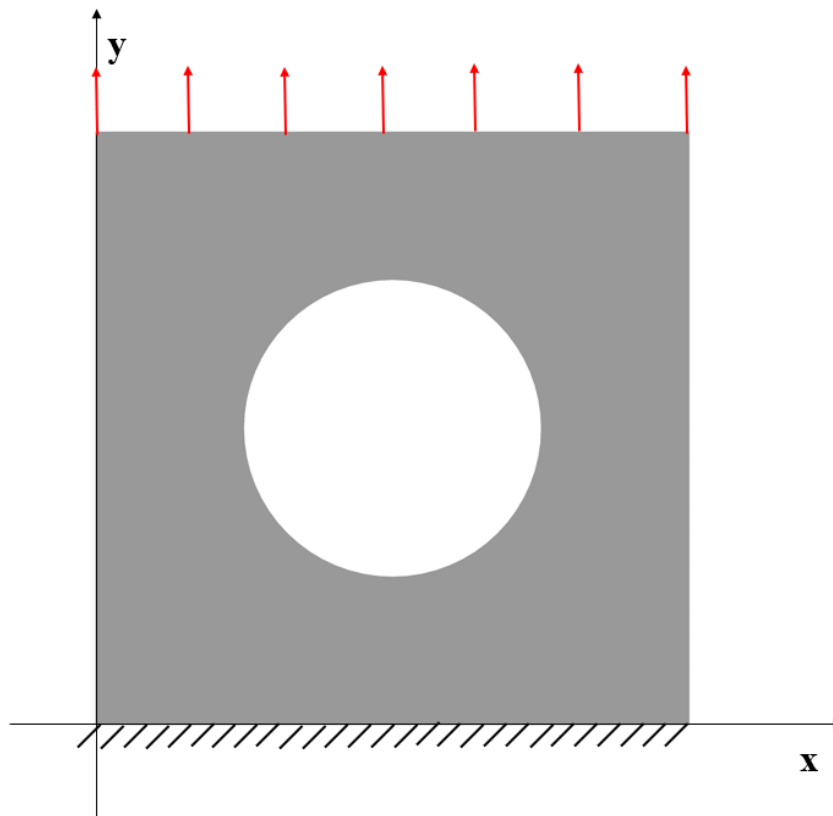
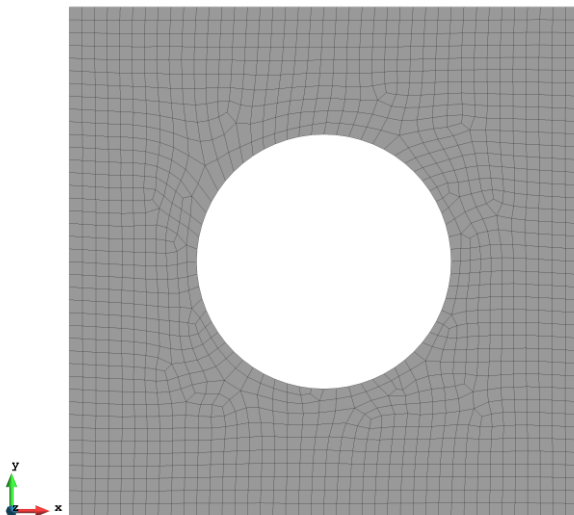
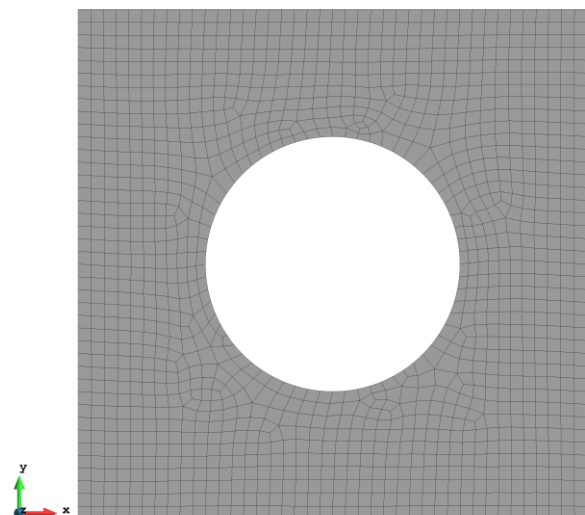


**Figure 5.15** The loading and boundary condition of Case 4



a). The mesh for the 4-node element (1288 elements)



b). The mesh for the 8-node element (1293 elements)

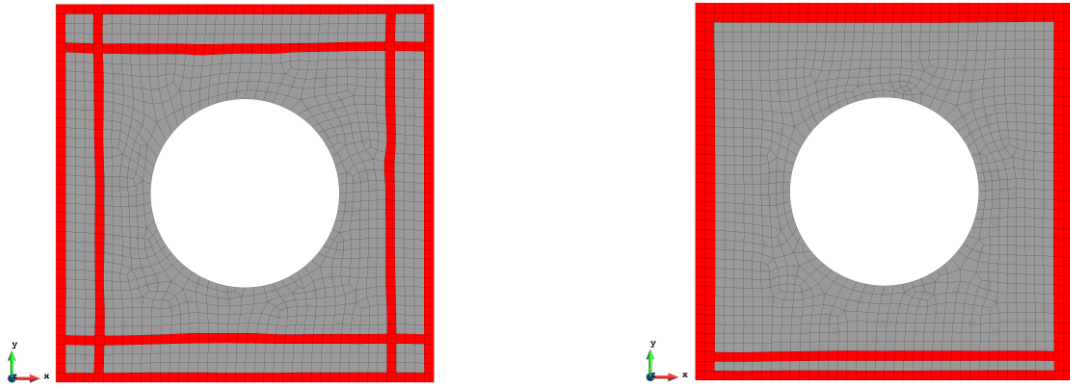
**Figure 5.16** The mesh for Case 4

A more complex case which is a plate with a hole at the center is selected as the last case. (Fig. 5.15) The plate has the same geometry as Case 1 and the radius of the hole is 0.5 m. Only dense

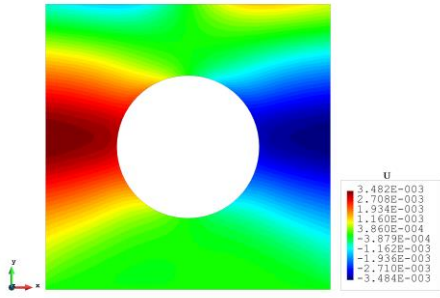
mesh is considered for Case 4 to ensure the accuracy of FEM analysis, and the plate has meshed with 1288 elements and 1293 elements for IQP4 and IQP8 elements separately. (Fig. 5.16) The reason for this difference is that around the hole, the mesh would be slightly different, but it will not influence the results. von Mises stress is also chosen for this case to further illustrate the comparison. As shown in Table 5.8, for the full sensor condition, all three results ( $U$ ,  $V$ , and  $\sigma_{vm}$ ) for both elements are close to the FEM reference. For instance, the von Mises stress is 1.959% less than the FEM value for the iQP4 element and the iQP8 element, it becomes further smaller as 1.240%. For two types of elements, the number of sensors is reduced to 304. (Fig. 5.17) It should be highlighted that the locations of the sensors are different between the two element types for relatively more accurate results. The current sensor locations can provide less than 10% error for major displacements and von Mises stress. The relatively large percentages of the x-displacements can also be explained by the explanation given in Case 2. For the plots of Case 4 (Figs. 5.18 and 5.19), first of all, the plots of the full sensor condition are almost the same as the FEM plots. The main features and tendencies of the plots are captured by the reduced sensor conditions. For example, from c) and f) of Fig. 5.19, it can be seen that the stress is concentrated around the left and right sides of the central hole, and the minimum stress is located around the bottom of the plate. These characteristics are also presented by the FEM plots. The comparison of the results and figures can prove that iQP4/iQP8 even with a limited number of sensors can still estimate accurate results.

**Table 5.8** The results of Case 4

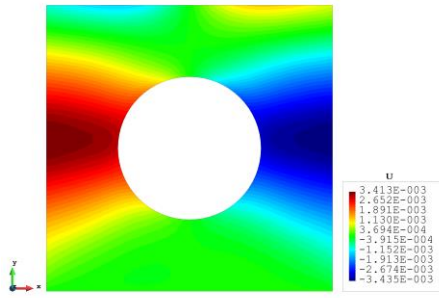
Case4		IQP4	IQP8
$U$	a. FEM	3.482E-03	3.577E-03
	b. iFEM	3.413E-03	3.547E-03
	c. iFEM-r	2.932E-03	3.079E-03
Differences between a and d		1.982%	0.839%
Differences between a and c		15.796%	13.922%
$V$	d. FEM	1.161E-02	1.183E-02
	e. iFEM	1.152E-02	1.178E-02
	f. iFEM-r	1.067E-02	1.070E-02
Differences between d and e		0.775%	0.423%
Differences between d and f		8.096%	9.552%
$\sigma_{vm}$	g. FEM	2.450E+09	2.501E+09
	h. iFEM	2.402E+09	2.470E+09
	i. iFEM-r	2.277E+09	2.332E+09
Differences between g and h		1.959%	1.240%
Differences between g and i		7.061%	6.757%



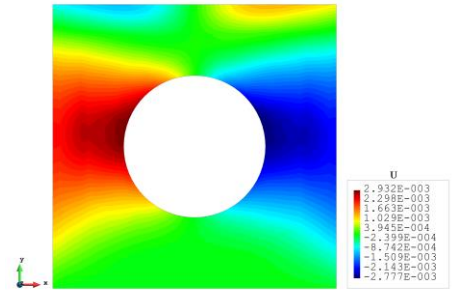
a). The sensors for the 4-node element (1288)      b). The sensors for the 8-node element (1293)  
**Figure 5.17** The sensor locations for Case 4



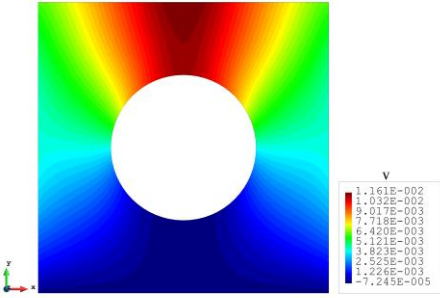
a). x-displacements of FEM QP4



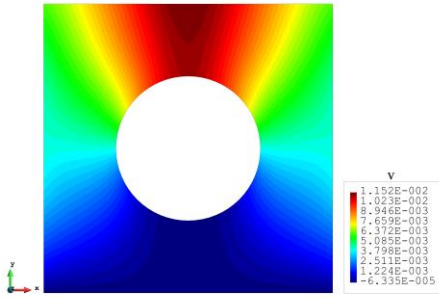
b). x-displacements of iFEM iQP4



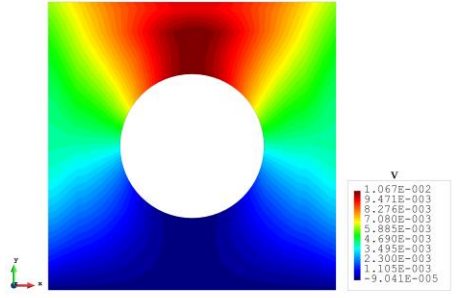
c). x-displacements of iFEM iQP4-r



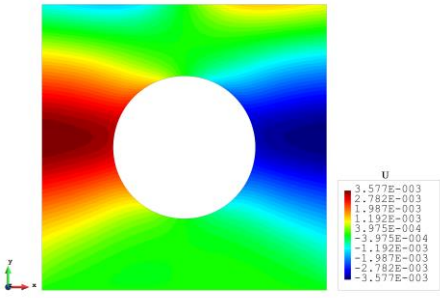
d). y-displacements of FEM QP4



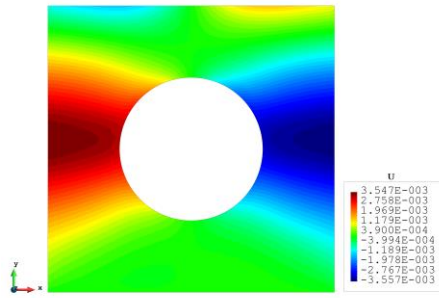
e). y-displacements of iFEM iQP4



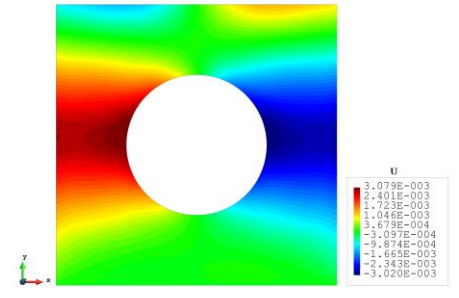
f). x-displacements of iFEM iQP4-r



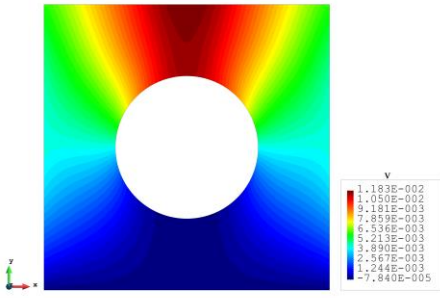
g). x-displacements of FEM QP8



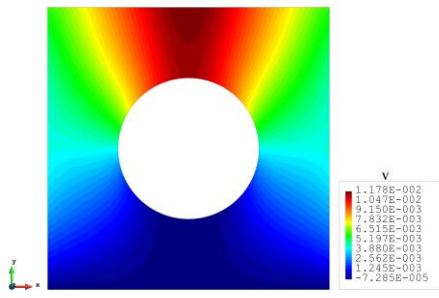
h). x-displacements of iFEM iQP8



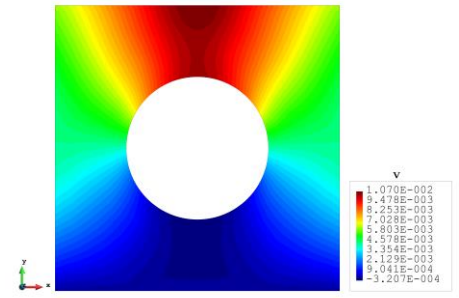
i). x-displacements of iFEM iQP8-r



j). y-displacements of FEM QP8



k). y-displacements of iFEM iQP8



l). x-displacements of iFEM iQP8-r

**Figure 5.18** The plots of displacements of Case 4

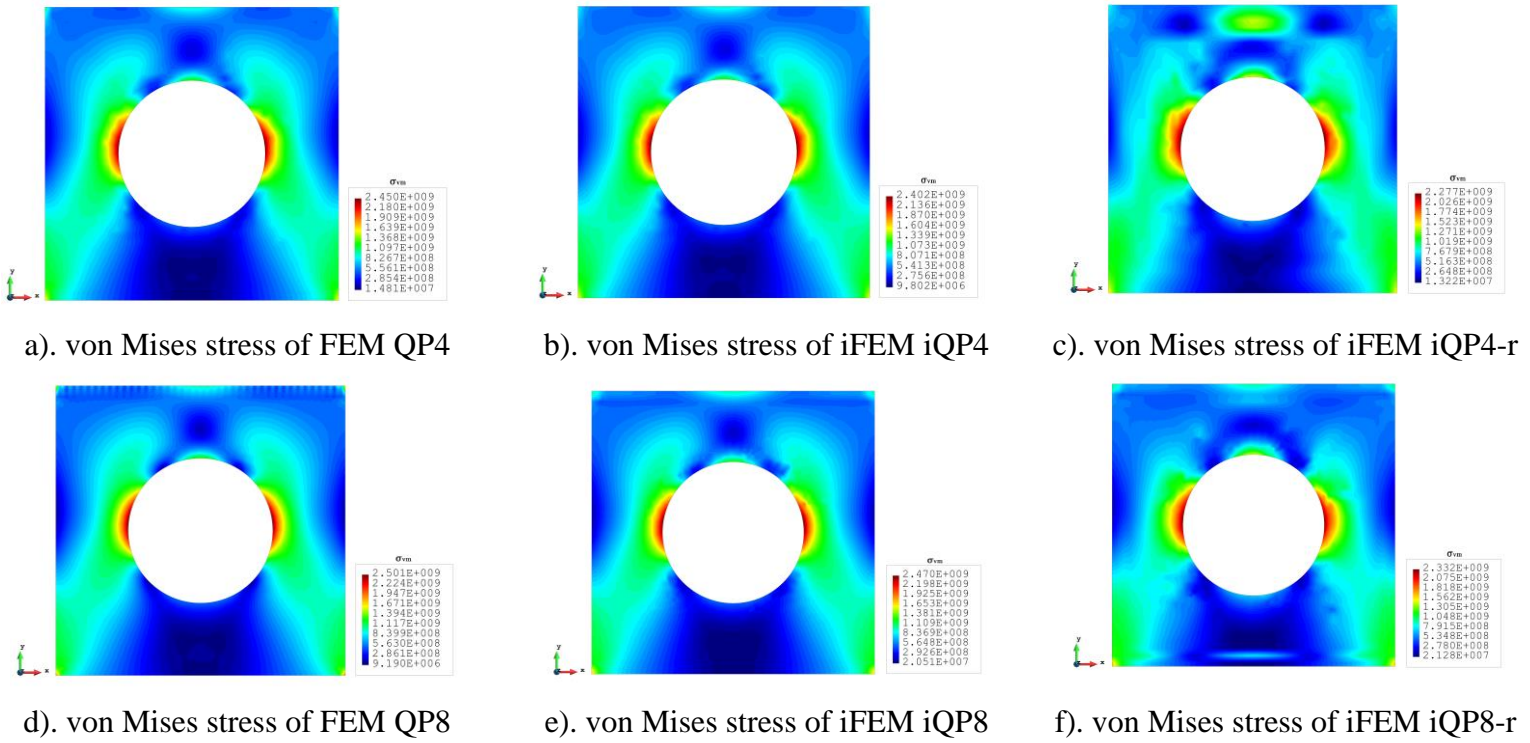


Figure 5.19 The plots of von Mises stress of Case 4

### 5.3 The 8-node inverse crack tip element

#### 5.3.1 Formulations of the inverse crack tip element

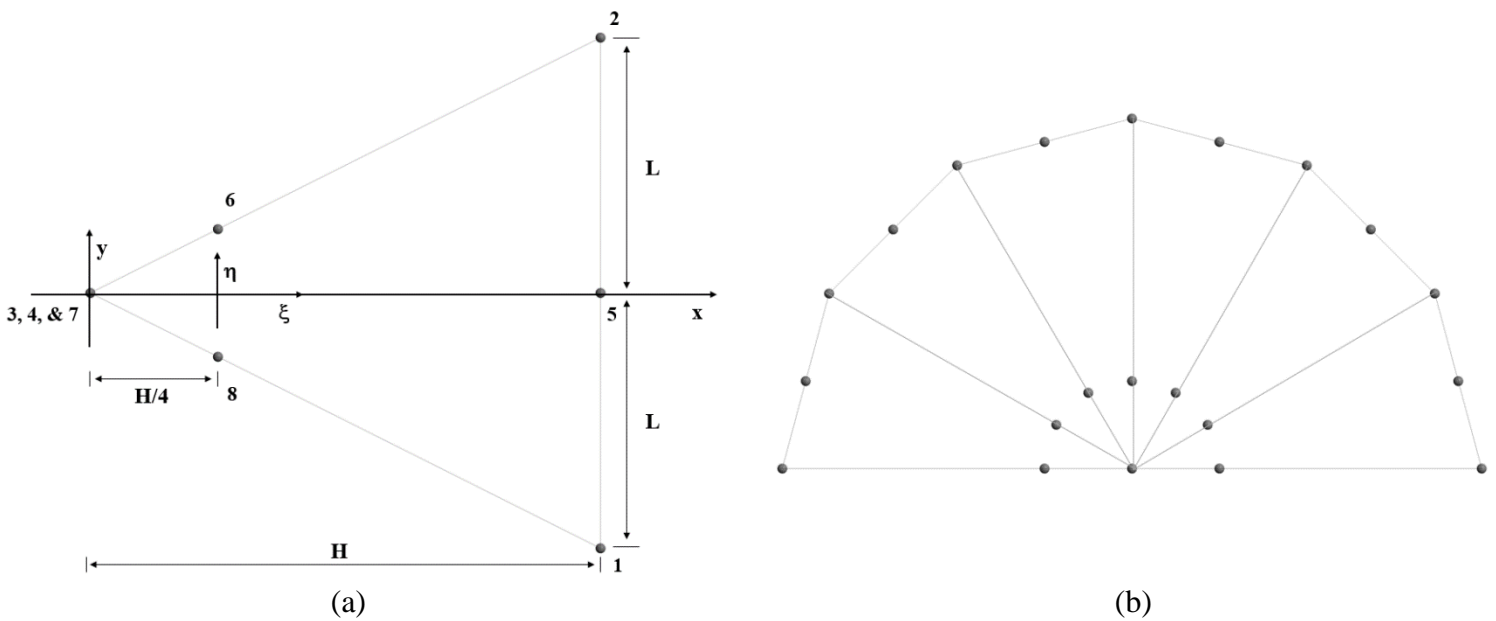


Figure 5.20 Quarter-point crack tip element (a) and quarter-point elements around the crack tip

The inverse 8-node crack tip element is developed by importing the weighted-least-squares theory into the plane crack tip element which was found by Barsoum. (Barsoum, 1976; Barsoum, 1977) For the finite crack tip element, it can achieve singularity by shifting two mid-side nodes to the quarter of the line. And usually, the original quadrilateral element will degenerate into a kind of triangular element (Fig. 5.20(a)). Nodes 3, 4, and 7 will be transformed to overlap each other, and node 6 and node 8 will be moved to the quarter of the line. (Nikishkov, 2013) The length of the element will be  $H$  in the x-direction and y-direction, and the height will be  $2L$  (Fig. 5.20(a)), which means that node 6 and node 8 will be located at  $(\frac{H}{4}, \frac{L}{4})$  and  $(\frac{H}{4}, -\frac{L}{4})$ , respectively, in the local coordinate system. And the parameters  $H$  and  $L$  can be calculated by the nodal distance. When this element is under application, these 3 overlapping nodes will be converted to a single node and share the same degree of freedom. The formulations of the crack tip element are given by Barsoum. (Barsoum, 1976) Generally speaking, most of the formulations of the 8-node quadrilateral plane element such as the shape functions, the transformation from random quadrilateral element to normalized quadrilateral element, and the relations between the nodal displacements and strains can still be utilized. But when defining the crack tip element, an additional transformation is transferred from the quadrilateral element in the normalized coordinate system to the degenerated triangular element in the local coordinate system. By doing so, it will contribute to another Jacobian matrix apart from the Jacobian which is used to link the shape functions between the global coordinate system and the normalized coordinate system. The Jacobian matrix can be obtained by the following relationship, according to the positional relation shown in (a) of Fig. 5.20.

$$x = \frac{H(1-\eta)^2}{4} \quad (5.10a)$$

$$y = \frac{L(1-\eta)^2 \xi}{4} \quad (5.10b)$$

By differentiating the  $x$  and  $y$  against  $\xi$  and  $\eta$ , the following Jacobian matrix can be gained:

$$[J] = \begin{bmatrix} \frac{\partial x}{\partial \xi} & \frac{\partial y}{\partial \xi} \\ \frac{\partial x}{\partial \eta} & \frac{\partial y}{\partial \eta} \end{bmatrix} = \begin{bmatrix} 0 & \frac{L(1-\eta)^2}{4} \\ \frac{(-1)H(1-\eta)}{2} & \frac{(-1)L(1-\eta)\xi}{2} \end{bmatrix} \quad (5.11)$$

Then the  $[J]$  will be used in the process of generating the stiffness matrix. It should be mentioned that the order of the node is not fixed but the expressions of the  $[J]$  should also be updated correspondingly.

For the inverse crack tip element, there will be three membrane strains  $\varepsilon_{xx}$ ,  $\varepsilon_{yy}$ , and  $\gamma_{xy}$  are taken into account. The differences between the analytical strains and the experimental strains which are collected from the geometric centre of the quadrilateral element can be expressed as:

$$\phi(\mathbf{u}^e) = w_e \left\| \left\{ \begin{array}{l} w_{xx}(\varepsilon_{xx} - \varepsilon_{xx}^{input}) \\ w_{yy}(\varepsilon_{yy} - \varepsilon_{yy}^{input}) \\ w_{xy}(\gamma_{xy} - \gamma_{xy}^{input}) \end{array} \right\} \right\|^2 \quad (5.12)$$

Where  $\mathbf{u}^e$  is the elemental displacements matrix and for each node, there are two DOFs.  $w_e$  is the weighting constants that can be valued by the existence of the experimental strain inputs. If the experimental data is available, 1 will be used, otherwise, a relatively smaller value  $10^{-3}$  or  $10^{-4}$  can be selected. Additionally, another group of weighting coefficients ( $w_{xx}$ ,  $w_{yy}$ , and  $w_{xy}$ ) is introduced to balance the relation among the three strains and usually, 1 will be used for all of the coefficients.

By differentiating the weighted-least-squares formula (Eq. (5.12)) against the nodal displacements to minimize the difference between the analytical and experimental strains for every single element, the following equation can be evaluated:

$$\frac{\partial \mathbf{e}}{\partial \mathbf{u}^e} = \mathbf{k}^e \mathbf{u}^e - \mathbf{f}^e = 0 \quad (5.13)$$

The calculation of the  $\mathbf{k}^e$  and  $\mathbf{f}^e$  will be slightly different from the general inverse 8-node plane quadrilateral element because the new Jacobian will be considered:

$$\mathbf{k}^e = \iint_A w_e (\mathbf{B}^m)^T \mathbf{B}^m \det(J) dx dy \quad (5.14a)$$

$$\mathbf{f}^e = \iint_A w_e (\mathbf{B}^m)^T \left\{ \begin{array}{l} \varepsilon_{xx}^{input} \\ \varepsilon_{yy}^{input} \\ \gamma_{xy}^{input} \end{array} \right\} \det(J) dx dy \quad (5.14b)$$

$\mathbf{B}^m$  is the matrix generated by the shape functions to connect the membrane strains with the nodal displacements and it will be the same as the one used for the general inverse 8-node plane quadrilateral elements.

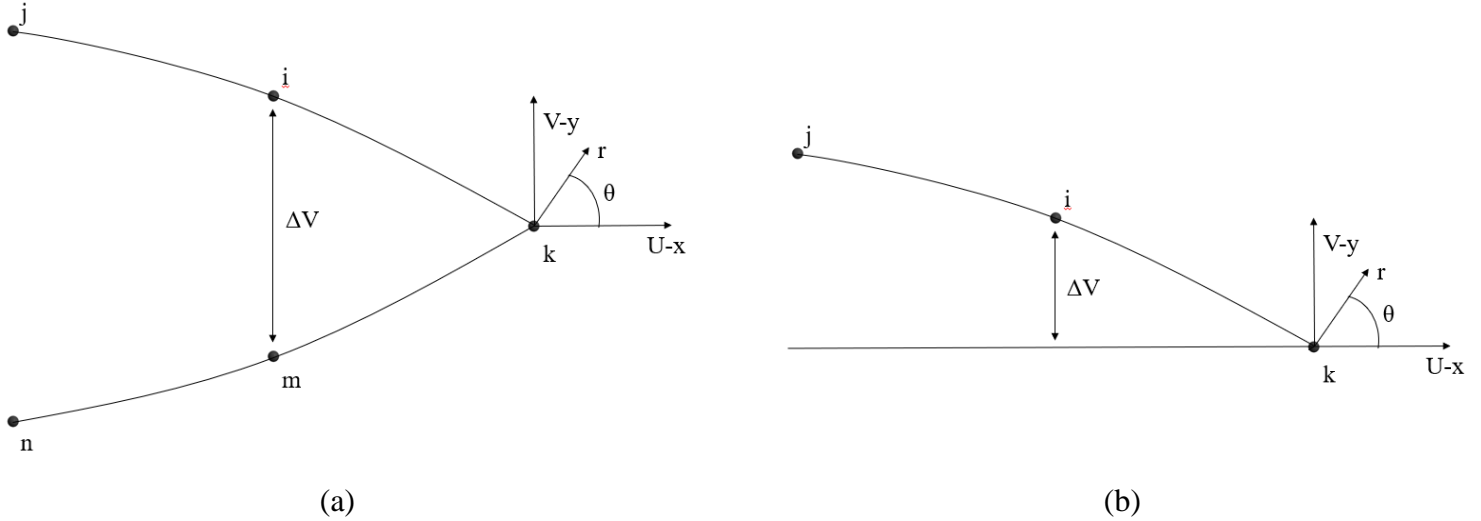


**Figure 5.21** The displacements of the crack tip for the displacement extrapolation method (a) full model, (b) half (symmetrical) model

After assembling the above single element equation to the global matrix and applying the boundary conditions to eliminate the singular problem of the calculation, the displacements of the structure especially the elements surrounding the crack tip (Fig. 5.20(b)) can be estimated. And after reforming the displacement field, the stress intensity factor (SIF) can be calculated by the Displacement Extrapolation Method. (Zhu and Oterkus, 2020) For plane elements and structure, only two types of SIF can occur, which are opening SIF ( $K_I$ ) and in-plane shear SIF ( $K_{II}$ ). Fig. 5.21 shows the nodes around the crack tip ( $r = 0$ ). For the nodes at the crack surface ( $\theta = 180^\circ$ ), the relation between the SIF and the nodal displacements can be linked by (Zhu and Oterkus, 2020):

$$K_I = \sqrt{2\pi} \frac{G}{1+k_b} \frac{|\Delta V|}{\sqrt{r}} \quad (5.15a)$$

$$K_{II} = \sqrt{2\pi} \frac{G}{1+k_b} \frac{|\Delta U|}{\sqrt{r}} \quad (5.15b)$$

$G$  is the shear modulus, and it can be calculated by the Elastic modulus ( $E$ ) and the Poisson's ratio ( $\nu$ ).  $k_b$  is the bulk modulus, and under the plane strain condition,  $k_b = 3 - 4\nu$ , and under the plane stress condition,  $k_b = \frac{3-\nu}{1+\nu}$ . And  $|\Delta V|$  is  $|\Delta U|$  the relative displacements in y- and x- directions. If the structure is fully modeled (Fig. 5.21 (a)),  $|\Delta V_{im}| = |V_i - V_m|$  and  $|\Delta U_{im}| = |U_i - U_m|$ . Otherwise (Fig. 5.21(b)),  $|\Delta V| = |2V_i|$  and  $|\Delta U| = |2U_i|$ .

$\frac{|\Delta V|}{\sqrt{r}}$  and  $\frac{|\Delta U|}{\sqrt{r}}$  are assumed to be linear at the crack surface and they can be obtained by approaching  $r$  to 0 for the crack tip.

$$\text{For } K_I: \quad \frac{|\Delta V|}{\sqrt{r}} = \frac{|\Delta V_{im}|(d_2)^{\frac{3}{2}} - |\Delta V_{jn}|(d_1)^{\frac{3}{2}}}{\sqrt{d_1 d_2 (d_2 - d_1)}} \quad (5.16a)$$

$$\text{For } K_{II}: \quad \frac{|\Delta U|}{\sqrt{r}} = \frac{|\Delta U_{im}|(d_2)^{\frac{3}{2}} - |\Delta U_{jn}|(d_1)^{\frac{3}{2}}}{\sqrt{d_1 d_2 (d_2 - d_1)}} \quad (5.16b)$$

Where  $d_1$  is the distance between  $k$  and  $i$  ( $k$  and  $m$ ) and  $d_2$  is the distance between  $k$  and  $j$  ( $k$  and  $n$ ).

### 5.3.2 Numerical examples of applying the inverse crack tip element

6 cases (Table 5.9) are provided to test the feasibility and accuracy of the inverse crack tip element in estimating the SIF. For all 6 cases,  $E$  will be  $210 \times 10^9$  Pa and  $\nu$  will be 0.3.

**Table 5.9** Cases for estimating the SIF at the crack tip

Case 1	Referenced rectangular bar with an edge crack
Case 2	Referenced rectangular bar with a central crack
Case 3	Dense mesh for Case 1 for opening SIF case
Case 4	Dense mesh for Case 2 for opening SIF case
Case 5	In-plane shear SIF case
Case 6	Combination of two SIF case

The initial four cases are prepared to compare with the reference results and investigate the effect of mesh size on the accuracy of the results. Then from Case 3 to Case 6, different types of SIF estimation are given to show the feasibility of the iPCT element.

### Case 1

The first case is a rectangular bar, like the one used in Barsoum's paper (Barsoum, 1976), with two edge cracks under plane strain conditions. The geometry of the plate is shown in (a) of Fig. 5.22. Since the plate is under tension (2000 MN and evenly distributed to the nodes) on the top and bottom edges, symmetrical boundary conditions can be applied. Therefore, only a quarter of the plate is modeled. And for Case 1, a very coarse mesh, which only has 20 elements and 65 nodes, is generated for the reference FEM analysis (Fig. 5.23(a)). For the iFEM analysis, to avoid the general triangular elements, the mesh has been refined with entire quadrilateral elements (still 20 elements but with 69 nodes) except the 6 elements around the crack tip (Fig. 5.23(b)). The results of Case 1 are collected in Table 5.10 and the plots of the deformations are given in Fig. 5.24.

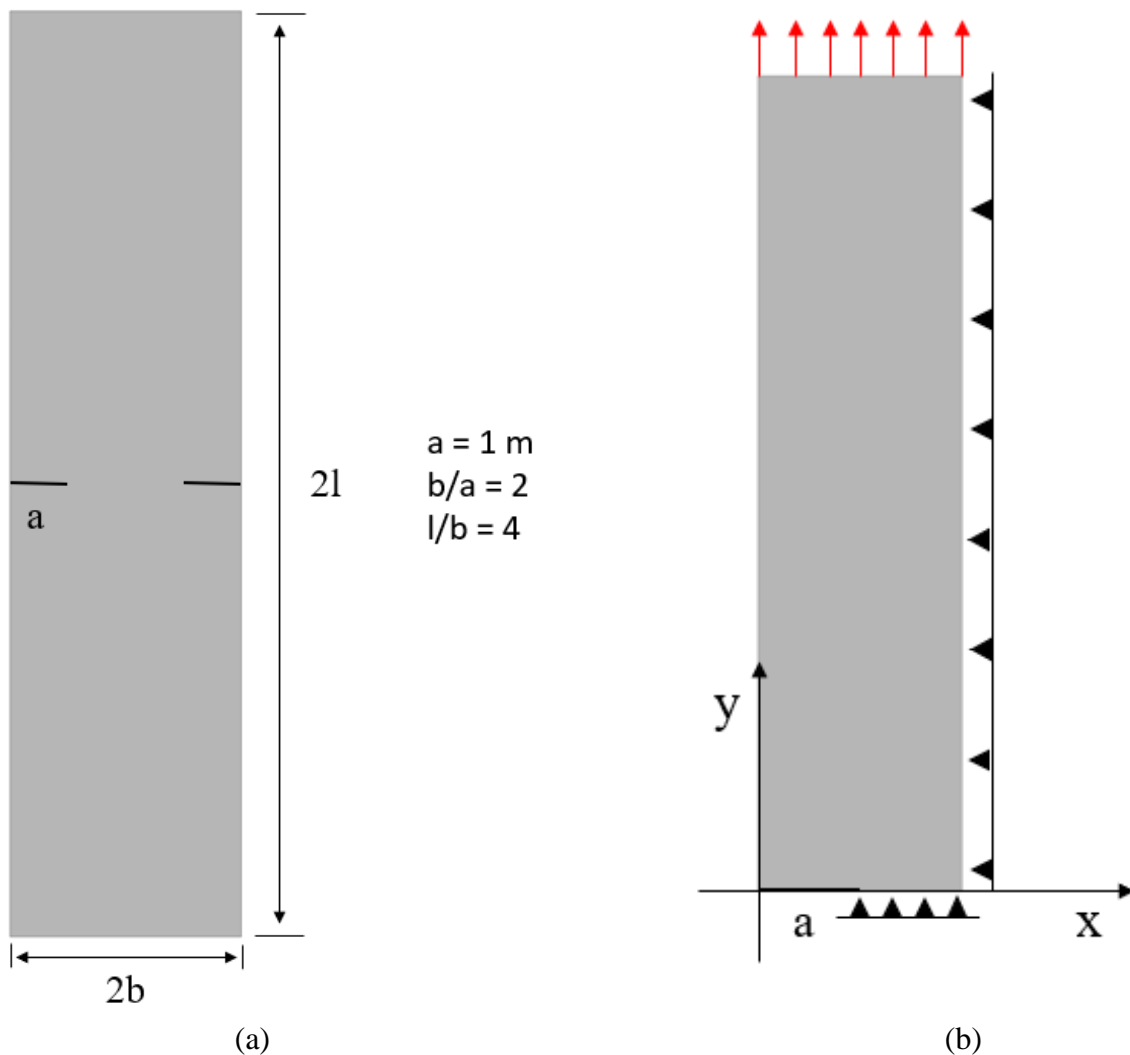


**Figure 5.22** The geometry of the plate with edge crack (a) and the loading and symmetrical boundary conditions of the quarter of the plate (b) for Case 1

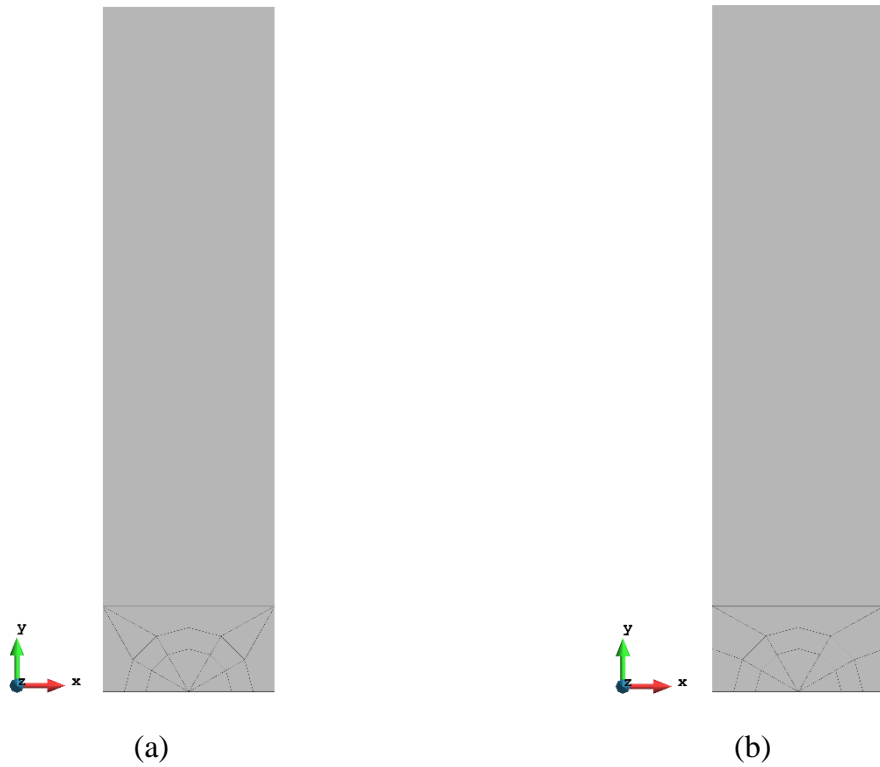
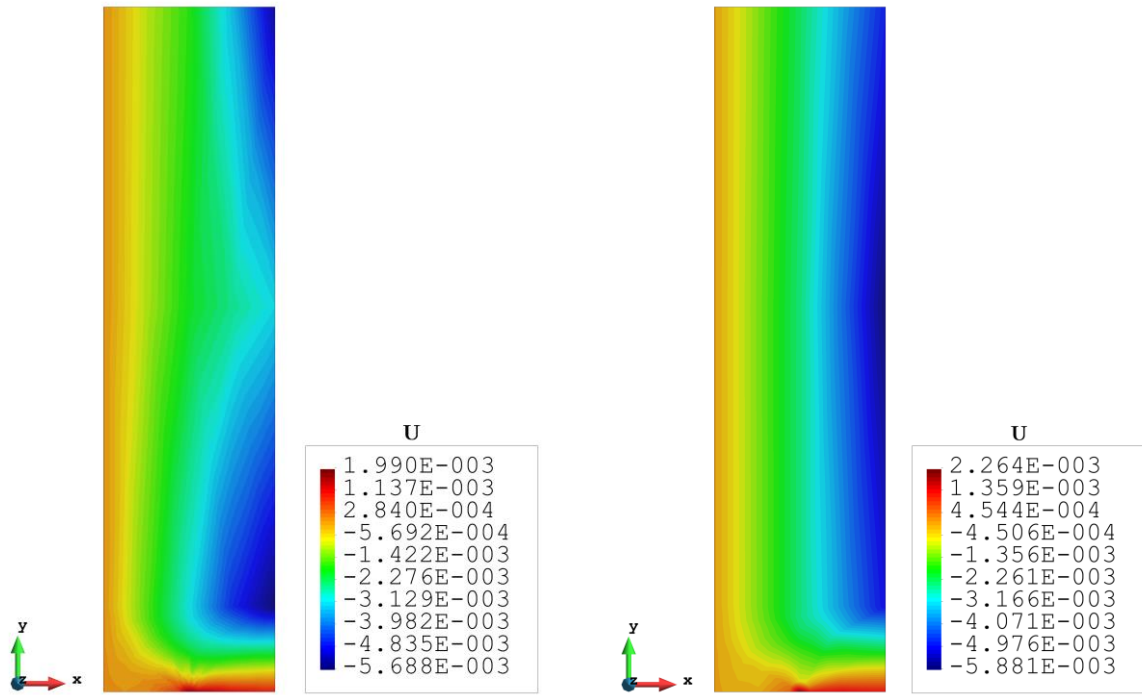


**Figure 5.23** The fine mesh for Case 1. (a) FEM, (b) iFEM

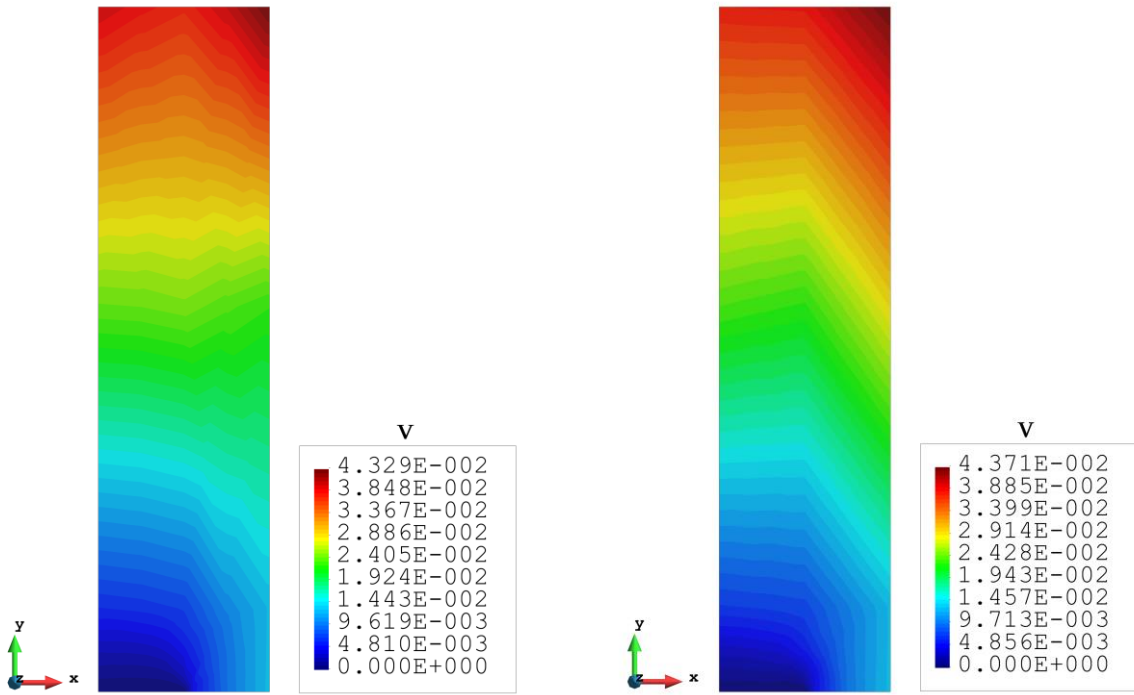
**Table 5.10** The results of Case 1

Case 1		$U$ (m)	$V$ (m)	SIF- $K_1$
(a)	FEM	5.668E-03	4.329E-02	2.017E+09
(b)	iFEM	5.881E-03	4.371E-02	1.870E+09
Differences between (a) and (b)		3.76%	0.97%	7.31%



(a)

(b)



(c)

(d)

**Figure 5.24** The plots for Case 1. The displacements in x-direction: (a) FEM, (b) iFEM. The displacements in y-direction: (c) FEM, (d) iFEM

From the extreme displacements' view, both  $U$  and  $V$  are in good agreement with FEM results and the percentages of the difference are smaller than 5%. Moreover, the plots of the iFEM are also similar to the FEM plots. Generally speaking, the inverse crack tip elements combined with the inverse 8-node plane quadrilateral element can provide accurate displacement results. For SIF, FEM shows a value of 2.017E9, and iFEM has slightly underestimated the value and achieves a value of 1.870E9, leading to a 7.31% error. But it is still in a reasonable range, proving that the inverse crack tip element can be used to monitor the SIF data.

## Case 2

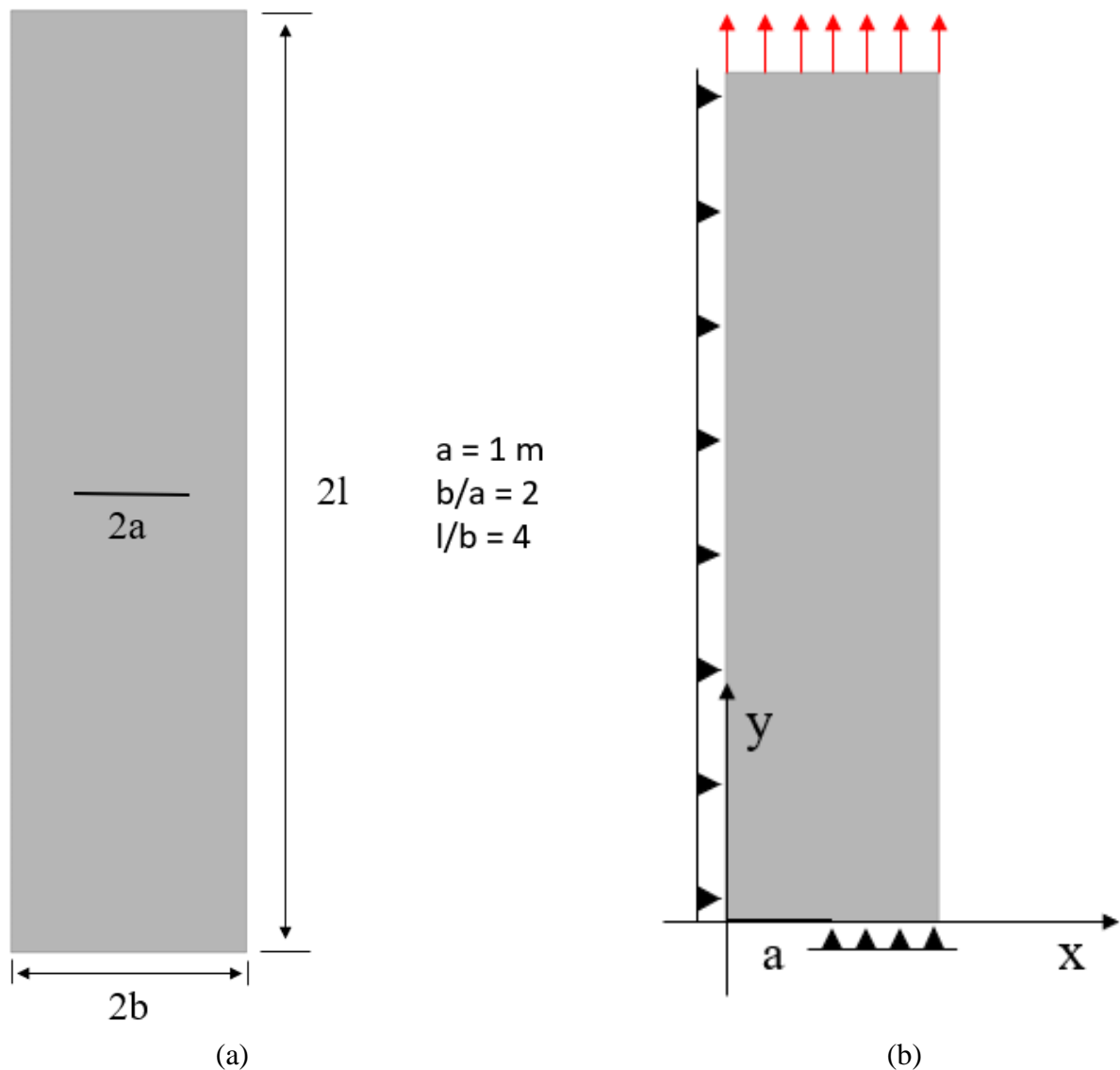
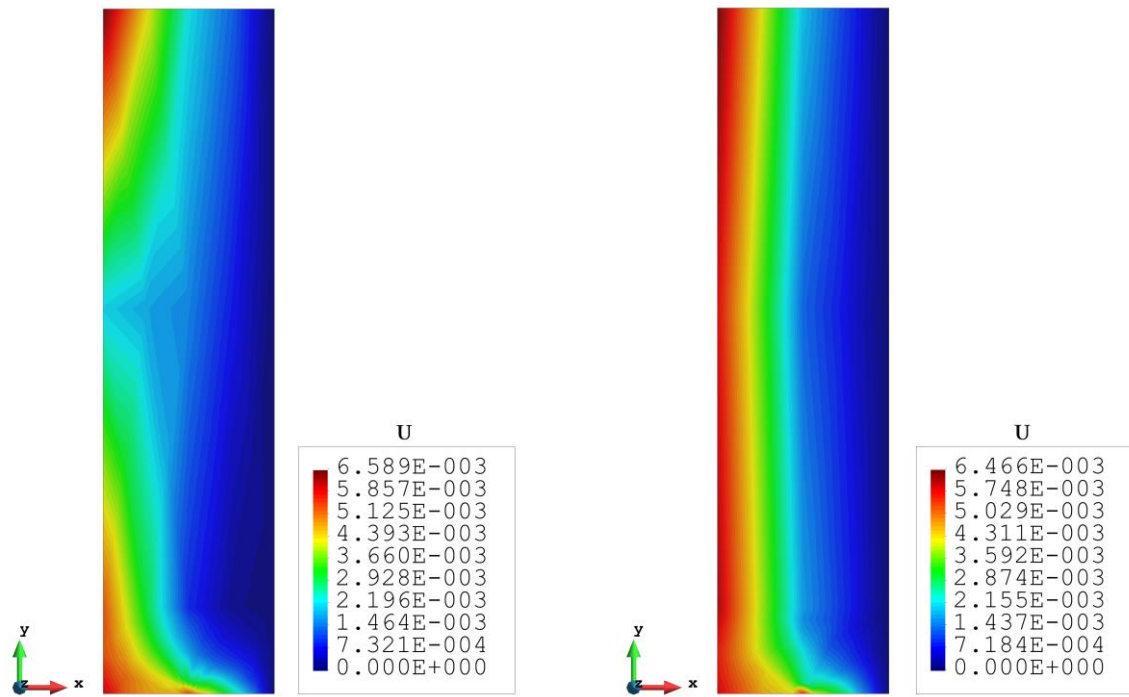


**Figure 5.25** The geometry of the plate with central crack (a) and the loadings and symmetrical boundary conditions of the quarter of the plate (b) for Case 2

In this case, the constrained boundary condition on the right edge is moved to the left edge making it become a quarter of a plate with a central crack (Fig. 5.25(a)). Other parameters including the length of the crack keep unchanged. It can be witnessed that from Table 5.11 and Fig. 5.26, the results including the plots still match well with FEM analysis. And the percentage of the difference between the two SIF is stable at about 7%. The reason why the error of the SIF is relatively higher is that the calculation process utilizes the displacements of the nodes around the crack tip. However, the displacements will be smaller than the extreme values at the top edge, so it is usually unavoidable to lead to some errors.

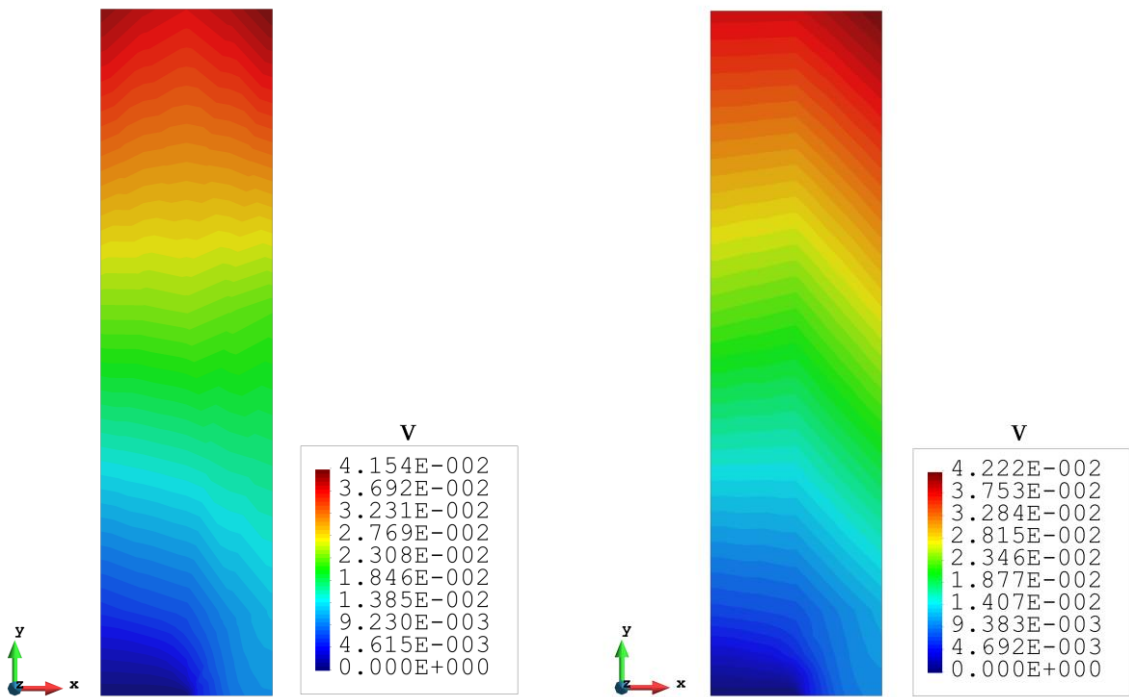
**Table 5.11** The results of Case 2

Case 2		$U$ (m)	$V$ (m)	SIF- $K_I$
(a)	FEM	6.589E-03	4.154E-02	2.089E+09
(b)	iFEM	6.466E-03	4.222E-02	1.924E+09
Differences between (a) and (b)		1.87%	1.64%	7.91%



(a)

(b)



(c)

(d)

**Figure 5.26** The plots for Case 2. The displacements in x-direction: (a) FEM, (b) iFEM. The displacements in y-direction: (c) FEM, (d) iFEM

### Case 3

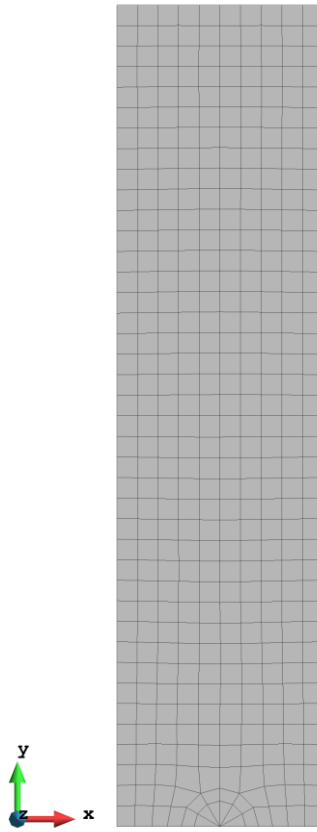


**Figure 5.27** The mesh for Case 3 (edge crack) and Case 4 (central crack)

Increasing the number of elements for the current analysis seems a useful tool to improve accuracy. Case 3 and Case 4 are the dense mesh condition for Case 1 and Case 2, respectively, and there will be 408 elements and 1321 nodes. (Fig. 5.27) And for the dense mesh cases, the reduced-sensor condition will also be considered to test the feasibility of the inverse crack tip element under limited strain inputs. For Cases 3 and 4, 64 sensors would be enough (Fig. 5.28).

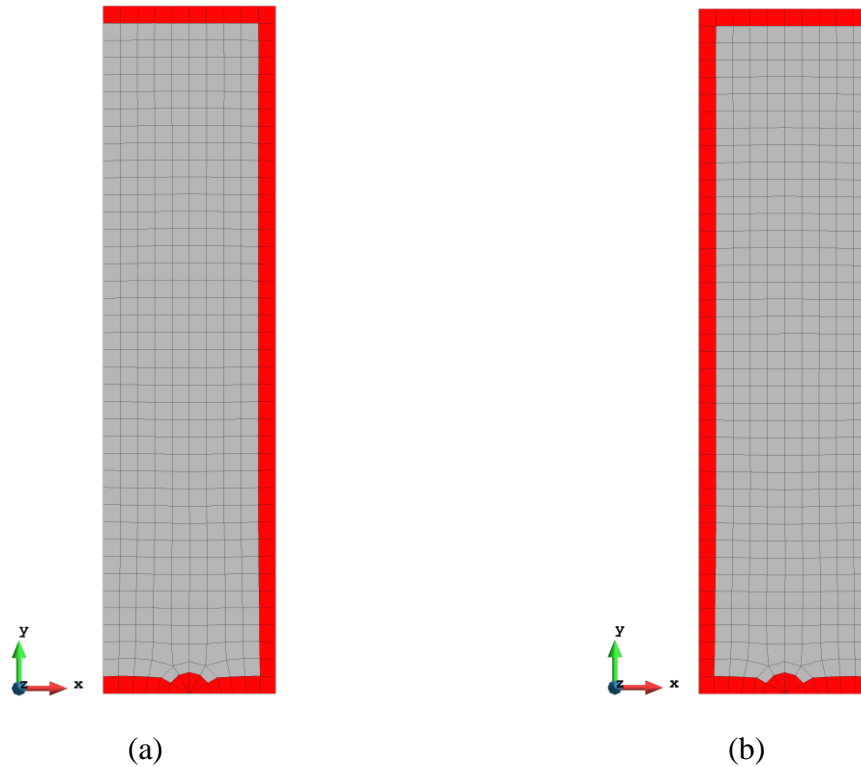


**Figure 5.28** The sensor locations for Case 3 (a) and Case 4 (b)

**Table 5.12** The results of Case 3

Case 3		$U$ (m)	$V$ (m)	SIF- $K_I$
(a)	FEM	5.056E-03	4.097E-02	2.077E+09
(b)	iFEM	4.596E-03	4.072E-02	2.001E+09
(c)	iFEM-r	4.775E-03	3.983E-02	2.012E+09
Differences between (a) and (b)		9.10%	0.61%	3.66%
Differences between (a) and (c)		5.56%	2.78%	3.12%

For Case 3, according to Table 5.12, it can be seen that both full-sensor and reduced-sensor conditions can give accurate displacements in the  $y$ -direction. But for  $U$ , the percentages of the difference raise especially for the full-sensor condition, which is 9.10%. On the one hand, compared with the major displacements ( $V$ ), the  $U$  is about 8 times smaller. On the other hand, the displacements in the  $x$ -direction will not have a big impact on the SIF calculation. Hence, about 10% is still acceptable. The SIF from the full-sensor condition is just 3.66% less than the reference value and for the analysis with 64 sensors, the value (3.12%) is even better than the full-sensor case. Concerning the plots of Case 3 (Fig. 5.29), the plots of the full-sensor condition are almost the same as the FEM plots. For the reduced-sensor condition, due to the

reduction of the sensors, some regions suffer a loss of accuracy, especially for the plots of  $U$ . But the main features like the locations of the large deformations can still be captured.

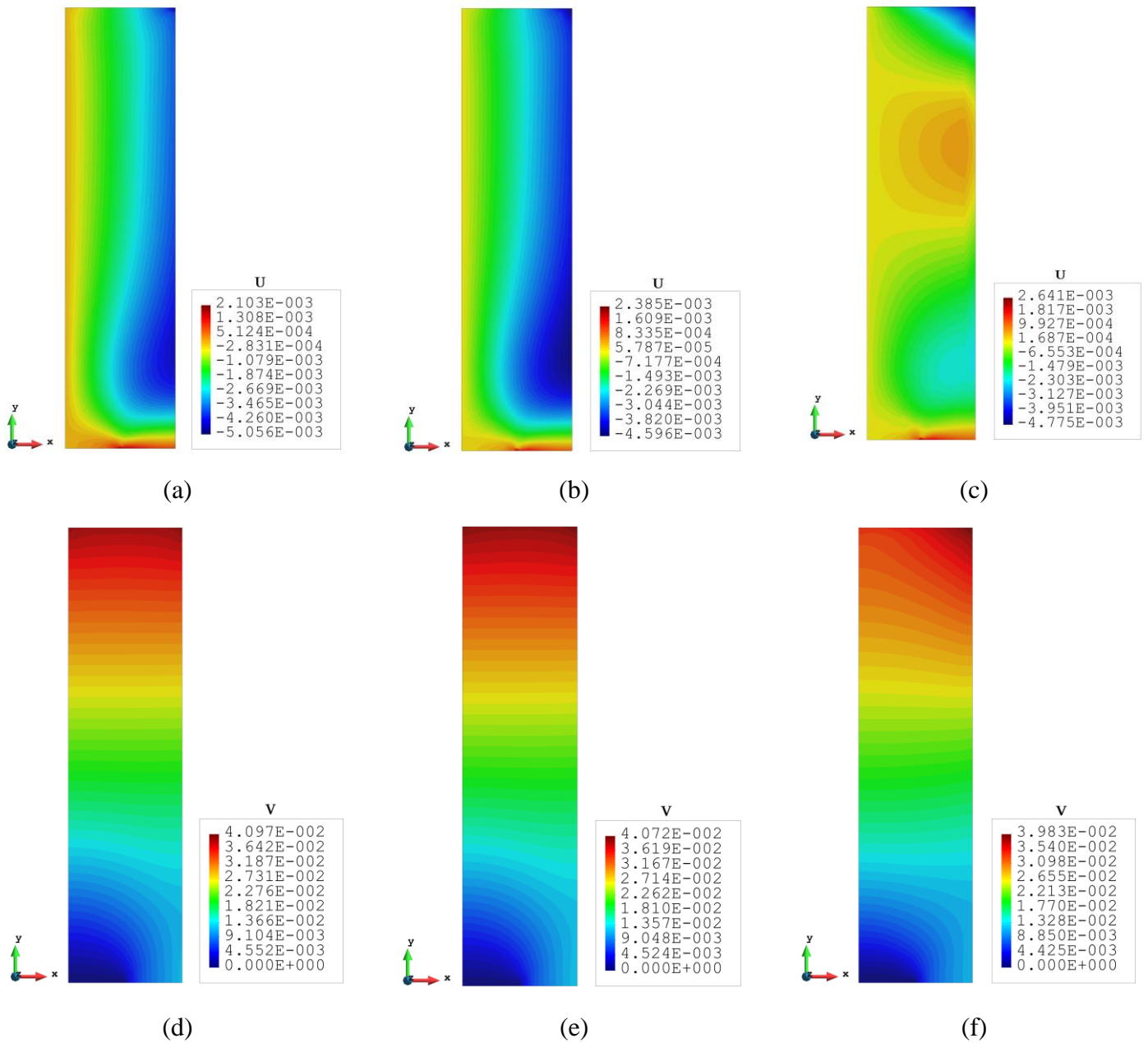


**Figure 5.29** The plots for Case 3. The displacements in x-direction: (a) FEM, (b) iFEM, (c) iFEM-r. The displacements in y-direction: (d) FEM, (e) iFEM, (f) iFEM-r

#### Case 4

When it comes to the central crack case, the performance of the full-sensor condition becomes much better. And all the values (Table 5.13) together with the plots (Fig. 5.30) are highly close to the FEM results. When the number of sensors is dropped to 64, although  $V$  is 5.63% less calculated, the other results especially the desired SIF are approximately the same as the FEM analysis. For the plots, they suffer similar problems to Case 3 and some regions do not have the quality as good as full-sensor plots. But considering the unimportance of these regions and also minimizing the requirement of the number of sensors, current sensor locations would be applicable and even with a limited number of sensors, not only the deformations but also the SIF can be captured.

**Table 5.13** The results of Case 4

Case 4		$U$ (m)	$V$ (m)	SIF- $K_I$
(a)	FEM	5.805E-03	4.067E-02	2.113E+09
(b)	iFEM	5.853E-03	4.041E-02	2.045E+09
(c)	iFEM-r	5.478E-03	4.005E-02	2.090E+09
Differences between (a) and (b)		0.83%	0.64%	3.25%
Differences between (a) and (c)		5.63%	1.52%	1.13%

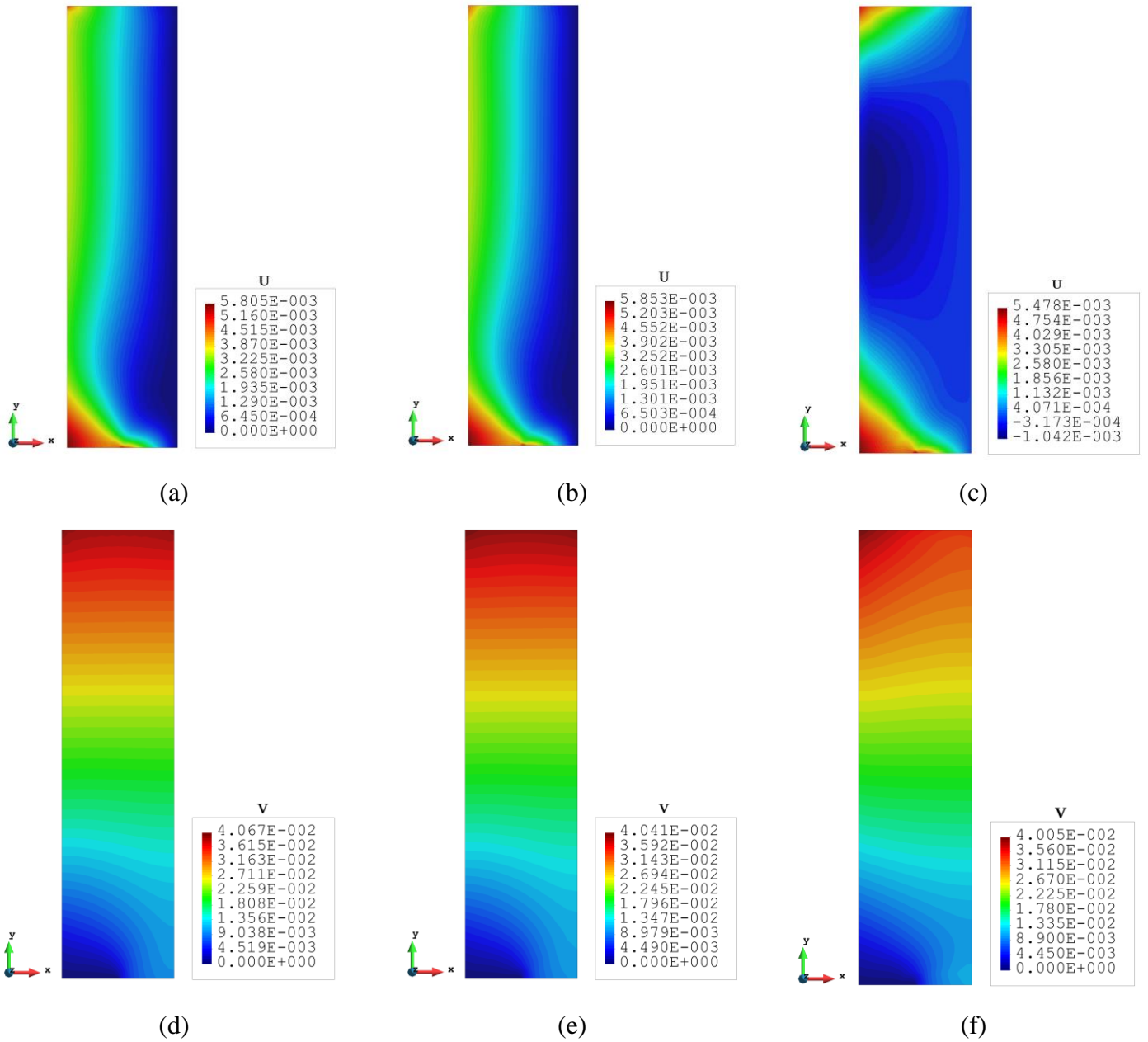


**Figure 5.30** The plots for Case 4. The displacements in x-direction: (a) FEM, (b) iFEM, (c) iFEM-r. The displacements in y-direction: (d) FEM, (e) iFEM, (f) iFEM-r

### Case 5

The previous 4 cases focus on the opening SIF, so the following two cases will give attention to the pure in-plane shear SIF condition (Case 5) ( $K_I$  still exists because of the Poisson's ratio, but it is quite small and can be neglected straightforwardly) and both  $K_I$  and  $K_{II}$  condition (Case 6).

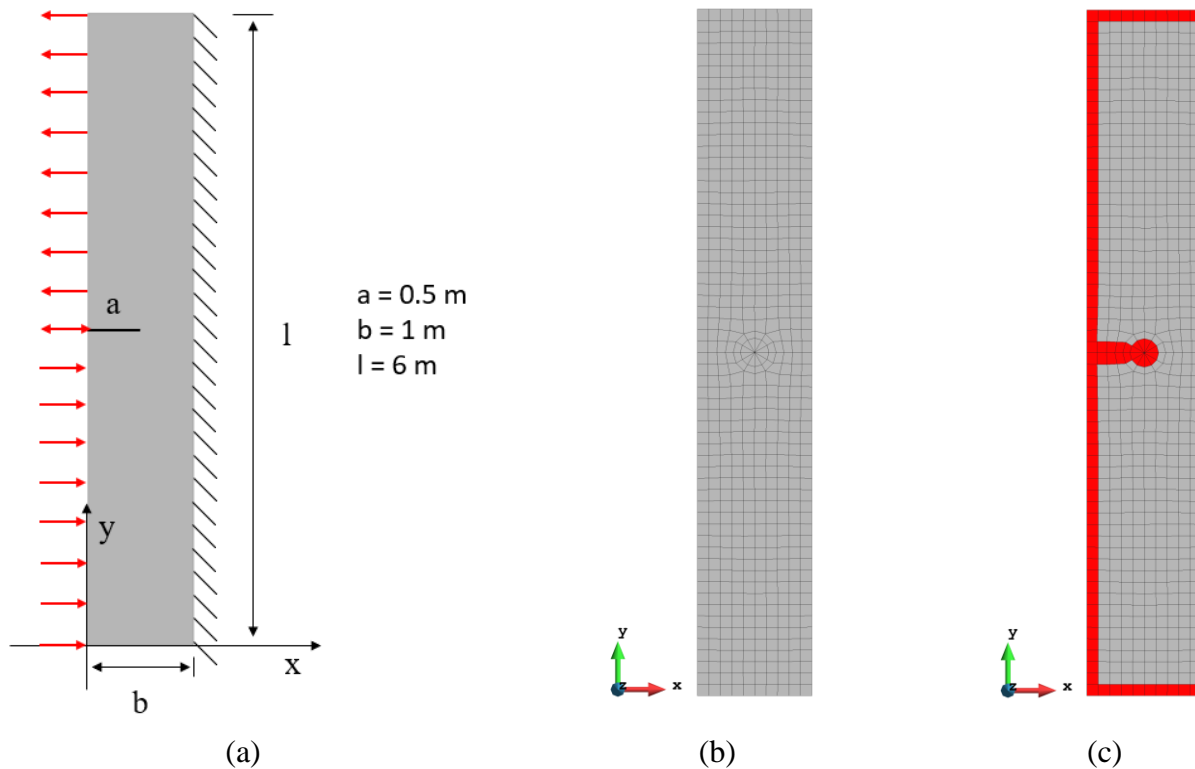


**Figure 5.31** (a) The geometry, loadings, and boundary conditions for Case 5. (b) The mesh of both FEM and iFEM analysis for Case 5. (c) The sensor locations for Case 5

The geometry of the plate is slightly updated (Fig. 5.31(a)) and the plane strain condition is changed to plane stress. Besides, because of changing the loadings (1000 kN for each node) and the boundary condition (fully constrained on the right edge), the symmetrical boundary condition can no longer be used. Therefore, the whole plate is modeled and meshed with 616 elements and 1989 nodes. Around the crack tip, there will be 12 finite/inverse crack tip elements. For the reduced-sensor condition, 98 elements are selected as the strain providers. And these sensors can be categorized into three groups: the boundary sensors, the crack tip sensors, and the connection sensors to join the previous two types together. It should be highlighted that for the crack tip, it is recommended that all 12 sensors should be chosen, otherwise, the accuracy of the SIF will be negatively influenced. For Case 5, the displacements in the x-direction become the major displacements and the in-plane shear SIF can be computed

by Eq. (5.15b). Table 5.14 shows the errors of the major displacements that are less than 5% for both sensor conditions.

**Table 5.14** The results of Case 5

Case 5		$U$ (m)	$V$ (m)	SIF- $K_{II}$
(a)	FEM	1.310E-04	6.126E-04	1.259E+07
(b)	iFEM	1.246E-04	5.576E-04	1.287E+07
(c)	iFEM-r	1.247E-04	5.512E-04	1.276E+07
Differences between (a) and (b)		4.89%	8.98%	2.15%
Differences between (a) and (c)		4.81%	10.02%	1.35%

Although the displacements in the y-direction are less-evaluated for Case 5, the values are still in the acceptable range. The in-plane shear SIFs are just a little higher than the reference value, which fulfils the aim of the analysis. The plots of Fig. 5.32 can be a kind of supplement for the above standpoints, and the main features and tendency of the deformation field are identical to the FEM plots, apart from some regions in the plots of the reduced-sensor condition are less accurate, for example, the region outside the crack tip elements is estimated with large y-displacement, which is not the same with FEM plot. It can be mentioned that, from the comparison between the plots of the full-sensor and reduced-sensor conditions, the problems that occur in the figures of the reduced-sensor case can be easily eliminated by increasing the number of sensors.

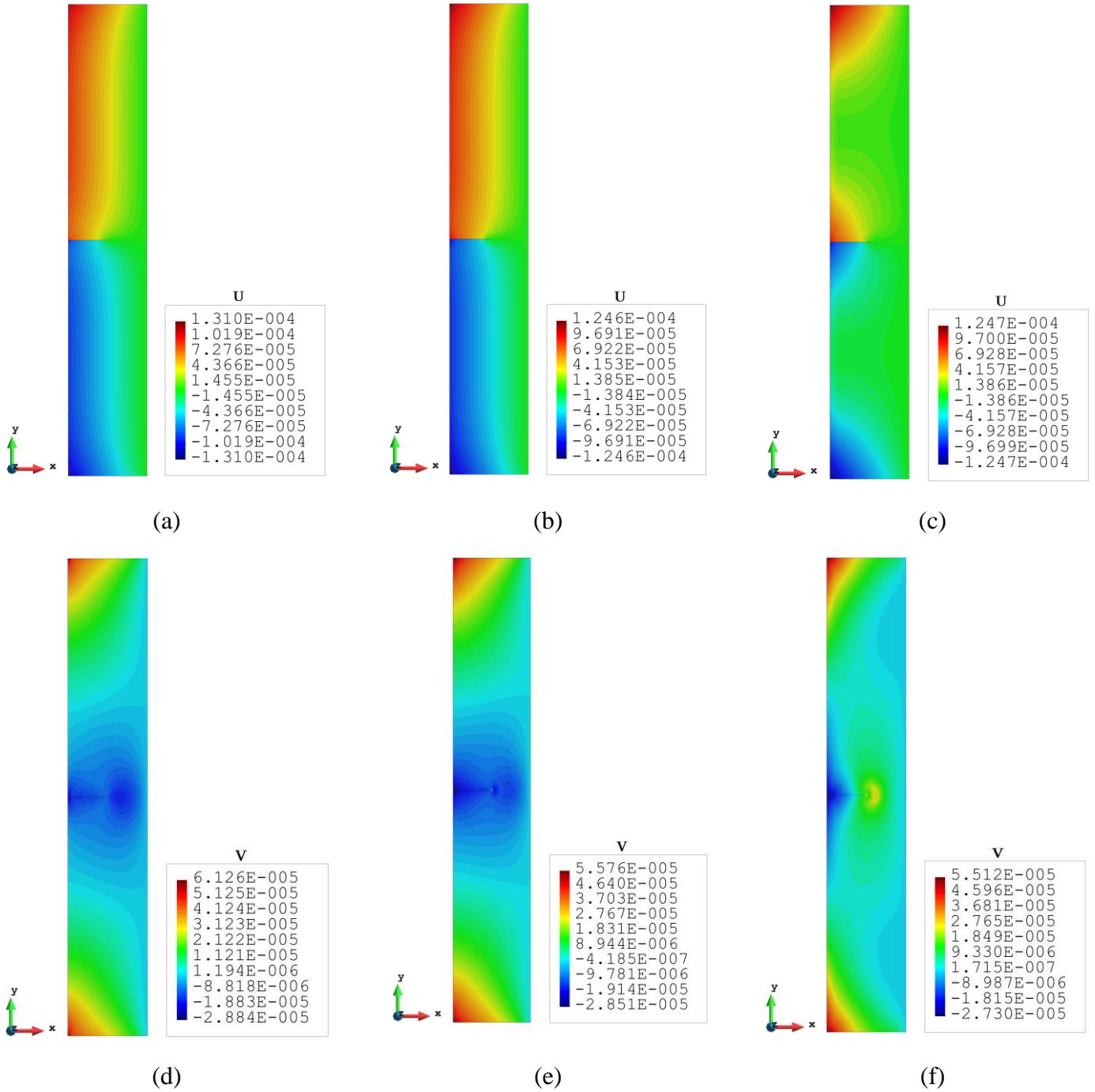


**Figure 5.32** The plots for Case 5. The displacements in x-direction: (a) FEM, (b) iFEM, (c) iFEM-r. The displacements in y-direction: (d) FEM, (e) iFEM, (f) iFEM-r

## Case 6

The last case is generated based on Case 5. The main change is replacing the distributed forces on the edge with two nodal forces in both positive axes and the forces will have the same values. Besides, the fully constrained boundary condition has been moved to the bottom of the plate. Thanks to the relatively more complex loadings and boundary conditions, the number of sensors increases to 156 by adding the boundary sensors along the right edge.

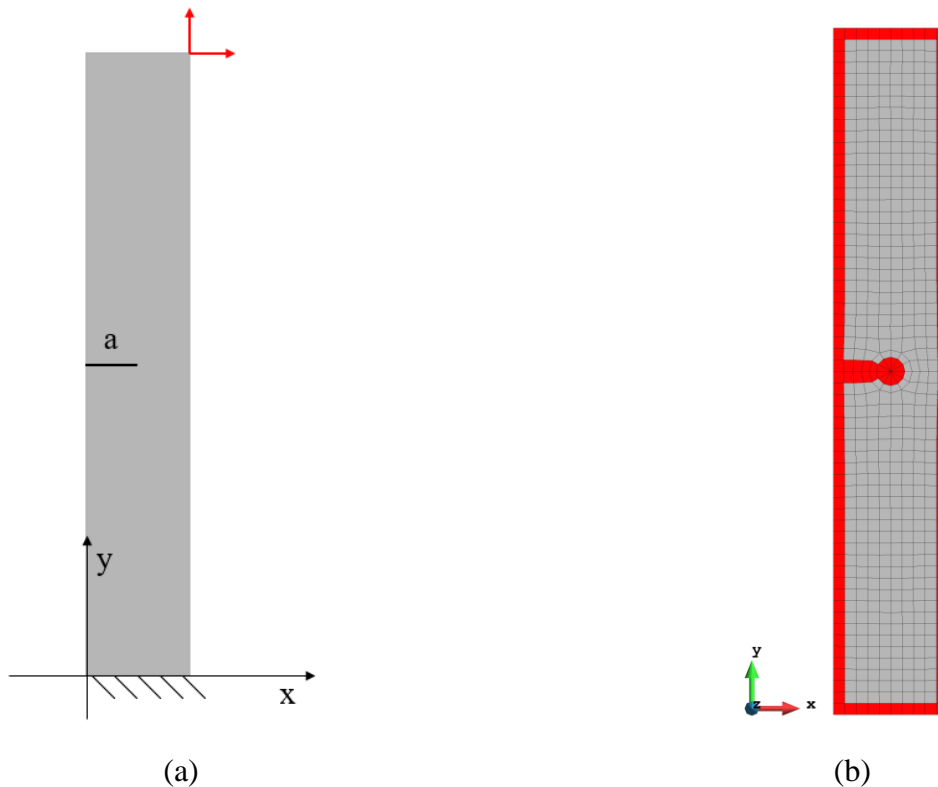


**Figure 5.33** (a) The geometry, loadings, and boundary conditions for Case 6. (b) The sensor locations for Case 6

**Table 5.15** The results of Case 6

Case 6		$U$ (m)	$V$ (m)	SIF- $K_I$	SIF- $K_{II}$
(a)	FEM	5.357E-03	8.839E-04	3.181E+07	1.691E+06
(b)	iFEM	5.501E-03	9.342E-04	3.428E+07	1.600E+06
(c)	iFEM-r	5.159E-03	8.612E-04	3.045E+07	1.512E+06
Differences between (a) and (b)		2.68%	5.69%	7.76%	5.40%
Differences between (a) and (c)		3.70%	2.57%	4.29%	10.61%

The results of Case 6 are listed in Table 5.15. Even though the extreme  $V$  is about 5.69% higher than the reference one, the errors of the displacements are held to a reasonable extent. For the SIF, since the in-plane shear SIF is relatively smaller than the opening SIF, it is

predictable that there is a chance that the error of  $K_{II}$  may be higher than the error of  $K_I$ . For the full-sensor condition, the gap between the two errors is not far away from each other. For the in-plane shear SIF, the value is 5.40% which is even better than the opening SIF (7.76%) and it is better than the expectation. But for the 156 sensors case, the above prediction happens, and the percentage of the opening SIF is over twice smaller as the percentage of in-plane shear SIF. But 10.61% is still within the accurate horizon. And note that  $K_I$  is about 20 times larger than  $K_{II}$ . The figures of iFEM analysis for both with full sensors and 156 sensors are not distinguishable against the FEM reference, which also supports the above descriptions. Case 5 and Case 6 present that for different types of SIF, the inverse crack tip element can estimate the SIF value with high accuracy.

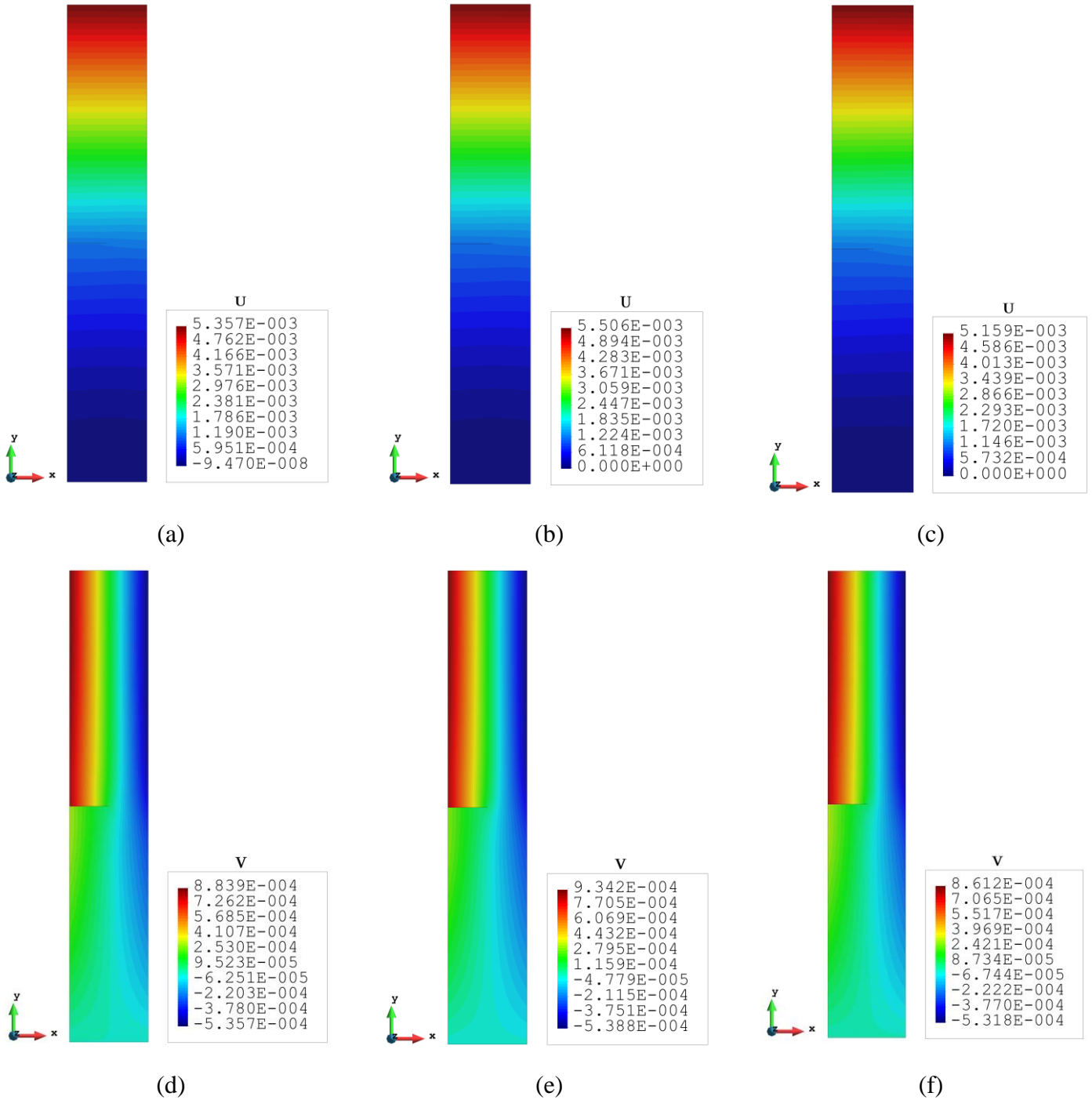


**Figure 5.34** The plots for Case 6. The displacements in x-direction: (a) FEM, (b) iFEM, (c) iFEM-r. The displacements in y-direction: (d) FEM, (e) iFEM, (f) iFEM-r

## 5.4 Summary

In conclusion, iQP4 and iQP8 elements can be utilized for the inverse analysis of plane problems, and inverse plane elements require fewer sensors than shell elements. With the increase of the mesh, the accuracy of the analysis will be significantly improved. But the accuracy of the results has no obvious relationship with the element type. Different loadings

and boundary conditions and different types of inverse elements will lead to a different distribution of the sensors. The advantage of the iQP8 element is it can be applied together with the iPCT element and build the fundamental model outside the crack tip region. The full sensor condition can always provide high accurate estimation and reducing sensors will negatively affect the correctness of the results. By logically selecting the sensor locations, reasonable results can still be guaranteed. There should be a balance between the sensor numbers and the accuracy of the results.

From what has been discussed in Section 5.3.2, it can be concluded that the newly developed inverse crack tip element can increase the ability of the inverse plane element by not only reforming the deformation field which would eliminate the limitation of iFEM when dealing with structure with cracks but also monitoring the SIF around the crack tip. If the strains for the inverse crack tip element are all available, even if the sensors of the other regions are reduced, the SIF together with the displacements can still be guaranteed. For future research, the inverse shell crack tip is highly suggested, which will make the out-of-plane shear SIF be estimated. Last but not least, for the current study, the inverse triangular plane element is also preferred because usually, the triangular element is inevitable during the model generation process. With the help of the triangular element, the iPCT element can be utilized for more complex problems.

# 6 Fatigue analysis of the triplate of the offshore wind turbine mooring line using Peridynamics

## 6.1 Introduction

In the initial section of Chapter 6, basic Peridynamic theory will be introduced. Then the effort will be given to explain the PD fatigue model and the three phases of PD fatigue failure: crack initiation (phase I), crack growth (phase II), and final failure controlled by quasi-static crack growth (phase III) will be illustrated in detail. Then the accuracy of the PD fatigue model will be verified by a referenced benchmark problem in Section 6.5.1. Afterward, the fatigue analysis for the given triplate under the constant amplitude loading condition with different mooring line angles will be presented step by step and the effect of the mooring line angles will be explored. This chapter will be finalized with a summary in Section 6.6.

## 6.2 Fundamental Peridynamics theory

Peridynamics is a reformulation of the CCM equations (Silling, 2000). As opposed to CCM, the motion of a material point is expressed in PD by using the integro-differential equation as

$$\rho(\mathbf{x})\ddot{\mathbf{u}}(\mathbf{x},t) = \int_{H_x} \mathbf{f}(\mathbf{u}' - \mathbf{u}, \mathbf{x}' - \mathbf{x}, t) dV' + \mathbf{b}(\mathbf{x}, t) \quad (6.1)$$

where  $\rho(\mathbf{x})$  is the density of the material point,  $\ddot{\mathbf{u}}(\mathbf{x}, t)$  is the acceleration of the material point at the time  $t$ ;  $dV_{x'}$  is the volume of the materials points within the horizon;  $\mathbf{b}(\mathbf{x}, t)$  is the body load externally exerted on the material point at  $\mathbf{x}$ .

The integro-differential equation given in Eq. (6.1) can be represented in a discrete form as

$$\rho_{(k)}\ddot{\mathbf{u}}_{(k)} = \sum_{j=1}^{N_k} \mathbf{f}_{(k)(j)}(\mathbf{u}_{(j)} - \mathbf{u}_{(k)}, \mathbf{x}_{(j)} - \mathbf{x}_{(k)}, t) V_{(j)} + \mathbf{b}_{(k)} \quad (6.2)$$

where  $\rho$  represents the mass density,  $\mathbf{x}$  represents the vector of coordinates,  $\ddot{\mathbf{u}}$  and  $\mathbf{u}$  represent acceleration and displacement vectors, respectively. In PD, the external loads are applied to the model by using the vector of body forces,  $\mathbf{b}$ .  $\mathbf{f}$  is the bond (interaction) force between material points  $\mathbf{x}_i$  and  $\mathbf{x}_j$ , and it can be calculated as:

$$\mathbf{f} = c s \frac{\mathbf{y}_j - \mathbf{y}_i}{|\mathbf{y}_j - \mathbf{y}_i|} \quad (6.3)$$

where  $c$  is the bond constant between two material points.  $\mathbf{y} = \mathbf{x} + \mathbf{u}$  is the position of the material point in the deformed configuration where  $\mathbf{u}$  is the displacement and  $\mathbf{x}$  is the position of the material point in the original configuration.

As shown in Eqs. (6.1) and (6.2), the motion of a material point in PD is influenced by collective deformations of surrounding material points within a domain  $H_x$  (shown in Fig. 6.1), which is called the horizon. The horizon of a material point is defined as the circle with a radius  $\delta$  surrounding that material point. Here,  $\delta$  is called the horizon size and usually the value is taken as  $\delta = 3 \times dx$  where  $dx$  is the grid size (Madenci and Oterkus, 2014). Material points within the horizon of a material point are called family members of that material point.

In Eq. (6.2),  $N_k$  represents the number of family members of the material point  $k$  and  $j$  represents the family member of the material point  $k$ . The term  $V_{(j)}$  is the volume of the material point  $j$ . The term  $\mathbf{f}_{(k)(j)}$  denotes the force density that the material point  $j$  exerts on the material point  $k$ .

The linear BBPD equations of motion (EOM) can be represented as

$$\rho \ddot{u}_{(k)} = \sum_{j=1}^{N_k} \psi_{(k)(j)} c s_{(k)(j)} \cos \varphi V_{(j)} + b_{x(k)} \quad (6.4a)$$

$$\rho \ddot{v}_{(k)} = \sum_{j=1}^{N_k} \psi_{(k)(j)} c s_{(k)(j)} \sin \varphi V_{(j)} + b_{y(k)} \quad (6.4b)$$

with

$$s_{(k)(j)} = \frac{(u_{(j)} - u_{(k)}) \cos \varphi + (v_{(j)} - v_{(k)}) \sin \varphi}{\xi} \quad (6.4c)$$

$$\cos \varphi = \frac{x_{(j)} - x_{(k)}}{\xi} \quad (6.4d)$$

$$\sin \varphi = \frac{y_{(j)} - y_{(k)}}{\xi} \quad (6.4e)$$

$$\xi = \sqrt{(x_{(j)} - x_{(k)})^2 + (y_{(j)} - y_{(k)})^2} \quad (6.4f)$$

The terms  $b_{x(k)}$  and  $b_{y(k)}$  represent external forces per unit volume. In Eq. (6.4c),  $s_{(k)(j)}$  represents the bond stretch between material points  $k$  and  $j$ . The parameter  $\xi$  in Eq. (6.4f) represents the distance between material points  $k$  and  $j$  in the undeformed configuration. The

parameter  $\varphi$  represents the angle between the line of interaction (between material points  $k$  and  $j$  in the undeformed configuration) and the  $x$  axis.

In Eqs. (6.4a) and (6.4b), the term  $c$  represents the BBPD bond constant. For 2-D isotropic materials, the bond constant can be written as (Madenci and Oterkus, 2014):

$$c = \frac{12k}{\pi h \delta^3} \quad (6.5a)$$

or

$$c = \frac{9E}{\pi h \delta^3} \quad (6.5b)$$

where  $E$  is the elastic modulus and  $h$  is the thickness. In Eq. (6.5a),  $k$  is the bulk modulus, i.e.  $k = E/2(1-\nu)$ , and  $h$  is the thickness of the plate.  $\delta$  is the radius of the horizon, usually taken as  $\delta = 3 \times dx$  where  $dx$  is the grid size (Madenci and Oterkus, 2014).  $E$  and  $\nu$  are material constants corresponding to elastic modulus and Poisson's ratio, respectively. It should be noted that  $\nu$  is constrained as  $1/3$  for 2-D problems due to the limitation of BBPD.

One of the most important parameters of BBPD is the stretch and it can be defined as:

$$s_{ij} = \frac{|\mathbf{y}_j - \mathbf{y}_i| - |\mathbf{x}_j - \mathbf{x}_i|}{|\mathbf{x}_j - \mathbf{x}_i|} \quad (6.6)$$

For the static case, the inertia terms on the left-hand sides Eqs. (6.4a) and (6.4b) vanishes. Therefore, Eqs. (6.4a) and (6.4b) can be rewritten as

$$-\sum_{j=1}^{N_k} \psi_{(k)(j)} c s_{(k)(j)} \cos \varphi V_{(j)} = b_{x(k)} \quad (6.7a)$$

$$-\sum_{j=1}^{N_k} \psi_{(k)(j)} c s_{(k)(j)} \sin \varphi V_{(j)} = b_{y(k)} \quad (6.7b)$$

In Eqs. (6.4) and (6.7), the term  $\psi_{(k)(j)}$  is the damage parameter that is used to represent the state of interaction, intact or broken. This parameter can be defined as

$$\psi_{(k)(j)}(\mathbf{x}_{(j)} - \mathbf{x}_{(k)}, t) = \begin{cases} 1 & \text{if interaction exists,} \\ 0 & \text{if no interaction.} \end{cases} \quad (6.8)$$

The state of interaction can be determined by using the critical stretch criterion. The damage criterion based on the critical stretch can be described as

$$\begin{aligned} s_{(k)(j)} < s_c &\rightarrow \text{interaction exists: } \psi_{(k)(j)} = 1 \\ s_{(k)(j)} \geq s_c &\rightarrow \text{interaction is broken: } \psi_{(k)(j)} = 0 \end{aligned} \quad (6.9)$$

where  $s_c$  represents the critical stretch. The critical stretch can be calculated under the plane-stress assumption as

$$s_c = \sqrt{\frac{4\pi G_c}{9E\delta}} \quad (6.10)$$

where  $G_c$  represents the critical energy release rate of the material.

The local damages on the structure can be represented by the damage index,  $\phi$ . This parameter is the ratio of broken interactions to the total number of interactions within the horizon of a material point, which can be represented as

$$\phi(\mathbf{x}_{(k)}, t) = 1 - \frac{\sum_{j=1}^{N_k} \psi_{(k)(j)}(\mathbf{x}_{(j)} - \mathbf{x}_{(k)}, t) V_{(j)}}{\sum_{j=1}^N V_{(j)}} \quad (6.11)$$

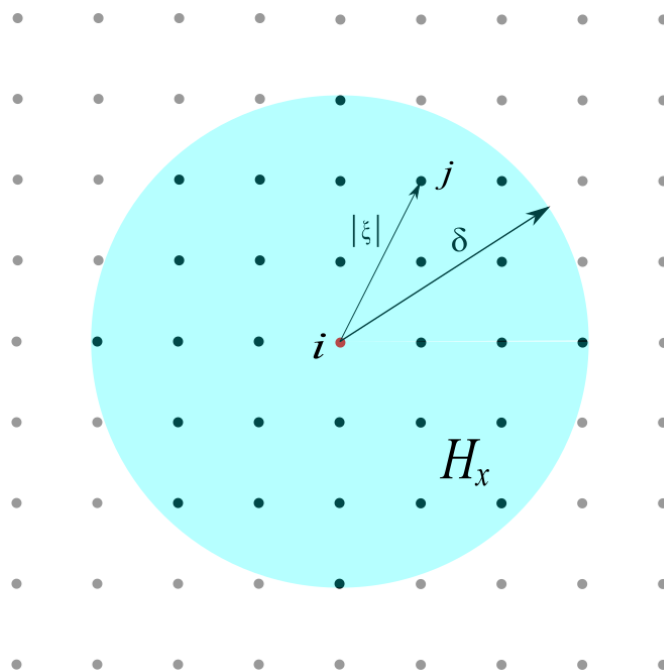


**Figure 6.1** PD horizon and interactions between material points

## 6.3 Peridynamic fatigue model

### 6.3.1 Basic definitions for the fatigue model

According to the PD fatigue model, a bond can be defined in either the crack nucleation phase (phase I) or the crack growth phase (phase II). Rapid crack growth (Phase III) can also be incorporated with the PD fatigue model when some interactions in the PD model have stretches

exceeding the critical value. The fatigue life of each bond is represented by its remaining life,  $\lambda(\mathbf{x}, \xi, N)$  which is defined as

$$\lambda_{(k)(j)}^{(N=0)} = 1, \quad \frac{d\lambda_{(k)(j)}^{(N)}}{dN} = -A_1 \left( \varepsilon_{(k)(j)}^{(N)} \right)^{m_1} \quad \text{with } A_1 > 0, m_1 > 0 \text{ for phase (I)} \quad (6.12a)$$

$$\lambda_{(k)(j)}^{(N=0)} = 1, \quad \frac{d\lambda_{(k)(j)}^{(N)}}{dN} = -A_2 \left( \varepsilon_{(k)(j)}^{(N)} \right)^{m_2} \quad \text{with } A_2 > 0, m_2 > 0 \text{ for phase (II)} \quad (6.12b)$$

where  $(A_1, m_1)$  and  $(A_2, m_2)$  represent the positive fatigue parameters for phase (I) and phase (II), respectively. The parameter  $\lambda_{(k)(j)}^{(N)}$  represents the remaining life of the interaction between material points  $k$  and  $j$  at  $N^{\text{th}}$  cycle of loading. The parameter  $\varepsilon_{(k)(j)}^{(N)}$  represents the cyclic bond strain range between material points  $k$  and  $j$  at  $N^{\text{th}}$  cycle of loading which can be defined as

$$\varepsilon_{(k)(j)}^{(N)} = \left| s_{(k)(j)}^+ - s_{(k)(j)}^- \right| = \left| s_{(k)(j)}^+ (1 - R) \right| \quad (6.13)$$

where  $s_{(k)(j)}^+$  represents bond stretch corresponding to the maximum load  $P_{\max}$ ,  $s_{(k)(j)}^-$  represents bond stretch corresponding to the minimum load  $P_{\min}$ . The term  $R$  represents the load ratio that can be defined as

$$R = P_{\min} / P_{\max} \approx s_{(k)(j)}^- / s_{(k)(j)}^+ \quad (6.14)$$

If the fatigue limit is considered, Eq. (6.12a) can be rewritten for phase (I) as

$$\lambda_{(k)(j)}^{(N=0)} = 1, \quad \frac{d\lambda_{(k)(j)}^{(N)}}{dN} = \begin{cases} -A_1 \left( \varepsilon_{(k)(j)}^{(N)} - \varepsilon_{\infty} \right)^{m_1}, & \text{if } \varepsilon_{(k)(j)}^{(N)} > \varepsilon_{\infty} \\ 0 & \text{otherwise} \end{cases} \quad (6.15)$$

where  $\varepsilon_{\infty} \geq 0$  represents the fatigue limit which is the lowest cyclic bond strain range that still results in fatigue damage. The fatigue limit,  $\varepsilon_{\infty}$  can be determined from the experiments. Note that  $\varepsilon_{\infty}$  can be set equal to zero if the fatigue limit is not considered.

By using the relations given in Eq. (6.15), the remaining life of a bond in phase (I) can be calculated as

$$\lambda_{(k)(j)}^{(N=0)} = 1, \quad \lambda_{(k)(j)}^{(N)} = \begin{cases} \lambda_{(k)(j)}^{(N-1)} - A_1 \left( \varepsilon_{(k)(j)}^{(N)} - \varepsilon_{\infty} \right)^{m_1}, & \text{if } \varepsilon_{(k)(j)}^{(N)} > \varepsilon_{\infty} \\ \lambda_{(k)(j)}^{(N-1)} & \text{otherwise} \end{cases} \quad (6.16)$$

By using the relations given in Eq. (6.12b), the remaining life of a bond in phase (II) can be calculated as

$$\lambda_{(k)(j)}^{(N=0)} = 1, \quad \lambda_{(k)(j)}^{(N)} = \lambda_{(k)(j)}^{(N-1)} - A_2 \left( \varepsilon_{(k)(j)}^{(N)} \right)^{m_2} \quad (6.17)$$

Beyond the crack growth phase (phase II), the structures can experience rapid crack growth (phase III). In this case, the traditional PD model for damage prediction can be used. Therefore, the interaction state of a bond can be defined as

$$\begin{cases} \lambda_{(k)(j)}^{(N)} \leq 0 & \text{or} & s_{(k)(j)} \geq s_c & \rightarrow & \psi_{(k)(j)} = 0 \\ \lambda_{(k)(j)}^{(N)} > 0 & \text{and} & s_{(k)(j)} < s_c & \rightarrow & \psi_{(k)(j)} = 1 \end{cases} \quad (6.18)$$

### 6.3.2 Fatigue parameters for phase (I)

Assuming that  $\xi_1$  is the bond that has the largest cyclic bond strain in the structure, crack nucleation occurs when

$$N_1 = \frac{1}{A_1 \varepsilon_1^{m_1}} \quad (6.19)$$

where  $\varepsilon_1$  represents the largest cyclic bond strain in the PD model.

If the fatigue limit,  $\varepsilon_\infty$  is considered, Eq. (6.19) can be rewritten as

$$N_1 = \frac{1}{A_1 (\varepsilon_1 - \varepsilon_\infty)^{m_1}} \quad (6.20)$$

The relations in Eqs. (6.19) and (6.20) can be rewritten as

$$\log(\varepsilon_1) = -\frac{1}{m_1} \log(N_1) - \frac{\log(A_1)}{m_1} \quad (6.21a)$$

and

$$\log(\varepsilon_1 - \varepsilon_\infty) = -\frac{1}{m_1} \log(N_1) - \frac{\log(A_1)}{m_1} \quad (6.21b)$$

By using the relations in Eq. (6.21), the parameters  $A_1$  and  $m_1$  can be obtained from  $\varepsilon - N$  test data for material as shown in Figure 6..

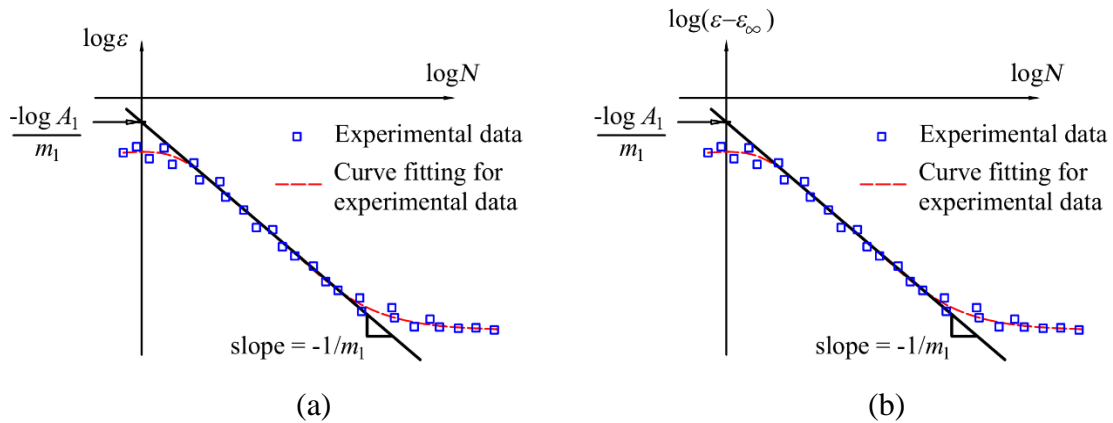


**Figure 6.2** Calibration phase (I) parameters  $A_1$  and  $m_1$  (a) without fatigue limit, (b) with fatigue limit

As shown in Fig. 6.2, the experimental results for  $\log \varepsilon$  versus  $\log N$  or  $\log(\varepsilon - \varepsilon_\infty)$  versus  $\log N$  are often represented with scatter data, shown in blue. Based on these scatter data, the fitted curves, shown in red, can be obtained. The slopes of the fitted curves are equal to  $-1/m_1$ . Meanwhile, the intersections of the slopes with the  $\log \varepsilon$  or  $\log(\varepsilon - \varepsilon_\infty)$  axis (the vertical axis) are equal to  $-\log(A_1)/m_1$ . Therefore, the fatigue parameters,  $(A_1, m_1)$ , for phase (I) can be obtained from the fitted curve.

### 6.3.3 Fatigue parameters for phase (II)

In phase (II), the fatigue crack growth follows the well-known Paris law that can be represented as

$$\frac{dq}{dN} = C \Delta K^M \quad (6.22)$$

where  $q$  represents the crack length,  $N$  represents the number of load cycles,  $\Delta K$  represents the stress intensity factor range but it will be eliminated during the trial simulation so its value will not have any impact on the calculation process.  $C$  and  $M$  are material constants for the Paris equation using the stress intensity factor.

The parameter  $m_2$  in Eq. (6.17) can be obtained directly from the material constant  $M$  as

$$m_2 = M \quad (6.23)$$

Meanwhile, the parameter  $A_2$  in Eq. (6.17) needs to be calibrated by conducting a trial PD fatigue simulation described as follows;

Step 1: Assume an arbitrary value for  $A_2$  as:  $A_2 = A_{2(\text{trial})}$

Step 2: Conduct a PD fatigue simulation with the trial value  $A_2 = A_{2(\text{trial})}$  and calculate the crack growth rate and stress intensity (SIF) range for this trial case:  $(dq/dN)_{(\text{trial})}$  and  $\Delta K_{(\text{trial})}$ .

Step 3: Plot the scatter data of  $(\Delta K - dq/dN)_{(\text{trial})}$  in the logarithmic scale and find the best-fit equation:  $(dq/dN)_{(\text{trial})} = C_{(\text{trial})} \Delta K^M$

Step 4: Calibrate the value for  $A_2$  as

$$A_2 = A_{2(\text{trial})} \frac{(dq/dN)_{(\text{experiment})}}{(dq/dN)_{(\text{trial})}} \quad (6.24a)$$

or

$$A_2 = A_{2(\text{trial})} \frac{C_{(\text{experiment})} \Delta K^M}{C_{(\text{trial})} \Delta K^M} = A_{2(\text{trial})} \frac{C_{(\text{experiment})}}{C_{(\text{trial})}} \quad (6.24b)$$

where

$$(dq/dN)_{(\text{experiment})} = C_{(\text{experiment})} \Delta K^M \quad (6.24c)$$

Here Eq. (6.24c) is the Paris law equation obtained from the experimental data.

Note that  $m_1$ ,  $A_1$  and  $m_2$  are material constants that are independent of the horizon size. However, the parameter  $A_2$  is dependent on the horizon size. The relationship between the parameter  $A_2$  and the horizon size  $\delta$  can be presented as

$$A_2(\delta) = \hat{A}_2 \delta^{(m_2-2)/2} \quad (6.25)$$

where  $\hat{A}_2$  is a constant and it is independent of  $\delta$ .

Therefore, the value of the parameter  $A_2$  can be scaled due to the change of horizon size as follows:

Assuming that  $A_2^{(1)}$  is the calibrated value for the parameter  $A_2$  obtained from a trial PD simulation by using the horizon size of  $\delta^{(1)}$ , for example  $\delta^{(1)} = 3\Delta x_1$  in which  $\Delta x_1$  represents the mesh size used in the trial PD simulation.

By substituting  $A_2^{(1)}$  and  $\delta^{(1)}$  into Eq. (6.25), the value for the parameter  $\hat{A}_2$  can be calculated as

$$\hat{A}_2 = \frac{A_2^{(1)}}{(\delta^{(1)})^{(m_2-2)/2}} \quad (6.26)$$

Now, assuming that a PD fatigue simulation with a different mesh size  $\Delta x_2 \neq \Delta x_1$  and a horizon size of  $\delta^{(2)} = 3\Delta x_2$  is needed. Therefore, by substituting Eq. (6.26) into Eq. (6.25) and by putting  $\delta = \delta^{(2)}$ , a new value of the parameter  $A_2$  for the PD fatigue simulation with a mesh size of  $\Delta x_2 \neq \Delta x_1$  and a horizon size of  $\delta^{(2)} = 3\Delta x_2$  can be obtained as

$$A_2^{(2)} = \hat{A}_2 (\delta^{(2)})^{(m_2-2)/2} = \frac{A_2^{(1)}}{(\delta^{(1)})^{(m_2-2)/2}} (\delta^{(2)})^{(m_2-2)/2} \quad (6.27)$$

### 6.3.4 Phase transition

The PD bond strains in the nucleation phase can agree with the measured strain data. However, in the growth phase, the actual process zone at a crack tip is usually smaller than the PD continuum-level model. Therefore, bond strains in phase (II) could be fictitious. As a result,

the transition from phase (I) to phase (II) might not be smooth because the bond strain can suddenly become fictitious.

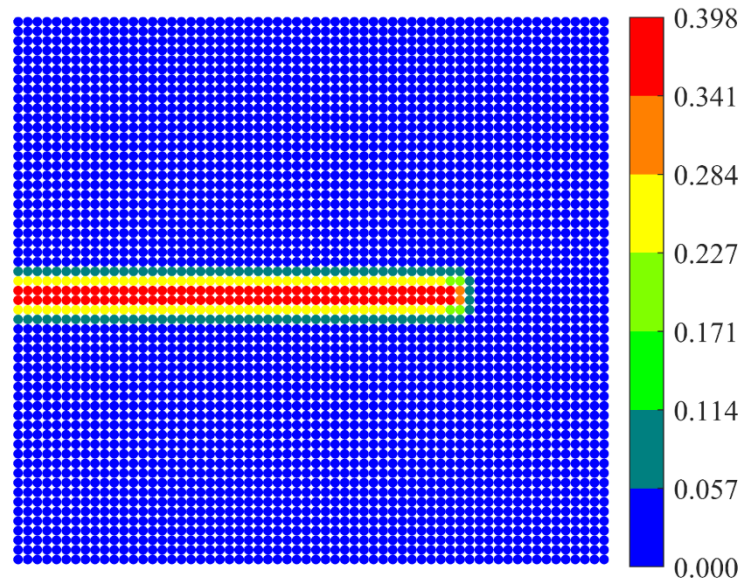


**Figure 6.3** Variation of damage index,  $\phi$ , on in plate with a pre-existing crack

In order to avoid the above phenomenon for phase transition, a method based on the information of the damage index  $\phi$  at each material point and its family members can be utilized. Specifically, the phase (I) fatigue equation given in Eq. (6.14) for a given material point  $k$  is valid, if all material points within its horizon (including itself) have the damage index  $\phi < \phi_0$ . By contrast, the phase (II) fatigue equation given in Eq. (6.15) is valid when the material point  $k$  or at least one of its family members has  $\phi \geq \phi_0$ . As shown in Fig 6.3 for an example of a plate with a crack, material points located along the crack have the damage index of  $\phi = 0.398$  for the horizon size of  $\delta = 3\Delta x$ . It means that the plate can be completely split when the damage indexes of material points reach the value of  $\phi \geq 0.398$ . The value  $\phi_0 = 0.398$  is used to decide the phase transition for each bond in two-dimensional models.

If some interactions have stretches exceeding the critical value,  $s_{(k)(j)} \geq s_c$ , the fatigue simulation is stopped and the conventional PD model for damage prediction (phase III) can be used. It should be highlighted that the fatigue analysis is considered as quasi-static, and the results are directly calculated by specifying inertia term as zero.

## 6.4 Numerical procedure of the fatigue analysis

In the PD model, the domain is uniformly discretized with material points associated with specific volumes. The behavior of the structure subjected to the statically extreme loading  $P = P_{\max}$  is obtained by solving the PD equations of motion given in Eq. (6.4). In the PD fatigue model, the remaining life of each interaction is updated by using Eq. (6.16) for phase (I) and Eq. (6.17) for phase (II). The state of interactions can be updated by using Eq. (6.18). The phase information for each interaction is updated after each load cycle to decide whether the phase (I) or phase (II) fatigue equation is valid for each interaction. Similarly, the interaction states for all bonds in the PD model are also updated after each load cycle. For the fatigue prediction, stretches and strain ranges of all interactions in the PD model are calculated at each load cycle.

## 6.5 Numerical results for the fatigue analysis of the triplate

### 6.5.1 Accuracy verification

To test the accuracy of the PD fatigue model, a benchmark problem is considered. Experimental results are available for justification of the accuracy of the model. The plate has a length and width of 75 mm and 72 mm, respectively. The thickness of the plate is 22 mm. A pre-existing crack is initially created at the horizontal central line of the plate with a length of 12 mm. Besides, two holes are located in the regions above and below the crack (see Fig. 6.4).

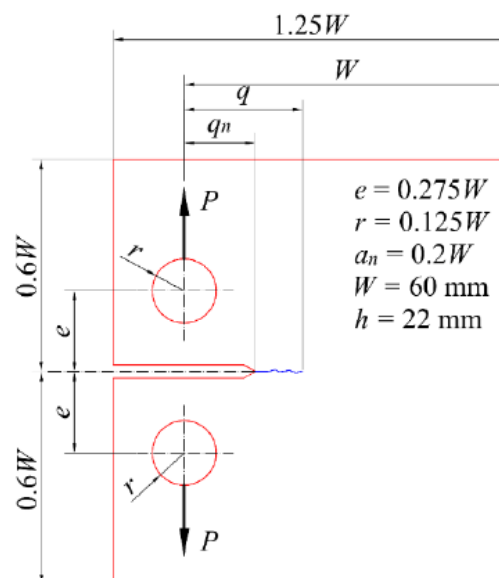


**Figure 6.4** The geometry of the plate (Sajith et al., 2020)

The plate is made from aluminum 6061-T6 and the material properties are listed in Table 6.1.

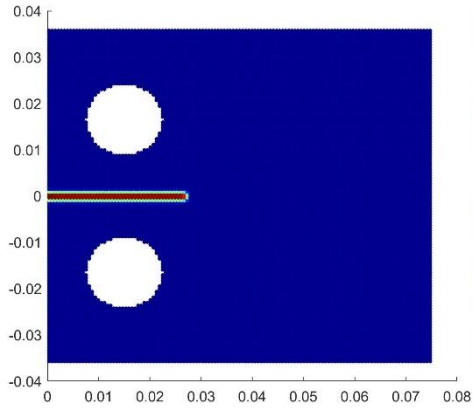
**Table 6.1** The basic material properties of aluminum 6061-T6 (Nguyen et al., 2021)

Material property	Value	Units
Elastic modulus (E)	$68 \times 10^9$	$N / m^2$
Poisson's ratio ( $\nu$ )	0.33	
Density ( $\rho$ )	2700	$Kg / m^3$
Fracture toughness ( $K_{IC}$ )	48.7	$MPa\sqrt{m}$

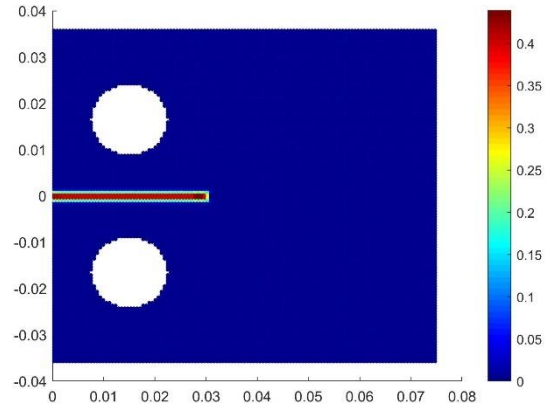
The fatigue parameters for both two phases are taken from (Nguyen et al., 2021). For phase I,  $m_1$  is 2.29153 and  $A_1$  is 103.7465 which are calculated from the modified experimental S-N curve. For phase II,  $m_2$  and  $A_2$  are 2.6182 and 1055, respectively. It should be mentioned for different horizons and grid sizes  $A_2$  should be modified correspondingly.

The model is generated by 125 PD points in the x-direction and 120 PD points in the y-direction leading to a grid size of 0.6 mm. Two rigid zones with an elastic modulus of  $200E$  are utilized to apply the loadings. There are two forces with an extreme value of  $14 \times 10^3 N$  (Loading ratio  $R=0.1$ ) applied at the central points of the rigid zones. Besides, the two points at the middle of the right edge are fixed as the boundary condition to avoid singularity problems.

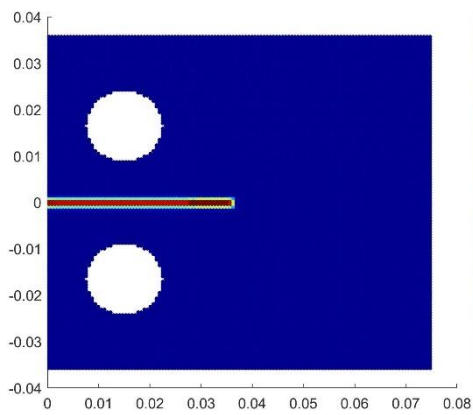
After setting up the PD model, the analysis is run for 2000, 15000, 30000, and 40850 load cycles. The initial crack starts to significantly propagate at around 15000 cycles and the plots for the crack propagation are shown in Fig. 6.5. The location of the crack tip is recorded and compared against the experimental results (Fig. 6.6). From Fig. 6.6, it can be seen that the PD results match well with the experimental data.



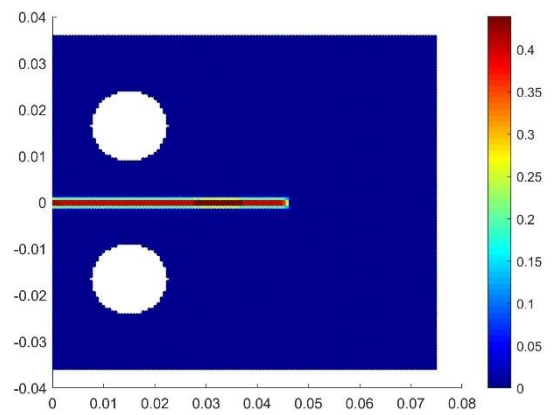
(a) 2000 cycles



(b) 15000 cycles



(c) 30000 cycles



(d) 40850 cycles

**Figure 6.5** The propagation of the crack at different load cycles

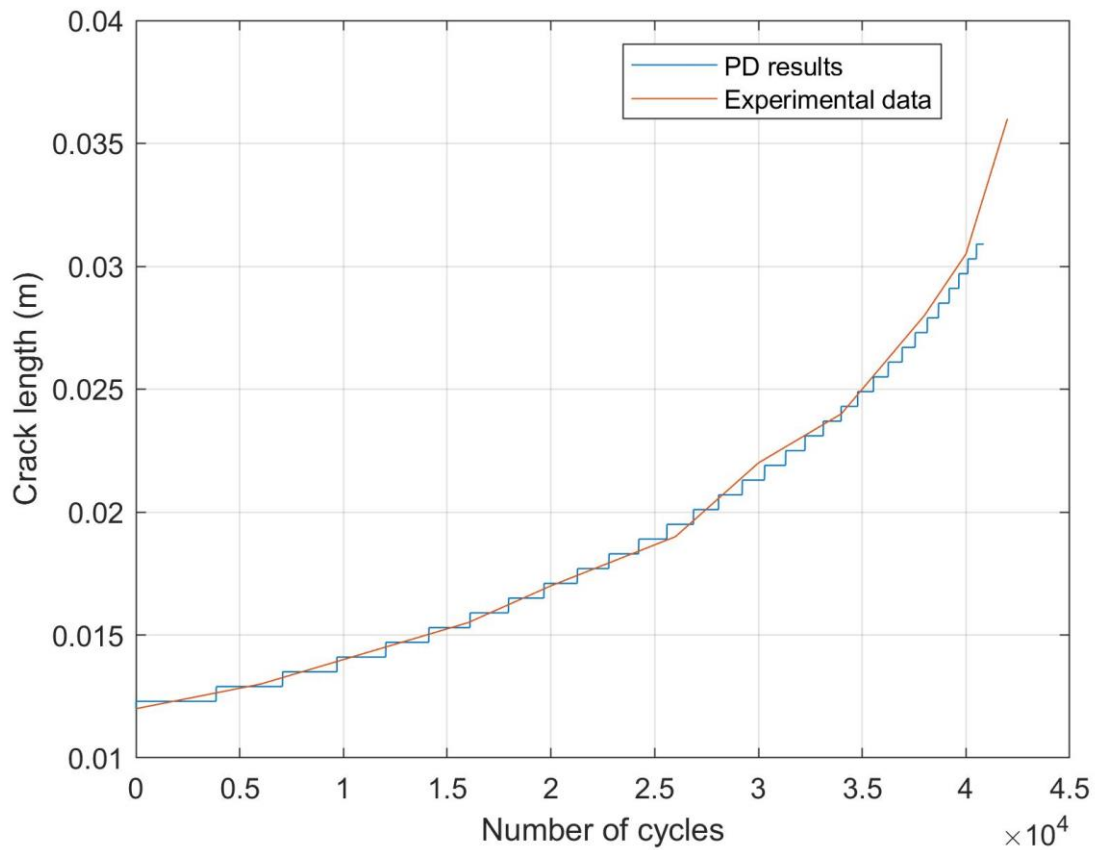


**Figure 6.6** The length of the crack tip against load cycles

### 6.5.2 Triplate model generation

The geometry of the triplate is decided according to the table of Standard Tri-plate based on the maximum tension loading data. Besides, the safety factor for the mooring chain which is suggested as 1.67 is also taken into consideration (Sound and Sea Technology, 2009). Finally, the following series of data for the triplate model given in Table 6.2 is selected and it gives a working load limit (WLL) slightly higher than the maximum calculated WLL.

**Table 6.2** The geometrical inputs for the triplate model

Items	A	B	C	R
Value	105 mm	100 mm	280 mm	170 mm

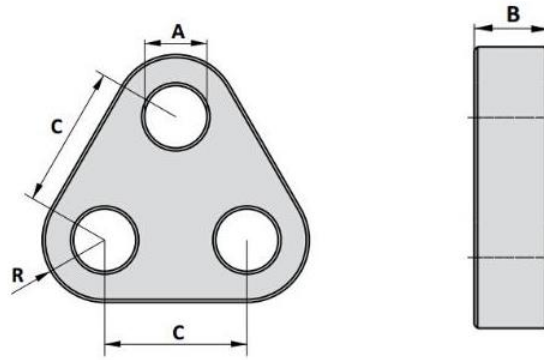


**Figure 6.7** The shape of the triplate (Hendrik Veder Group)

High-tensile strength steel is generally used to manufacture triplates. Usually, several types of steel grades can be chosen such as R3, R4, and R5. After considering the available data, grade R4 is utilized. The basic material properties are listed in Table 6.3 (Zarandi and Skallerud, 2020).

**Table 6.3** The material properties of R4 steel

Material property	Value	Units
Elastic modulus (E)	207	<i>GPa</i>
Poisson's ratio ( $\nu$ )	0.3	
Density ( $\rho$ )	7850	<i>Kg / m<sup>3</sup></i>
Average toughness (CVN)	151	<i>J</i>

The provided average toughness cannot be directly used for the PD model. Therefore, the Barsom-Rolfe correlation is used to convert the average toughness to the required fracture toughness (Tauscher, 1981). Although this correlation may result in some small errors, it is recommended that it would be the most suitable correlation for various applications (Tauscher, 1981). The formula of the correlation is given as:

$$K_{IC}^2 = 5CVN \cdot \sigma_{ys} - 0.25\sigma_{ys}^2 \quad (6.28)$$

where  $\sigma_{ys}$  is the yield stress and for R4 steel, 580 *MPa* is applicable. It should be emphasized that the unit of the whole equation is in the British unit system. Hence, there should be some

transformations of the units. After obtaining the fracture toughness ( $233.36 \text{ MPa}\sqrt{m}$ ), the critical energy release rate, and then the critical stretch can be calculated.

The fatigue parameters, due to the limitation of the available experimental data, the DNV rules, and the British Standard are used (DNV and Lloyd, 2015; Standard, 2015). First of all, for phase I, the S-N curve constants for studless chain material are given as  $a_D = 6 \times 10^{10}$  and  $m = 3$  (Fig. 6.8). The stress-number of cycles relationship is given as below: (DNV and Lloyd, 2015)

$$\log(N) = \log(a_D) - m \log(S) \quad (6.29)$$

where  $N$  is the number of the load cycles,  $a_D$  is the intercept value of the S-N curve

,  $S$  is the stress and the unit is  $\text{MPa}$ .

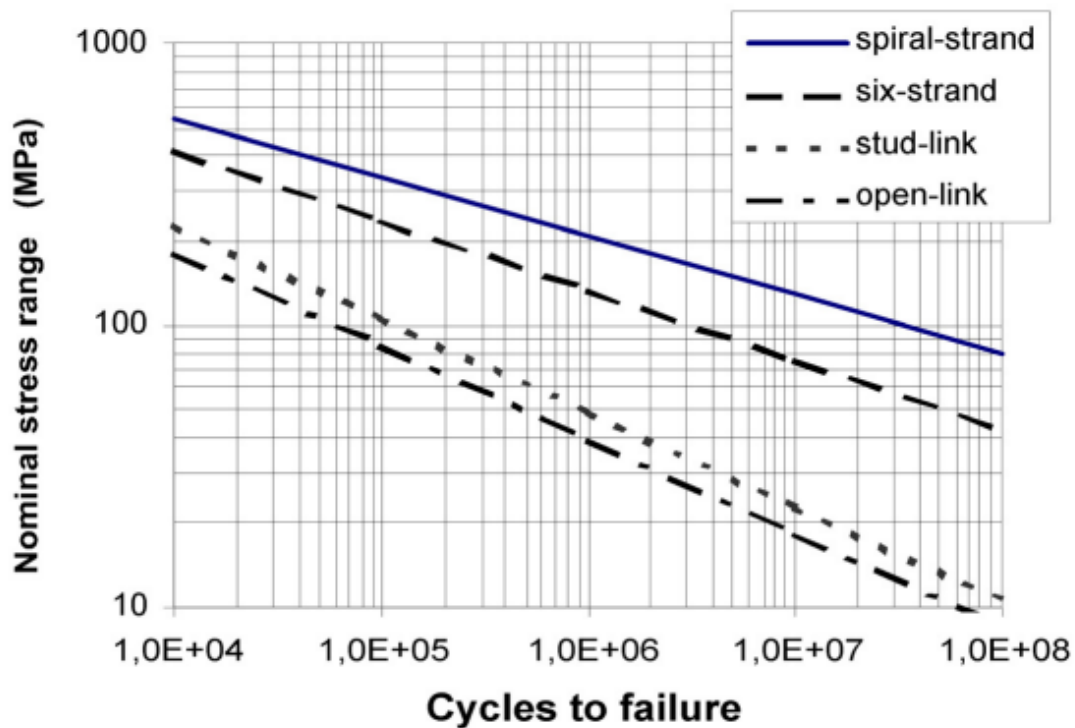


**Figure 6.8** The S-N curve for chain steel (DNV and Lloyd, 2015)

For the PD fatigue model, the relationship between strain and the number of cycles is required. Therefore, it is necessary to convert the above equation from stress-cycles to strain-cycles. A simplified relationship ( $strain = stress / E$ ) is utilized to transform Eq. (6.29) from stress to

strain. After dividing the stress by the elastic modulus of the R4 steel, the final fatigue inputs for the phase I can be obtained as:  $A_1 = 1.4783 \times 10^5$  and  $m_1 = 3$ .

After obtaining the S-N curve constants,  $A_2$  the constant of the Paris' law can be calibrated by the following steps ( $m_2$  value is directly given as 3 from the British Standard): (Standard, 2015; Nguyen et al., 2021)

- 1). A trial  $A_2$  value is assumed. For the current analysis, the assumed  $A_2$  is  $2 \times 10^5$ .
- 2). Then a similar analysis as in Section 6.5.1 is performed but the material properties are replaced by R4 steel and the above constants including the assumed trial  $A_2$  is used as the fatigue parameters.
- 3). After running the analysis, Fig. 6.9 shows the relation of crack tip length ( $q_{trial}$ ) versus loading cycles ( $N_{trial}$ ) can be plotted. The crack growth rate ( $\frac{dq_{trial}}{dN_{trial}}$ ) can be calculated.

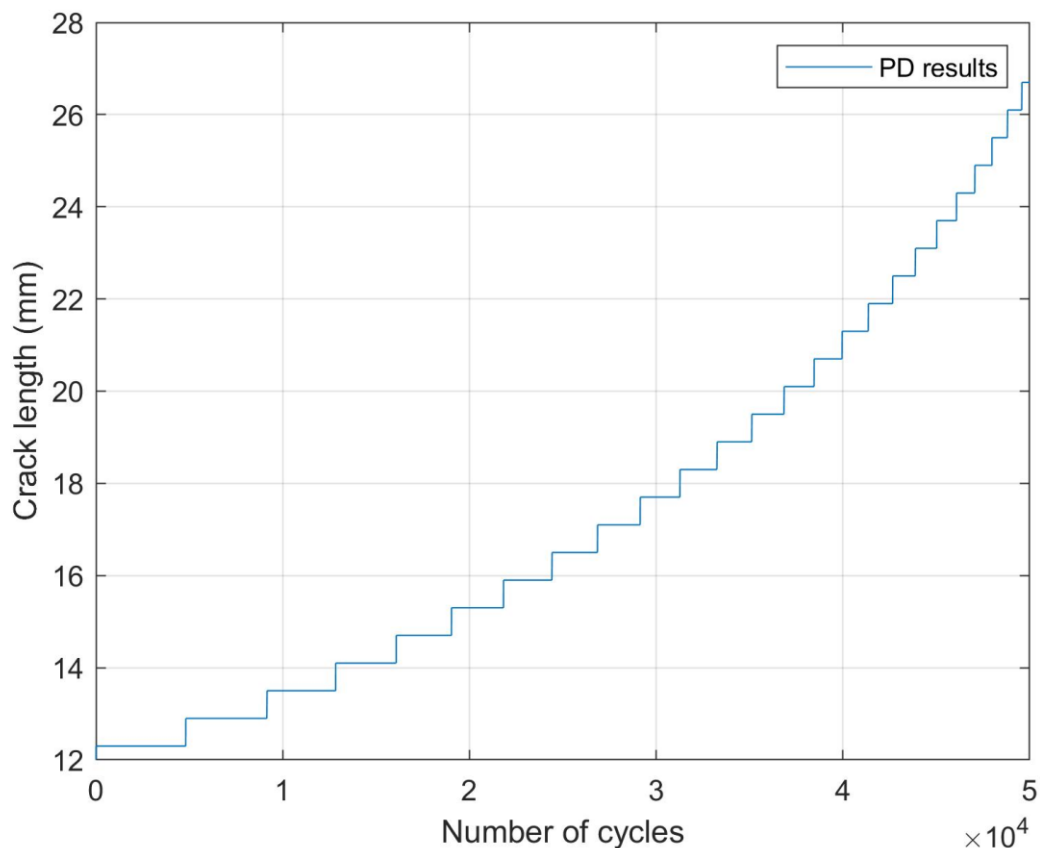


**Figure 6.9** The plot for crack tip length versus the number of load cycles

4). With the help of Eq. (6.30), the SIF ( $\Delta K_{trial}$ ) in  $MPa\sqrt{m}$  can be calculated by inputting the crack tip length.

$$\Delta K_{trial} = \frac{\Delta P}{h\sqrt{W}} \frac{2 + \bar{q}}{(1 - \bar{q})^{3/2}} (0.886 + 4.64\bar{q} - 13.32\bar{q}^2 + 14.72\bar{q}^3 - 5.6\bar{q}^4) \quad (6.30)$$

where  $\bar{q} = \frac{q_{trial}}{W}$  and  $\Delta P = P_{max}(1 - R)$ .

5). The Paris' law from the British Standard for steel in the marine environment is given as:

$$\frac{dq_{exp}}{dN_{exp}} = C_{exp} \Delta K^{m_2}$$

where  $C_{exp} = 2.3 \times 10^{-12}$  and  $m_2 = 3$ .

By comparing the trial and experimental equations,  $A_2$  can be calculated through

$$A_2 = A_{2trial} \frac{C_{exp}}{C_{trial}} \text{ as } 3.775.$$

For the current analysis, the parameters  $A_1$  and  $A_2$  will be increased by  $10^5$  to reduce the running time, but it will only have some influence on the scale of the number of loading cycles and for the other parts of the analysis, it will not be affected. A whole square plate is defined by  $200 \times 200$  material points at the first stage. Then, according to the relative locations of these points, the irrelevant points are ignored to generate the model of the triplate. Finally, the total number of material points is 14404.

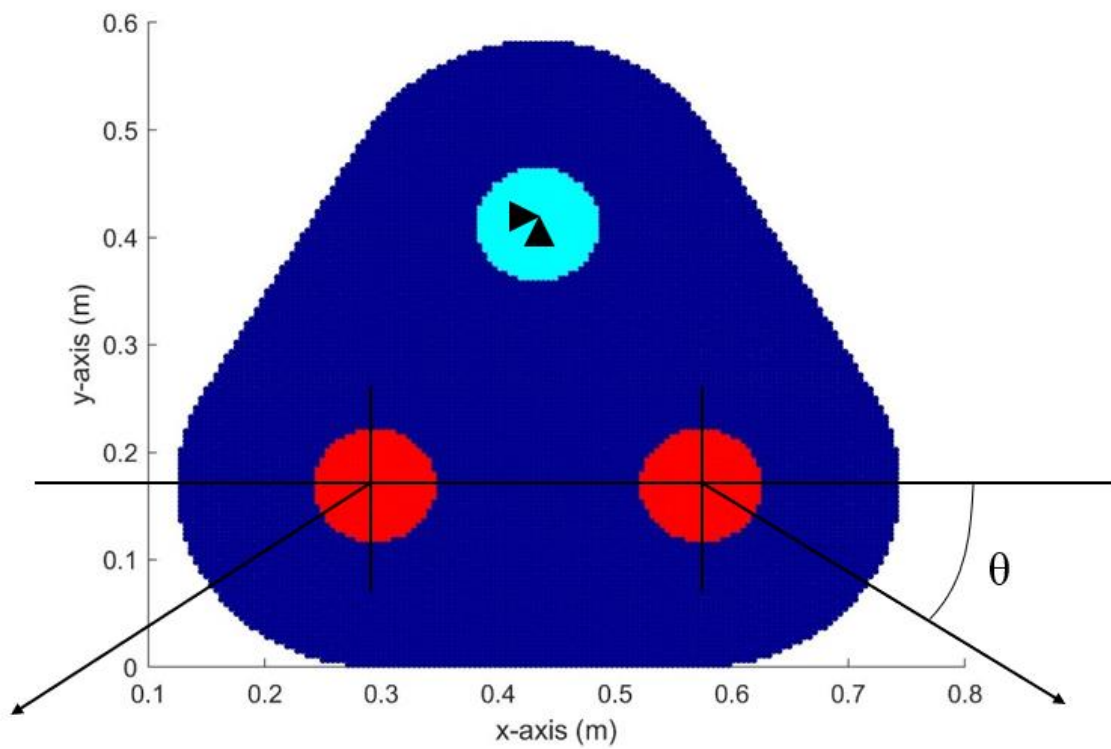


**Figure 6.10** The PD model of the triplate

Similar to the example in Section 6.5.1, three rigid zones inside the holes are created to apply the boundary conditions and loadings. For the boundary condition, to simplify the problem, the top rigid zone of the triplate (light blue in Fig. 6.10) is fixed in both x- and y- directions to achieve a constrained condition.

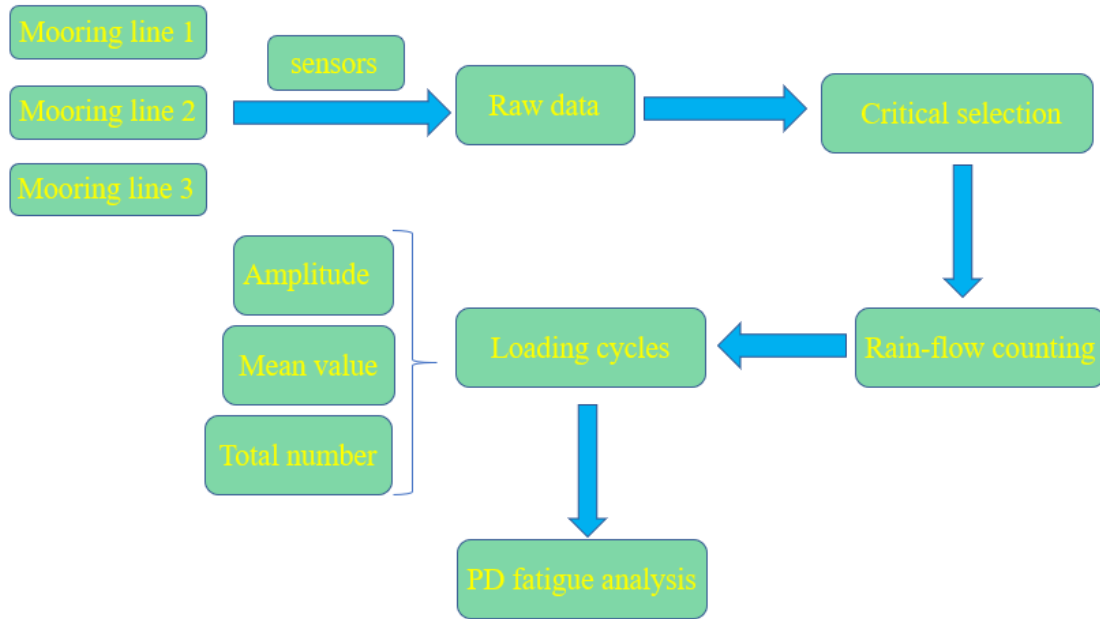


**Figure 6.11** The flow chart of processing the loading data

For the loadings, the raw data is required to be collected from the mooring line directly by sensors. However, it cannot be used straightforwardly for fatigue analysis. First of all, the raw data of these three mooring lines will be considered critically to find out the most severe location and case. The loading data for the most severe condition was considered and this data was used as the input for the Rainflow counting approach as suggested in (Thies et al. 2012). The Rainflow counting method is widely used for fatigue analysis in engineering applications. After the calculation, the raw data is converted to a series of loading cycles, which can be utilized for the PD fatigue analysis, and the output information includes the total number, amplitudes, and mean values of these load cycles. Finally, the R ratio of each cycle will also be calculated for the PD analysis.

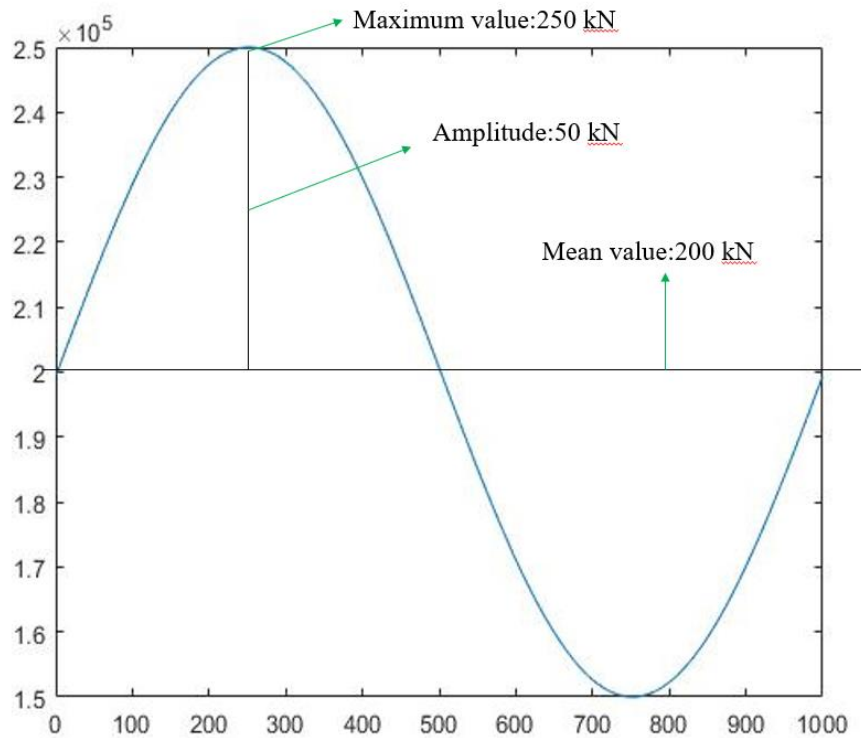


**Figure 6.12** The sinusoidal loadings cycle on the bottom bridle eyes

For the current analysis, the loadings are assumed based on the real data, collected from the Hywind Scotland, after the Rainflow calculation. Initially, there will be three forces from each mooring line. (Fig. 6.10) But, honestly speaking, according to the provided data, the tension forces on the holes of the triplate are not equal. That may be caused by the complex hydrodynamic environment. Therefore, the forces are simplified, and they will be treated in a plane rather than in three-dimensional, i.e., the forces will be hypothesized as being along the mooring line direction and in the same plane. Besides, considering the force balance state, the resultant force of the tensions on the two bottom bridle eyes is similar to the tension on the top eye but just opposite in the directions, i.e., the joint force of the forces on the two bottom holes will be equal to the large force on the top holes. And the force on the top eye will be replaced by the constrained boundary condition. After the above process, for each single load cycle, the maximum loading is 250 kN with an R ratio of 0.6, and the amplitude and the mean value of the force are 50 kN and 200 kN. (Fig. 6.12) During the following analysis, the constant amplitude loading condition will be considered and the effect of the angle  $\theta$  which is the angle between the mooring line direction and the horizontal axis will also be explored.

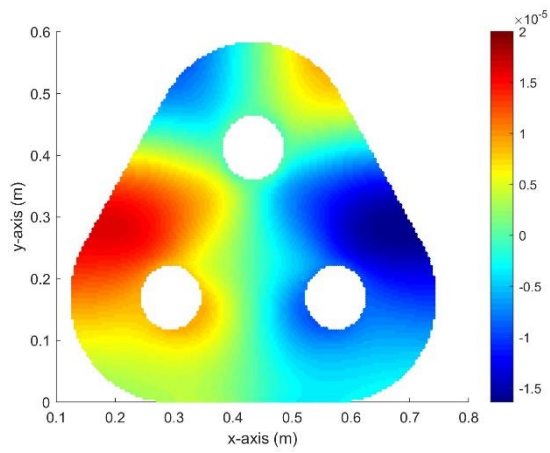
### 6.5.3 Model test

Before performing the fatigue analysis, the triplate model is tested by applying simple loading and compared against FEM results. Two equivalent forces ( $1 \times 10^3 \text{ kN}$ ) are applied in a downwards direction at the central points of the two bottom rigid zones. Different strength of the rigid zone is tested, and the results are collected in Table 6.4:

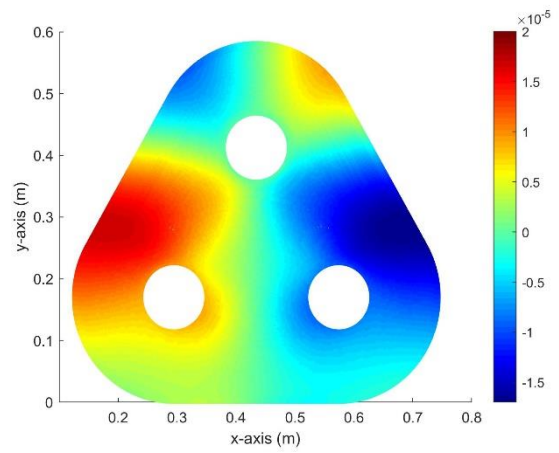
**Table 6.4** The results of different strengths of rigid zones

Strength	FEM $U_x$ (m)	PD $U_x$ (m)	Difference of $U_x$	FEM $U_y$ (m)	PD $U_y$ (m)	Difference of $U_y$
$1E$	2.02E-05	2.04E-05	0.70%	1.38E-04	1.62E-04	17.60%
$5E$	1.75E-05	1.71E-05	2.30%	8.48E-05	8.71E-05	2.70%
$10E$	1.70E-05	1.64E-05	3.65%	7.77E-05	7.63E-05	1.80%
$200E$	1.65E-05	1.51E-05	8.50%	7.07E-05	6.36E-05	10.10%

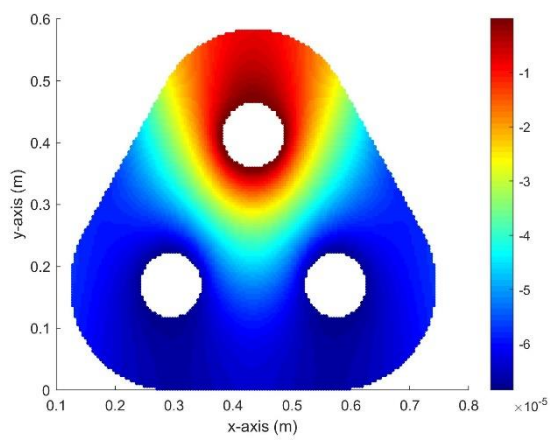
It can be seen that the rigid zone with  $10E$  gives better results. The plots of displacements in x- and y- directions obtained from both PD and Finite Element Method (FEM) are shown in Fig. 6.13. The differences in the plots are indistinguishable which shows that the PD model can provide the same results as the FEM.



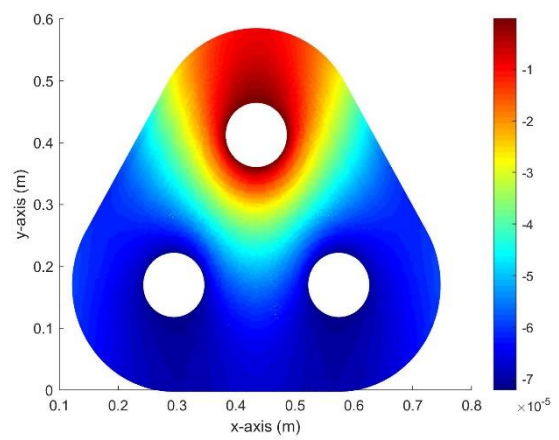
(a) PD displacements in x- direction



(b) FEM displacements in x- direction



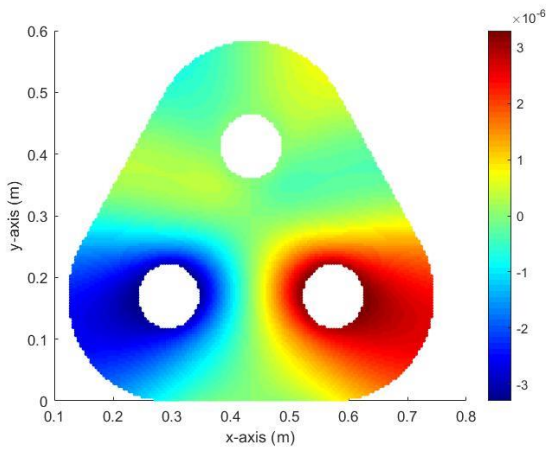
(c) PD displacements in y- direction



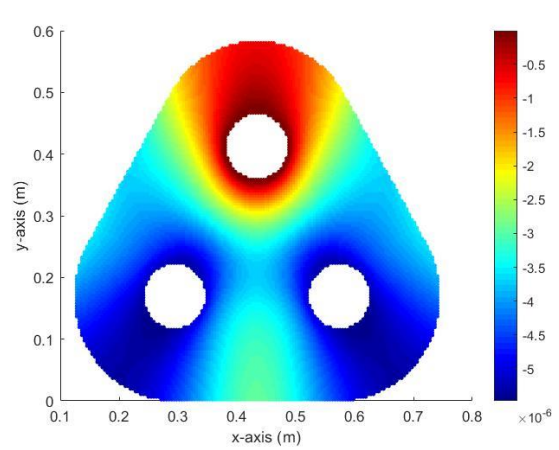
(d) FEM displacements in y- direction

**Figure 6.13** The plots of deformations for PD and FEM results

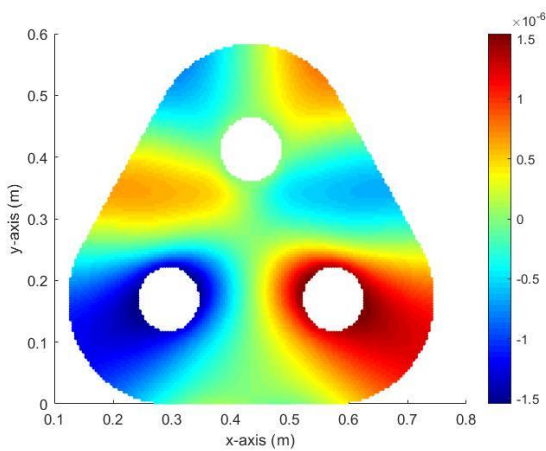
### 6.5.4 Fatigue analysis with constant amplitude loading



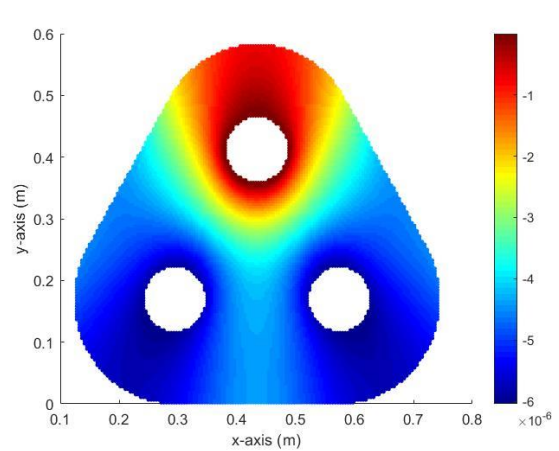
(a) Displacements in x- direction when  $\theta = 30^\circ$



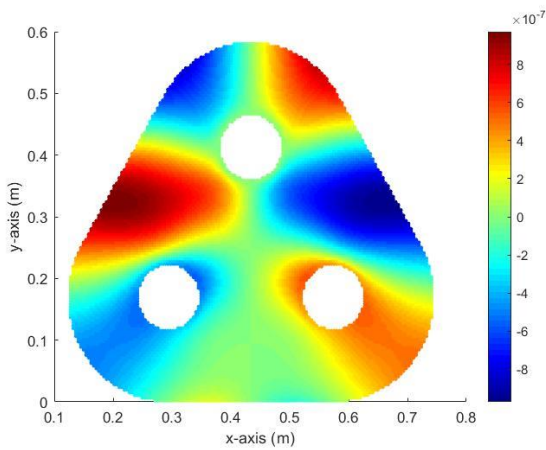
(b) Displacements in y- direction when  $\theta = 30^\circ$



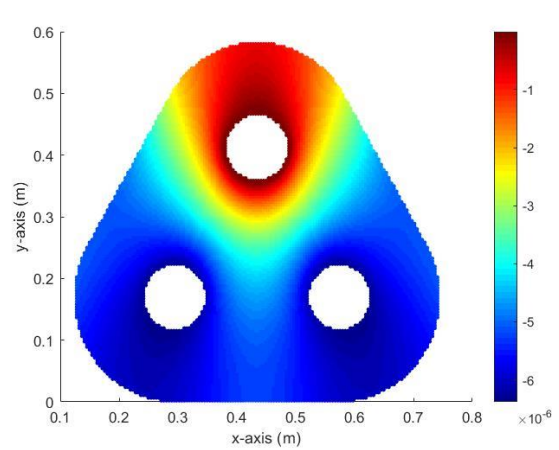
(c) Displacements in x- direction when  $\theta = 45^\circ$



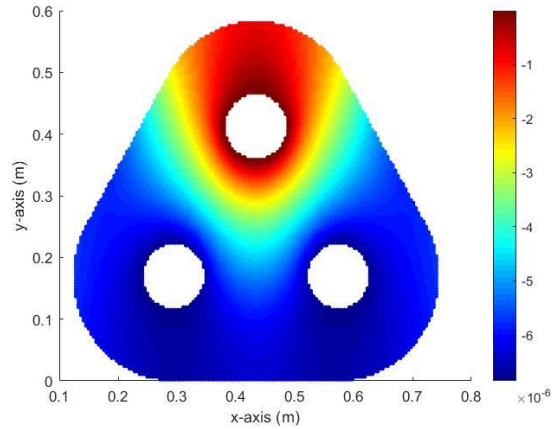
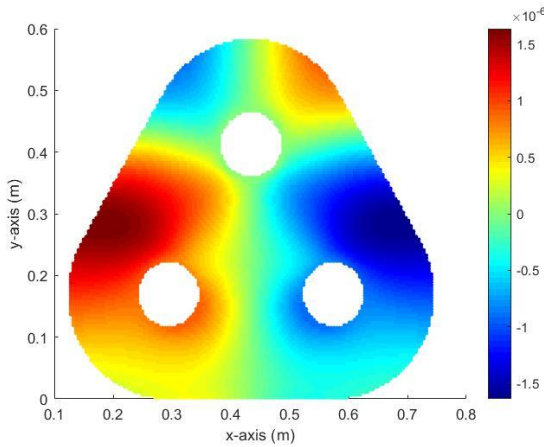
(d) Displacements in y- direction when  $\theta = 45^\circ$



(e) Displacements in x- direction when  $\theta = 60^\circ$



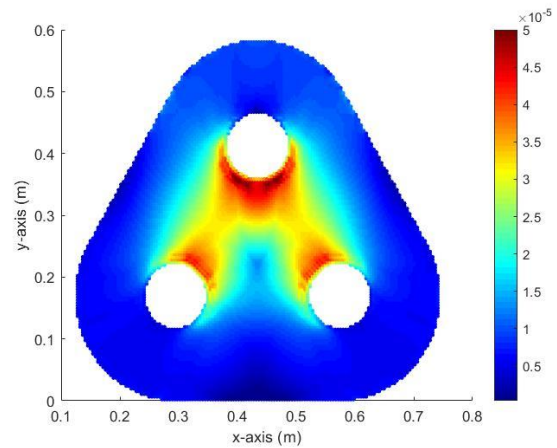
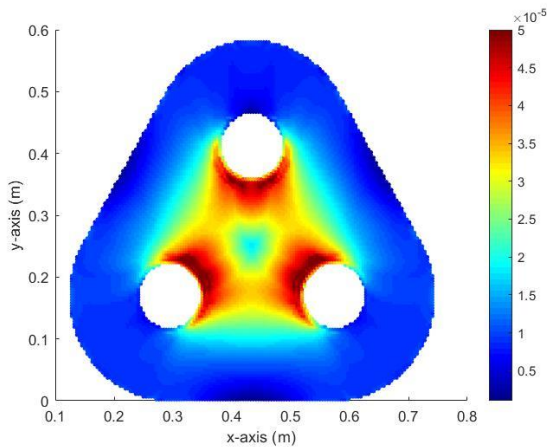
(f) Displacements in y- direction when  $\theta = 60^\circ$



(g) Displacements in x- direction when  $\theta = 90^\circ$

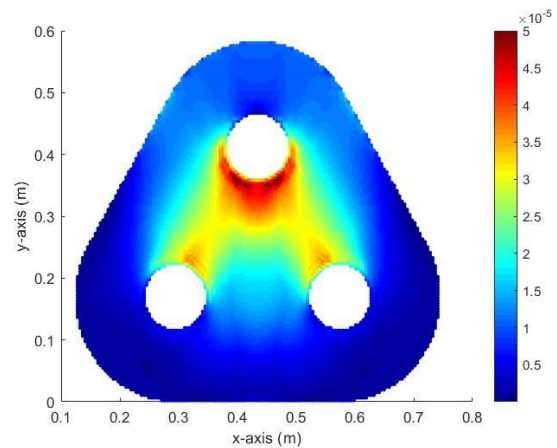
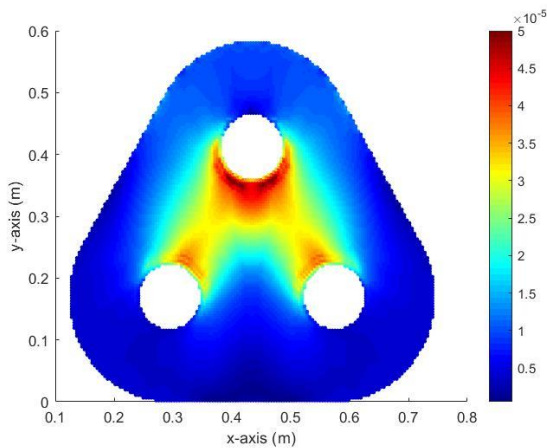
(h) Displacements in y- direction when  $\theta = 90^\circ$

**Figure 6.14** The plots of displacements for the triplate under constant amplitude but variable  $\theta$  loading condition



(a) The stretch value when  $\theta = 30^\circ$

(b) The stretch value when  $\theta = 45^\circ$



(c) The stretch value when  $\theta = 60^\circ$

(d) The stretch value when  $\theta = 90^\circ$

**Figure 6.15** The distribution of the stretch value for the constant amplitude but variable  $\theta$  loading condition

After applying the constant amplitude loading with different mooring line angles to the triplate model in the static condition, the plots of the axial displacements can be obtained in Fig. 6.14.

For the displacements in the y-direction, the plots are similar to each other, and the maximum deformation occurs around the two bottom holes. But for the displacements along the x-axis, there is an obvious change in the locations of the extreme values, which are transformed from the positions around the holes to the edge regions between the top and bottom holes with the increase of the mooring angle. The distribution of the stretch values of the PD points is also plotted. From Fig. 6.15, the locations of the maximum stretch can be observed in the region just below the fixed rigid zone. Nevertheless, another typical feature is that when the mooring angle is small ( $\theta = 30^\circ$  and  $\theta = 45^\circ$ ), the stretch values around the two bottom holes are relatively large. When the angle is bigger than  $45^\circ$ , this feature becomes less obvious. The locations of the large stretch values usually indicate the initiation zones of the crack. It can be expected that the locations around the two bottom holes would be more dangerous when the mooring angle is lower than  $45^\circ$ . The maximum stretch values of the four cases are collected in Table 6.5 and the table also includes the maximum critical stretch of the whole triplate regarding the R constant and the estimated number of loading cycles that will lead to the fatigue crack initiation by the S-N curve. It can play a role as a judging criterion for the following results.

**Table 6.5** The stretch values and number of loading cycles for four different angles

The angle of mooring lines	$\theta = 30^\circ$	$\theta = 45^\circ$	$\theta = 60^\circ$	$\theta = 90^\circ$
The maximum stretch	5.47380E-05	5.45230E-05	5.43990E-05	5.42300E-05
The maximum critical stretch	2.18952E-05	2.18092E-05	2.17596E-05	2.16920E-05
The estimated number of loading cycles	6445	6522	6566	6628

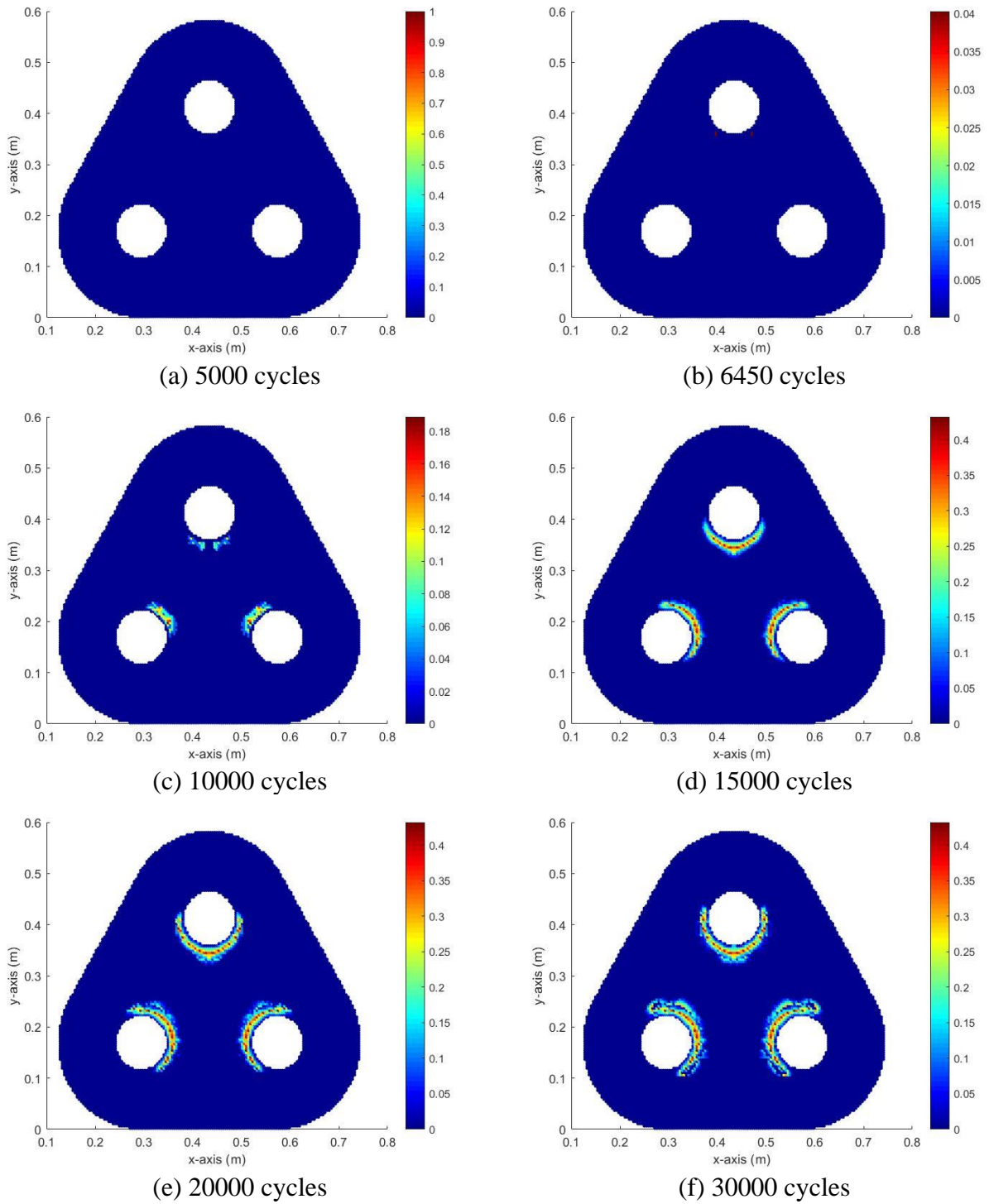


**Figure 6.16** Plots of the damage of different load cycles under constant amplitude loading when  $\theta = 30^\circ$

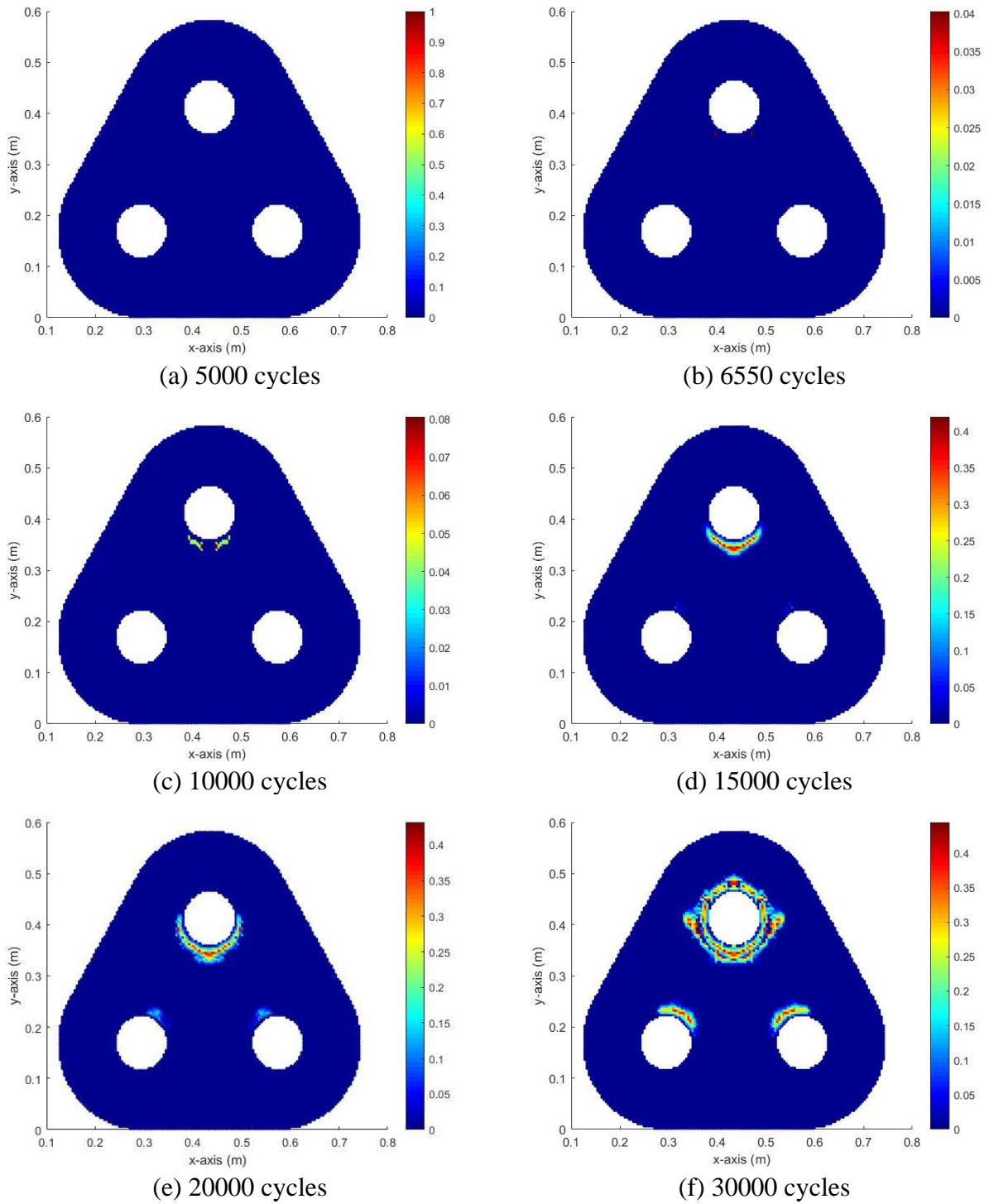


**Figure 6.17** Plots of the damage of different load cycles under constant amplitude loading when  $\theta = 45^\circ$

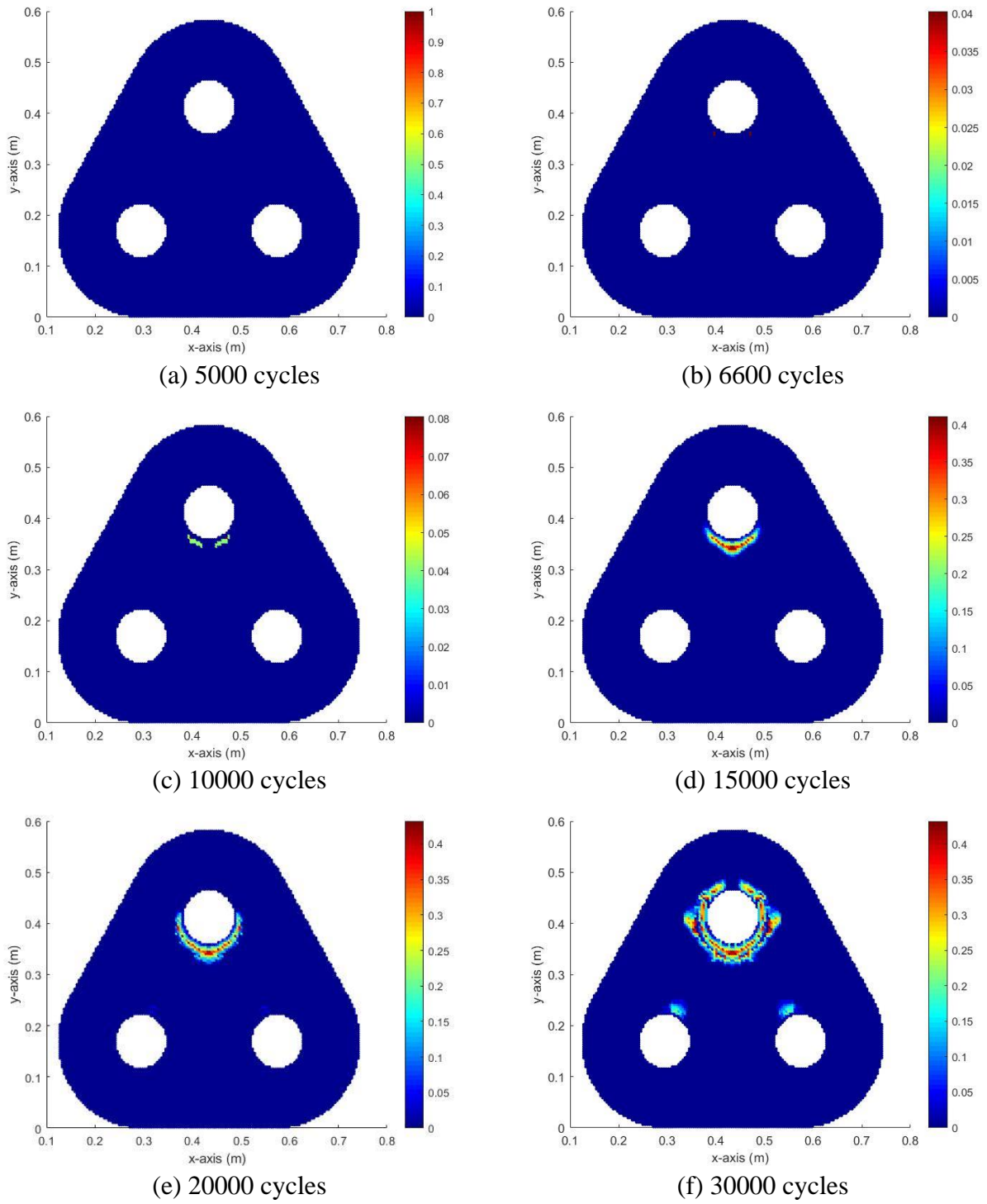


**Figure 6.18** Plots of the damage of different load cycles under constant amplitude loading when  $\theta = 60^\circ$

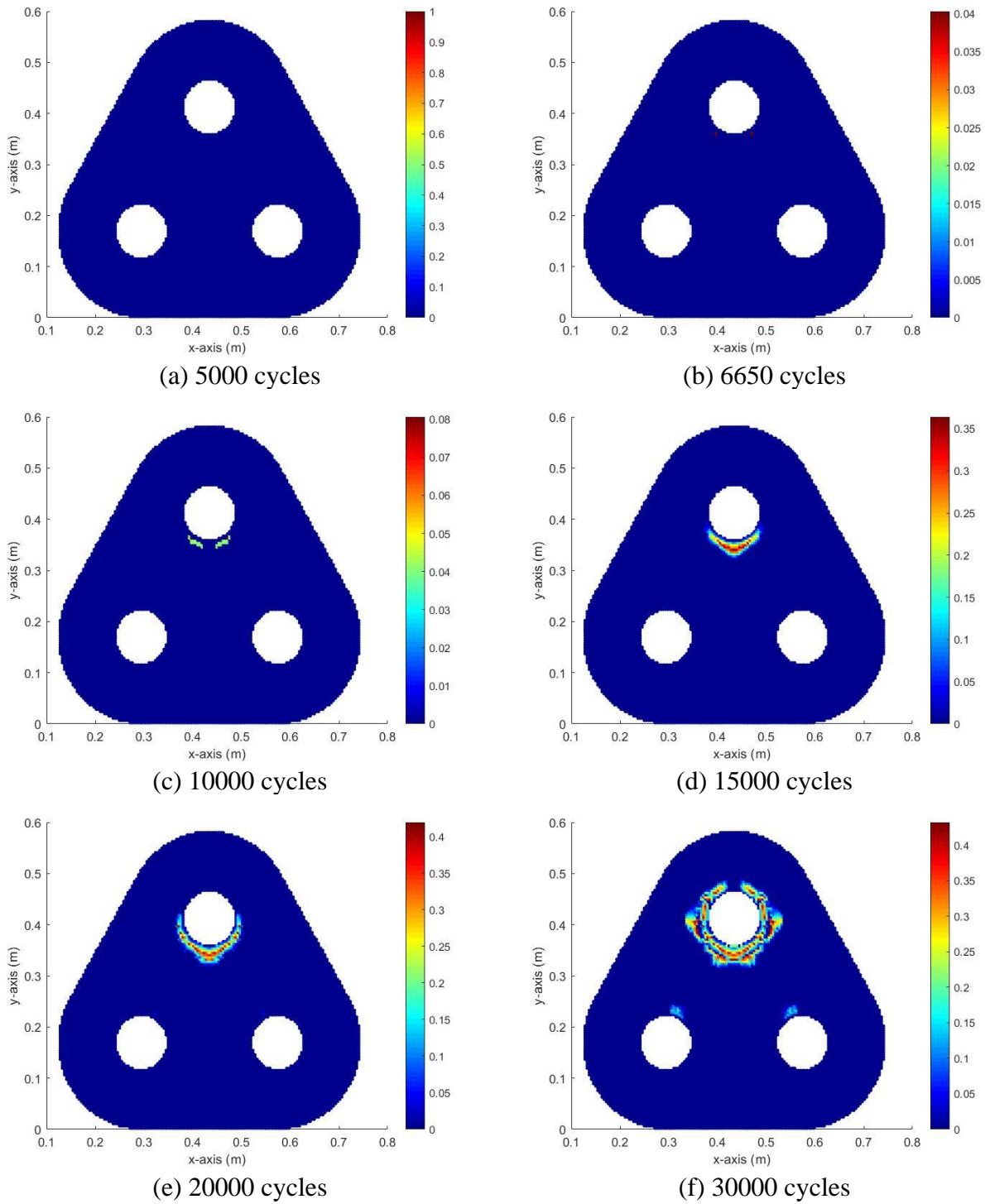


**Figure 6.19** Plots of the damage of different load cycles under constant amplitude loading when  $\theta = 90^\circ$

The damage at different load cycles and variable  $\theta$  values is provided to show the initiation and propagation of the crack. During the first 5000 cycles, there is no damage occurs in the model. When the number of the loading cycles reaches and exceeds the estimated values (listed in Table 6.5), for all the cases, the damage starts at the PD points below the top hole. The

number of load cycles and the initiation locations of the fracture match well with the above estimation. Then the crack initiating from the two points propagates toward each other to form the major crack, which can be seen from the plots of 10000 loading cycles. However, it should be highlighted that, apart from the major crack, when  $\theta = 30^\circ$ , there are two additional branches of crack that occur around the bottom holes which are also the regions suffering relatively large stretches. And it meets the expectation mentioned in the last paragraph. It can also be witnessed that this phenomenon becomes difficult to happen with the increase of  $\theta$  angle. For the case when  $\theta = 90^\circ$ , this feature will only become obvious at over 30000 loading cycles. For the major crack, at around 20000 loading cycles, it has already reached half circumference of the top bridle eye. Then, the main crack is going to branch at both sides except the case of  $\theta = 30^\circ$ , and it has a tendency of approaching the edge of the triplate and easing the fixed boundary condition. Then it will result in the failure of the triplate. But it is interesting to find that although the branch crack is much more severe than the other cases, the propagation of the major crack seems to be hindered. And not like the other plots at 30000 loading cycles, the plots of the case of  $\theta = 30^\circ$  still do not have a glimpse of the initiation of branching at either side of the top hole. It can be summarized that with the increase of the  $\theta$  angle, the initiation of the crack will take fewer loading cycles. Additionally, the propagation of the major crack will become more serious, and the major crack will become much easier to propagate toward the edges of the triplate but the crack around the bottom rigid zones will be slightly blocked.

## 6.6 Summary

In this study, a PD model for fatigue damage prediction is presented. PD fatigue is capable of predicting all three phases of fatigue failure: crack initiation (phase I), crack growth (phase II), and final failure controlled by quasi-static crack growth (phase III). PD fatigue model is validated by considering a plate with an existing crack problem. PD fatigue model results are compared against experimental results of the evolution of crack growth as the number of cycles increases. A very good agreement was obtained between PD and experimental results. Then, PD fatigue model parameters were obtained for the triplate which is a component used as part of floating wind mooring lines. The fatigue analysis of a triplate was performed under the constant amplitude loading condition with different mooring line angles. PD results for fatigue damage initiation agreed very well with the expected analytical results for all mooring line angles. Moreover, PD analysis provided a complete picture of fatigue damage evolution from

damage initiation to final failure. Finally, the effect of the mooring line angles has been explored. Compared with the conventional S-N curve methods which can only provide information about fatigue life corresponding to the point of fatigue damage initiation, the PD fatigue model can provide more accurate information and decrease the level of conservatism. Moreover, the information that PD analysis provided can be beneficial for a digital twin system since the operators will be able to capture when and where damage starts and how it propagates. As such, it is a useful input into any inspection process of the mooring lines as the failure pattern to look for. For future research, on the one hand, the variable loading condition would be a reasonable direction and on the other hand, the PD fatigue analysis can be performed for the other components of the offshore wind turbine, such as the mooring lines.

## 7 Peridynamic model for cubic polycrystal material

### 7.1 Introduction

This study lays emphasis on peridynamic modeling of the fracture behavior at the microscale for cubic polycrystalline materials. In Section 7.2, the interaction force of the PD points will be updated with the thermal expansion coefficient. Then the PD model for the single cubic crystal followed by the PD model for polycrystalline material will be separately presented in Section 7.3 and Section 7.4. The described PD cubic polycrystal model will be utilized in two aspects: the effect of porosity on intergranular fracture and the thermally-induced fracture. The research about the porosity at the grain boundaries will be concentrated in Section 7.5. After that, the exploration of the influence of thermal loading on fracture behavior at the microscale will be provided in five parts: the initial three static analyses from isotropic material to the cubic polycrystals (Section 7.6.1 to Section 7.6.3) are aimed to offer the verification of the accuracy of the PD thermal equations; the remaining two sections are mainly the dynamic analysis of the single cubic polycrystals and ceramic made of two cubic materials with pre-existing cracks under thermal loading. Finally, conclusions for the numerical analysis in Section 7.5 and Section 7.6 will be given.

### 7.2 Updated Peridynamic formulations with the thermal expansion coefficient

If the temperature loading is taken into account, the equation of the PD force (Eq. 6.3) can be updated with the thermal expansion coefficient ( $\alpha$ ) as:

$$\mathbf{f} = (cs - \alpha\Delta T) \frac{\mathbf{y}_j - \mathbf{y}_i}{|\mathbf{y}_j - \mathbf{y}_i|} \quad (7.1)$$

where  $\Delta T$  is the temperature change of the bond. The temperature change of the bond can be calculated by averaging the temperature changes of the two interacting material points.

### 7.3 Peridynamic equations for single cubic crystals

Under the plane-stress condition, the local stiffness matrix for a single cubic crystal can be written as:

$$[c] = \begin{bmatrix} c_{11} & c_{12} & 0 \\ c_{12} & c_{11} & 0 \\ 0 & 0 & c_{44} \end{bmatrix} \quad (7.2)$$

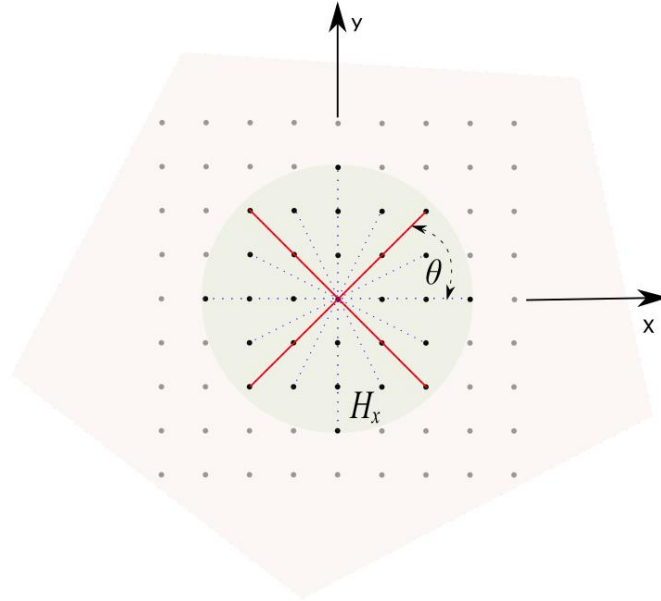


**Figure 7.1** PD model for polycrystalline when the orientation of the crystal is  $0^\circ$  (blue lines represent Type-1 bonds and red lines represent Type-2 bonds)

Based on the PD model developed by De Meo et al. (De Meo et al., 2016), bonds for a single cubic crystal can be divided into two different groups. Type-1 bonds shown as blue lines in Fig. 7.1 are located in all directions of the material. For plane-stress condition, the bond constant for Type-1 bonds can be calculated from the components of the stiffness matrix as:

$$c_{T1} = \frac{12(c_{11}^2 - c_{11}c_{12})}{\pi h \delta^3 c_{11}} \quad (7.3)$$

Type-2 bonds shown as red lines in Fig. 7.1 exist in some specific directions. These directions are defined according to the orientations of the crystals. Type-2 bond angle with respect to the crystal orientation is specified as  $\frac{\pi}{4}(2 \times i - 1)$ , ( $i = 1, 2, 3, 4$ ). The bond constant for Type-2

bonds can be calculated as:

$$c_{T2} = \frac{4(3c_{11}c_{12} - 2c_{12}^2 - c_{11}^2)}{\beta c_{11}} \quad (7.4)$$

where  $\beta = \sum_{j=1}^N \xi_{ij} V_j$ ,  $\xi_{ij}$  is the bond length between material points  $i$  and  $j$ .

The accuracy of this model under mechanical loading was verified by De Meo et al. (De Meo et al., 2016). For cubic crystals, the thermal expansion coefficient  $\alpha$  is the same in all directions. Therefore, the thermal loading can be directly taken into account by using the bond force expression given in Eq. (7.1).

## 7.4 Peridynamic model for polycrystalline material

In order to generate the polycrystalline model, the Voronoi tessellation method was utilized. The seeds were randomly distributed over the plate and the nodes were divided into different crystals by minimizing the distance between the seeds and nodes. Besides, for cubic polycrystals, the grain size and grain orientations were randomly determined. The plot of the crystals is shown in Fig. 7.2. In this study, the grain boundary width is assumed to be zero. Moreover, for the bonds crossing the grain boundaries, their bond constant values are calculated as the average of the bond constant values of the associated material points. One definition that should be noted here is the grain boundary coefficient (GBC) and it is the ratio of the strength of the bond crossing the grain boundary to the strength of the bond inside the grains. It is an important parameter for the investigation of the influence of the grain boundary strength.

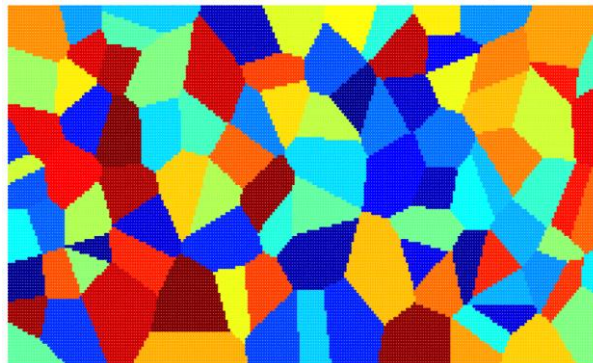


**Figure 7.2** Crystals generated by the Voronoi tessellation method

## 7.5 Investigation of the effect of porosity on intergranular brittle fracture

### 7.5.1 Model generation and initial parameters

In order to study the effect of porosity on the fracture of polycrystals, the polycrystalline material model considered in De Meo et al. was utilized. (De Meo et al., 2016) The plate has a size of 5 mm  $\times$  5 mm and the thickness of the plate is 0.5 mm. The plate is made of AISI 4340

steel with material properties of  $c_{11}=208.9$  GPa ,  $c_{12}=126.4$  GPa , and  $c_{44}=97.7$  GPa . (Rimoli, 2009) There are two initial cracks defined at the top and bottom edges of the plate with a length of 0.4 mm and are located along the vertical central-line of the plate. For the basic PD parameters, there are  $150 \times 150$  PD points and the grid distance is decided as  $dx = 0.0333$  mm. Based on the suggestion provided in (Madenci and Oterkus, 2014), the horizon size of the analysis is fixed as  $3dx$  . The critical stretch is specified as  $s_0 = 0.0328$  . A velocity boundary condition of 25 m/s was applied at the right and left boundaries of the plate by defining additional three layers of PD points (Fig. 7.3). The total number of the times steps is 2000 with a time step size of 1 ns. The variables of the analysis are the number of grains (crystals) and their distribution, the number of pores and their distribution, and grain boundary strength. It should be mentioned that the grain boundary strength is represented by GBC. The GBC value is kept as 0.5 except for the final case.

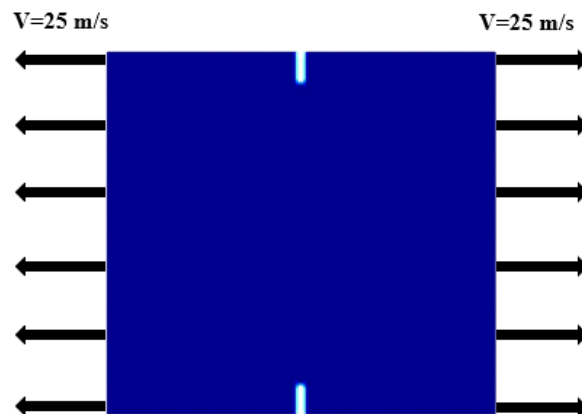


**Figure 7.3** The polycrystalline material model subjected to velocity boundary conditions

### 7.5.2 Numerical results for different cases

In the first case, the results are provided for the plate with 150 grains without porosity as shown in Fig. 7.4. From the plots, it can be seen that the crack propagates through the grain boundaries from the pre-existing cracks to form the major crack. The majority of the cracks concentrate around the central region of the plate.

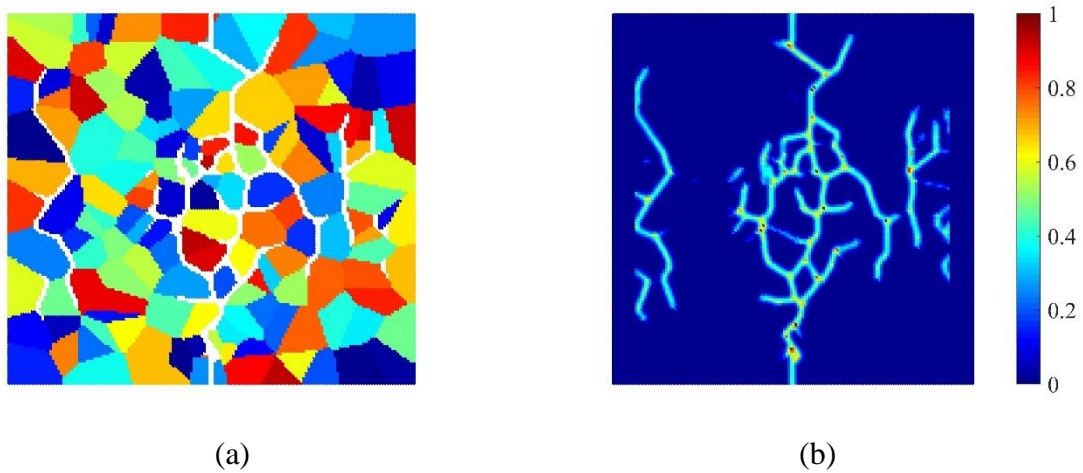


**Figure 7.4** Results of crack propagation without porosity at 2  $\mu$ s; (a) crack distribution with grains, (b) damage

Then, the porosity was introduced by creating randomly distributed small circles around the grain boundaries. (Chakraborty et al., 2016) The total number of pores is 16 and each has a diameter of 0.2 mm. Eventually, the porosity ratio reaches approximately 2%. The distribution of the pores and the propagation of the crack with grains are shown in Fig. 7.5. The plots of the damage at 4 different time steps are also provided to give a clearer illustration of the fracture behavior as time progresses.

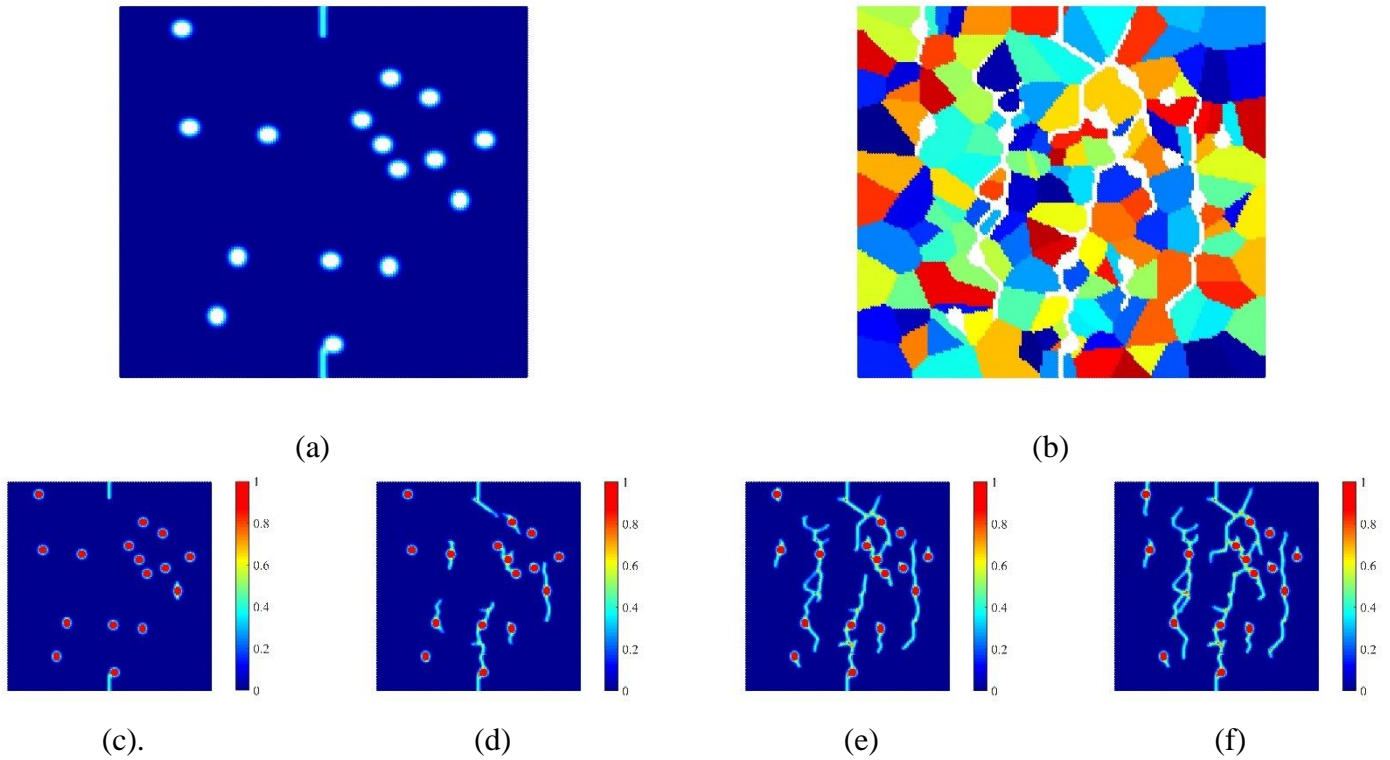


**Figure 7.5** The case with 150 grains and 2% porosity; (a) the distribution of pores, (b) crack distribution with 150 grains, (c) damage at  $0.5 \mu\text{s}$ , (d) damage at  $1 \mu\text{s}$ , (e) damage at  $1.5 \mu\text{s}$ , (f) damage at  $2 \mu\text{s}$

Compared to the without porosity case, the main crack still propagates towards the opposite edge. However, there is a tendency for the main crack to propagate towards the pores, i.e. the propagation of the main crack has been appealed by the pores, especially those pores around the central region. Moreover, the branches of the main crack are slightly reduced at the same time. Additionally, there are small cracks that initiate from the pores and the direction of the propagation of these cracks is perpendicular to the loading direction. These small cracks propagate along the grain boundary to form newly generated branches of crack. Last but not least, the more intensive the pores, the more serious the newly initiated cracks.

Another numerical case includes the same grain distribution, but different locations of the pores to further support the former observations (Fig. 7.6). All of the previously mentioned features can still be captured as expected. Furthermore, an extra case with both different distributions of grains and pores is given to explore their effects. As shown in Fig. 7.7, crack behaviors are not significantly influenced by the distribution of grains or pores. From what has been shown, it can be concluded that porosity causes the initiation of small cracks which propagate perpendicular to the loading direction to form new branches of crack. If the pores are intensive, this phenomenon becomes more obvious. These observations agree with the conclusions drawn

by Chakraborty et al. (Chakraborty et al., 2016) The propagation of the major crack has also been changed. It prefers to propagate toward the pores and the branches have also been reduced. More importantly, grain distribution or pore distribution does not have a big impact on these observations

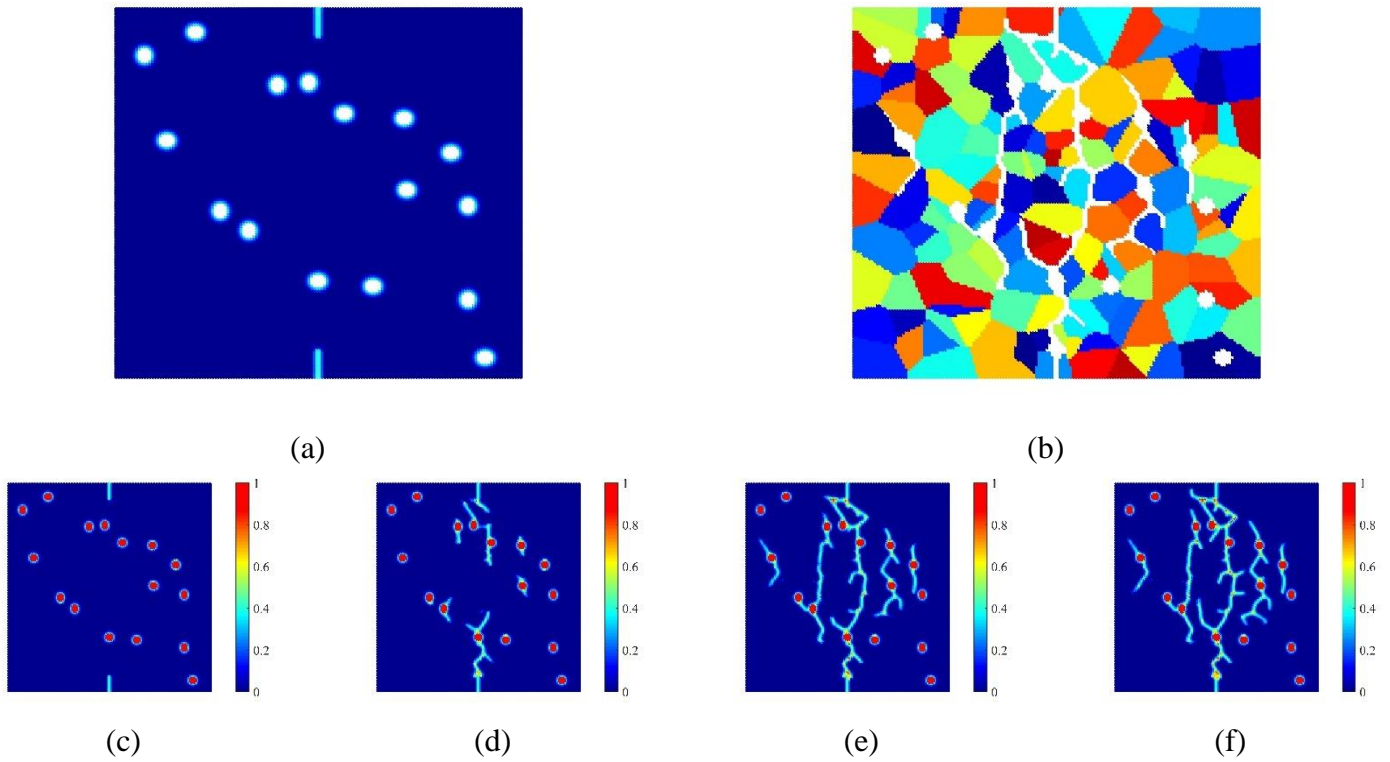


**Figure 7.6** The case with 150 grains but different 2% porosity distribution; (a) the distribution of pores, (b) crack distribution with 150 grains, (c) damage at  $0.5 \mu\text{s}$ , (d) damage at  $1 \mu\text{s}$ , (e) damage at  $1.5 \mu\text{s}$ , (f) damage at  $2 \mu\text{s}$

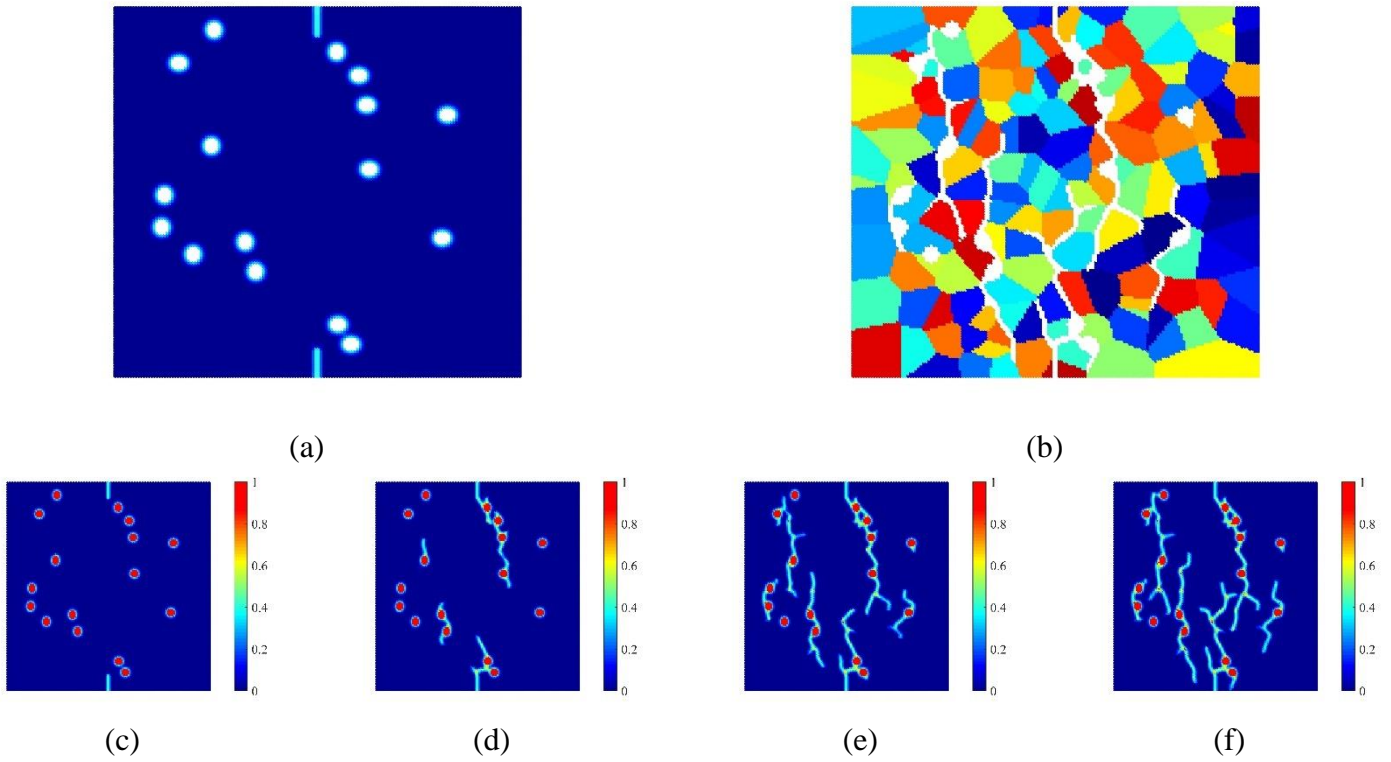


**Figure 7.7** The case with both different grain distribution and 2% porosity, (a) the distribution of pores, (b) crack distribution with 150 grains, (c) damage at 0.5  $\mu\text{s}$ , (d) damage at 1  $\mu\text{s}$ , (e) damage at 1.5  $\mu\text{s}$ , (f) damage at 2  $\mu\text{s}$

Additional three cases are considered to explore the effects of the number of grains, porosity distribution, and grain boundary strength. First of all, the number of grains is reduced from 150 to 100 and then to 50. The plots of the results are presented in Fig. 7.8. When the grain number is 100, although the severity of the fracture is decreased, the change is not obvious. However, when it comes to 50 grains, only the characteristic of the major crack is dominant. Next, the grain number is constrained as 150, but the porosity ratio is increased from 2% to 5%, by rising 1% for each case (Fig. 7.9). Although the change is not obvious initially, with the rise of the porosity ratio, the severity of the fracture especially the main crack becomes increasingly significant.

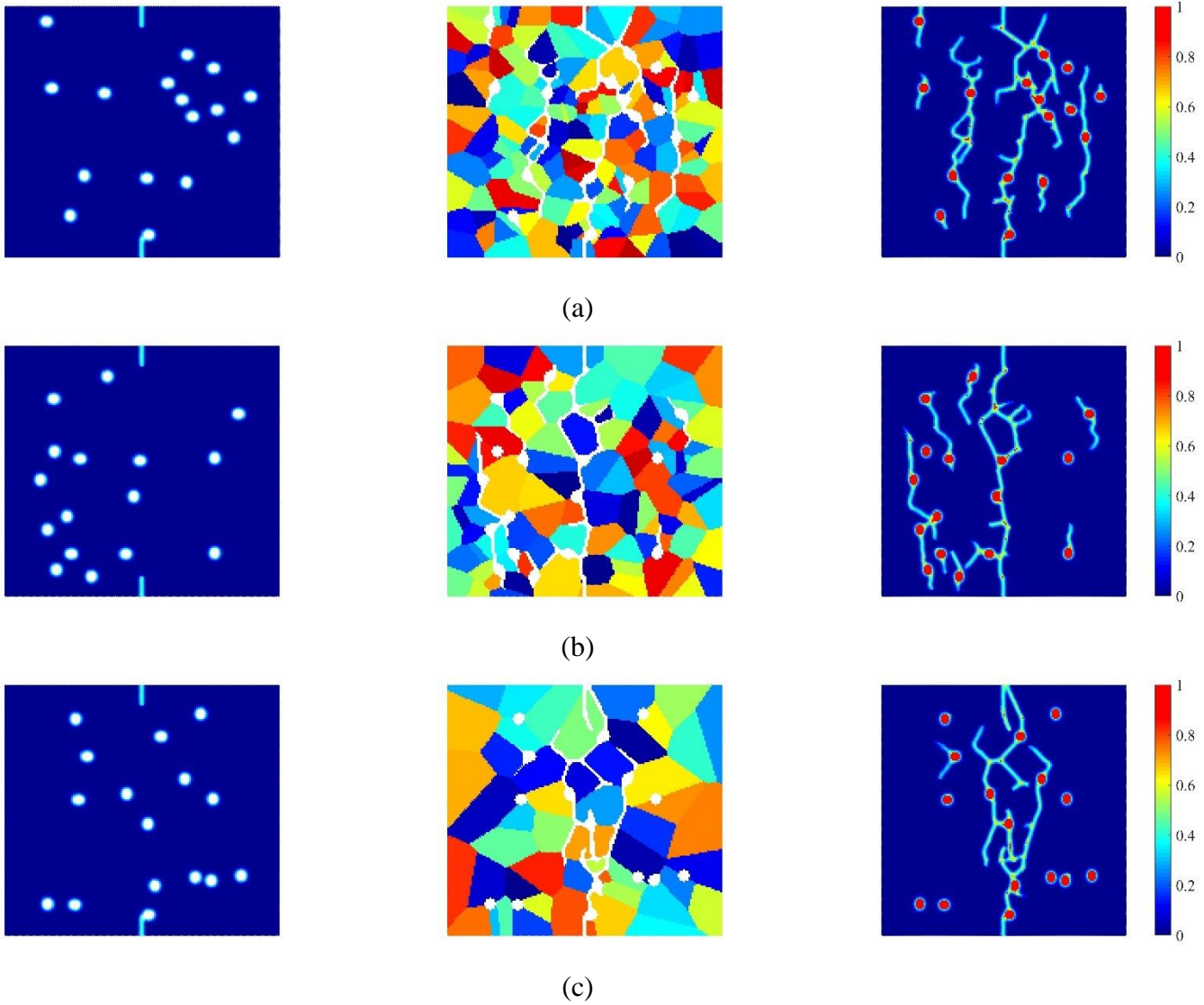


**Figure 7.8** Porosity distribution (left), crack distribution with grains (middle) and damage at 2  $\mu\text{s}$  (right), (a) 150 grains, (b) 100 grains, (c) 50 grains

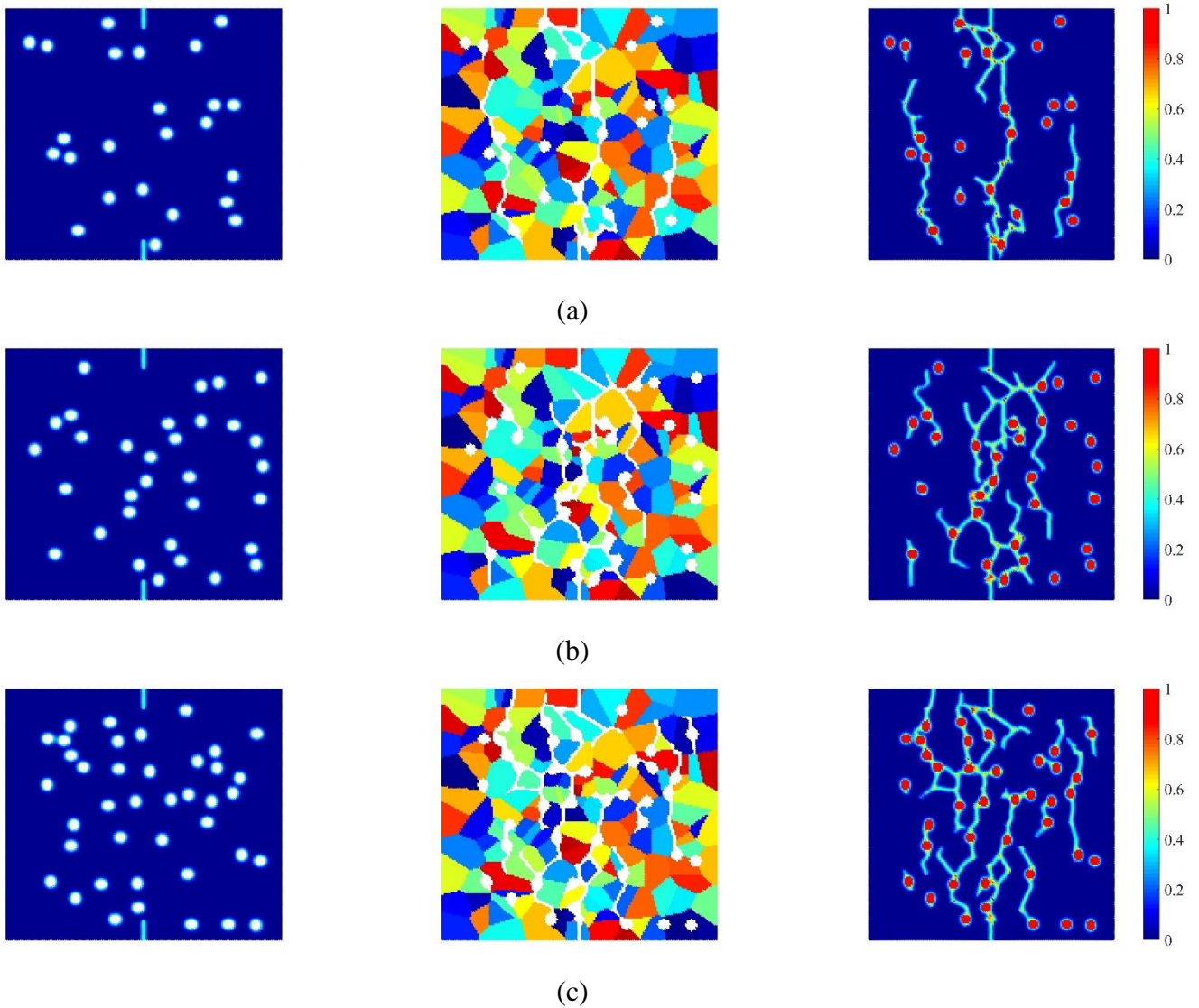


**Figure 7.9** Porosity distribution (left), crack distribution with grains (middle) and damage at  $2 \mu\text{s}$  (right), (a) 3% porosity, (b) 4% porosity, (c) 5% porosity

Finally, the GBC value is increased from 0.5 to 1. The remaining variables are kept the same. By doing so, the behavior at the microscale becomes more identical to the macroscopic material. It is obvious that the behavior of the main cracks is converted from the intergranular pattern to the transgranular pattern (Fig. 7.10).

In conclusion, the severity of the cracks especially the newly created cracks is influenced by the number of grains and porosity. Concerning the influence of grain boundary strength, with the increase of GBC, the effect of porosity dramatically decreases and the fracture pattern on the microscale becomes identical to the macroscale crack pattern.

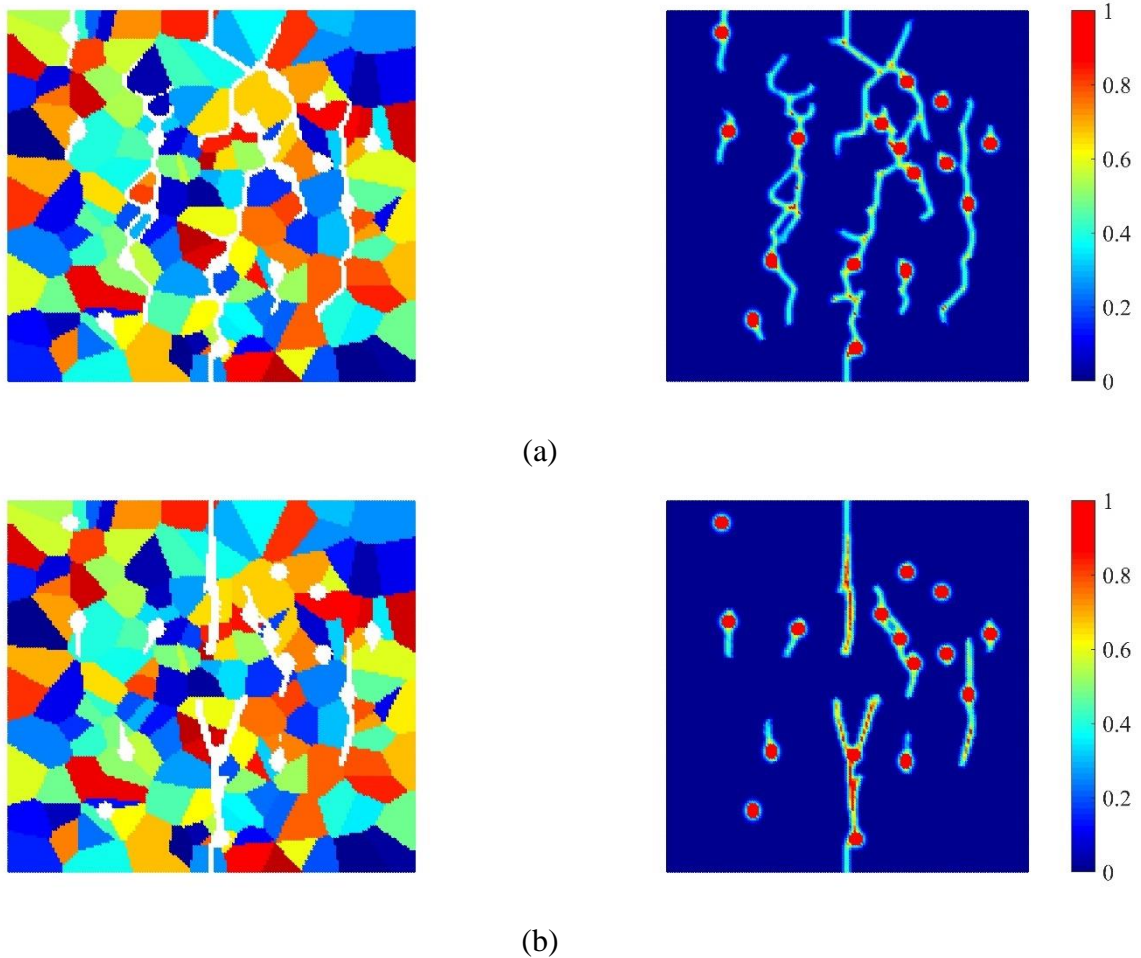


**Figure 7.10** Crack distribution with grains (left) and damage at  $2 \mu\text{s}$  (right), (a)  $\text{GBC} = 0.5$ , (b)  $\text{GBC} = 1.0$

## 7.6 Thermally-Induced Fracture Analysis of Polycrystalline Materials

In this section, several numerical cases are considered to verify the current formulation and demonstrate its capabilities. First, static analysis of an isotropic plate subjected to a thermal loading problem is considered to verify the thermo-mechanical peridynamic formulation. Next, the same analysis is repeated by considering a single cubic crystal and cubic polycrystals instead of isotropic material. The solution to the static cases is obtained by utilizing an implicit scheme by directly equating the inertia term to 0 in the peridynamic equation of motion given in Eqs. (6.1) and (6.2) and solving a matrix system to obtain the solution as explained in (Bobaru et al., 2009).

Following static analyses, dynamic analysis of cubic polycrystals, with pre-existing cracks subjected to thermal loading, problems are performed. Finally, a similar case is considered by

investigating the thermos-mechanical behavior of a ceramic material made of two materials. The solution to the dynamic analysis is obtained by using explicit time integration and utilizing a stable time step size to obtain a stable solution as explained in (Madenci and Oterkus, 2014).

All problem cases have two-dimensional models based on plane-stress assumption. The thickness of the plate is provided for the completeness of the information. The discretization size and horizon size used in numerical cases are sufficient to obtain accurate results with reasonable computational time. To demonstrate the suitability of the discretization and horizon size utilized in this study, convergence studies are performed and demonstrated in Appendix.

### 7.6.1 Static analysis of isotropic material under thermal loading

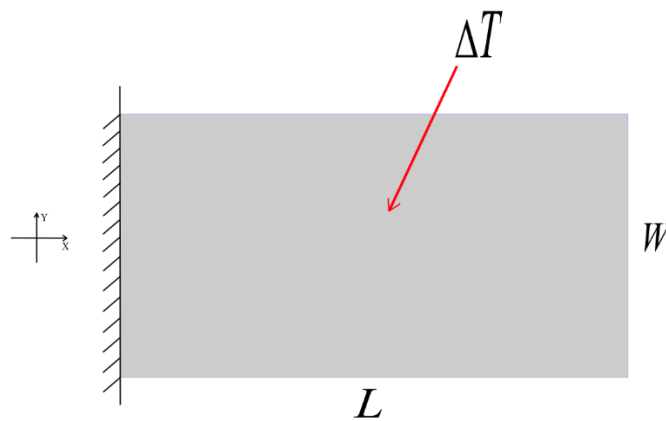


**Figure 7.11** Two-dimensional plate subjected to thermal loading

The two-dimensional model shown in Fig. 7.11 has a length of  $L = 0.1542$  m and a width of  $W = 0.0762$  m. The thickness of the plate is  $0.1651 \times 10^{-3}$  m. The elastic modulus and Poisson's ratio are 200 GPa and  $1/3$ , respectively, and the density of the material is  $7850 \text{ Kg/m}^3$ . The thermal expansion coefficient is given as  $23 \times 10^{-6} / ^\circ\text{C}$ . The PD model is generated by  $240 \times 120$  points and the grid spacing is  $dx = 0.635 \times 10^{-3}$  m. The horizon size is selected as  $\delta = 3 \times dx$ . The left edge of the plate is fully constrained by creating a fictitious boundary region with a thickness equivalent to the horizon size. Both displacement components in  $x$ - and  $y$ -directions are constrained inside the fictitious region. The thermal loading is applied in the form of a temperature change as  $900 \text{ }^\circ\text{C}$  for all nodes, i.e.,  $\Delta T = 900^\circ\text{C}$ . The results of the points on the vertical and horizontal centerlines of the plate are chosen to compare with the FEM results and the variation of the displacements along the centerlines is shown in Fig. 7.12.

It can be seen that the results of PD are identical to the FEM results and the accuracy of the model for the thermal expansion problem of isotropic material is verified.

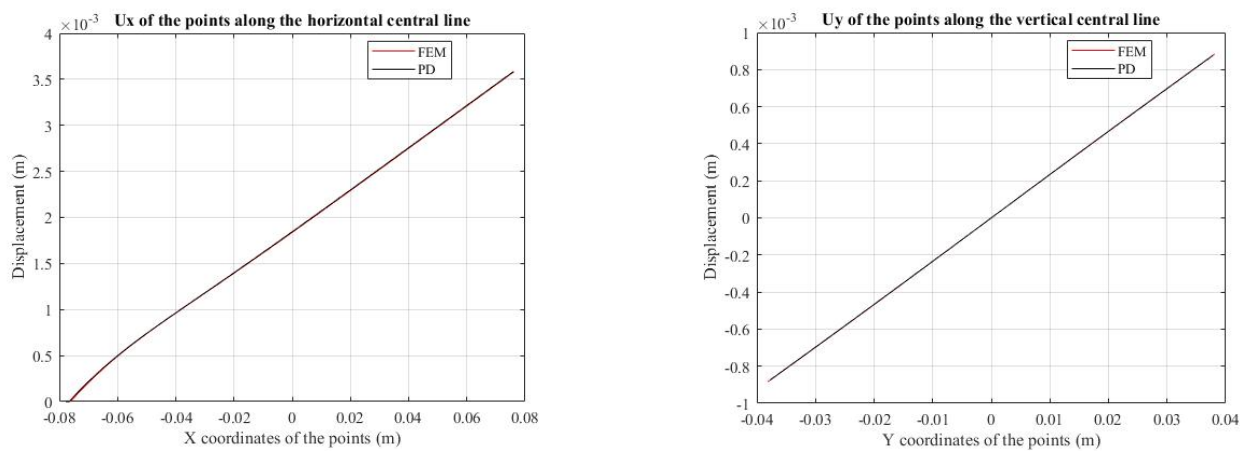


**Figure 7.12** Displacements of material points along the central lines of an isotropic material

### 7.6.2 Static analysis of a single cubic crystal under thermal loading

For the second numerical case, a single cubic crystal is considered. The size of the model for the thermal single-crystal analysis is the same as defined in Section 7.6.1. The material of the cubic crystal is iron and for iron crystal, the stiffness matrix coefficients are given as  $c_{11} = 231.4$  GPa ,  $c_{12} = 134.7$  GPa , and  $c_{44} = 116.4$  GPa . The orientation of the crystal is defined as  $0^\circ$ , i.e., Type-2 bonds are placed at  $45^\circ$ ,  $135^\circ$ ,  $225^\circ$ , and  $315^\circ$  orientations. The loading condition and boundary condition are also the same as in the previous section. The PD displacements, in  $x$ - and  $y$ - directions, of the two orthogonal centerlines are collected and their comparison against FEM is given in Fig. 7.13. Results from both approaches are in good agreement with each other which shows that the microscale PD model can provide accurate results for the thermal loading problems of a cubic crystal under the static loading condition.

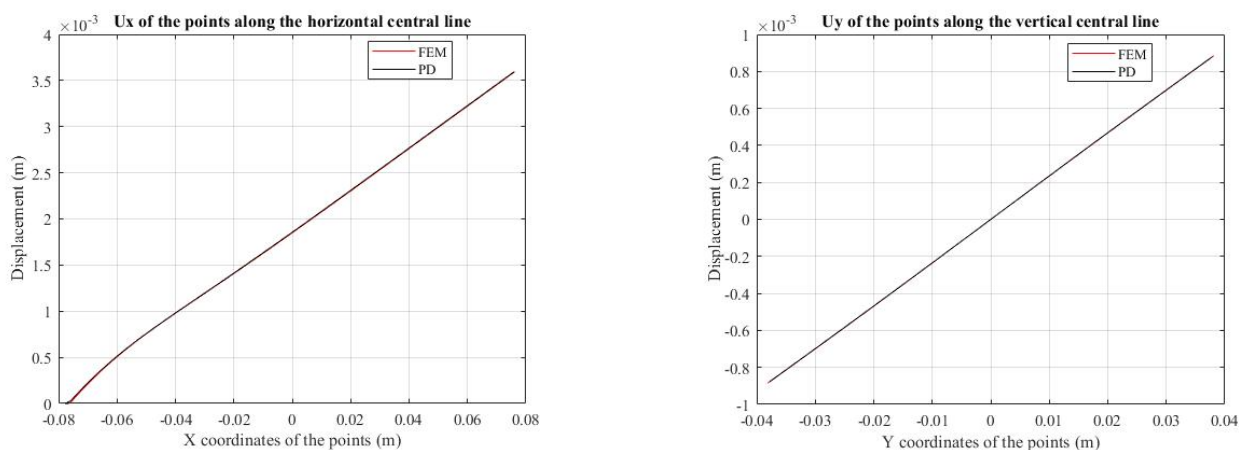


**Figure 7.13** Displacements of material points along the central lines of a single cubic crystal

### 7.6.3 Static analysis of cubic polycrystals under thermal loading

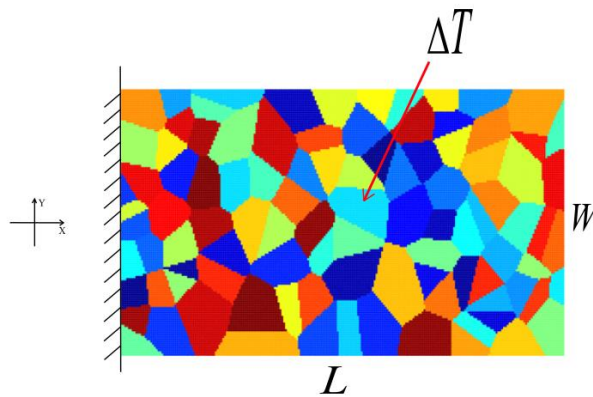


**Figure 7.14** Polycrystalline structure subjected to thermal loading

In order to further test the accuracy of the model for cubic polycrystals, a  $5 \text{ mm} \times 2.5 \text{ mm}$  iron plate with a thickness of  $0.5 \text{ mm}$  is considered with 100 grains (Fig. 7.14). Apart from the change in the geometry of the plate, the remaining parameters are the same as in the single-crystal example. For each grain, the orientation of the crystal is randomly selected. By comparing the displacements between PD and FEM results as shown in Fig. 7.15, it can be concluded that for cubic polycrystals, the PD model can capture correct results for the thermally-induced deformation problem.

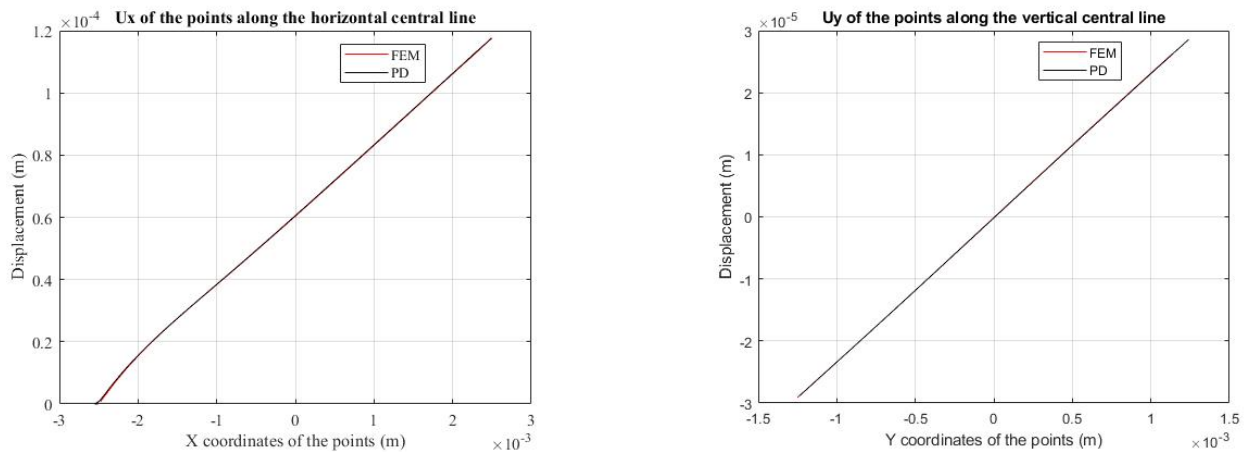


**Figure 7.15** Displacements of the material points along the central lines of cubic polycrystals

### 7.6.4 Dynamic analysis of cubic polycrystals with pre-existing cracks under thermal loading

For the purpose of investigating the fracture behavior and the effects of grain size and grain boundary strength for the cubic polycrystalline materials under thermal loading, a  $10 \text{ mm} \times 10 \text{ mm}$  plate made of  $\beta$ -silicon carbide was chosen and the model was created using  $200 \times 200$  PD points. The thickness of the plate is the same as the PD grid size  $dx$  which is

equal to 0.05 mm. The stiffness matrix coefficients for the silicon carbide are given as  $c_{11} = 395$  GPa,  $c_{12} = 123$  GPa, and  $c_{44} = 236$  GPa (Dirras et al., 2004). The density of the silicon carbide is  $3100 \text{ Kg/m}^3$  and the thermal expansion coefficient is  $6.58 \times 10^{-6} / ^\circ\text{C}$ . The critical stretch of the silicon carbide was calculated using the fracture toughness of  $3.46 \times 10^6 \text{ MPa}\sqrt{\text{m}}$  (Pharr et al., 2006). The time step size for explicit time integration is specified as  $1 \times 10^{-9}$  s. For the dynamic cooling process, the model is free from any mechanical constraints, and the temperature decreases by  $300 \text{ }^\circ\text{C}$ , i.e.  $\Delta T = -300^\circ\text{C}$ , over a short period of time ( $3 \times 10^{-6}$  s). Two different types of pre-existing cracks were considered. The first one is a 2 mm crack horizontally located at the centre of the plate. For the second type, two small cracks were located at the top and bottom edges of the plate with a length of 1 mm (Fig. 7.16).

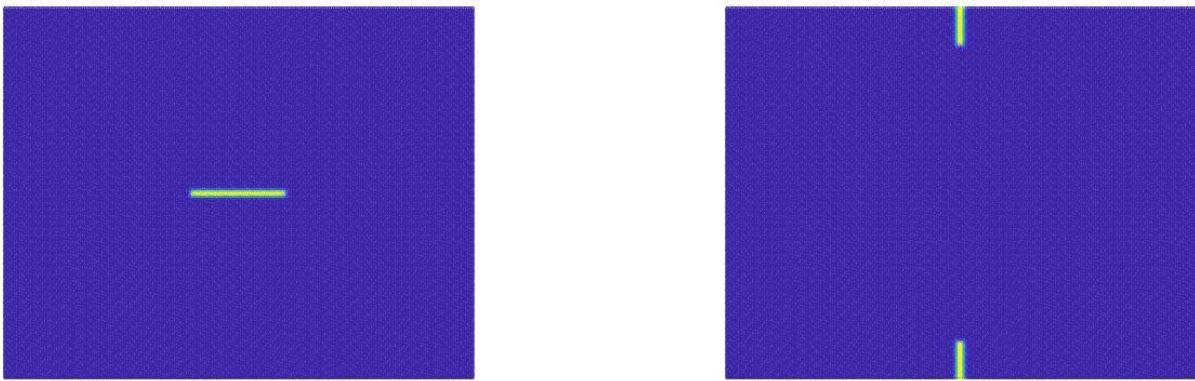


**Figure 7.16** Pre-existing cracks (a) horizontal, (b) vertical

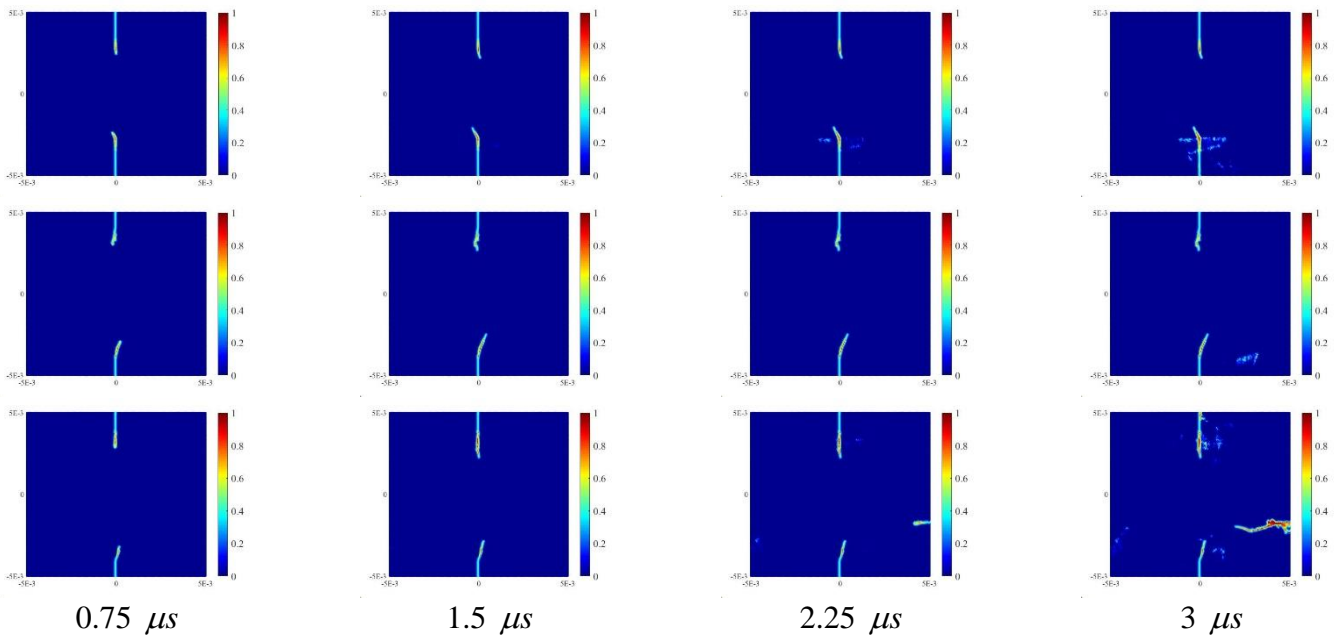


**Figure 7.17** Crack propagation for the vertical pre-existing crack case for the different number of grains. From the top to the bottom the number of the grains are: 20, 50, and 100

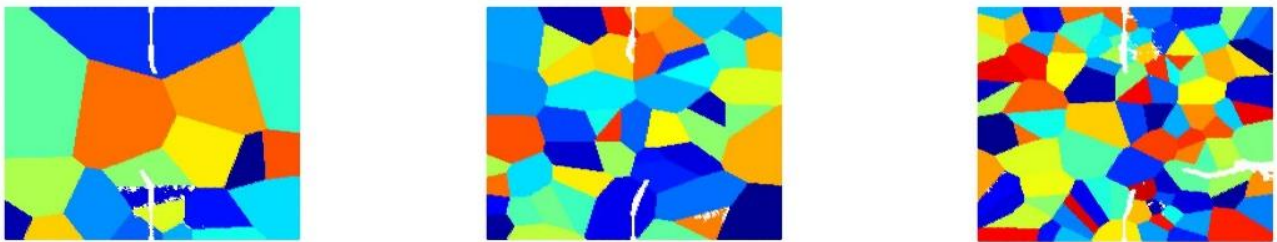


**Figure 7.18** Crack propagation for the vertical pre-existing crack case at 3  $\mu s$  for 20, 50, and 100 grains

The plate was created using a different number of grains (20, 50, and 100) to explore the effect of grain size on fracture behavior. The grain Boundary Coefficient is specified as  $GBC = 1$ . The plots of the propagation of the cracks are shown in Figs. 7.17 and 7.19 and the crack propagation inside the crystals are also presented in Figs. 7.18 and 7.20. For the vertical crack, with the decrease of the temperature and shrinkage of the plate, the crack starts to propagate from the initial notch. However, it can be seen that the speed of the crack propagation is slowing down and there is no significant crack propagation after 1.5  $\mu s$ . During the entire process, there is no obvious crack branch occurrence. Based on the plots of the final stage, the number of grains does not have a big impact on the main crack. However, for the 100 grains plate, there is an initiation of a new crack from the boundary of the plate. On the basis of the crystal plots with cracks, all three cases are showing the transgranular crack pattern and the cracks propagate through the crystals rather than along the crystal boundaries. The crack nucleation at the right

edge, for the 100 grains case, is mainly caused due to increase in grain boundaries as the number of grains increases.

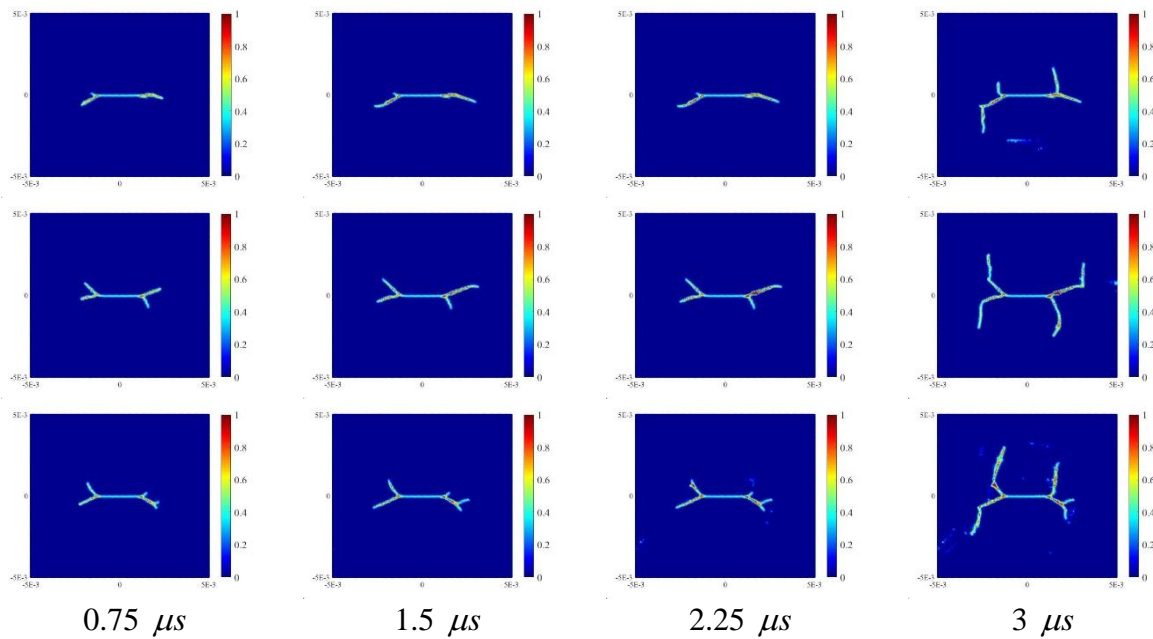


**Figure 7.19** Crack propagation for the horizontal pre-existing crack case for the different number of grains. From the top to the bottom the number of the grains are: 20, 50, and 100

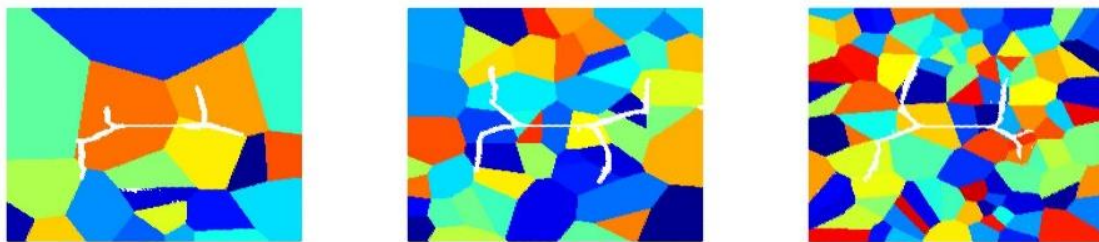


**Figure 7.20** Crack propagation for the horizontal pre-existing crack case at 3  $\mu s$  for 20, 50, and 100 grains

For the horizontal pre-existing crack case, with the shrinkage of the plate, the crack branches to propagate but the propagation is not severe until the temperature change is over 225 °C and then the crack propagates dramatically from the branch tip. It can be seen that the plate with 100 grains has more branches and the boundary has more potential to initiate new cracks than in the remaining two cases. This can also be explained by the increase of grain boundaries similar to the vertical crack condition. It can be concluded that with the increase in the number of grains, the possibility of new crack initiation increases. Moreover, at the final stage, even if the crack path is not the same, the fracture severity of the three cases is still in a similar manner. This means that the patterns of the main crack are not significantly influenced by the number of grains, which is also in accordance with the conclusion of De Meo et al. (De Meo et al., 2016)

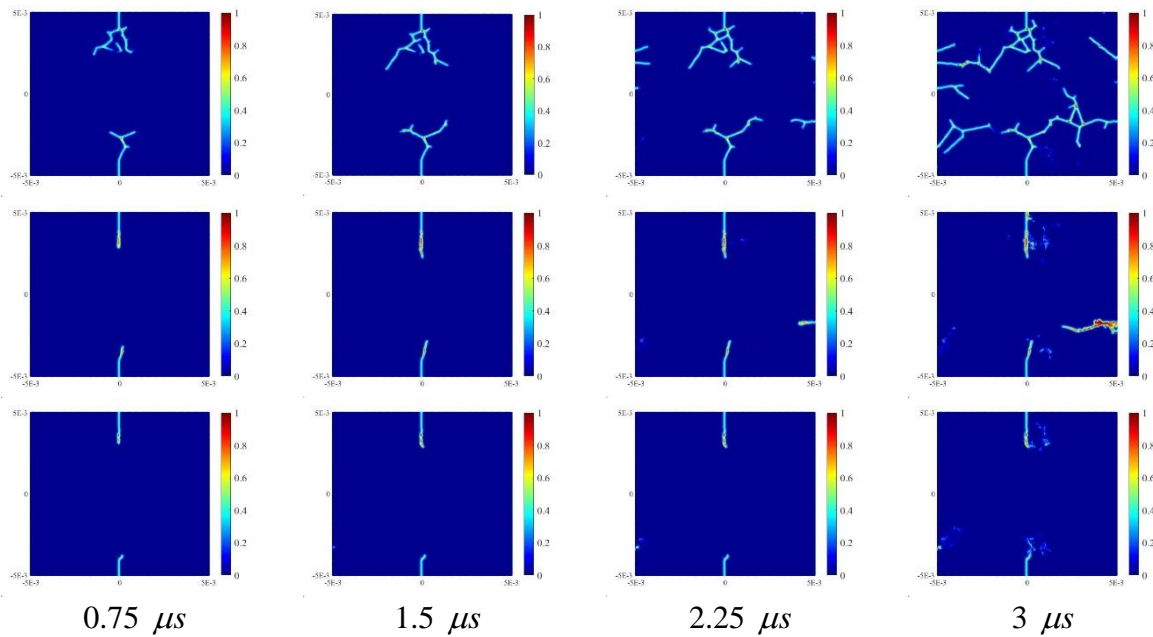


**Figure 7.21** Crack propagation for the vertical pre-existing crack for different values of GBC. From the top to the bottom the values of GBC are: 0.5, 1, and 2

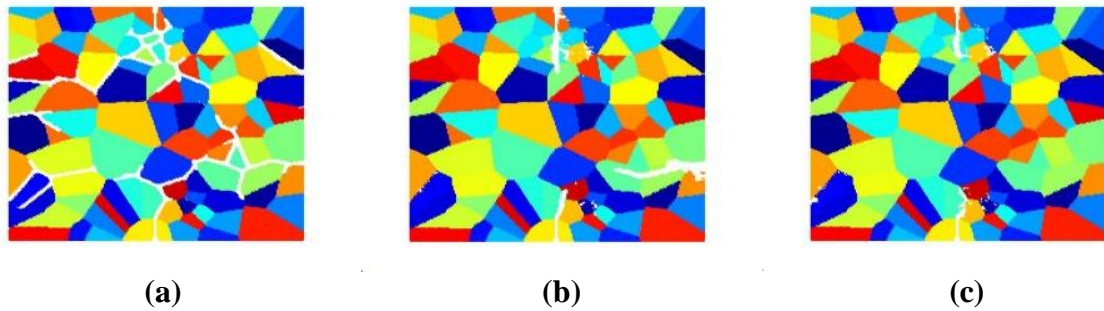


**Figure 7.22** Crack propagation for the vertical pre-existing crack at  $3 \mu s$  for GBC values of (a) 0.5, (b) 1, and (c) 2

Next, different values of the GBC are considered for 100 grains and both types of cracks to investigate the effect of grain boundary strength. It is expected that if the GBC is less than 1, the fracture behavior becomes more intergranular because the strength of the bond crossing the grain boundary becomes weaker than the bonds inside the grains. On the contrary, the crack pattern becomes transgranular with the growth of the value of GBC and the crack prefers to propagate within the crystals rather than along the grain boundaries. As shown in Figs. 7.21-7.24, Regardless of the crack being vertical or horizontal, when  $GBC=0.5$ , the crack propagates from the pre-existing crack and the newly generated crack becomes much more severe than in the remaining two cases. Additionally, it can be seen from the plots of the grains that the crack starts to propagate along the grain boundaries when  $GBC=0.5$ . It should also be mentioned that the crack patterns are not strongly influenced when  $GBC=2$  with respect to  $GBC=1$  and the

plots for these two cases are roughly identical except that there are new cracks initiated from the grain boundaries for the vertical crack condition for GBC=1. Actually, this phenomenon also meets the observation of De Meo et al. (De Meo et al., 2016) and it can be inferred that the strong grain boundaries will be beneficial for reducing the possibility of initiation of new cracks.

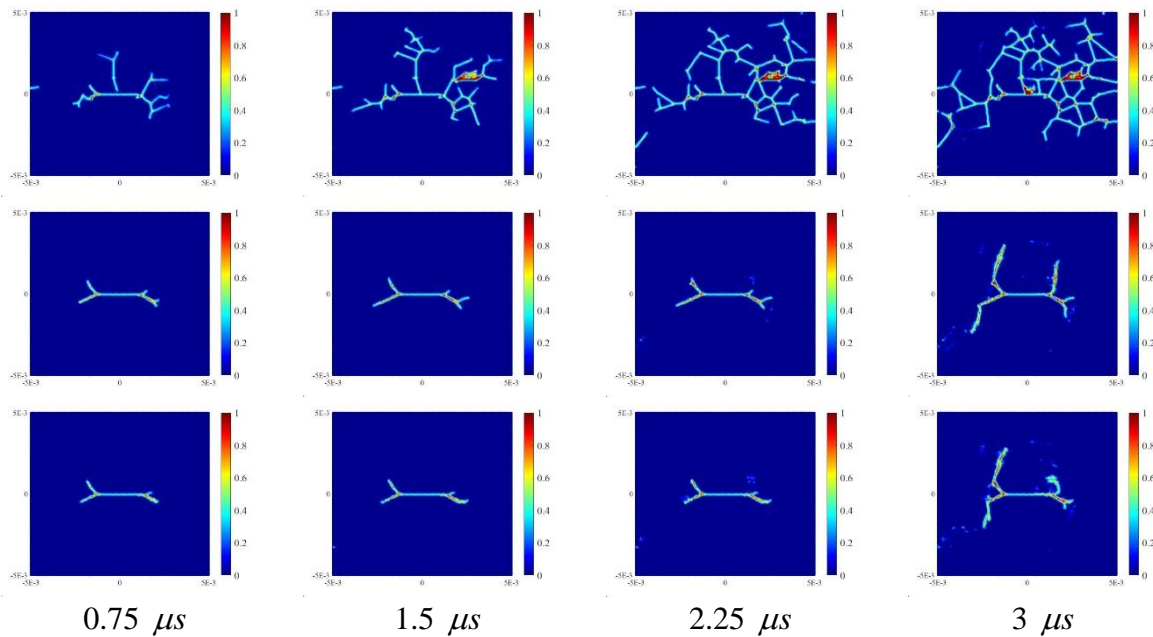


**Figure 7.23** Crack propagation for the horizontal pre-existing crack case for different values of GBC. From the top to the bottom the values of GBC are: 0.5, 1, and 2

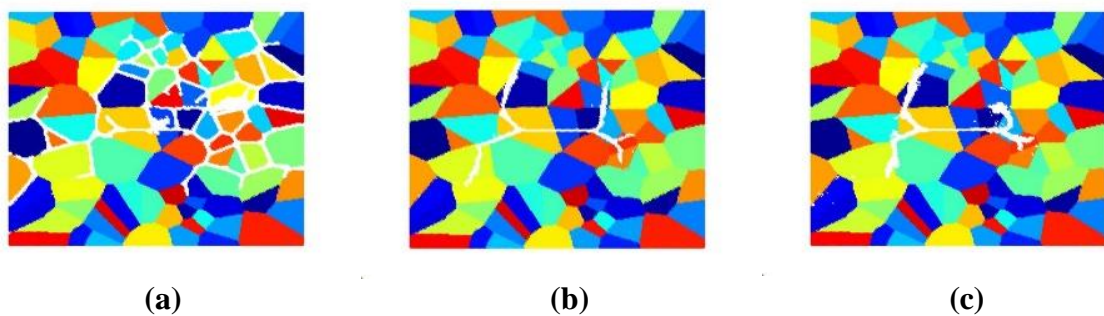


**Figure 7.24** Crack propagation for the horizontal pre-existing crack case at 3  $\mu s$  for GBC values of (a) 0.5, (b) 1, and (c) 2

### 7.6.5 Dynamic analysis of ceramic made of two materials with pre-existing cracks under thermal loading

In this section, a type of ceramic, which is constituted of two materials (silicon carbide and alumina), is considered under the thermal loading condition based on an earlier study by Geraci and Aliabadi (Geraci and Aliabadi, 2017). They utilize the BZM to investigate the effect of the number of grains and material composition (the percentages of the silicon carbide). In this

study, the PD model is used to analyze the same problem and the effect of the GBC is also taken into consideration. Although the crystal system for silicon carbide and alumina are cubic/hexagonal and trigonal, respectively, according to (Geraci and Aliabadi, 2017), these two materials can be treated as isotropic materials for simplification. To be able to compare PD results with the results given in (Geraci and Aliabadi, 2017), the same approach is utilized by treating two materials as isotropic materials. The required parameters for the two materials are collected and summarized in Table 7.1 (Geraci and Aliabadi, 2017):

**Table 7.1** Material information for silicon carbide and alumina

Materials	Elastic Modulus (GPa)	Thermal Expansion Coefficient ( $^{\circ}\text{C}$ )	Density ( $\text{Kg} / \text{m}^3$ )	Fracture toughness ( $\text{MPa}\sqrt{\text{m}}$ )
Silicon carbide	470	$4 \times 10^{-6}$	3100	3
Alumina	431	$8.4 \times 10^{-6}$	3690	3

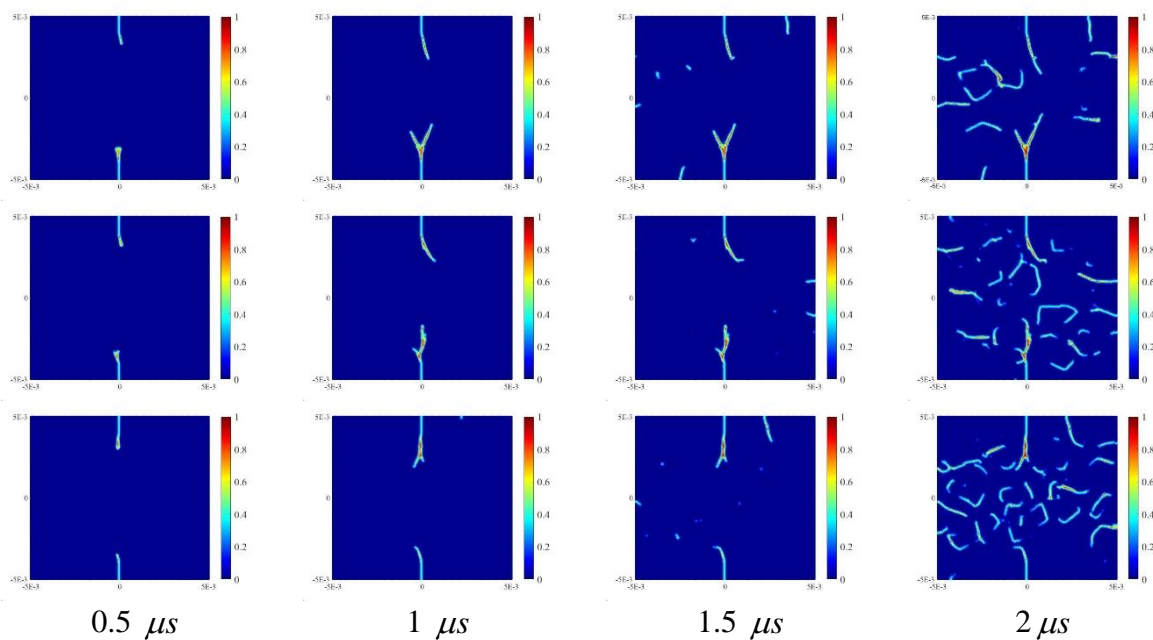
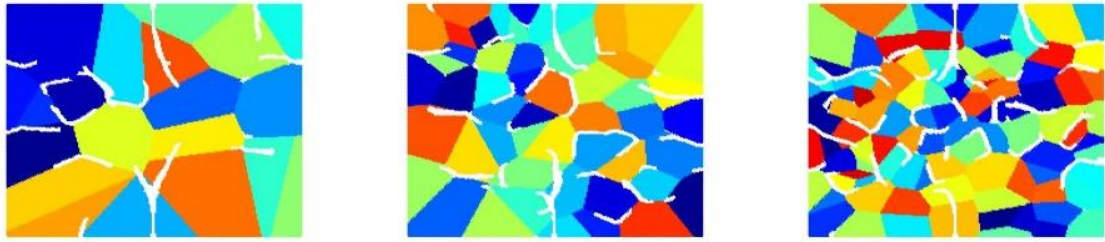
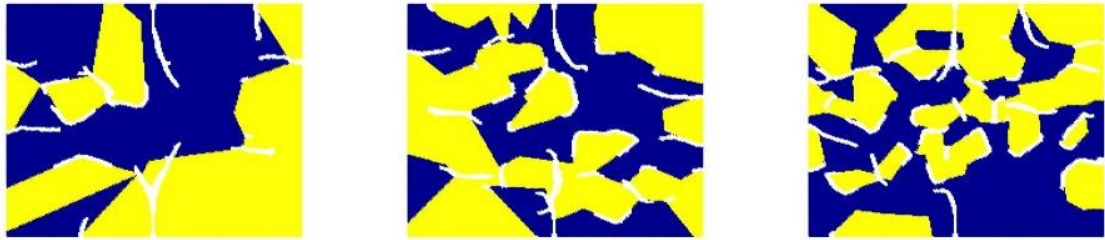


**Figure 7.25** Crack propagation for the vertical pre-existing crack case for the different number of grains with 50% silicon carbide. From the top to the bottom the number of the grains are: 20, 50, and 100



(a) Crack propagation showing the distribution of crystals.



(b) Crack propagation showing the material composition (blue represents silicon carbide)

**Figure 7.26** Crack propagation for the vertical pre-existing crack case with crystals and material composition at  $2 \mu s$  for 20, 50, and 100 grains with 50% silicon carbide

The geometry of the model (number of PD points, the patterns of the pre-existing cracks, and the size of the plate) is the same as the previous Section 7.6.4. The only difference is the range of temperature change which has been reduced to  $200 \text{ }^\circ\text{C}$  because the currently used materials are more sensitive to thermal loading. For the condition of the different numbers of grains, 20, 50, and 100 grains are considered with  $GBC=1$ . The percentage of silicon carbide is kept at 50%, i.e., almost half of the grains are made of silicon carbide and the rest is alumina. As shown in Fig. 7.25, for the vertical crack, with the decrease in the number of grains, the main crack becomes easier to branch and the crack is more likely to propagate approaching the other edge of the plate. These results agree with the conclusion drawn by Geraci and Aliabadi (Geraci and Aliabadi, 2017). The damage plots with the distribution of crystals and the two materials are also provided in Fig. 7.26 to support the conclusion.

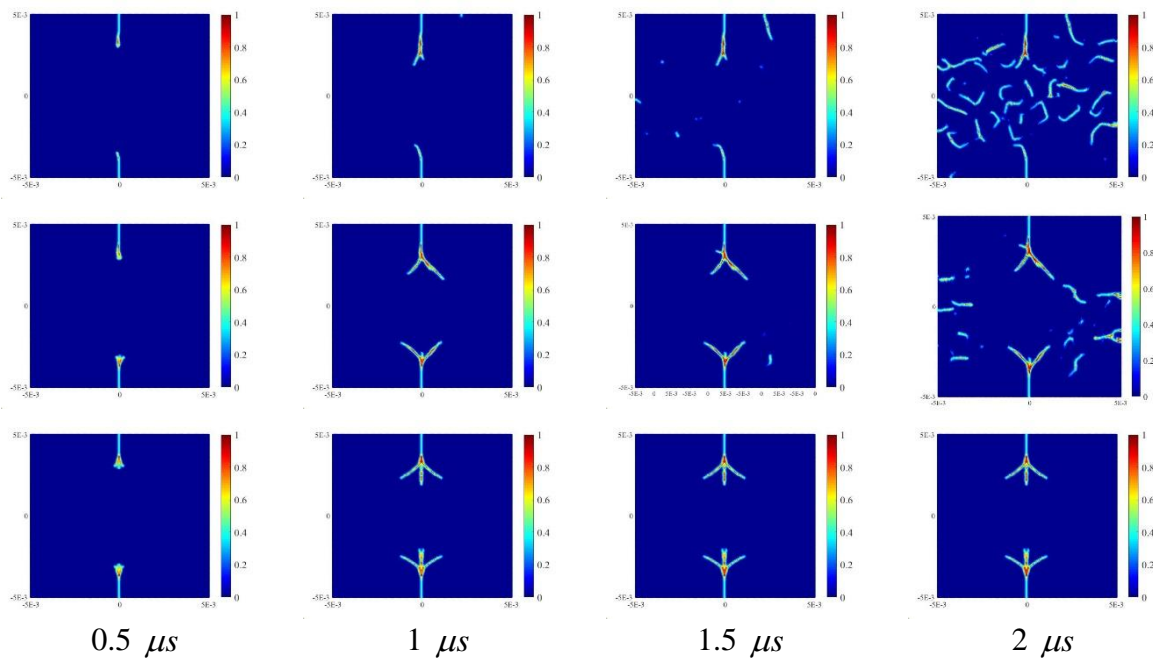


**Figure 7.27** Crack propagation for the vertical pre-existing crack for different percentages of silicon carbide with 100 grains. From the top to the bottom the percentages of the silicon carbide are: 50%, 10%, and 0%



(a) Crack propagation showing the distribution of crystals.



(b) Crack propagation showing the material composition (blue represents silicon carbide).

**Figure 7.28** Crack propagation for the vertical pre-existing crack case with crystals and material composition at 2  $\mu s$  for 50%, 10%, and 0% silicon carbide with 100 grains

In order to test the influence of the percent of silicon carbide, the plate with 100 grains is considered. The number of silicon carbide crystals was reduced from 50% to 10% and then to 0%. Due to the fact that the thermal expansion coefficient of silicon carbide is about half of the alumina and the strength and fracture toughness of the two materials are quite close, it is much

easier for the crack to propagate in alumina rather than in silicon carbide. As can be seen from the plots in Fig. 7.27, the main crack is branching although this is not obvious for the 50% silicon carbide case. However, when the percentage has been reduced to 10%, there exist two branches at the initial crack tip and the number of branched cracks increases to 3 when the material is pure alumina. It can be concluded that with the increase of silicon carbide, the severity of the main crack is limited. However, the drawback is also prominent, there are small cracks initiating from the grain boundaries which can be further observed in Fig. 7.28. It can also be shown that the difference of the coefficient of thermal expansion,  $\alpha$ , between different materials will lead to the initiation of new cracks.

For the plate with 100 grains and 50% silicon carbide, different GBC is also considered. As shown in Figs. 7.29 and 7.30, cracks initiating from the grain boundaries become much more severe with  $GBC=0.5$ , and the shape of the single crystals made of different materials can be seen clearly. Furthermore, the crack patterns of the remaining two conditions are quite similar, which can also further enhance the conclusion about the effect of GBC in Section 7.6.4.

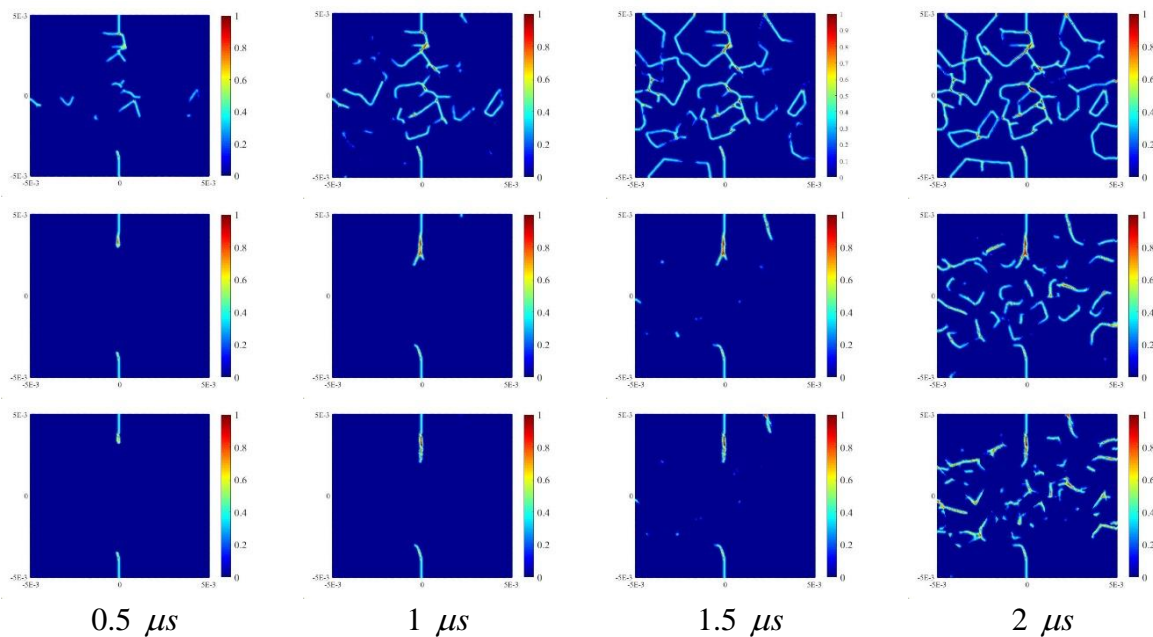
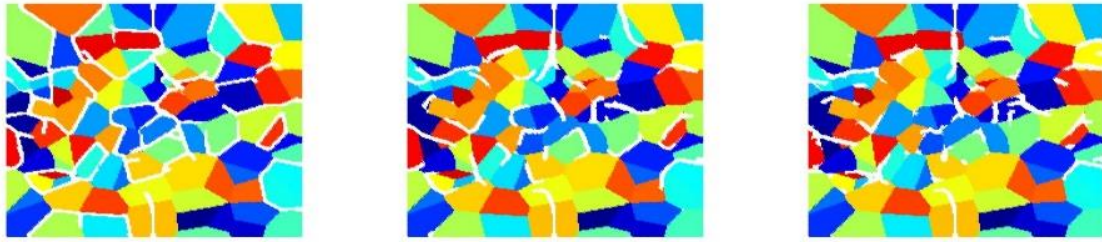
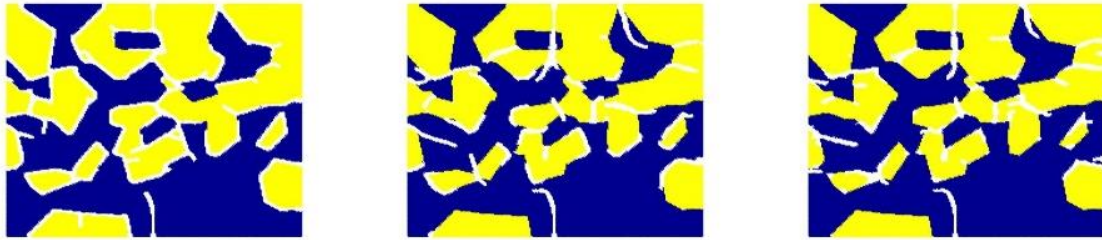


**Figure 7.29** Crack propagation for the vertical pre-existing crack case for different values of GBC with 100 grains and 50% silicon carbide. From the top to the bottom the values of GBC are: 0.5, 1, and 2



(a) Crack propagation showing the distribution of crystals.



(b) Crack propagation showing the material composition (blue represents silicon carbide).

**Figure 7.30** Crack propagation for the vertical pre-existing crack case with crystals and material composition at  $2 \mu s$  for 0.5, 1, and 2 GBC with 100 grains

Horizontal pre-existing crack is also considered. After comparing the plots for various conditions (Fig. 7.31 to Fig. 7.36), the same conclusions can be obtained as the vertical pre-existing crack and they can be summarized as: 1) with the increase of the number of grains, the propagation of the main crack and its branches become relatively hindered but the initiation of small cracks at the grain boundary becomes serious, 2) with the increase of silicon carbide, the severity of the main crack decreases due to the decrease of the branches, 3) if the grain boundary strength becomes weaker, the crack pattern becomes intergranular but increasing the value of GBC does not significantly influence the results. These conclusions are immune to the type of pre-existing crack and match well with Geraci and Aliabadi (Geraci and Aliabadi, 2017).

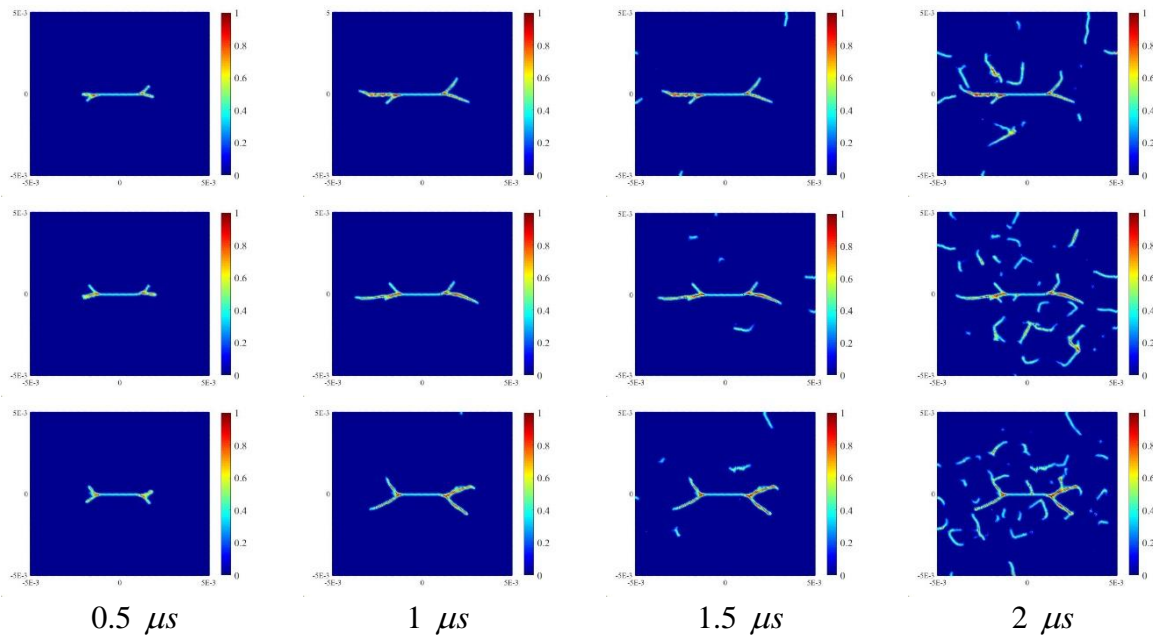


**Figure 7.31** Crack propagation for the horizontal pre-existing crack case for the different number of grains with 50% silicon carbide. From the top to the bottom the number of the grains are: 20, 50, and 100



(a) Crack propagation showing the distribution of crystals.



(b) Crack propagation showing the material composition (blue represents silicon carbide).

**Figure 7.32** Crack propagation for the horizontal pre-existing crack case with crystals and material composition at 2  $\mu s$  for 20, 50, and 100 grains with 50% silicon carbide

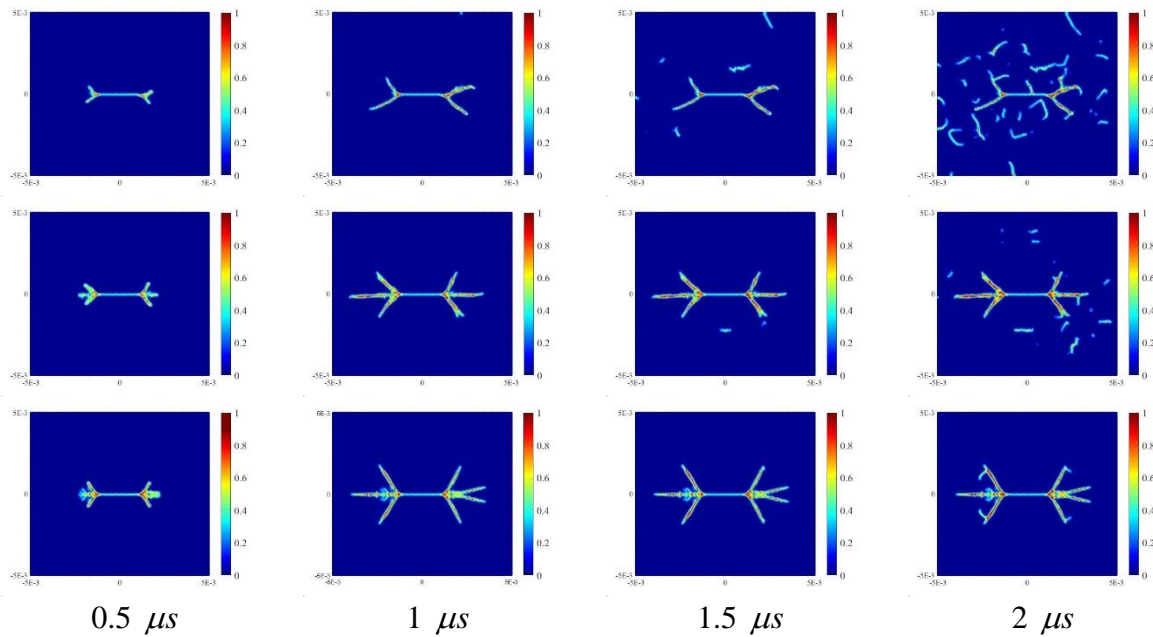
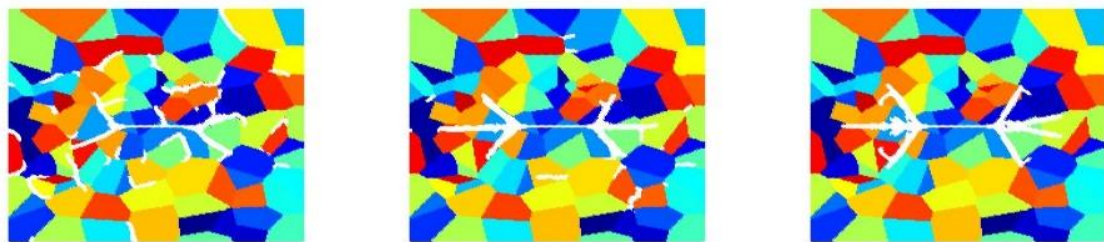


**Figure 7.33** Crack propagation for the horizontal pre-existing crack case for different percentages of silicon carbide with 100 grains. From the top to the bottom the percentages of the silicon carbide are: 50%, 10%, and 0%



(a) Crack propagation showing the distribution of crystals.



(b) Crack propagation showing the material composition (blue represents silicon carbide).

**Figure 7.34** Crack propagation for the horizontal pre-existing crack case with crystals and material composition at 2  $\mu s$  for 50%, 10%, and 0% silicon carbide with 100 grains

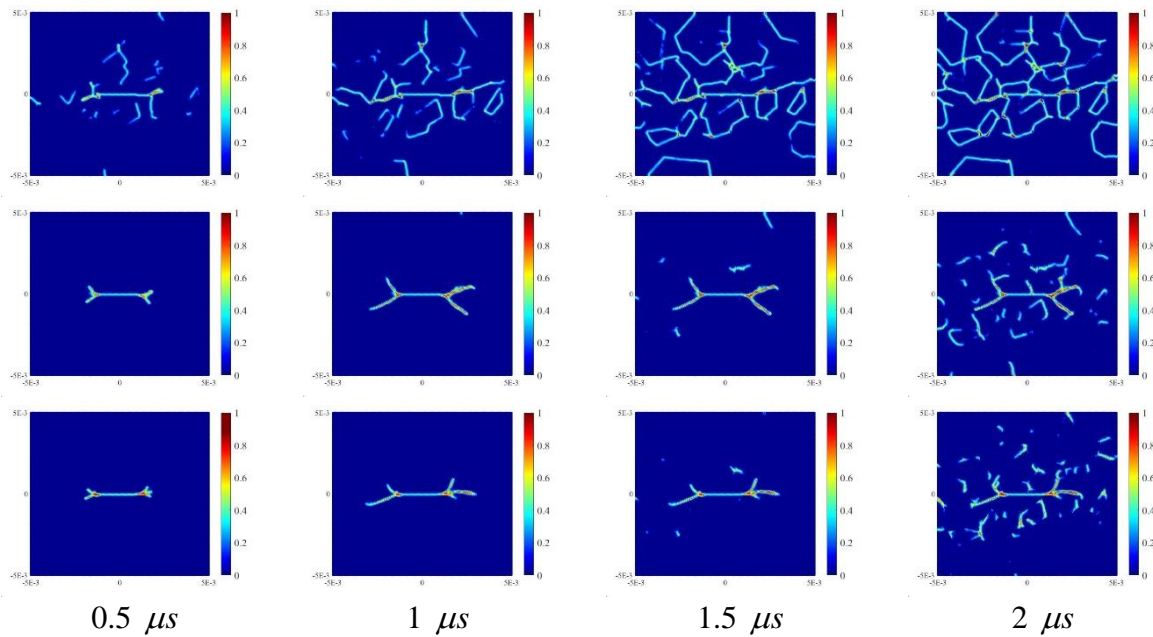
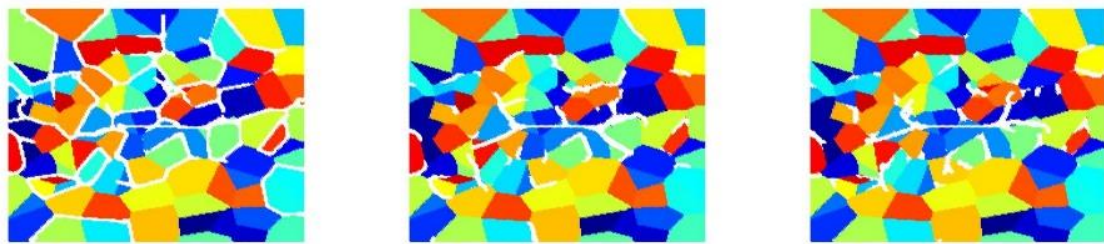
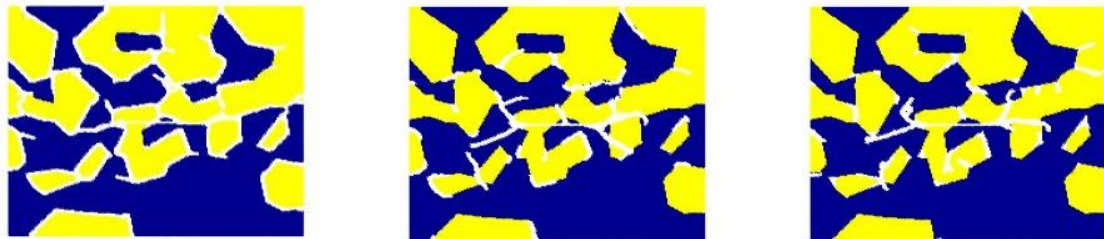


**Figure 7.35** Crack propagation for the horizontal pre-existing crack case for different values of GBC with 100 grains and 50% silicon carbide. From the top to the bottom the values of GBC are: 0.5, 1, and 2



(a) Crack propagation showing the distribution of crystals.



(b) Crack propagation showing the material composition (blue represents silicon carbide).

**Figure 7.36** Crack propagation for the horizontal pre-existing crack case with crystals and material composition at  $2 \mu s$  for 0.5, 1, and 2 GBC with 100 grains

## 7.7 Summary

In this study, firstly, the effect of porosity on intergranular brittle fracture was investigated by using peridynamics. Different numbers of cases were considered for different numbers of grains, different porosity ratios, different locations of pores, and different grain boundary

strengths. It was concluded that the severity of the crack especially the newly created cracks is influenced by the number of grains and porosity. Concerning the influence of grain boundary strength, with the increase of GBC, the effect of porosity dramatically decreases and the fracture pattern at the microscale becomes identical to the macroscale crack pattern.

Secondly, thermally-induced crack propagation in polycrystalline materials was simulated using peridynamics. The accuracy of the model was tested and verified with three static cases under thermal loading for three different material models including isotropic, single cubic crystal, and cubic polycrystal. The PD analysis displacement results were identical to conventional FEM results. Afterward, a cubic polycrystalline material with two different types of pre-existing cracks, i.e., vertical and horizontal, was analyzed by applying dynamic cooling temperature change. The effects of grain size and grain boundary strength were investigated. The effect of grain size was much more obvious in the horizontal crack case in which branching crack behavior was observed. For the vertical crack case, initial main cracks propagated in a self-similar manner. Grain boundary strength has a significant influence on crack behavior. As expected, for weaker grain boundaries intergranular fracture pattern was observed whereas for stronger grain boundaries transgranular crack pattern was more dominant. Finally, a ceramic material made of two different materials, i.e., silicon carbide and alumina, was considered. As opposed to the cubic polycrystalline case, crack branching occurred for both vertical and horizontal cracks. Crack branching was much more significant when the silicon carbide ratio is higher due to the difference in coefficients of thermal expansion of two different materials. As in the cubic polycrystalline case, as the grain boundary strength decreases, the fracture mode turns into an intergranular character. The reached conclusions are in good agreement with the reference studies available in the literature.

Lastly, based on the current PD model, there are still a large number of research aspects such as stress corrosion cracking and the pit-to-crack transition phenomenon that can be explored. The 2-D bond-based model can be extended to 3-D state-based model. Furthermore, more types of crystals like trigonal crystals can be researched.

## 8 Discussions

### 8.1 Achievements

The main achievements of this research are summarized below:

- iFEM-iQS4 element is applied to the tower of the referenced OWT. By using the strain data from the FEM analysis and considering the aerodynamic and hydrodynamic loadings, both static and dynamic numerical iFEM analyses are performed which makes the study more practical. iQS4 can be used for the SHM of the tower even with reduced sensors. Four longitudinal and two ring cables with suggested discretized sensor locations are decided and this can provide guidance for the real iFEM application. The composite blade of the NREL 5MW OWT is modeled, and the real loading condition is considered. The analysis with the iFEM-iQS4 element builds the accurate 3-D displacement fields for the blade with a practical number of sensors.
- iFEM-iQS4 element is used for monitoring and predicting the structural damage (geometrical defects) on offshore thin-walled structures. The cylindrical structure is modeled with both FEM and iFEM and the FEM analysis will act as the strain input provider for the iFEM analysis. The iFEM analysis is firstly validated against the referenced FEM results under the undamaged condition. By using the newly introduced damage judgment criterion, the accurate iFEM results of four cases with damage prove the potential of the iQS4 element for detecting the location and shape of the damage on this type of structure.
- The simpler and easier to be used inverse plane elements-iQP4 and iQP8 are developed as the initial step of the study in Chapter 5. After the analysis of several examples with both elements, it is found that the accuracy of the results has a close relation to the mesh of the iFEM model, but the element type does not have a significant impact on the results. Although reducing the number of sensors will lead to the loss of the accuracy of the analysis, by logically selecting the sensor locations, reasonable results can still be guaranteed. Different distributions of the sensors are required for different elements. Then the iPCT element is developed and it has the ability to reform the displacement fields for the crack tip region which allows the iFEM can be applied to structures with cracks. By adopting the displacement extrapolation method, the SIF at the crack tip can be computed and the accuracy of the results can still be kept in the reduced sensor condition.

- The PD fatigue model is applied to fatigue damage prediction. The initiation, growth, and rapid propagation of the crack caused by fatigue can be captured. The PD fatigue model is verified with a benchmark problem and the results are in good agreement with the experimental results. Then the PD fatigue model is employed to the given triplate of the OWT mooring lines. A constant amplitude loading, simplified from the provided real-time data, is applied to the triplate and different mooring line angles are taken into account. The results of the triplate fatigue analysis match well with the expected analytical results. And the evolution of the fracture can be clearly observed.
- The brittle fracture with porosity is analyzed by the PD polycrystal model. The number of grains, porosity ratio, locations of pores, and grain boundary strength are the variables of this work. And the influences of these variables are explored. Then the PD theory is extended with the thermal expansion coefficient. Together with the PD cubic polycrystalline model, thermally-induced crack propagation is under research. The model is successfully validated with three cases. Two types of pre-existing cracks are analyzed in dynamic conditions for both single cubic material and ceramic made from silicon carbide and alumina. The effects of the number of grains, grain size, GBC, and material composition are explored.

## **8.2 Novelty and contribution to the field**

Offshore wind turbines are always surrounded by harsh marine environments which leads to a reliable SHM system being necessary. Although there are some SHM systems that have been introduced for single components of the OWT (vid. Section 1.1), these studies cannot reform the 3-D full-field displacements for the components. Additionally, relatively complete SHM systems for the majority of components of the OWT are also not available. iFEM based on the iQS4 element provides a reasonable and practical choice for overcoming these limitations. Despite the iFEM has been employed in the marine field such as the Chemical tanker and bulk carrier, it is the first time to apply this method to the OWT. According to the study in Chapter 4, the shape and stress sensing of the tower and blade of the OWT can be successfully finished even with a limited number of sensors. The cost-effectively practical sensor locations are approached and suggested. The potential of the iFEM-iQS4 element for the whole SHM system is obviously manifested. And this study can provide beneficial guidance for the real application of iFEM to the OWT. Besides, with the new damage identification parameter, the range of

iFEM-iQS4 application is extended to damage identification in offshore structures and the locations and shapes of structural dent damages can be accurately detected. (Chapter 4.5) The literature was lacking such novel applications and frameworks, but the studies can now be found in the first and second journal papers in Section 8.4.1 and the report of the first project in Section 8.4.3.

SIF is a major parameter for judging the capability of resisting cracks and estimating the tendency of crack propagation. 8-node degenerated triangular crack tip element gives access to the calculation of the value of SIF by FEM and extensive use of this type of element can be witnessed even in commercial software like ANSYS. On the basis of this element combined with the fundamental theory of iFEM, the iPCT element is found in Chapter 5. With the iQP8 elements for the outside region of the crack tip and the harvested strain data from the sensors, the displacement fields of the structure can be regenerated. It shows the potential of applying iFEM to cracked structures which can help to overcome the weakness of the current iFEM. After utilizing the displacement extrapolation method, the value of the SIF at the crack tip can be evaluated. The current iPCT element allows the estimation of the opening and in-plane shear SIF. This element can enrich the function of iFEM and the engineering practice can also benefit from this development. The literature was lacking such a novel framework.

The fatigue phenomenon and its induced fracture are always capital problems for offshore structures. It is difficult to accurately forecast the remaining life of the structures and research about the fracture caused by fatigue is more difficult. PD fatigue model is, for the first time, applied to the real offshore components under the close-to-reality loading condition. The loading cycles leading to the initiation of the crack on the triplate are in good agreement with the analytical value for different mooring line angles. The current PD fatigue model provides a useful tool for the fatigue analysis of the OWT, and it can form a critical part of the entire SHM system. Moreover, the growth and rapid propagation of the fatigue-induced crack can also be captured clearly. The whole picture of the fatigue damage can be obtained, and it would be beneficial for the offshore operators by indicating the time and location of the fracture and its propagation progress. The inspection procedure for the offshore components can be guided to a certain extent. The PD fatigue analysis can also supply academic research about the fatigue phenomenon with a better understanding. The literature was lacking such a novel framework and this study was included in the report of the second project in Section 8.4.3.

Polycrystalline materials especially cubic polycrystals are the most commonly used materials in the offshore field, like steel. The fracture of these materials is affected by many factors, especially on the microscale. However, experiments with these materials are usually not available because of the great complexity and expensive cost. Computational modeling is a more reasonable way to research these materials. According to the literature, the PD model for the cubic polycrystalline material is mainly used in the field of corrosion (vid. [Sections 2.6](#)). It is the first time to use this model to explore the effect of porosity on brittle fracture. The severity of the crack especially the newly created cracks is influenced by the number of grains and porosity. But if the grain boundary strength is reinforced, the above impact will be weakened, and the fracture pattern will also be changed. Then in Chapter 7, the PD model with consideration of the thermal expansion coefficient is developed and the new model is also used for the fracture analysis, after validation, to research the parameters that influence the propagation of the crack at the microscale. Two types of materials (single cubic silicon carbide and ceramic made from silicon carbide and alumina) are chosen, and two kinds of pre-existing cracks are also defined. The crack propagation can be clearly shown, and the result of the ceramic is in good agreement with the reference. The PD model used in Chapter 7 can be an efficient tool for the computational analysis of the fracture behaviors of the general isotropic and cubic polycrystalline materials. The literature was lacking such novel frameworks and the results were published as the third and fourth journal papers in Section 8.4.3.

### **8.3 Gaps and recommended future work**

Despite the aimed tasks having been utterly finished as the achievements in this thesis, there are still gaps that need to be filled for each research aspect.

Concerning the iFEM analysis for the OWT, other components like foundations are still not implemented and a complete SHM system for the entire OWT would be preferred. Furthermore, current iFEM analyses are based on numerical strain inputs. Experiments with sensor-collected real strain data and then carrying out the iFEM analysis for the real offshore structures are highly recommended. For the composite blade, the dynamic analysis for the effects of different blade locations and variable wind velocities can be done. At the same time, because of the composite characteristic, the stress monitoring of the blade should also be made.

Concerning the iFEM damage prediction, the damage detection procedure for larger and more complex offshore installations could be a feasible way. The current parameter is limited to

isotropic materials, and it would be better to introduce the expression for composite materials so that it can be applied to structures such as blades. But the heavy burden comes from building an iFEM tool that can predict both structural defects and cracks. Combining the iFEM theory with the Peridynamics together would be a suitable direction.

Concerning the iPCT element, inverse triangular plane elements which can improve the application range of the iPCT element are essential. If the inverse triangular element is available, more complex structures with cracks can be modeled. More importantly, the inverse shell crack tip element which can estimate the SIF of the out-of-plane crack can be developed.

Concerning the PD fatigue analysis, the PD model for the fatigue analysis under variable loadings would be appealing. The fatigue analysis for other offshore components can be another option.

Concerning the PD cubic polycrystalline model, the difficulties would be enhancing the model from 2-D BBPD to 3-D SBPD. Additionally, the PD model for other types of crystals like trigonal is also a reasonable direction.

## 8.4 Research outputs

In this section, all of the author's research outputs have been provided and the majority of these outputs are straightforwardly related to the work in this thesis. These outputs can be divided into journal papers, conference and papers, and research projects with reports, and these works have already been published or submitted.

### 8.4.1 Journal papers

- **Li, M.**, Kefal, A., Cerik, B.C. and Oterkus, E., 2020. Dent damage identification in stiffened cylindrical structures using inverse Finite Element Method. *Ocean Engineering*, 198, p.106944.
- **Li, M.**, Kefal, A., Oterkus, E. and Oterkus, S., 2020. Structural health monitoring of an offshore wind turbine tower using iFEM methodology. *Ocean Engineering*, 204, p.107291.
- **Li, M.**, Lu, W., Oterkus, E. and Oterkus, S., 2020. Thermally-induced fracture analysis of polycrystalline materials by using peridynamics. *Engineering Analysis with Boundary Elements*, 117, pp.167-187.

- **Li, M.**, Oterkus, S. and Oterkus, E., 2020. Investigation of the effect of porosity on intergranular brittle fracture using peridynamics. *Procedia Structural Integrity*, 28, pp.472-481.
- Lu, W., **Li, M.**, Vazic, B., Oterkus, S., Oterkus, E. and Wang, Q., 2020. Peridynamic modelling of fracture in polycrystalline ice. *Journal of Mechanics*, 36(2), pp.223-234.

#### 8.4.2 Conference and papers

- **Li, M.**, Oterkus, S. and Oterkus, E., 2020, “Investigation of the Effect of Porosity on Intergranular Brittle Fracture Using Peridynamics,” 1<sup>st</sup> Virtual European Conference on Fracture (VECF1), Online, June 29 – July 1, 2020.
- **Li, M.**, Kefal, A., Cerik, B. C. and Oterkus, E., 2019, “Dent Damage Prediction by Using iFEM” ASME 2019 International Mechanical Engineering Congress & Exposition, 11-14 November 2019, Salt Lake City, UT, USA.
- **Li, M.Y.**, Kefal, A., Cerik, B. and Oterkus, E., 2019. Structural health monitoring of submarine pressure hull using inverse finite element method. *Trends in the Analysis and Design of Marine Structures*, pp.293-302.
- Lu, W., **Li, M.**, Vazic, B. Oterkus, S. and Oterkus, E., 2019, “Peridynamic Modelling of Polycrystalline Ice,” 25<sup>th</sup> International Conference on Port and Ocean Engineering under Arctic Conditions (POAC), 9-13 June 2019, Delft, Netherlands.
- Lu, W., **Li, M.**, Vazic, B., Oterkus, S. and Oterkus, E., 2019, “Polycrystalline Ice Modelling Using Peridynamics” ASME 2019 International Mechanical Engineering Congress & Exposition, 11-14 November 2019, Salt Lake City, UT, USA.
- Oterkus, E., Yang, Z., **Li, M.** and Oterkus, S., 2018, “Finite element implementation of peridynamics,” 10<sup>th</sup> European Solid Mechanics Conference, 2-6 July 2018, Bologna, Italy.
- Oterkus, S., Lu, W., **Li, M.**, Vazic, B. and Oterkus, E., 2020, “Peridynamic Polycrystalline Ice Model,” 3rd Annual Meeting of the SIAM Texas-Louisiana Section, 16-18 October 2020, College Station, TX, USA.
- Yang, Z., **Li, M.**, Oterkus, E. and Oterkus, S., 2018, “Peridynamic Modeling Using a Commercial Finite Element Software” ASME 2018 International Mechanical Engineering Congress & Exposition, 9-15 November 2018, Pittsburgh, PA, USA.

### **8.4.3 Research projects with reports**

- “Structural Health Monitoring of Offshore Wind Turbine” project funded by ORE Catapult
- “Condition Monitoring of Floating Wind Mooring Lines” project funded by Carbon Trust

## 9 Conclusions

### 9.1 Key findings

- For the tower and blade of the OWT, the iFEM-iQS4 element can generate a SHM system with high accuracy even with practical sensors during the real loading conditions. If the FBG technology is utilized, 6x2 cables of sensors would be sufficient for the monitoring of these components.
- With the help of the new damage parameter and the von Mises strain plot, iFEM can also predict the location and size of the dent damage on the offshore cylindrical structure without any disturbance on the daily monitoring.
- For the inverse plane element, increasing the mesh of the iFEM model will improve the accuracy. But there should be a balance between the level of accuracy and cost-effective purpose. The element type will not obviously affect the results, but it will change the sensor locations. These two types of inverse plane elements are feasible for the plane iFEM analysis. The newly introduced iPCT element can enhance the application of iFEM to the structures with cracks and the SIF at the crack tip can be computed.
- For the fatigue analysis of the triplate, the results from the PD fatigue model match well with the expected analytical results calculated from the conventional S-N curve for different mooring angles. The entire process of the fatigue fracture can be clearly observed. The PD fatigue model can act as the fatigue analysis tool for the OWT. It is also found that, with the increase of the mooring line angles, it will be faster to initiate the major crack and the major crack will also become severer. At the same time, the branched crack at the top rigid zone will become easier to propagate toward the edges of the triplate but the new crack around the bottom bridle eyes will be slightly hindered.
- There are also some findings collected from the analysis of the cubic polycrystal in the microscale: pores will initiate small cracks and they will also attract the propagation of the major crack; With the growth of the number of grains and pores, the fracture will become more serious, but this feature will not be impacted by the distribution of the grain and pore; The stronger the grain boundary, it will be more willing to propagate transgranular rather than intergranular and the fracture pattern will be more similar to the macroscale pattern; Finally, for the thermal case, there will be more newly created crack when the ratio of the silicon carbide is rising. These findings agree well with the

reference. The microscale fracture phenomenon of the OWT material can be researched by the PD polycrystal model.

## **9.2 Final remarks**

The formulation generated and the obtained results of this thesis support that the state-of-the-art methodologies which are iFEM and PD, respectively, owing to their advantages, can be used to perform comprehensive structural health monitoring for the OWTs. In summary, the iFEM and PD studies in this PhD thesis can be helpful for building a complete SHM system for the entire OWT from multiple perspectives.

## Appendix

For Section 7.6, the convergence study is performed for the dynamic analysis of ceramic made of two materials case. During the m-convergence test,  $100 \times 100$ ,  $200 \times 200$ , and  $400 \times 400$  PD points are chosen, and the number of the PD points is the only variable. The GBC is fixed at 1 and two different types of pre-existing cracks are considered. The results of the three cases are computed and the plots are shown in Fig. A.1 to Fig. A.4.

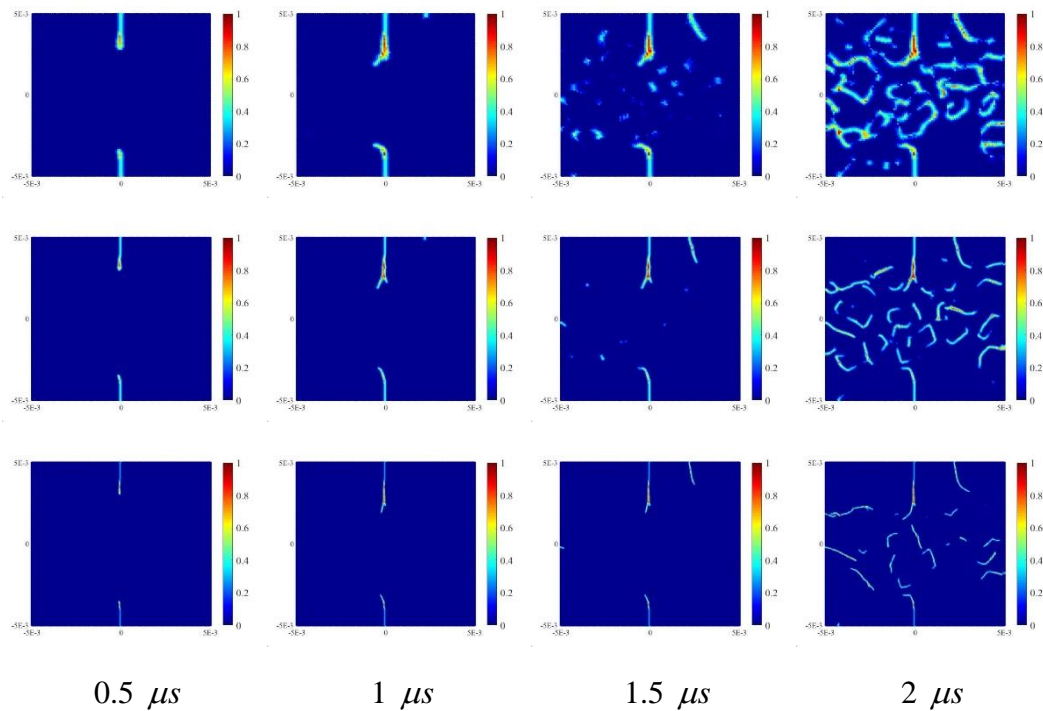
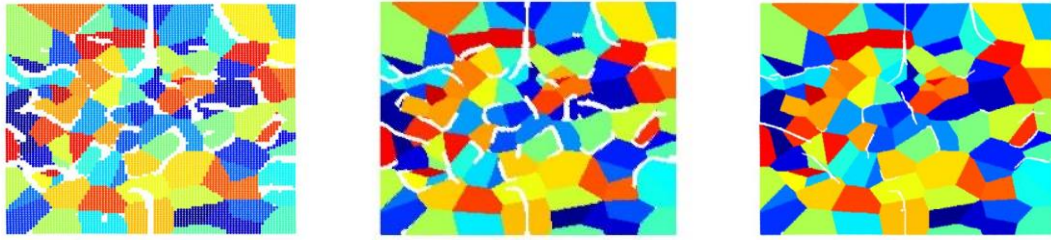
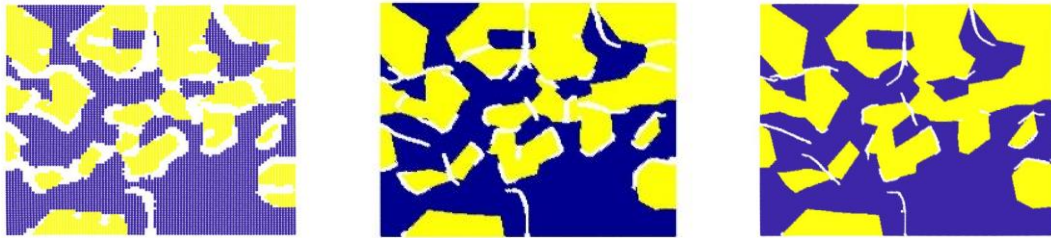


**Figure A.1** Crack propagation for the vertical pre-existing crack case for different numbers of PD points. From the top to the bottom the number of the points is:  $100 \times 100$ ,  $200 \times 200$ , and  $400 \times 400$



(a) Crack propagation showing the distribution of crystals



(b) Crack propagation showing the material composition (blue represents silicon carbide)

**Figure A.2** Crack propagation for the vertical pre-existing crack case at  $2 \mu s$  for  $100 \times 100$ ,  $200 \times 200$ , and  $400 \times 400$  points

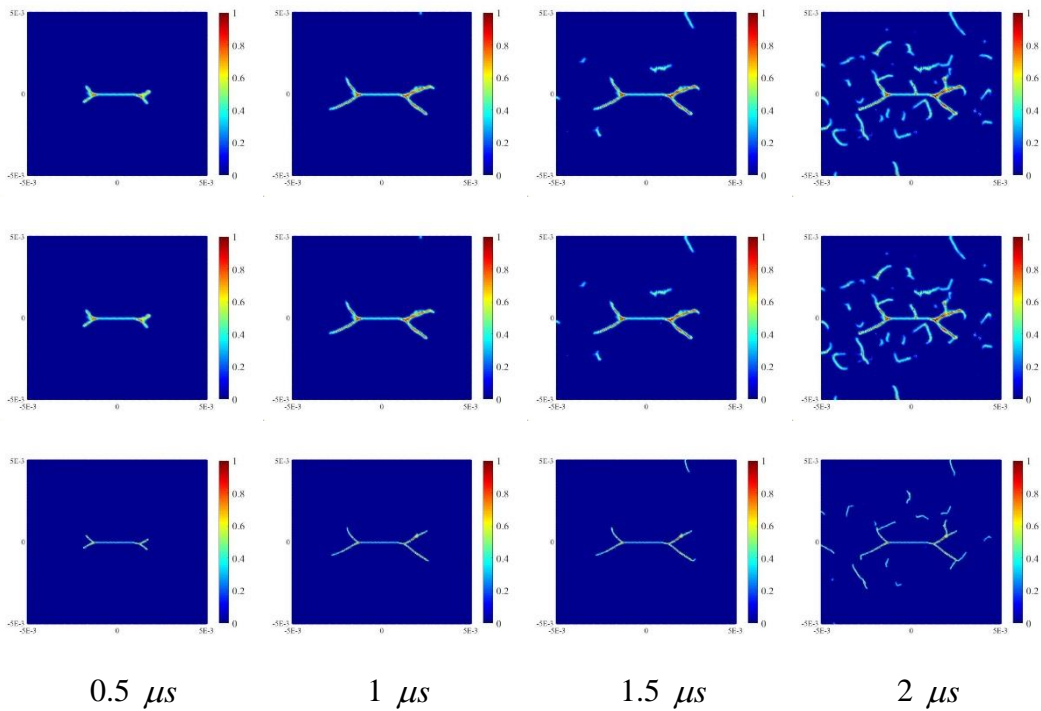
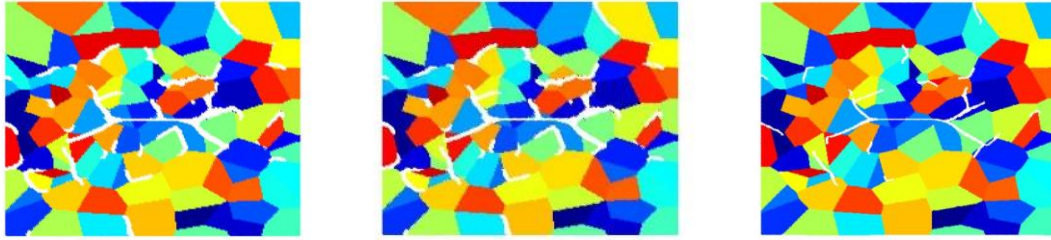
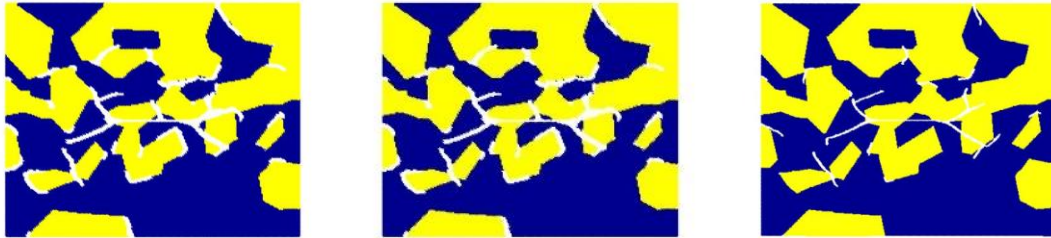


**Figure A.3** Crack propagation for the horizontal pre-existing crack case for different numbers of PD points. From the top to the bottom the number of the points is:  $100 \times 100$ ,  $200 \times 200$ , and  $400 \times 400$



(a) Crack propagation showing the distribution of crystals



(b) Crack propagation showing the material composition (blue represents silicon carbide)

**Figure A.4** Crack propagation for the horizontal pre-existing crack case at  $2 \mu s$  for  $100 \times 100$ ,  $200 \times 200$ , and  $400 \times 400$  points

From the plots, it can be seen that with the increase of the number of material points, the damage patterns especially the major fractures are not strongly influenced. It can be concluded that the discretization will affect the resolutions of the plots rather than the main features of the crack propagation. Compared to  $100 \times 100$  (low resolution) and  $400 \times 400$  (time-consuming),  $200 \times 200$  PD points are a reasonable choice to keep the critical features of the crack as well as high resolutions of the plots.

For the  $\delta$ -convergence, as shown in Figs. A.5-A.8, the horizon size does not have a significant influence on the pattern of the main crack. Therefore,  $\delta = 3dx$  since this is the suggested horizon size according to (Madenci and Oterkus, 2014) and (De Meo et al., 2016) it can provide accurate results with less computational time.

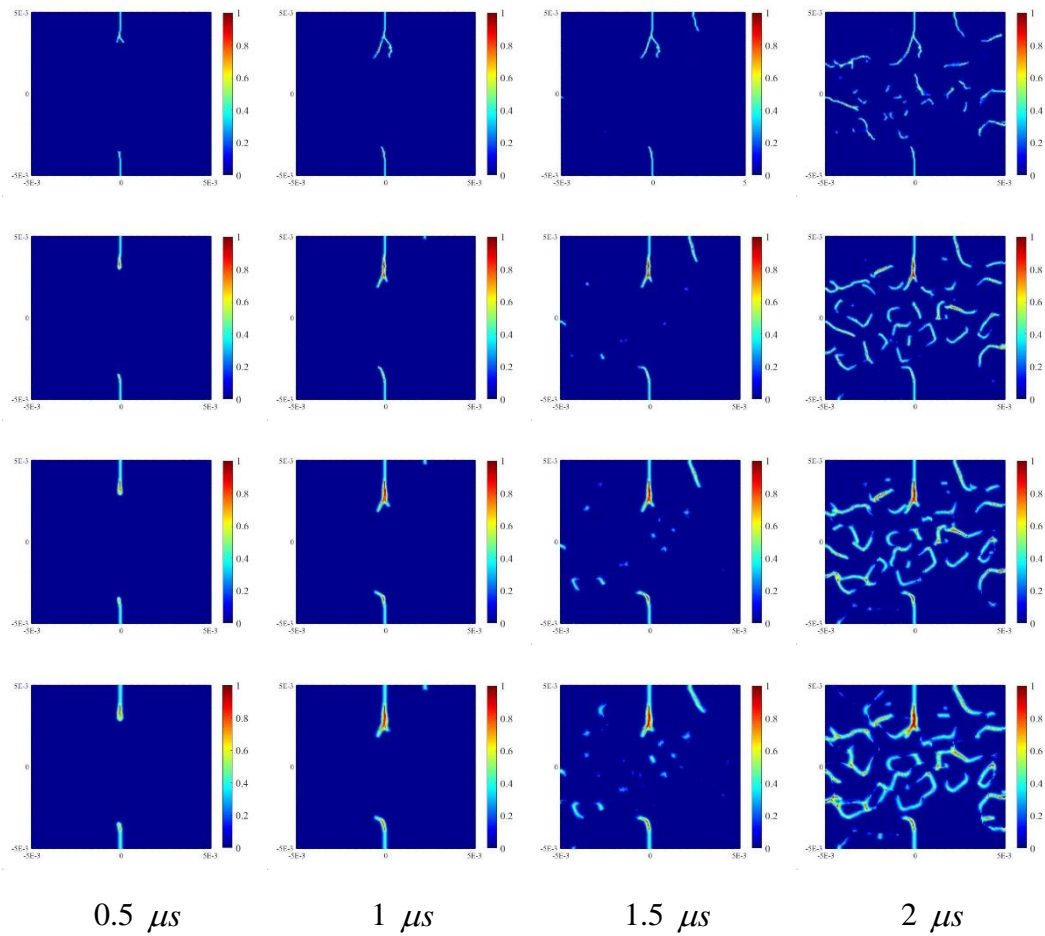
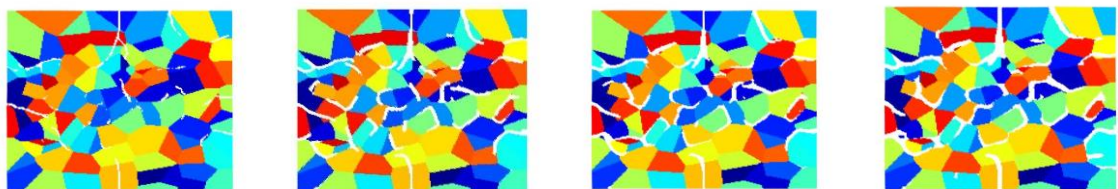
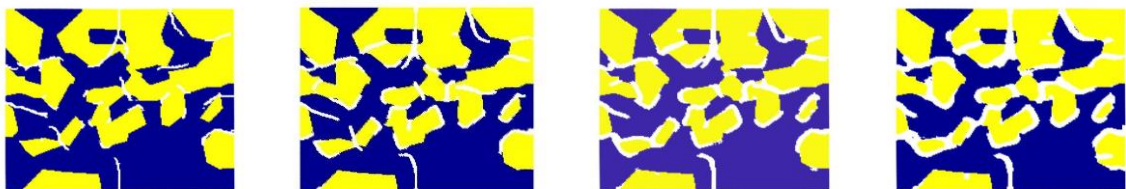


**Figure A.5** Crack propagation for the vertical pre-existing crack case for different horizon sizes. From the top to the bottom the horizon size is:  $2dx$ ,  $3dx$ ,  $4dx$ , and  $5dx$



(a) Crack propagation showing the distribution of crystals



(b) Crack propagation showing the material composition (blue represents silicon carbide)

**Figure A.6** Crack propagation for the vertical pre-existing crack case at  $2 \mu s$  for  $2dx$ ,  $3dx$ ,  $4dx$ , and  $5dx$  horizon sizes

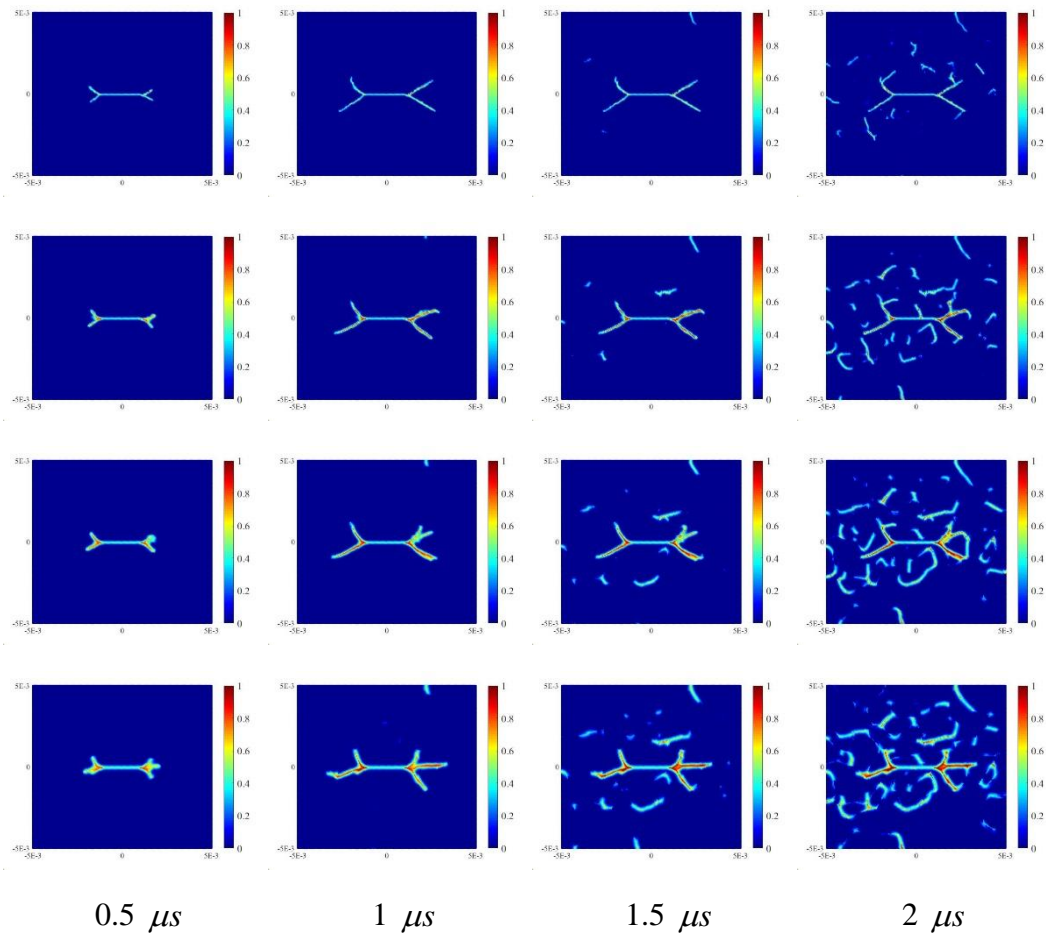
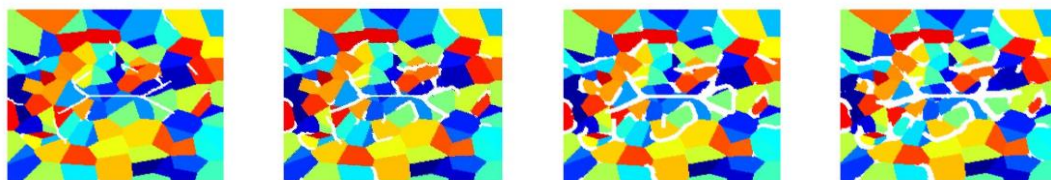
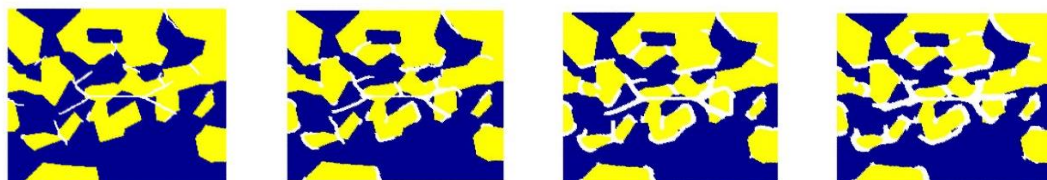


**Figure A.7** Crack propagation for the horizontal pre-existing crack case for different horizon sizes. From the top to the bottom the horizon size is:  $2dx$ ,  $3dx$ ,  $4dx$ , and  $5dx$



(a) Crack propagation showing the distribution of crystals



(b) Crack propagation showing the material composition (blue represents silicon carbide)

**Figure A.8** Crack propagation for the horizontal pre-existing crack case at  $2 \mu s$  for  $2dx$ ,  $3dx$ ,  $4dx$ , and  $5dx$  horizon sizes

## References

- Abdelaziz, Y., 2013. A new scheme for crack growth modeling by coupling modified quarter point crack-tip element and the level set method. *The Journal of Engineering Research [TJER]*, 10(2), pp.46-51.
- Abdelaziz, Y., Benkheira, S., Rikioui, T. and Mekkaoui, A., 2010. A double degenerated finite element for modeling the crack tip singularity. *Applied mathematical modelling*, 34(12), pp.4031-4039.
- Adams, D., White, J., Rumsey, M. and Farrar, C., 2011. Structural health monitoring of wind turbines: method and application to a HAWT. *Wind Energy*, 14(4), pp.603-623.
- Adams, J.W., Nakamura, H.H., Ingel, R.P. and Rice, R.W., 1985. Thermal Expansion Behavior of single-Crystal Zirconia. *Journal of the American Ceramic Society*, 68(9), pp.C-228.
- Ahmadi, H. and Ghaffari, A., 2015. Probabilistic analysis of stress intensity factor (SIF) and degree of bending (DoB) in axially loaded tubular K-joints of offshore structures. *Latin American Journal of Solids and Structures*, 12(11), pp.2025-2044.
- Ahn, H. and Shin, H., 2018, June. Fatigue Analysis of a 12-MW Wind Turbine Blade. In *International Conference on Offshore Mechanics and Arctic Engineering* (Vol. 51319, p. V010T09A063). American Society of Mechanical Engineers.
- Albrecht, P. and Yamada, K., 1977. Rapid calculation of stress intensity factors. *Journal of the Structural Division*, 103(2), pp.377-389.
- Alexander, C. and Brownlee, K., 2007, March. Methodology for assessing the effects of plain dents, wrinkle bends, and mechanical damage on pipeline integrity. In *CORROSION 2007*. OnePetro.
- Antoniadou, I., Dervilis, N., Papatheou, E., Maguire, A.E. and Worden, K., 2015. Aspects of structural health and condition monitoring of offshore wind turbines. *Philosophical Transactions of the Royal Society A: Mathematical, Physical and Engineering Sciences*, 373(2035), p.20140075.
- Arsenault, T.J., Achuthan, A., Marzocca, P., Grappasonni, C. and Coppotelli, G., 2013. Development of a FBG based distributed strain sensor system for wind turbine structural health monitoring. *Smart Materials and Structures*, 22(7), p.075027.
- Askari, E., Bobaru, F., Lehoucq, R.B., Parks, M.L., Silling, S.A. and Weckner, O., 2008. Peridynamics for multiscale materials modeling. In *Journal of Physics: Conference Series* (Vol. 125, No. 1, p. 012078). IOP Publishing.
- Bang, D.J. and Ince, A., 2022. Integration of a peridynamic fatigue model with two-parameter crack driving force. *Engineering with Computers*, pp.1-19.

- Bang, D.J., Ince, A., Oterkus, E. and Oterkus, S., 2021. Crack growth modeling and simulation of a peridynamic fatigue model based on numerical and analytical solution approaches. *Theoretical and Applied Fracture Mechanics*, 114, p.103026.
- Bang, H.J., Kim, H.I. and Lee, K.S., 2012. Measurement of strain and bending deflection of a wind turbine tower using arrayed FBG sensors. *International journal of precision engineering and manufacturing*, 13(12), pp.2121-2126.
- Bang, H.J., Kim, H.I., Jang, M. and Han, J.H., 2012, February. Tower deflection monitoring of a wind turbine using an array of fiber Bragg grating sensors. In *ASME 2011 Conference on Smart Materials, Adaptive Structures and Intelligent Systems* (pp. 473-479). American Society of Mechanical Engineers Digital Collection.
- Bang, H.J., Ko, S.W., Jang, M.S. and Kim, H.I., 2012, May. Shape estimation and health monitoring of wind turbine tower using a FBG sensor array. In *2012 IEEE International Instrumentation and Measurement Technology Conference Proceedings* (pp. 496-500). IEEE.
- Banks-Sills, L. and Bortman, Y., 1984. Reappraisal of the quarter-point quadrilateral element in linear elastic fracture mechanics. *International Journal of Fracture*, 25(3), pp.169-180.
- Banks-Sills, L. and Sherman, D., 1986. Comparison of methods for calculating stress intensity factors with quarter-point elements. *International Journal of Fracture*, 32(2), pp.127-140.
- Banthia, V., 1985. Singularity of collapsed Q-8 finite element. *International journal for numerical methods in engineering*, 21(5), pp.959-965.
- Barrera, C., Battistella, T., Guanache, R. and Losada, I.J., 2020. Mooring system fatigue analysis of a floating offshore wind turbine. *Ocean Engineering*, 195, p.106670.
- Barsoum, R.S., 1976. A degenerate solid element for linear fracture analysis of plate bending and general shells. *International Journal for Numerical Methods in Engineering*, 10(3), pp.551-564.
- Barsoum, R.S., 1976. On the use of isoparametric finite elements in linear fracture mechanics. *International journal for numerical methods in engineering*, 10(1), pp.25-37.
- Barsoum, R.S., 1977. Triangular quarter-point element as elastic and perfectly-plastic crack tip elements. *int. J. numer. Merh. Engng* 11, 85, 98.
- Barsoum, R.S., Loomis, R.W. and Stewart, B.D., 1979. Analysis of through cracks in cylindrical shells by the quarterpoint elements. *International Journal of Fracture*, 15(3), pp.259-280.
- Basoglu, M.F., Zerir, Z., Kefal, A., Oterkus, E., 2019. A computational model of peridynamic theory for deflecting behavior of crack propagation with micro-cracks. *Computational Materials Science* 162, 33–46.

- Bavanish, B. and Thyagarajan, K., 2013. Optimization of power coefficient on a horizontal axis wind turbine using bem theory. *Renewable and Sustainable Energy Reviews*, 26, pp.169-182.
- Benedetti, I. and Aliabadi, M.H., 2013. A three-dimensional cohesive-frictional grain-boundary micromechanical model for intergranular degradation and failure in polycrystalline materials. *Computer Methods in Applied Mechanics and Engineering*, 265, pp.36-62.
- Berg, J.C. and Resor, B.R., 2012. Numerical manufacturing and design tool (NuMAD V2. 0) for wind turbine blades: User's guide. *Sandia National Laboratories Technical Report, SAND2012-7028*.
- Bergara, A., Arredondo, A., Altuzarra, J. and Martínez-Esnaola, J.M., 2020. Calculation of stress intensity factors in offshore mooring chains. *Ocean Engineering*, 214, p.107762.
- Bhattacharya, S., Singh, I.V., Mishra, B.K. and Bui, T.Q., 2013. Fatigue crack growth simulations of interfacial cracks in bi-layered FGMs using XFEM. *Computational Mechanics*, 52(4), pp.799-814.
- Binchao, L.I.U., Rui, B.A.O. and Fucheng, S.U.I., 2021. A fatigue damage-cumulative model in peridynamics. *Chinese Journal of Aeronautics*, 34(2), pp.329-342.
- Blanco, M.I., 2009. The economics of wind energy. *Renewable and sustainable energy reviews*, 13(6-7), pp.1372-1382.
- Blandino, J., Duncan, R., Nuckels, M. and Cadogan, D., 2005. Three-dimensional shape sensing for inflatable booms. In *46th AIAA/ASME/ASCE/AHS/ASC Structures, Structural Dynamics and Materials Conference* (p. 1807).
- Bobaru, F., Yang, M., Alves, L.F., Silling, S.A., Askari, E. and Xu, J., 2009. Convergence, adaptive refinement, and scaling in 1D peridynamics. *International Journal for Numerical Methods in Engineering*, 77(6), pp.852-877.
- Bocher, M., Mehmanparast, A., Braithwaite, J. and Shafiee, M., 2018. New shape function solutions for fracture mechanics analysis of offshore wind turbine monopile foundations. *Ocean Engineering*, 160, pp.264-275.
- Bosch, J., Staffell, I. and Hawkes, A.D., 2019. Global levelised cost of electricity from offshore wind. *Energy*, 189, p.116357.
- Branco, R., Antunes, F.V. and Costa, J.D., 2015. A review on 3D-FE adaptive remeshing techniques for crack growth modelling. *Engineering Fracture Mechanics*, 141, pp.170-195.
- Camacho, G.T. and Ortiz, M., 1996. Computational modelling of impact damage in brittle materials. *International Journal of solids and structures*, 33(20-22), pp.2899-2938.
- Case, E.D., Smyth, J.R. and Hunter, O., 1980. Grain-size dependence of microcrack initiation in brittle materials. *Journal of Materials Science*, 15(1), pp.149-153.

- Castro-Santos, L. and Diaz-Casas, V. eds., 2016. *Floating offshore wind farms* (p. 204). Cham, Switzerland: Springer International Publishing.
- Cerik, B.C., 2015. Ultimate strength of locally damaged steel stiffened cylinders under axial compression. *Thin-Walled Structures*, 95, pp.138-151.
- Cerik, B.C., Shin, H.K. and Cho, S.R., 2015. On the resistance of steel ring-stiffened cylinders subjected to low-velocity mass impact. *International Journal of Impact Engineering*, 84, pp.108-123.
- Cerracchio, P., Gherlone, M., Di Sciuva, M. and Tessler, A., 2015. A novel approach for displacement and stress monitoring of sandwich structures based on the inverse Finite Element Method. *Composite Structures*, 127, pp.69-76.
- Chakraborty, P., Zhang, Y., Tonks, M.R., 2016. Multi-scale modeling of microstructure dependent intergranular brittle fracture using a quantitative phase-field based method. *Computational Materials Science* 113, 38–52.
- Chen, J., 2011. Development of offshore wind power in China. *Renewable and Sustainable Energy Reviews*, 15(9), pp.5013-5020.
- Cheng, P., Huang, Y. and Wan, D., 2019. A numerical model for fully coupled aero-hydrodynamic analysis of floating offshore wind turbine. *Ocean Engineering*, 173, pp.183-196.
- Ciang, C.C., Lee, J.R. and Bang, H.J., 2008. Structural health monitoring for a wind turbine system: a review of damage detection methods. *Measurement science and technology*, 19(12), p.122001.
- Colmenar-Santos, A., Perera-Perez, J., Borge-Diez, D. and dePalacio-Rodríguez, C., 2016. Offshore wind energy: A review of the current status, challenges and future development in Spain. *Renewable and Sustainable Energy Reviews*, 64, pp.1-18.
- Colombo, L., Sbarufatti, C. and Giglio, M., 2019. Definition of a load adaptive baseline by inverse finite element method for structural damage identification. *Mechanical Systems and Signal Processing*, 120, pp.584-607.
- Currie, M., Saafi, M., Tachtatzis, C. and Quail, F., 2013. Structural health monitoring for wind turbine foundations. *Proceedings of the ICE-Energy*, 166(4), pp.162-169.
- Dagli, B.Y., Tuskan, Y. and Gökkuş, Ü., 2018. Evaluation of Offshore Wind Turbine Tower Dynamics with Numerical Analysis. *Advances in Civil Engineering*, 2018.
- Dai, J.C., Hu, Y.P., Liu, D.S. and Long, X., 2011. Aerodynamic loads calculation and analysis for large scale wind turbine based on combining BEM modified theory with dynamic stall model. *Renewable Energy*, 36(3), pp.1095-1104.
- Das, P.K., Thavalingam, A. and Bai, Y., 2003. Buckling and ultimate strength criteria of stiffened shells under combined loading for reliability analysis. *Thin-Walled Structures*, 41(1), pp.69-88.

- De Meo, D. and Oterkus, E., 2017. Finite element implementation of a peridynamic pitting corrosion damage model. *Ocean Engineering*, 135, pp.76-83.
- De Meo, D., Diyaroglu, C., Zhu, N., Oterkus, E. and Siddiq, M.A., 2016. Modelling of stress-corrosion cracking by using peridynamics. *International Journal of Hydrogen Energy*, 41(15), pp.6593-6609.
- De Meo, D., Russo, L., Oterkus, E., 2017. Modeling of the onset, propagation, and interaction of multiple cracks generated from corrosion pits by using peridynamics. *Journal of Engineering Materials and Technology* 139(4), 041001.
- De Meo, D., Zhu, N., Oterkus, E., 2016. Peridynamic modeling of granular fracture in polycrystalline materials. *Journal of Engineering Materials and Technology* 138(4), 041008.
- Dervilis, N., Barthorpe, R., Staszewski, W.J. and Worden, K., 2012. Structural Health Monitoring of composite material typical of wind turbine blades by novelty detection on vibration response. In *Key Engineering Materials* (Vol. 518, pp. 319-327). Trans Tech Publications Ltd.
- Devriendt, C., Magalhães, F., Weijtjens, W., De Sitter, G., Cunha, Á. and Guillaume, P., 2014. Structural health monitoring of offshore wind turbines using automated operational modal analysis. *Structural Health Monitoring*, 13(6), pp.644-659.
- Dirras, G.F., Djemia, P., Roussigne, Y. and Jackson, K.M., 2004. Investigating the elastic properties of  $\beta$ -SiC films. *Materials Science and Engineering: A*, 387, pp.302-306.
- Diyaroglu, C., Oterkus, E., Oterkus, S., 2019. An Euler–Bernoulli beam formulation in an ordinary state-based peridynamic framework. *Mathematics and Mechanics of Solids* 24(2), 361–376.
- Diyaroglu, C., Oterkus, E., Oterkus, S., Madenci, E., 2015. Peridynamics for bending of beams and plates with transverse shear deformation. *International Journal of Solids and Structures*, 69, 152–168.
- Diyaroglu, C., Oterkus, S., Oterkus, E., Madenci, E., 2017. Peridynamic modeling of diffusion by using finite-element analysis. *IEEE Transactions on Components, Packaging and Manufacturing Technology* 7(11), 1823–1831.
- Diyaroglu, C., Oterkus, S., Oterkus, E., Madenci, E., Han, S., Hwang, Y., 2017. Peridynamic wetness approach for moisture concentration analysis in electronic packages. *Microelectronics Reliability* 70, 103–111.
- DNV, G. and Lloyd, D.N.V.G., 2015. *Offshore standard: Position mooring*. DNVGL-OS-E301.
- Dorduncu, M., 2019. Stress analysis of laminated composite beams using refined zigzag theory and peridynamic differential operator. *Composite Structures*, 218, pp.193-203.

- Dorduncu, M., 2020. Stress analysis of sandwich plates with functionally graded cores using peridynamic differential operator and refined zigzag theory. *Thin-Walled Structures*, 146, p.106468.
- Dorduncu, M., 2021. Peridynamic modeling of delaminations in laminated composite beams using refined zigzag theory. *Theoretical and Applied Fracture Mechanics*, 112, p.102832.
- Dorduncu, M. and Apalak, M.K., 2020. Elastic flexural analysis of adhesively bonded similar and dissimilar beams using refined zigzag theory and peridynamic differential operator. *International Journal of Adhesion and Adhesives*, 101, p.102631.
- Dorduncu, M., Kutlu, A., Madenci, E. and Rabczuk, T., 2022. Nonlocal modeling of bi-material and modulus graded plates using peridynamic differential operator. *Engineering with Computers*, pp.1-17.
- Erdogan, F. and Sih, G.C., 1963. On the crack extension in plates under plane loading and transverse shear.
- Eshelby, J.D., 1951. The force on an elastic singularity. *Philosophical Transactions of the Royal Society of London. Series A, Mathematical and Physical Sciences*, 244(877), pp.87-112.
- European Wind Energy Association, 2009. *The economics of wind energy*. EWEA.
- Fernandez, G., Usabiaga, H. and Vandepitte, D., 2018. An efficient procedure for the calculation of the stress distribution in a wind turbine blade under aerodynamic loads. *Journal of Wind Engineering and Industrial Aerodynamics*, 172, pp.42-54.
- Freese, C.E. and Tracey, D.M., 1976. The natural isoparametric triangle versus collapsed quadrilateral for elastic crack analysis. *International Journal of Fracture*, 12(5), pp.767-770.
- Furguele, F.M. and Luchi, M.L., 1989. A note on some crack tip elements employed in two-dimensional elasto-plastic fracture mechanics. *Engineering fracture mechanics*, 33(5), pp.831-837.
- Galvis, A.F. and Sollero, P., 2016. 2D analysis of intergranular dynamic crack propagation in polycrystalline materials a multiscale cohesive zone model and dual reciprocity boundary elements. *Computers & Structures*, 164, pp.1-14.
- Gao, X., Liu, X., Xue, X. and Chen, N.Z., 2021. Fracture mechanics-based mooring system fatigue analysis for a spar-based floating offshore wind turbine. *Ocean Engineering*, 223, p.108618.
- Geraci, G. and Aliabadi, M.H., 2017. Micromechanical boundary element modelling of transgranular and intergranular cohesive cracking in polycrystalline materials. *Engineering Fracture Mechanics*, 176, pp.351-374.

- Geraci, G. and Aliabadi, M.H., 2018. Micromechanical modelling of cohesive thermoelastic cracking in orthotropic polycrystalline materials. *Computer Methods in Applied Mechanics and Engineering*, 339, pp.567-590.
- Geraci, G. and Aliabadi, M.H., 2019. Micromechanical modeling of cohesive thermoelastic steady-state and transient cracking in polycrystalline materials. *International Journal for Numerical Methods in Engineering*, 117(12), pp.1205-1233.
- Ghajari, M., Iannucci, L. and Curtis, P., 2014. A peridynamic material model for the analysis of dynamic crack propagation in orthotropic media. *Computer Methods in Applied Mechanics and Engineering*, 276, pp.431-452.
- Gherlone, M., Cerracchio, P. and Mattone, M., 2018. Shape sensing methods: Review and experimental comparison on a wing-shaped plate. *Progress in Aerospace Sciences*, 99, pp.14-26.
- Gherlone, M., Cerracchio, P., Mattone, M., Di Sciuva, M. and Tessler, A., 2012. Shape sensing of 3D frame structures using an inverse finite element method. *International Journal of Solids and Structures*, 49(22), pp.3100-3112.
- Gherlone, M., Cerracchio, P., Mattone, M., Di Sciuva, M. and Tessler, A., 2014. An inverse finite element method for beam shape sensing: theoretical framework and experimental validation. *Smart Materials and Structures*, 23(4), p.045027.
- Gherlone, M., Cerracchio, P., Mattone, M., Di Sciuva, M. and Tessler, A., 2011. *Beam shape sensing using inverse finite element method: theory and experimental validation*. POLITECNICO DI TORINO (ITALY).
- Gray, L.J., Phan, A.V., Paulino, G.H. and Kaplan, T., 2003. Improved quarter-point crack tip element. *Engineering Fracture Mechanics*, 70(2), pp.269-283.
- Griffith, D.T., 2013. The SNL100-01 blade: carbon design studies for the Sandia 100-meter blade. *Sandia National Laboratories Technical Report, SAND2013-1178*.
- Griffith, D.T., 2013. The SNL100-02 blade: advanced core material design studies for the Sandia 100-meter blade. *Sandia National Laboratories Technical Report, SAND2013-10162*.
- Groeber, M.A., Haley, B.K., Uchic, M.D., Dimiduk, D.M. and Ghosh, S., 2006. 3D reconstruction and characterization of polycrystalline microstructures using a FIB–SEM system. *Materials Characterization*, 57(4-5), pp.259-273.
- Gücüyen, E., 2017. Analysis of offshore wind turbine tower under environmental loads. *Ships and Offshore Structures*, 12(4), pp.513-520
- Harrop, L.P., 1982. The optimum size of quarter-point crack tip elements. *International journal for numerical methods in engineering*, 18(7), pp.1101-1103.

- Hellen, T.K. and Blackburn, W.S., 1975. The calculation of stress intensity factors for combined tensile and shear loading. *International Journal of Fracture*, 11(4), pp.605-617.
- Hendrik Veder group. Mooring & towing
- Henshell RD, Shaw KG. Crack tip finite elements are unnecessary. *International journal for numerical methods in engineering*. 1975;9(3):495-507.
- Herbig, M., King, A., Reischig, P., Proudhon, H., Lauridsen, E.M., Marrow, J., Buffière, J.Y. and Ludwig, W., 2011. 3-D growth of a short fatigue crack within a polycrystalline microstructure studied using combined diffraction and phase-contrast X-ray tomography. *Acta Materialia*, 59(2), pp.590-601.
- Hibbitt, H.D., 1977. Some properties of singular isoparametric elements. *International Journal for Numerical Methods in Engineering*, 11(1), pp.180-184.
- Hong, K., Oterkus, S. and Oterkus, E., 2021. Peridynamic analysis of fatigue crack growth in fillet welded joints. *Ocean Engineering*, 235, p.109348.
- Hussain, M.A., Pu, L. and Underwood, J., 1974. Strain Energy Release Rate for. In *Proceedings of the 1973 National Symposium on Fracture Mechanics, University of Maryland, College Park, Md., 27-29 Aug. 1973* (Vol. 559, p. 2).
- IEA, I., 2017. International Energy Agency. Key World Energy Statistics.
- Imachi, M., Tanaka, S., Bui, T.Q., Oterkus, S., Oterkus, E., 2019. A computational approach based on ordinary state-based peridynamics with new transition bond for dynamic fracture analysis. *Engineering Fracture Mechanics* 206, 359–374.
- Imachi, M., Tanaka, S., Ozdemir, M., Bui, T.Q., Oterkus, S., Oterkus, E., 2020. Dynamic crack arrest analysis by ordinary state-based peridynamics. *International Journal of Fracture* 221(2), pp.155–169.
- Irwin, G.R., 1957. Analysis of stresses and strains near the end of a crack traversing a plate.
- ISO, P., 2005. natural gas industries. Specific req
- Jonkman, J., Butterfield, S., Musial, W. and Scott, G., 2009. *Definition of a 5-MW reference wind turbine for offshore system development* (No. NREL/TP-500-38060). National Renewable Energy Lab.(NREL), Golden, CO (United States).
- Joose, P.A., Blanch, M.J., Dutton, A.G., Kouroussis, D.A., Philippidis, T.P. and Vionis, P.S., 2002. Acoustic emission monitoring of small wind turbine blades. *J. Sol. Energy Eng.*, 124(4), pp.446-454.
- Jureczko, M.E.Z.Y.K., Pawlak, M. and Mężyk, A., 2005. Optimisation of wind turbine blades. *Journal of materials processing technology*, 167(2-3), pp.463-471.

- Kamaya, M., Kawamura, Y. and Kitamura, T., 2007. Three-dimensional local stress analysis on grain boundaries in polycrystalline material. *International Journal of Solids and Structures*, 44(10), pp.3267-3277.
- Kang, L.H., Kim, D.K. and Han, J.H., 2007. Estimation of dynamic structural displacements using fiber Bragg grating strain sensors. *Journal of sound and vibration*, 305(3), pp.534-542.
- Karpenko, O., Oterkus, S. and Oterkus, E., 2022. Peridynamic analysis to investigate the influence of microstructure and porosity on fatigue crack propagation in Additively Manufactured Ti6Al4V. *Engineering Fracture Mechanics*, p.108212.
- Kefal, A., 2017. *Structural health monitoring of marine structures by using inverse finite element method* (Doctoral dissertation, University of Strathclyde).
- Kefal, A., 2019. An efficient curved inverse-shell element for shape sensing and structural health monitoring of cylindrical marine structures. *Ocean Engineering*, 188, p.106262.
- Kefal, A. and Oterkus, E., 2016. Displacement and stress monitoring of a chemical tanker based on inverse finite element method. *Ocean Engineering*, 112, pp.33-46.
- Kefal, A. and Oterkus, E., 2016. Displacement and stress monitoring of a Panamax containership using inverse finite element method. *Ocean Engineering*, 119, pp.16-29.
- Kefal, A. and Oterkus, E., 2017. Shape and stress sensing of offshore structures by using inverse finite element method. *Progress in the Analysis and Design of Marine Structures; Guedes Soares, C., Garbatov, Y., Eds*, pp.141-148.
- Kefal, A. and Yildiz, M., 2017. Modeling of sensor placement strategy for shape sensing and structural health monitoring of a wing-shaped sandwich panel using inverse finite element method. *Sensors*, 17(12), p.2775.
- Kefal, A., Hizir, O. and Oterkus, E., 2015, August. A smart system to determine sensor locations for structural health monitoring of ship structures. In *Proceedings of the 9th International Workshop on Ship and Marine Hydrodynamics, Glasgow, UK* (pp. 26-28).
- Kefal, A., Mayang, J.B., Oterkus, E. and Yildiz, M., 2018. Three dimensional shape and stress monitoring of bulk carriers based on iFEM methodology. *Ocean Engineering*, 147, pp.256-267.
- Kefal, A., Oterkus, E., Tessler, A. and Spangler, J.L., 2016. A quadrilateral inverse-shell element with drilling degrees of freedom for shape sensing and structural health monitoring. *Engineering science and technology, an international journal*, 19(3), pp.1299-1313.
- Kefal, A., Sohoulis, A., Oterkus, E., Yildiz, M., Suleman, A., 2019. Topology optimization of cracked structures using peridynamics. *Continuum Mechanics and Thermodynamics* 31(6), 1645–1672.

- Kefal, A., Tessler, A. and Oterkus, E., 2017. An enhanced inverse finite element method for displacement and stress monitoring of multilayered composite and sandwich structures. *Composite Structures*, 179, pp.514-540.
- Kim, H.C., Kim, M.H. and Choe, D.E., 2019. Structural health monitoring of towers and blades for floating offshore wind turbines using operational modal analysis and modal properties with numerical-sensor signals. *Ocean Engineering*, 188, p.106226.
- Kim, S.W., Kang, W.R., Jeong, M.S., Lee, I. and Kwon, I.B., 2013. Deflection estimation of a wind turbine blade using FBG sensors embedded in the blade bonding line. *Smart Materials and Structures*, 22(12), p.125004.
- Ko, W.L., Richards, W.L. and Fleischer, V.T., 2009. *Applications of Ko displacement theory to the deformed shape predictions of the doubly-tapered Ikhana Wing* (No. NASA/TP-2009-214652).
- Ko, W.L., Richards, W.L. and Tran, V.T., 2007. *Displacement theories for in-flight deformed shape predictions of aerospace structures* (No. H-2652).
- Koh, J.H. and Ng, E.Y.K., 2016. Downwind offshore wind turbines: Opportunities, trends and technical challenges. *Renewable and Sustainable Energy Reviews*, 54, pp.797-808.
- Kuszyk, J.A. and Bradt, R.C., 1973. Influence of grain size on effects of thermal expansion anisotropy in MgTi<sub>2</sub>O<sub>5</sub>. *Journal of the American Ceramic Society*, 56(8), pp.420-423.
- Lee, M.M.K., 1999. Strength, stress and fracture analyses of offshore tubular joints using finite elements. *Journal of Constructional Steel Research*, 51(3), pp.265-286.
- Li, H., Díaz, H. and Soares, C.G., 2021. A failure analysis of floating offshore wind turbines using AHP-FMEA methodology. *Ocean Engineering*, 234, p.109261.
- Li, H., Soares, C.G. and Huang, H.Z., 2020. Reliability analysis of a floating offshore wind turbine using Bayesian Networks. *Ocean Engineering*, 217, p.107827.
- Li, M.Y., Kefal, A., Cerik, B. and Oterkus, E., 2019, April. Structural health monitoring of submarine pressure hull using inverse finite element method. In *Trends in the Analysis and Design of Marine Structures: Proceedings of the 7th International Conference on Marine Structures (MARSTRUCT 2019, Dubrovnik, Croatia, 6-8 May 2019)* (p. 293). CRC Press.
- Li, S., Zeng, X., Ren, B., Qian, J., Zhang, J. and Jha, A.K., 2012. An atomistic-based interphase zone model for crystalline solids. *Computer Methods in Applied Mechanics and Engineering*, 229, pp.87-109.
- Li, X. and Zhang, W., 2020. Long-term fatigue damage assessment for a floating offshore wind turbine under realistic environmental conditions. *Renewable Energy*, 159, pp.570-584.

- Lian, J., Cai, O., Dong, X., Jiang, Q. and Zhao, Y., 2019. Health monitoring and safety evaluation of the offshore wind turbine structure: a review and discussion of future development. *Sustainability*, 11(2), p.494.
- Liao, D., Zhu, S.P., Correia, J.A., Jesus, A.M., Veljkovic, M. and Berto, F., 2022. Fatigue reliability of wind turbines: Historical perspectives, recent developments and future prospects. *Renewable Energy*.
- Lin, L., Wang, X. and Zeng, X., 2017. The role of cohesive zone properties on intergranular to transgranular fracture transition in polycrystalline solids. *International Journal of Damage Mechanics*, 26(3), pp.379-394.
- Liu, X., He, X., Wang, J., Sun, L., Oterkus, E., 2018. An ordinary state-based peridynamic model for the fracture of zigzag graphene sheets. *Proceedings of the Royal Society A: Mathematical, Physical and Engineering Sciences* 474(2217), p.20180019.
- Liu, Y., Deng, L., Zhong, W., Xu, J. and Xiong, W., 2020. A new fatigue reliability analysis method for steel bridges based on peridynamic theory. *Engineering Fracture Mechanics*, 236, p.107214.
- Loghin, A., Ozkan, U., Kaya, A., LeMonds, J., McClain, R., Decesare, D., Akkaram, S. and Laflen, J., 2012. 3DFAS: framework for conducting 3D crack growth simulation. *Propulsion-Safety Affordable Readiness*.
- Lu, B., Li, Y., Wu, X. and Yang, Z., 2009, June. A review of recent advances in wind turbine condition monitoring and fault diagnosis. In *2009 IEEE Power Electronics and Machines in Wind Applications* (pp. 1-7). IEEE.
- Lu, W., Li, M., Vazic, B., Oterkus, S., Oterkus, E., Wang, Q., 2020. Peridynamic modelling of fracture in polycrystalline ice. *Journal of Mechanics* 36(2), 223–234.
- Ludwig, W., Reischig, P., King, A., Herbig, M., Lauridsen, E.M., Johnson, G., Marrow, T.J. and Buffiere, J.Y., 2009. Three-dimensional grain mapping by x-ray diffraction contrast tomography and the use of Friedel pairs in diffraction data analysis. *Review of Scientific Instruments*, 80(3), p.033905.
- Lynn, P.P. and Ingraffea, A.R., 1978. Transition elements to be used with quarter-point crack-tip elements. *International Journal for Numerical Methods in Engineering*, 12(6), pp.1031-1036.
- Ma, X., Xu, J., Liu, L., Wang, P., Feng, Q. and Xu, J., 2020. A 2D peridynamic model for fatigue crack initiation of railheads. *International Journal of Fatigue*, 135, p.105536.
- Macdonald, K.A., Cosham, A., Alexander, C.R. and Hopkins, P., 2007. Assessing mechanical damage in offshore pipelines—Two case studies. *Engineering Failure Analysis*, 14(8), pp.1667-1679.

- Madenci, E. and Oterkus, E., 2014. Peridynamic theory. In *Peridynamic theory and its applications* (pp. 19-43). Springer, New York, NY.
- Madenci, E., Barut, A. and Futch, M., 2016. Peridynamic differential operator and its applications. *Computer Methods in Applied Mechanics and Engineering*, 304, pp.408-451.
- Madenci, E., Barut, A. and Dorduncu, M., 2019. *Peridynamic differential operator for numerical analysis* (Vol. 10, pp. 978-3). Berlin: Springer International Publishing.
- Madenci, E., Dorduncu, M., Barut, A. and Futch, M., 2017. Numerical solution of linear and nonlinear partial differential equations using the peridynamic differential operator. *Numerical Methods for Partial Differential Equations*, 33(5), pp.1726-1753.
- Maiti, S.K. and Smith, R.A., 1984. Comparison of the criteria for mixed mode brittle fracture based on the preinstability stress-strain field. *International Journal of Fracture*, 24(1), pp.5-22.
- Manu, C., 1985. Complete quadratic isoparametric finite elements in fracture mechanics analysis. *International journal for numerical methods in engineering*, 21(8), pp.1547-1553.
- Martinez, J. and Dominguez, J., 1984. On the use of quarter-point boundary elements for stress intensity factor computations. *International journal for numerical methods in engineering*, 20(10), pp.1941-1950.
- Micallef, D. and Rezaeiha, A., 2021. Floating offshore wind turbine aerodynamics: Trends and future challenges. *Renewable and Sustainable Energy Reviews*, 152, p.111696.
- Mieloszyk, M. and Ostachowicz, W., 2017. An application of Structural Health Monitoring system based on FBG sensors to offshore wind turbine support structure model. *Marine Structures*, 51, pp.65-86.
- Murti, V. and Valliappan, S., 1986. The use of quarter point element in dynamic crack analysis. *Engineering Fracture Mechanics*, 23(3), pp.585-614.
- Nguyen, C.T., Oterkus, S. and Oterkus, E., 2021. An energy-based peridynamic model for fatigue cracking. *Engineering Fracture Mechanics*, 241, p.107373.
- Nguyen, C.T., Oterkus, S. and Oterkus, E., 2021. Implementation of modified Wheeler model in peridynamic fatigue model to predict effects of overload and underload on fatigue crack growth rate. *Theoretical and Applied Fracture Mechanics*, 116, p.103115.
- Nikishkov, G.P., 2013. Accuracy of quarter-point element in modeling crack-tip fields. *CMES Comp Model Eng*, 93(5), pp.335-361.
- Ohlenforst, K., Sawyer, S., Dutton, A., Backwell, B., Fiestas, R., Lee, J., Qiao, L., Zhao, F. and Balachandran, N., 2019. Global wind report 2018. *Global Wind Energy Council: Brussels, Belgium*, pp.11-12.

- Olsen, F. and Dyre, K., 1993. Vindeby off-shore wind farm-construction and operation. *Wind Engineering*, pp.120-128.
- Ortiz, M. and Pandolfi, A., 1999. Finite-deformation irreversible cohesive elements for three-dimensional crack-propagation analysis. *International journal for numerical methods in engineering*, 44(9), pp.1267-1282.
- Oterkus, E., Barut, A., Madenci, E., 2010a. Damage growth prediction from loaded composite fastener holes by using peridynamic theory. In 51st AIAA/ASME/ASCE/AHS/ASC Structures, Structural Dynamics, and Materials Conference 18th AIAA/ASME/AHS Adaptive Structures Conference, Orlando, Florida, USA, p. 3026.
- Oterkus, E., Guven, I. and Madenci, E., 2010, June. Fatigue failure model with peridynamic theory. In 2010 12th IEEE Intersociety Conference on Thermal and Thermomechanical Phenomena in Electronic Systems (pp. 1-6). IEEE.
- Oterkus, E., Guven, I. and Madenci, E., 2010b. Fatigue failure model with peridynamic theory. In 12th IEEE Intersociety Conference on Thermal and Thermomechanical Phenomena in Electronic Systems, Las Vegas, Nevada, USA, p. 1-6.
- Oterkus, E., Guven, I., Madenci, E., 2012. Impact damage assessment by using peridynamic theory. *Open Engineering* 2(4), 523–531.
- Oterkus, E., Madenci, E., 2012a. Peridynamics for failure prediction in composites. In 53rd AIAA/ASME/ASCE/AHS/ASC Structures, Structural Dynamics and Materials Conference 20th AIAA/ASME/AHS Adaptive Structures Conference, Honolulu, Hawaii, USA, p. 1692.
- Oterkus, E., Madenci, E., 2012b. Peridynamic theory for damage initiation and growth in composite laminate. *Key Engineering Materials* 488, 355–358.
- Oterkus, S., Madenci, E., Oterkus, E., Hwang, Y., Bae, J., Han, S., 2014, May. Hygro-thermo-mechanical analysis and failure prediction in electronic packages by using peridynamics. In 2014 IEEE 64th Electronic Components and Technology Conference (ECTC), Orlando, Florida, USA, p. 973-982.
- Pathak, H., Singh, A. and Singh, I.V., 2013. Fatigue crack growth simulations of 3-D problems using XFEM. *International Journal of Mechanical Sciences*, 76, pp.112-131.
- Pham, H.D., Schoefs, F., Cartraud, P., Soulard, T., Pham, H.H. and Berhault, C., 2019. Methodology for modeling and service life monitoring of mooring lines of floating wind turbines. *Ocean Engineering*, 193, p.106603.
- Pharr, M., Katoh, Y. and Bei, H., 2006. Dependence of Fracture Toughness on Crystallographic Orientation in Single-Crystalline Cubic ( $\beta$ ) Silicon Carbide. *Journal of Undergraduate Research*, 6.

- Piscopo, V., Scamardella, A., Rossi, G.B., Crenna, F. and Berardengo, M., 2021. Fatigue Assessment of Moorings for Floating Offshore Wind Turbines by Advanced Spectral Analysis Methods. *Journal of Marine Science and Engineering*, 10(1), p.37.
- Premalatha, M., Abbasi, T. and Abbasi, S.A., 2014. Wind energy: Increasing deployment, rising environmental concerns. *Renewable and Sustainable Energy Reviews*, 31, pp.270-288.
- Price, S.J. and Figueira, R.B., 2017. Corrosion protection systems and fatigue corrosion in offshore wind structures: current status and future perspectives. *Coatings*, 7(2), p.25.
- Qian, J. and Li, S., 2011. Application of multiscale cohesive zone model to simulate fracture in polycrystalline solids. *Journal of Engineering Materials and Technology*, 133(1), p.011010.
- Quach, C., Vazquez, S., Tessler, A., Moore, J., Cooper, E. and Spangler, J., 2005, August. Structural anomaly detection using fiber optic sensors and inverse finite element method. In *AIAA Guidance, Navigation, and Control Conference and Exhibit* (p. 6357).
- Rapp, S., Kang, L.H., Han, J.H., Mueller, U.C. and Baier, H., 2009. Displacement field estimation for a two-dimensional structure using fiber Bragg grating sensors. *Smart Materials and Structures*, 18(2), p.025006.
- Ren, Z., Verma, A.S., Li, Y., Teuwen, J.J. and Jiang, Z., 2021. Offshore wind turbine operations and maintenance: A state-of-the-art review. *Renewable and Sustainable Energy Reviews*, 144, p.110886.
- Resor, B.R., 2013. Definition of a 5MW/61.5 m wind turbine blade reference model. *Albuquerque, New Mexico, USA, Sandia National Laboratories, SAND2013-2569, 2013*.
- Rimoli, J.J., 2009. A computational model for intergranular stress corrosion cracking. Doctoral dissertation, California Institute of Technology.
- Rolfes, R., Zerbst, S., Haake, G., Reetz, J. and Lynch, J.P., 2007, September. Integral SHM-system for offshore wind turbines using smart wireless sensors. In *Proceedings of the 6th International Workshop on Structural Health Monitoring* (pp. 11-13). DEStech Publications Inc. Stanford, CA, USA.
- Rooke, D.P., Baratta, F.I. and Cartwright, D.J., 1981. Simple methods of determining stress intensity factors. *Engineering Fracture Mechanics*, 14(2), pp.397-426.
- Rybicki, E.F. and Kanninen, M.F., 1977. A finite element calculation of stress intensity factors by a modified crack closure integral. *Engineering fracture mechanics*, 9(4), pp.931-938.
- Sajith, S., Murthy, K.S.R.K. and Robi, P.S., 2020. Experimental and numerical investigation of mixed mode fatigue crack growth models in aluminum 6061-T6. *International Journal of Fatigue*, 130, p.105285.

- Salic, T., Charpentier, J.F., Benbouzid, M. and Le Boulluec, M., 2019. Control strategies for floating offshore wind turbine: challenges and trends. *Electronics*, 8(10), p.1185.
- Saouma, V.E. and Schwemmer, D., 1984. Numerical evaluation of the quarter-point crack tip element. *International Journal for Numerical Methods in Engineering*, 20(9), pp.1629-1641.
- Schijve, J., 2001. Stress intensity factors of cracks. *Fatigue of Structures and Materials*, pp.84-114.
- Schroeder, K., Ecke, W., Apitz, J., Lembke, E. and Lenschow, G., 2006. A fibre Bragg grating sensor system monitors operational load in a wind turbine rotor blade. *Measurement Science and Technology*, 17(5), p.1167.
- Schubel, P.J., Crossley, R.J., Boateng, E.K.G. and Hutchinson, J.R., 2013. Review of structural health and cure monitoring techniques for large wind turbine blades. *Renewable energy*, 51, pp.113-123.
- Schweigler, K., 2012. *Aerodynamic analysis of the nrel 5-mw wind turbine using vortex panel method* (Master's thesis).
- Seyr, H. and Muskulus, M., 2016. Safety indicators for the marine operations in the installation and operating phase of an offshore wind farm. *Energy Procedia*, 94, pp.72-81.
- Sfantos, G.K. and Aliabadi, M.H., 2007. A boundary cohesive grain element formulation for modelling intergranular microfracture in polycrystalline brittle materials. *International journal for numerical methods in engineering*, 69(8), pp.1590-1626.
- Sfantos, G.K. and Aliabadi, M.H., 2007. Multi-scale boundary element modelling of material degradation and fracture. *Computer Methods in Applied Mechanics and Engineering*, 196(7), pp.1310-1329.
- Shen, W.Z., Mikkelsen, R., Sørensen, J.N. and Bak, C., 2005. Tip loss corrections for wind turbine computations. *Wind Energy: An International Journal for Progress and Applications in Wind Power Conversion Technology*, 8(4), pp.457-475.
- Sieminski, A., 2014. International energy outlook. *Energy information administration (EIA)*, 18, pp.1-24.
- Silling, S.A. and Askari, A., 2014. Peridynamic model for fatigue cracking. *SAND2014-18590. Albuquerque: Sandia National Laboratories*.
- Silling, S.A. and Askari, E., 2005. A meshfree method based on the peridynamic model of solid mechanics. *Computers & structures*, 83(17-18), pp.1526-1535.
- Silling, S.A. and Lehoucq, R.B., 2010. Peridynamic theory of solid mechanics. *Advances in applied mechanics*, 44, pp.73-168.
- Silling, S.A., 2000. Reformulation of elasticity theory for discontinuities and long-range forces. *Journal of the Mechanics and Physics of Solids*, 48(1), pp.175-209.

- Silling, S.A., Epton, M., Weckner, O., Xu, J. and Askari, E., 2007. Peridynamic states and constitutive modeling. *Journal of elasticity*, 88(2), pp.151-184.
- Skaare, B., Nielsen, F.G., Hanson, T.D., Yttervik, R., Havmøller, O. and Rekdal, A., 2015. Analysis of measurements and simulations from the Hywind Demo floating wind turbine. *Wind Energy*, 18(6), pp.1105-1122.
- Sound and Sea Technology, 2009. Advanced Anchoring and Mooring Study.
- Standard, B., 2015. BS 7910: 2013+ A1: 2015 Guide to methods for assessing the acceptability of flaws in metallic structures. *London, UK: BSI Stand Publ.*
- Sukumar, N., Srolovitz, D.J., Baker, T.J. and Prévost, J.H., 2003. Brittle fracture in polycrystalline microstructures with the extended finite element method. *International Journal for Numerical Methods in Engineering*, 56(14), pp.2015-2037.
- Sun, C. and Jahangiri, V., 2019. Fatigue damage mitigation of offshore wind turbines under real wind and wave conditions. *Engineering Structures*, 178, pp.472-483.
- Sun, X., Huang, D. and Wu, G., 2012. The current state of offshore wind energy technology development. *Energy*, 41(1), pp.298-312.
- Swartz, R.A., Lynch, J.P., Zerbst, S., Sweetman, B. and Rolfes, R., 2010. Structural monitoring of wind turbines using wireless sensor networks. *Smart structures and systems*, 6(3), pp.183-196.
- Taheri-Behrooz, F. and Bakhshan, H., 2018. Characteristic length determination of notched woven composites. *Advanced Composite Materials*, 27(1), pp.67-83.
- Tang, J., Soua, S., Mares, C. and Gan, T.H., 2016. An experimental study of acoustic emission methodology for in service condition monitoring of wind turbine blades. *Renewable Energy*, 99, pp.170-179.
- Tauscher, S., 1981. *The correlation of fracture toughness with Charpy V-notch impact test data.* ARMY ARMAMENT RESEARCH AND DEVELOPMENT CENTER WATERVLIET NY LARGE CALIBER WEAPON SYSTEMS LAB.
- Tchakoua, P., Wamkeue, R., Ouhrouche, M., Slaoui-Hasnaoui, F., Tameghe, T.A. and Ekemb, G., 2014. Wind turbine condition monitoring: State-of-the-art review, new trends, and future challenges. *Energies*, 7(4), pp.2595-2630.
- Tcherniak, D. and Mølgaard, L.L., 2017. Active vibration-based structural health monitoring system for wind turbine blade: Demonstration on an operating Vestas V27 wind turbine. *Structural Health Monitoring*, 16(5), pp.536-550.
- Tessler, A. and Hughes, T.J., 1983. An improved treatment of transverse shear in the Mindlin-type four-node quadrilateral element. *Computer methods in applied mechanics and engineering*, 39(3), pp.311-335.

- Tessler, A. and Hughes, T.J., 1985. A three-node Mindlin plate element with improved transverse shear. *Computer Methods in Applied Mechanics and Engineering*, 50(1), pp.71-101.
- Tessler, A. and Spangler, J.L., 2003. A variational principle for reconstruction of elastic deformations in shear deformable plates and shells. NASA/TM-2003-212445.
- Tessler, A. and Spangler, J.L., 2004. Inverse FEM for full-field reconstruction of elastic deformations in shear deformable plates and shells. 2<sup>nd</sup> European Workshop on Structural Health Monitoring, 7-9 July 2004, Munich, Germany.
- Tessler, A., Spangler, J.L., Gherlone, M., Mattone, M. and Di Sciuva, M., 2012. Deformed shape and stress reconstruction in plate and shell structures undergoing large displacements: application of inverse finite element method using fiber bragg grating strains. In *Proceedings of 10th World Congress on Computational Mechanics, Sao Paulo, Brazil*.
- Thies, P.R., Johanning, L. and Smith, G.H., 2012. Lifecycle fatigue load spectrum estimation for mooring lines of a floating marine energy converter. ASME.
- Tian, S., Yang, Z., Chen, X. and Xie, Y., 2015. Damage detection based on static strain responses using FBG in a wind turbine blade. *Sensors*, 15(8), pp.19992-20005.
- Timmer, W.A. and Van Rooij, R.P.J.O.M., 2003. Summary of the Delft University wind turbine dedicated airfoils. *J. Sol. Energy Eng.*, 125(4), pp.488-496.
- Tvergaard, V. and Hutchinson, J.W., 1992. The relation between crack growth resistance and fracture process parameters in elastic-plastic solids. *Journal of the Mechanics and Physics of Solids*, 40(6), pp.1377-1397.
- Van Der Tempel, J., 2006. Design of support structures for offshore wind turbines. PhD Thesis, Technical University of Delft.
- Vazic, B., Oterkus, E., Oterkus, S., 2020. Peridynamic model for a Mindlin plate resting on a Winkler elastic foundation. *Journal of Peridynamics and Nonlocal Modeling*, pp.1–10.
- Vazic, B., Wang, H., Diyaroglu, C., Oterkus, S., Oterkus, E., 2017. Dynamic propagation of a macrocrack interacting with parallel small cracks. *AIMS Materials Science* 4(1), pp.118–136.
- Vazquez, S.L., Tessler, A., Quach, C.C., Cooper, E.G., Parks, J. and Spangler, J.L., 2005. *Structural health monitoring using high-density fiber optic strain sensor and inverse finite element methods* (No. L-19083).
- Wang, H., Oterkus, E., Oterkus, S., 2018. Predicting fracture evolution during lithiation process using peridynamics. *Engineering Fracture Mechanics* 192, 176–191.
- Wang, L., Liu, X., Renevier, N., Stables, M. and Hall, G.M., 2014. Nonlinear aeroelastic modelling for wind turbine blades based on blade element momentum theory and geometrically exact beam theory. *Energy*, 76, pp.487-501.

- Wang, L., Sheng, X. and Luo, J., 2022. A peridynamic frictional contact model for contact fatigue crack initiation and propagation. *Engineering Fracture Mechanics*, 264, p.108338.
- Wang, S., Wang, S. and Liu, J., 2019. Life-cycle green-house gas emissions of onshore and offshore wind turbines. *Journal of Cleaner Production*, 210, pp.804-810.
- Wang, X., Zeng, X., Li, J., Yang, X. and Wang, H., 2018. A review on recent advancements of substructures for offshore wind turbines. *Energy conversion and management*, 158, pp.103-119.
- Weijtjens, W., Verbelen, T., De Sitter, G. and Devriendt, C., 2016. Foundation structural health monitoring of an offshore wind turbine—a full-scale case study. *Structural Health Monitoring*, 15(4), pp.389-402.
- Wen, B., Wei, S., Wei, K., Yang, W., Peng, Z. and Chu, F., 2017. Power fluctuation and power loss of wind turbines due to wind shear and tower shadow. *Frontiers of Mechanical Engineering*, 12(3), pp.321-332.
- Wu, X., Hu, Y., Li, Y., Yang, J., Duan, L., Wang, T., Adcock, T., Jiang, Z., Gao, Z., Lin, Z. and Borthwick, A., 2019. Foundations of offshore wind turbines: A review. *Renewable and Sustainable Energy Reviews*, 104, pp.379-393.
- Yamada, Y., Ezawa, Y., Nishiguchi, I. and Okabe, M., 1979. Reconsiderations on singularity or crack tip elements. *International Journal for Numerical Methods in Engineering*, 14(10), pp.1525-1544.
- Yang, S.J. and Baeder, J.D., 2016, September. Effect of wavy trailing edge on 100meter flatback wind turbine blade. In *Journal of Physics: Conference Series* (Vol. 753, No. 2, p. 022060). IOP Publishing.
- Yang, W., Tavner, P.J., Crabtree, C.J., Feng, Y. and Qiu, Y., 2014. Wind turbine condition monitoring: technical and commercial challenges. *Wind Energy*, 17(5), pp.673-693.
- Yang, Y., Bashir, M., Wang, J., Michailides, C., Loughney, S., Armin, M., Hernández, S., Urbano, J. and Li, C., 2020. Wind-wave coupling effects on the fatigue damage of tendons for a 10 MW multi-body floating wind turbine. *Ocean Engineering*, 217, p.107909.
- Yang, Z., Oterkus, E., Nguyen, C.T., Oterkus, S., 2019. Implementation of peridynamic beam and plate formulations in finite element framework. *Continuum Mechanics and Thermodynamics* 31(1), 301–315.
- Yang, Z., Vazic, B., Diyaroglu, C., Oterkus, E., Oterkus, S., 2020. A Kirchhoff plate formulation in a state-based peridynamic framework. *Mathematics and Mechanics of Solids* 25(3), 727–738.
- Yeter, B., Garbatov, Y. and Soares, C.G., 2020. Risk-based maintenance planning of offshore wind turbine farms. *Reliability Engineering & System Safety*, 202, p.107062.

- Yi, J.H., Park, J.S., Han, S.H. and Lee, K.S., 2013. Modal identification of a jacket-type offshore structure using dynamic tilt responses and investigation of tidal effects on modal properties. *Engineering Structures*, 49, pp.767-781.
- Zarandi, E.P. and Skallerud, B.H., 2020. Cyclic behavior and strain energy-based fatigue damage analysis of mooring chains high strength steel. *Marine Structures*, 70, p.102703.
- Zeng, X. and Li, S., 2010. A multiscale cohesive zone model and simulations of fractures. *Computer methods in applied mechanics and engineering*, 199(9-12), pp.547-556.
- Zhang, C., 2018. *Reliability-based fatigue damage assessment and optimum maintenance strategy of offshore horizontal wind turbine blades* (Doctoral dissertation, University of Greenwich).
- Zhang, C., Chen, H.P. and Huang, T.L., 2018. Fatigue damage assessment of wind turbine composite blades using corrected blade element momentum theory. *Measurement*, 129, pp.102-111.
- Zhang, J., Kang, J., Sun, L. and Bai, X., 2021. Risk assessment of floating offshore wind turbines based on fuzzy fault tree analysis. *Ocean Engineering*, 239, p.109859.
- Zhu, N. and Oterkus, E., 2020. Calculation of stress intensity factor using displacement extrapolation method in peridynamic framework. *Journal of Mechanics*, 36(2), pp.235-243.
- Zhu, N., De Meo, D., Oterkus, E., 2016. Modelling of granular fracture in polycrystalline materials using ordinary state-based peridynamics. *Materials* 9(12), p.977.
- Zhu, N., Kochan, C., Oterkus, E. and Oterkus, S., 2021. Fatigue analysis of polycrystalline materials using Peridynamic Theory with a novel crack tip detection algorithm. *Ocean Engineering*, 222, p.108572.